Polymerizable ionic liquid based inhibitors; synthesis, characterization and application

By

Mona Taghavikish

(B.Eng., M.Sc)

A thesis submitted for the degree of

Doctor of Philosophy

School of Engineering: Energy and advanced manufacturing

Future Industries Institute

Division of Information Technology, Engineering and the Environment



University of South Australia

August 2016

Dedication

This thesis is dedicated to
the memory of the best chemistry teacher of my life
my father

Table of contents

Abstract vi

Abbreviations xi

Declaration xiii

Acknowledgements xiv

List of publications xvi

Chapter 1: Introduction and Literature Review 1

1.1 Introduction 1

1.2 Chemistry of Corrosion 2

1.3 Corrosion prevention methods 6

1.3.1 Cathodic protection 7

1.3.2 Anticorrosive coating 7

1.3.3 Corrosion inhibitors 8

1.4 Classification of corrosion inhibitors 8

1.4.1 Inorganic inhibitors 9

1.4.1.1 Cathodic type corrosion inhibitors 9

1.4.1.2 Anodic type corrosion inhibitors 10

1.4.2 Organic inhibitors 11

1.4.2.1 Adsorption type corrosion inhibitors 11

1.4.3 Environmentally friendly organic corrosion inhibitors (EFCIs) 13

1.5 Corrosion inhibition using Ionic liquids (ILs) 14

1.5.1 Effect of IL structure on corrosion inhibition 16

1.5.1.1 Cation effect 16

1.5.1.2 Anion effect 18

1.5.2 Synergistic corrosion inhibition using ILs 19

1.6 Introduction to polymerized ionic liquids (PILs) 20

1.6.1 Insight into synthesis and chemistry of PILs 21

1.6.1.1 Application of Thiol-ene chemistry in synthesis of PIL 22

1.6.2 PIL structural diversity 23

1.6.2.1 PIL colloidal particles 24

1.6.2.3 PIL gels 26

1.7. Mechanism of inhibitor adsorption on the carbon steel 27

1.7.1 Mechanism of adsorption of ILs and PILs on metal surface 30

1.8 Incorporation of corrosion inhibitors into the coating 32

1.9 Evaluation of corrosion inhibitors using advanced characterization techniques .. 37

1.9.1 Evaluation of corrosion performance of IL based corrosion inhibitors using electrochemical techniques 37
1.9.2 Advanced method for evaluation of adsorption behaviour of corrosion inhibitors 39
1.9.3 Advanced method for understanding the interfacial properties of the coatings 40
1.10 Aims and scope of the project 42
1.11 References 44
Chapter 2: Experimental: materials and methodology 53
2.1 Chemicals, solvents and materials 53
2.2 Chemistry of synthesis and fabrication methods 55
2.2.1 Thiol-ene chemistry 55
2.2.2 Emulsion polymerization 56
2.3 Preparation of inhibitor loaded coating and surface preparation of steel 57
2.3.1 Surface preparation of steel 57
2.3.2 Synthesis of self-assembled nanoparticle phase (SNAP) coating 58
2.3.3 Preparation of SNAP loaded PIL gel and nanoparticle based inhibitors 59
2.4 Characterization techniques 60
2.4.1 Spectroscopic techniques 60
2.4.1.1 Photo-acoustic fourier transform infrared (PA-FTIR) Spectroscopy 60
2.4.1.2 Nuclear magnetic resonance (NMR) spectroscopy 61
2.4.2 Scattering techniques 61
2.4.2.1 Dynamic light scattering (DLS) 61
2.4.3 Morphological investigation 62
2.4.3.1 Scanning electron microscopy (SEM) 62
2.4.3.2 Transmission electron microscopy (TEM) 63
2.4.4 Thermal analysis techniques 64
2.4.4.1 Differential scanning calorimetry (DSC) 64
2.4.4.2 Thermogravimetric analysis (TGA) 65
2.4.5 Mechanical testing 66
2.4.5.1 Dynamic mechanical analysis (DMA) 66
2.4.6 Wettability study - sessile drop technique 67
2.4.7. Electrochemical analysis 67
2.4.7.1. Potentiodynamic 67
2.4.7.2. Impedance spectroscopy 69
2.4.7.3 Scanning kelvin probe (SKP) 70
2.4.8 Quartz crystal microbalance (QCM) 71
2.5 References 73

Chapter 3: Facile fabrication of polymerizable ionic liquid based-gel beads via thiol−ene chemistry 75

3.1 Research article 76

3.2 Supplementary information 85

Chapter 4: Electrochemical performance of polymerized ionic liquid (PIL) based gel inhibitor in sol-gel coating 90

4.1 Abstract 91

4.2 Introduction 91

4.3 Experimental 93
4.3.1 Materials 93
4.3.2 Preparation of SNAP, SNAP loaded PIL gel inhibitor (SNAP/PIL) 93
4.3.3 Electrochemical measurements 94

4.4 Results and discussion 95
4.4.1 Electrochemical studies 95
4.4.1.1 Potentiodynamic polarization studies 96
4.4.1.2 EIS investigation 99
4.4.2 Microscopy Analysis 104
4.4.3 SKP measurements 106

4.5 Conclusion 109

4.6 References 110

Chapter 5: Polymeric ionic liquid nanoparticle emulsion as corrosion inhibitor in anticorrosion coating 112

5.1 Abstract 113

5.2 Introduction 113

5.3 Experimental 115
5.3.1 Materials 115
5.3.2 Synthesis of 1,4-Di(vinyl imidazolium)butane Bisbromide 116
5.3.3 Miniemulsion thiol−ene photopolymerization 116
5.3.4 Preparation of the PIL nanoparticles based coating 118
5.3.5 Characterization 118

5.4 Result and discussion 120
5.4.1 PIL nanoparticles by miniemulsion photo-polymerisation 120
5.4.2 Structure and morphology study of PIL nanoparticles 122
5.4.3 Phase behaviour of PIL nanoparticles 125

5.5 Evaluation of corrosion resistance 127
5.5.1 Potentiodynamic polarization studies 127
5.5.2 EIS investigation 130

5.6 Surface characterization 133

5.7 Wettability study on coated substrate with Wilhelmy Balance technique 135
5.8 Conclusion 138
5.9 Reference 139
Chapter 6: Fundamental understanding of inhibitive effect and adsorption behaviour of various ILs and PILs 141
6.1 Abstract 142
6.2 Introduction 142
6.3 Experimental 144
6.3.1 Materials 144
6.3.2 Synthesis of 1,4-di(vinyl imidazolium)butane bisbromide (IL1) 144
6.3.3 Synthesis of 1,6-di-(3-vinylimidazolium) hexane dibromide $[C_6(VIm)_2][Br]_2$ (IL2) 144
6.3.4 Synthesis of 1,8-di-(3-vinylimidazolium) octane dibromide $[C_8(vim)_2][Br]_2$ (IL3) 145
6.3.5 Fabrication of different chain length PILs 145
6.4 Characterizations 146
6.5 Results and discussion 147
6.5.1 Characterization of the effect of various spacer chain length of IL on PIL gels: Compositional and phase behaviour 147
6.5.1.1 Compositional analysis by TGA 147
6.5.1.2 Phase behaviour of various gels 148
6.5.2 Adsorption study of various ILs using QCM-D 149
6.5.3 Adsorption mechanism and rate of the adsorption 153
6.5.4 Inhibition effect and adsorption study using PIL gel 156
6.6 Conclusion 162
6.7 Reference 163
Chapter 7: Novel Thiol-Ene Hybrid Coating for Metal Protection 165
7.1 Research article 166
Chapter 8: Summary and Recommendations 181
8.1 Summary 181
8.2 Recommendations 184

Abstract

The use of corrosion inhibitors is one of the most effective ways of protecting metal surfaces against corrosion. Their effectiveness is related to the chemical composition, molecular structures, and affinities for adsorption on the metal surface. Organic compounds containing heteroatoms like N, O and S play an important role in inhibition due to the free electron pairs they possess. Also, electronegative functional groups and π-electrons in conjugated double or triple bonds generally exhibit good inhibitive properties by supplying electrons via π orbitals. When both these features are combined in a single compound, increased inhibition can be observed. Ionic liquids (ILs) are compounds that can possess such combined features in their structure. Ionic liquids are also known to provide inhibition effect for various metals and alloys, forming an adsorbed flexible film at interfaces and reducing both interfacial tension and the wetting of aggressive media on steel surfaces. While significant work has been done with direct delivery of IL in solution, however, the use of such IL inhibitors in polymeric form offers a sustainable approach with significant opportunity for effective long term protection of metals. Polymerized ionic liquids (PILs) containing both heteroatoms such as sulphur, phosphorus, and nitrogen as well as heterocyclic rings have the potential to be highly suitable candidates as controlled delivery inhibitors to reduce or arrest corrosion. However, so far very little in-depth work has been done on these PILs. A combination of vinyl imidazolium-based ILs with thiol containing compounds has the potential to offer a powerful platform to develop such corrosion inhibitors for metal protection. The facile fabrication of such PILs will also represent a significant step towards the advancement of corrosion inhibitors. With this aim, this PhD thesis explores and presents a strategic route of click chemistry for synthesis of a new class of polymerizable ionic liquid-based corrosion inhibitors in three different forms; gels, nanoparticles, and hybrid films. Thiol-ene based click chemistry provides a powerful platform to combine thiol with the imidazole and nitrogen containing polymerizable IL monomer. PILs were thus fabricated in all three forms using thiol-ene click chemistry. A fundamental understanding of the structure-property relationship of these PILs has been developed using advanced characterization tools, and their performances as corrosion inhibitors have been evaluated with a sol-gel coating.

The thesis is presented in 8 chapters. Chapter 1 gives an introduction to the fundamentals of corrosion and the different types of corrosion protection methods with major focus on corrosion

inhibition. Various types of corrosion inhibitors and their associated adsorption mechanism are presented. Next, a brief introduction to ILs and PILs, their synthesis, physical and chemical properties, and finally the structural diversity of PILs with various cation and anion effect is presented based on a review of earlier works from the literature. A brief introduction to sol-gel coating is then presented, including the incorporation of corrosion inhibitors in such coatings, their limitations, and finally the current state of research and development used for performance study of corrosion inhibitors. In the last section, the aims and scope of the present research are discussed.

Chapter 2 outlines and summarises the materials, synthesis, and fabrication methods used in this research. Also, the working principles of different instruments, including spectroscopic, microscopic, and thermal analysis techniques are discussed. Furthermore, the details of the electrochemical methods used to assess the corrosion inhibition performance of the materials and evaluate their potential for fabricating advanced coatings with improved barrier function and corrosion protection are presented.

In Chapter 3 the novel and facile preparation of multifunctional PIL-based gel using thiol-ene click chemistry is presented. A detailed study into the effect of reactant ratios is examined. The gel formation is confirmed through fourier transform infrared spectroscopy (FTIR), thermal analysis, and kinetic studies. These gels also show self-healing characteristics because of their rubbery nature. The PIL gels also demonstrate the ability to uptake active molecules such as small molecular corrosion inhibitors with additional capabilities such as pH sensing or controlled release of active anticorrosion agents. This work provides new insight into the ability of the PIL based gel beads for the control, detection and inhibition of corrosion.

Chapter 4 investigates the inhibition effects of PIL gel based corrosion inhibitors in a self-assembled nanophase particles (SNAP) coating on mild steel substrates. A detailed study into the effect of the PIL gel as a corrosion inhibitor on the protection of metal is presented using a range of techniques, including potentiodynamic polarization and electrochemical impedance spectroscopy (EIS). Also, scanning kelvin probe (SKP) measurements were carried out to establish further understanding on the interfacial properties of the coatings. The present work confirms that the addition of PIL gel particles to the SNAP coating in the interfacial layer of the coating provides the steel substrate with an additional protection, which reinforces the inherent barrier properties of this layer. The corrosion studies using electrochemical techniques demonstrated the potential for these PIL gels in corrosion inhibition applications. This work

provides a unique way of applying the PIL corrosion inhibitors in a coating, which has not been previously demonstrated.

Chapter 5 demonstrates the facile preparation of crosslinked polymerizable ionic liquid (PIL)-based nanoparticles via thiol-ene photo-polymerization in a mini-emulsion process for the first time. Also, the PIL nanoparticles have been characterised using a range of techniques, including fourier transform infrared spectroscopy (FTIR), thermogravimetric analysis (TGA), scanning electron microscopy (SEM), and transmission electron microscopy (TEM). The electrochemical investigation on the application of the PIL nanoparticles as an inhibitor in a SNAP coating highlights the corrosion protection ability of the resultant coating. This work provides another new and rapid way for the synthesis of PIL based nanoparticle corrosion inhibitors, which enhances the corrosion protection ability of SNAP-based coatings.

Chapter 6 is concerned with understanding of the mechanism and differences in inhibition effect of ILs and PIL using three different imidazolium ILs with different alkyl chain lengths through their adsorption behaviour study as corrosion inhibitors onto steel surface. Adsorption behaviour of IL corrosion inhibitors on the steel surface were studied using quartz crystal microbalance with dissipation (QCM-D). This unique technique has not been applied before for inhibitor adsorption study. This study demonstrates that all three ILs form adsorbed layers on the metal surface and inhibit corrosion in the experimental timescale. The ILs with longer alkyl chain length as the spacer between imidazolium groups and higher concentrations show higher inhibition effect compared to that with shorter chain length. The PILs fabricated using thiol-ene chemistry showed corrosion inhibition behaviour for prolonged time. The difference in inhibition effect is due to the different structure of IL and PILs. The presence of thiols in PIL increases the inhibition effect of PILs.

In chapter 7 the formation of a unique hybrid interfacial network combining the functionalities of sol-gel, thiol-ene chemistry, and PIL is presented for the first time. In this study, a multilayered thin film coating was formed by the application of a SNAP coating on top of a PIL hybrid film for better corrosion protection. A detailed characterisation of the novel PIL hybrid film's surface morphology and thermal properties using, SEM, DSC, and TGA is presented. In-depth understanding on the completion of the condensation reaction is investigated using FTIR and solid state NMR. Furthermore, the anticorrosion property of the PIL hybrid film was examined using potentiodynamic polarization and electrochemical impedance spectroscopy (EIS). The results show an enhanced corrosion protection of the metal surface which makes this

PIL hybrid film a promising candidate for use as an interfacial layer in anti-corrosion applications. This work provides new insights into the application PILs in the formation of thin film hybrid coating for multilayer coating application.

Chapter 8 summarizes and concludes the study and presents some future recommendations. The work presented in this thesis demonstrates that PIL corrosion inhibitors containing various heteroatoms can be employed in various forms (gels, nanoparticles, and hybrid films) for corrosion protection applications, providing higher barrier properties and improved protection of metal surfaces. The current work has established a platform for the formation of new generation of PIL based corrosion inhibitors and there is significant scope to further develop new structures of PIL based corrosion inhibitors and study their behaviour in the protection of metals from corrosion.

List of Abbreviations and Symbols

|Z|	Impedance modulus
µs	Microsiemens
$A.cm^{-2}$	Ampere/square meter
AIBN	Azobis(isobutyronitrile)
BP	Benzophenone
CPD	Contact potential
CPE_{coat}	Coating capacitance
CPE_{int}	Interfacial capacitance
D_2O	Deuterium oxide
DDW	Double distilled water
DLS	Dynamic light scattering
DMA	Dynamic mechanical analysis
DMF	N,N'-dimethylformamide
DSC	Differential scanning calorimetry
DVIMBr	1,4-di(vinyl imidazolium)butane bisbromide
E_{corr}	Corrosion potential
EDS	Energy dispersive spectroscopy
E_I	Inhibitor efficiency
EIS	Electrochemical impedance spectroscopy
EIS	Impedance spectroscopy
eV	Electron volt
F	Farad
GPTMS	Glycidoxy propyl trimethoxy silane
I'_{corr}	Inhibited corrosion current
I_{corr}	Uninhibited corrosion current
I_{corr}	Corrosion current
ILs	Ionic liquids
ITO	Indium tin oxide
kΩ	Kilo ohm
meV	Mega electron volt

mN/m	Milli newton/millimetre
mPas	Mega Pascal
MPTS	3-methacryloxypropyltrimethoxysilan
n	Overtone number
NMR	Nuclear magnetic resonance
OCP	Open circuit potential
P	Porosity
PA-FTIR	Photo-acoustic fourier transform infrared
PETKMP	Pentaerythritol tetrakis(3-mercaptopropionate
PILs	Polymerized ionic liquids
Q	Pseudo capacitance
QCM-D	Quartz crystal microbalance with dissipation
R_{coat}	Coating resistance
R_{int}	Interfacial resistance
Rp	Polarization resistances
R_{ps}	Polarization resistances of the uncoated steel
R_s	Solution resistance
SCE	Saturated calomel electrode
SDS	Sodium dodecyl sulfate
SEM	Scanning electron microscopy
SKP	Scanning kelvin probe
SNAP	Self-assembled nanophase particle
T	Absolute temperature
TEM	Transmission electron microscopy
TEOS	Tetraethylorthosilicate
TEOS	Tetraethylorthosilicat
Tg	Glass transition temperature
TGA	Thermogravimetric analysis
WF	Work function
β	Anodic Tafel slope
ΔD	Dissipation changes
Δf	Variation in frequency
Δm	Adsorbed mass

Declaration

I declare that this thesis does not incorporate without acknowledgement any material previously submitted for a degree or diploma in any university. To the best of my knowledge it does not contain any materials previously published or written by another person except where due reference is made in the text; and all contributions by others to the work presented, including jointly authored publications, are clearly acknowledged.

Mona Taghavikish

Acknowledgments

First, I would like to express my sincere gratitude to my supervisor, Professor Namita Roy Choudhury and my co-supervisor, Professor Naba Dutta for their tremendous academic support during my PhD. I appreciate all your contributions of ideas, time, and funding to make my PhD experience productive and stimulating. Finishing my PhD journey would not have been possible without both of your support, and I thank you sincerely for that. I would also like to especially thank Dr. Surya Subianto for his scientific advice and knowledge and many insightful discussions and suggestions. He was my primary resource for getting my questions answered. Thanks for being such a helpful co-worker.

In addition, I would like to thank all of the administration and technical support staff at the Wark, including Louise Jennings, Scott Abbott and Andrew Robinson, John Denman and Nobuyuki Kawashima for their assistance for instrument training and administration matters. I am also grateful to the Wark, Future Industries Institute, UniSA, Wave rider Energy and the Australian Research Council (ARC) for financial support during my PhD through scholarship and project funding. Very special thanks to Louise Jennings for all of her kind supports before I start my program and thereafter. You were the solution for everything for international students with your up to date knowledge, and following up every single issue we had. Words cannot express my gratitude to you, Thank you for being such a great lady.

I am very fortunate and thankful to have Jasmin Whittiker, Xuan Wu, Raj Balun and Surya Subianto in my research group who have been my friends; constantly supporting and motivating me during my PhD. Thanks Raj for being a solution for everything during this journey, you are the most patient person I have ever seen. Jasmin and Xuan, these two friends formed the core of my research time. I couldn't have survived without them. I know that I could always ask them for advice and opinions on everything. Jasmin, my Australian sister, you are a wonderful friend that backed me up and shared with me all of my hardships and happiness and I admire your positive support during all of my difficult times. I'll never forget the many wonderful lunches and fun activities we've done together, especially that beautiful night in Mount Lofty. You were the one who was there for me during the thesis writing and messaging me and reminding me the

happy end of this journey. I know that when we are old, you will still be there as a supportive and caring friend. Xuan, I feel lucky to have known you and I am grateful for knowing that you are always there for me.

I especially thank my mom, dad, and my brother. My hard-working parents have sacrificed their lives for my brother and myself and provided unconditional love and care. Love them so much, and I would not have made it this far in life without them. I know dad, you will hear me now when I am writing these gratitude sentences to you. I know you always wanted me to do my PhD and I hope you hear me in the heaven now; I did it because of you. I can't say how much I wanted you to be here and to be proud of your little girl. Love you dad and wish you will be happy with me now even more. My beautiful mom, I always feel so sorry to leave you alone back home but I feel this PhD was the only thing that encourages you to bare that much loneliness. So I tried my best to finish it in the best way I could. My lovely brother has been my best friend all my life and I love you dearly and thank you for all the advice and support. Special thanks my greater family members, Azam, Helen and Davood who all have been supportive and caring. Azam and Helen, thanks to be there for me and to help me with your positive feedbacks in my stressful times.

Last but not least, thank you my best friend, my soul-mate and husband. I have married the best person out there for me. There are no words to convey how much I love you. Houman has been a true and great supporter and have unconditionally loved me during my good and bad times. You had faith in me and my intellect even when I felt like digging a hole and crawling into one because I didn't have faith in myself. These past several years have not been an easy ride, both academically and personally for both of us. I truly appreciate your kindness, support and patience and thank you for sticking by my side even when I was irritable and depressed. I feel that we both learned a lot about life and strengthened our commitment and determination to each other and to live life to the fullest. I love you more than anything in the world and I couldn't have done it without you.

List of publications

Journal articles

1) Taghavikish, M., Subianto, S., Dutta, N., de Campo, L., Mata, J., Rehm, C. and Roy Choudhury, N. Polymeric ionic liquid nanoparticle emulsions as a corrosion inhibitor in anticorrosion coatings. *ACS omega* **2016**, 1, 29-40.
2) Taghavikish, M., Subianto, S., Dutta, N., Roy Choudhury, N. Novel thiol-ene hybrid coating for metal protection. Coatings **2016**, 6, 17.
3) Taghavikish, M., Subianto, S., Dutta, N. K., Choudhury, N. R. Facile fabrication of polymerizable ionic liquid based-gel beads via thiol–ene chemistry. *ACS Applied Materials & Interfaces* **2015,** *7*, 17298-17306.
4) Taghavikish, M., Subianto, S., Gu, Y., Sun, X., Zhao, X., S., and N. Roy Choudhury. Poly(ionic liquid)-based gel electrolyte for electric double-layer capacitors. *To be submitted for peer review publication*
5) Taghavikish, M., Subianto, S., Dutta, N., Roy Choudhury, N. Electrochemical performance of polymerizable ionic liquid (PIL) based inhibitor in sol-gel coating. *To be submitted to ACS, Industrial & Engineering Chemistry Research for peer review publication*
6) Taghavikish, M., Subianto, S., Larsson, M., Dutta, N., Roy Choudhury, N. Fundamental understanding of inhibitive effect and adsorption behaviour of various ILs and PILs. *To be submitted for peer review publication*

Conference publications

7) Taghavikish, M.; Thiol-ene chemistry micro-bead based anticorrosion coating, RACI National Congress, Adelaide, SA. 7-12 December 2014. Published in conference proceedings
8) Taghavikish, M., Dutta, N., Roy Choudhury, Engineering microgel beads for self-healing coating, 248th American Chemical Society, ACS National Meeting, San Francisco, California, August 10-14, 2014.(Invited)

Chapter 1: Introduction and Literature Review

1.1 Introduction

Corrosion is the deterioration of materials through chemical interaction with their environment. The consequences of corrosion are significant and it affects our society on a daily basis, causing degradation and damage to household appliances, automobiles, airplanes, highway bridges, energy production and distribution systems, and much more. According to the recent U.S. corrosion study, the direct cost of metallic corrosion is $276 billion on an annual basis (Figure 1.1). This represents 3.1% of the U.S. Gross Domestic Product (GDP).[1] In Australia, a recent study suggests that corrosion may be costing the Australian economy more than $30 billion each year which is more than $1,500 per capita.[2]

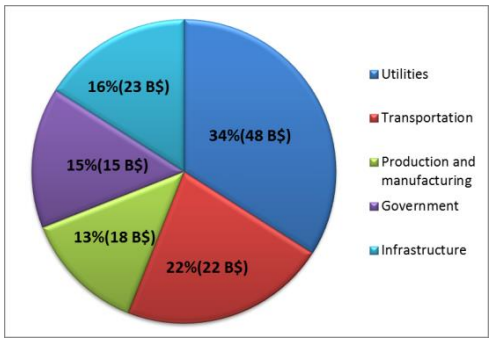


Figure 1.1 Corrosion costs breakdown across industrial sectors.[2]

When iron or steel is exposed to atmospheric oxygen in the presence of water, corrosion takes place. Corrosion is an electrochemical two-step process involving the flow of charges (electrons and ions), and occurs in both wet and dry conditions. It can be initiated when there is a potential difference between two surfaces (or two areas of one surface) and an electrolyte to conduct a current between them. This allows a flow of ions followed by removal of the material (corrosion). Generally, dry corrosion is a very slow reaction and is not a problem at room temperature, while wet corrosion is the major type of corrosion, which occurs at or near room temperature and in the presence of water. Many methods have been used to prevent/mitigate corrosion process such as upgrading the materials, blending of production fluids, process control and the use of corrosion inhibitors.[3-4] Among these methods, the use of corrosion inhibitors is one of the best known methods for corrosion protection due to its low cost and practicality.[5-6]

A corrosion inhibitor works by "passivating" the surface of the material, forming a monolayer on it, which then blocks the electrolyte from contacting the surface and conducting a current. In addition, the corrosion inhibitor acts as a buffer solution which controls pH, thus preventing changes of the pH of the electrolyte which would allow faster corrosion. When choosing a corrosion inhibitor for a particular application, several things need to be considered, including the materials to be protected, the type of protection required (in process, storage or shipping), protection effectiveness timeframe, method of application (dip, spray, brush, etc.), interaction with subsequent processes, (for example coating), type of product (oil/solvent or water-based), and environmental health and safety requirements. The most widely used inhibitors contain chromate and phosphate. Although chromate is an effective inhibitor that provides immediate repair in defects and long-term corrosion protection to the underlying metal, its usage is restricted or gradually reduced in many countries due to their high environmental toxicity.[7-8] As a consequence, there is an ongoing challenge in recent years to develop a new class of corrosion inhibitors with low toxicity, eco-friendliness and good efficiency, in order to find a replacement for chromate coatings.

1.2 Chemistry of Corrosion

Generally all corrosion reactions are electrochemical in nature. For example, in iron, at the anodic sites on the metal surface the iron flows into the solution as ferrous ions, establishing the anodic reaction. At the cathodic sites the electrons react with some reducible component of the electrolyte and are themselves removed from the metal. According to Faraday's Laws the rates of the anodic and the cathodic reactions must be equivalent in which the total flow of electrons from anodes to cathodes, which is called the "corrosion current", I_{corr} which can be determined experimentally. Figure 1.2,[9] shows the chemistry of the wet corrosion at active sites.

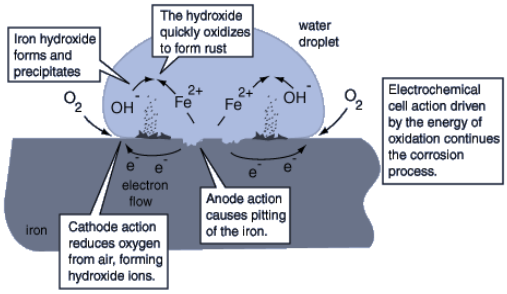


Figure 1.2 Schematic diagram of structure of corrosion cells on iron.[9]

Where the metal is under stress on the anode side, iron atoms lose electrons and become ferrous ions. This process is called a half-cell oxidation reaction, or the anodic reaction. This is followed by the reaction at the cathode called a reduction reaction where the electrons migrate to another location and are taken up by a depolarizer such as Oxygen. The resulting hydroxide ions react with the Fe^{2+} to form the mixture of hydrous iron oxides known as rust (Eq.1). [10-11]

$$2Fe^{2+} + 4OH^{-} \rightarrow 2Fe(OH)_2 \qquad \text{Eq.1}$$

The potential difference at the interface between a metallic electrode and an electrolyte solution is the key factor to control both the products of an electrode reaction and the rate at which they are formed. The potential difference itself is formed by layers of charges at the surface, which is caused by the electrons in the metal and the excess anions or cations in the solution. This layers of charges is known as the double layer or the Helmholtz layer (Figure 1.3). The Helmholtz double layer is formed by two planar sheets of charges. One is due to the ions in solution adsorbed at the surface of the solid; the other is due to the ions of opposite charge attracted by adsorbed ions.[12-13]

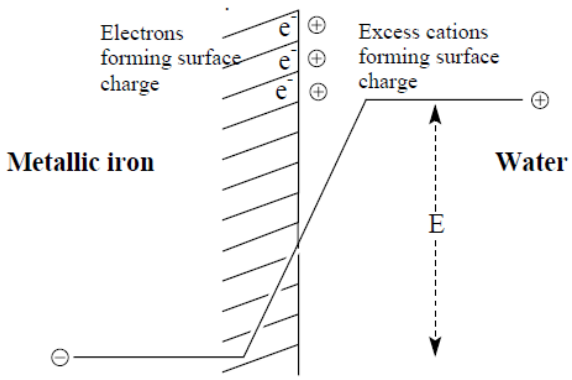


Figure 1.3 Schematic of electric double layer at a metal surface.[12]

Figure 1.4 illustrates the electrode potential's role in explaining the products of corrosion reactions. This figure shows the equilibrium diagram on iron in which the corrosion products are presented as a function of electrode potential and pH at room temperature in the presence of water as the solvent. At negative potentials, metallic iron itself is thermodynamically stable and immune to corrosion, which is referred to the immunity condition. At higher potentials and acidic pH, ferrous ions will form, giving rise to active corrosion. Ferric ions are produced only at potentials above 0.7 V. In the

alkaline pH range, insoluble surface oxides will form. At more positive potentials, the oxide formed is Fe_2O_3 and is usually present as a thin adherent film. This oxide formed at the surface is able to block the surface reactions and reduce the corrosion rate. This is called passivation and the oxide film on the surface is known as a passive layer. The corrosion rate is very low in the passivation region (Figure 1.4).[13] The information in this diagram can be used for controlling corrosion of pure metals in aqueous environments. However, the diagram does not tell the rate of corrosion, which is important information required in a practical situation.

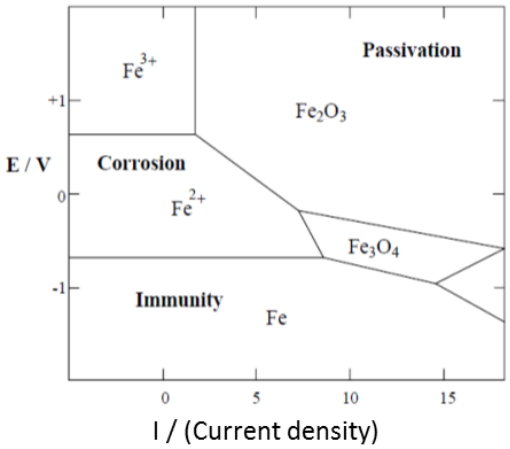


Figure 1.4 Iron equilibrium diagram.[13]

In order to understand the rate of the corrosion process, a study of the mechanism of the corrosion cell is required. Figure 1.5 illustrates the mechanism of the corrosion cell using the Evans diagram.[14] As shown in Figure 1.5, E_a shows the single potential for metal/metal ion equilibria at the anode, and E_C shows the single potential for H_2/H^+, or for O_2/OH^- equilibria at the cathode. The single potential is given by the Nernst equation, which is

$$E = E^0 + \frac{RT}{nf} Ln\, a \qquad \text{Eq.2}$$

where E is the single potential, E^o is the standard single potential, R is the gas constant, T is the absolute temperature, n is the charge on the ion, F is the Faraday constant, and a is the activity of the ion.

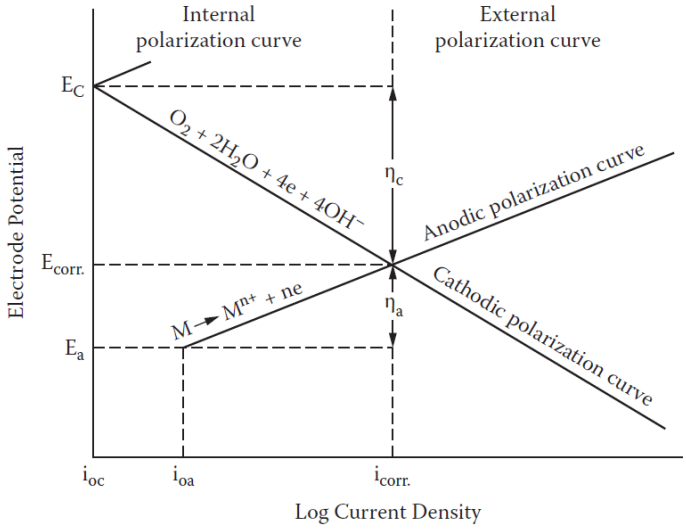


Figure 1.5 Mechanism of the corrosion cell.[14]

When "a" is equal to 1, E is equal to E^o. The standard single potential is E^o and it shows the degree of activity. Table 1.1 shows the standard single potential of various metals.[15] When the electromotive force ($E_C - E_a$) is applied, the corrosion circuit is formed followed by a current flow between the anode and the cathode. As a result, the anode electrode potential is shifted to the noble direction and the cathodic electrode potential is shifted to the less noble direction. The behaviours of these electrode potentials are called anodic and cathodic polarization. Each reaction-rate curve is called an anodic or cathodic polarization curve. The polarization diagram can be used to predict changes of corrosion rate. The intersection of anodic and cathodic polarization curves shows the corrosion potential, E_{corr} and the corrosion current, I_{corr}. The polarization curves in the current density range smaller than I_{corr} are called internal polarization curves and those in the current density range higher than I_{corr} are called external polarization curves.[15] The difference in potential between E_{corr} and E_a or between E_{corr} and E_C is called the anodic overpotential or the cathodic overpotential, and is expressed by η_a or η_c; that is,

$$\eta_a = E_{corr} - Ea \qquad \eta a > 0 \qquad \text{Eq.3}$$

$$\eta_c = E_{corr} - E_C \qquad \eta_c < 0 \qquad \text{Eq.4}$$

The importance of anodic and cathodic overpotential is to determine the corrosion rate, which is determined by the slopes of two polarization curves. When the cell circuit is formed, the corrosion reaction starts. That is,

$$E_c - E_a = |\eta_c| + \eta_a + I_{corr} R \qquad \text{Eq.5}$$

where R is the resistance of the electrolyte between the anode and cathode.

Table 1.1 Electrochemical potential series.[15]

Standard Single Potentials, E^o

Active		Inert	
Electrode (V, SHE, 25°C)	E^o	Electrode (V, SHE, 25°C)	E^o
Li/Li^+	–3.01	Mo/Mo^{3+}	–0.2
Rb/Rb^+	–2.98	Sn/Sn^{2+}	–0.140
Cs/Cs^+	–2.92	Pb/Pb^{2+}	–0.126
K/K^+	–2.92	H_2/H^+	±0
Ba/Ba^{2+}	–2.92	Bi/BiO^+	+0.32
Sr/Sr^{2+}	–2.89	Cu/Cu^{2+}	+0.34
Ca/Ca^+	–2.84	Cu/Cu^+	+0.52
Na/Na^+	–2.71	Rh/Rh^{2+}	+0.6
Mg/Mg^{2+}	–2.38	Hg/Hg^+	+0.798
Th/Th^{4+}	–2.10	Ag/Ag^+	+0.799
Ti/Ti^{2+}	–1.75	Pd/Pd^{2+}	+0.83
Be/Be^{2+}	–1.70	Ir/Ir^{3+}	+1.0
$A1/A1^{3+}$	–1.66	Pt/Pt^{2+}	+1.2
V/V^{2+}	–0.5	Au/Au^{3+}	+1.42
Mn/Mn^{2+}	–1.05	Au/Au^+	+1.7
Zn/Zn^{2+}	–0.763	O_2/OH^-	+0.401
Cr/Cr^{3+}	–0.71	I^2/I^-	+0.536
Fe/Fe^{2+}	–0.44	Br_2/Br^-	+1.066
Cd/Cd^{2+}	–0.402	Cl_2/Cl^-	+1.356
In/In^{3+}	–0.34	F_2/F^-	+2.85
Ti/Ti^+	–0.355	S/S^{2-}	–0.51
Co/Co^{2+}	–0.27	Se/Se^{2+}	–0.78
Ni/Ni^{2+}	–0.23	Te/Te^{2+}	–0.92

In order to control the rate of the corrosion, several preventive methods are employed, which will be discussed in following sections.

1.3 Corrosion prevention methods

By impeding either the anodic or cathodic reactions the rate of corrosion can be reduced. This can be achieved in several ways including:[14-16]

1. Cathodic protection
2. Protection with anticorrosive coating
3. Corrosion inhibitors

1.3.1 Cathodic protection

Cathodic protection is one of the effective methods of corrosion control and could be achieved in either of two ways: by the use of an applied current from an electrical source to change the amount of charge on the metal surface or by the use of sacrificial anodes (galvanic action). The principle of cathodic protection is to change the electrode potential of the metal so that it lies in the immunity region. Sacrificial anodes achieve this by making the corrosion potential more negative than that of the substrate thus increasing the cathodic overpotential of the surface. The metals that could be used for cathodic control protection for iron are zinc, aluminium, manganese, cadmium, and their alloys, of which the electrode potentials are more negative than those of the iron or steel. As a result, the layers of these metals act as sacrificial anodes for iron and steel substrates when the substrates are exposed to the environment. These metals are called sacrificial metals.[14]

1.3.2 Anticorrosive coating

Anticorrosive coating is the oldest and most widely used method of corrosion protection. It acts by forming a physical barrier between the corrosive environments and the metal. Anticorrosive coatings are classified based on the mechanism of their protection.[17] Generally, three different mechanisms have been used in corrosion protection: 1) barrier protection that create a barrier for corrosive species; 2) sacrificial protection that uses cathodic protection, impressed current or sacrificial anodes; 3) passivation by formation of nonreactive layer on metal surface.[18] This method of protection can be applied only to metals and alloys that exhibit active-passive behaviour.[10-11] A typical protective coating usually consists of an interfacial layer that can act as functional corrosion prevention layer, a primer and a topcoat acting as barrier element of the coating against the diffusion of small molecules such as oxygen, water and corrosive species to the metal surface. Figure 1.6 shows a typical multilayered protective coating. Interfacial layers play a major and crucial role in protective coating system. The role of the interfacial layer is to protect the substrate from corrosion and

provide good adhesion to the substrate. Interfacial layers are typically a thin film, 10–40 μm in thickness.

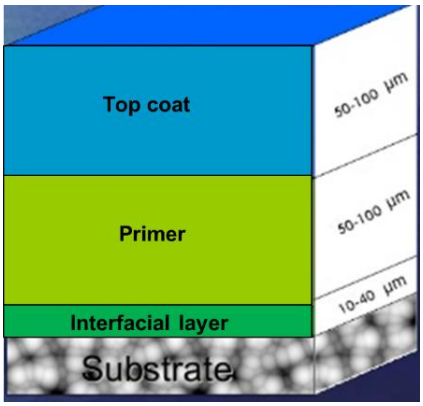


Figure 1.6 A typical multilayered protective coating system.

1.3.3 Corrosion inhibitors

Corrosion processes, being surface reactions, can be controlled by adding a corrosion inhibitor in very small concentration to an interfacial layer to prevent or reduce the corrosion rate of a metal exposed in aggressive environment. Corrosion inhibitors are normally only one molecular layer thick and are attached directly to the surface, and does not penetrate into the bulk of the metal itself.[19] Generally there are three mechanisms of the corrosion inhibitors that are cited below:

1. Adsorption: the inhibitor is chemically adsorbed on the surface of the metal and forms a protective thin film with inhibitor effect.
2. Surface layer: formation of an oxide film for protection of the metal surface.
3. Passivation: the inhibitor reacts with corrosive elements of aqueous media, forming protective precipitates.

Based on the mechanism of corrosion inhibitors, they can be classified to three different types, which will be discussed in the next section

1.4 Classification of corrosion inhibitors

Corrosion inhibitors are classified into three types based on their protection mechanism: cathodic, anodic, and mixed or adsorption type inhibitors. Corrosion inhibitors that delay the cathodic reaction are known as cathodic inhibitors. Similarly, the inhibitors that retard the anodic reaction are known as anodic inhibitors. Some compounds that

affect both the cathodic and the anodic reactions are known as mixed inhibitors, and these inhibitors generally work by an adsorption mechanism and known as adsorption inhibitors. In general, inorganic inhibitors have either cathodic or anodic actions, while organic inhibitors have both cathodic and anodic actions. (Figure 1.7).[20]

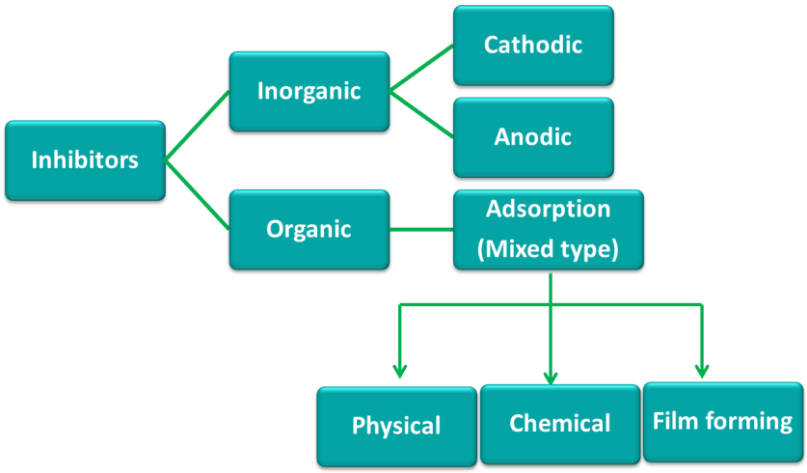


Figure 1.7 Classification of corrosion inhibitors.

1.4.1 Inorganic inhibitors

1.4.1.1 Cathodic type corrosion inhibitors

Cathodic type corrosion inhibition mechanism is based on restricting the metal contact with the environment. In this method the cathodic reaction of the metal is prevented by either slowing the cathodic reaction itself or forming a barrier on cathodic areas over the metal by producing insoluble compounds.[21] Figure 1.8 illustrates the mechanism of cathodic inhibitors to prevent corrosion and an example of a polarization curve of the metal on the solution with and without a cathodic inhibitor. The cathodic inhibitors change the corrosion potential to more negative values.[20] Some examples of cathodic inhibitors are sulfite and bisulfite ions, tannins, lignins, and calcium salts.[22]

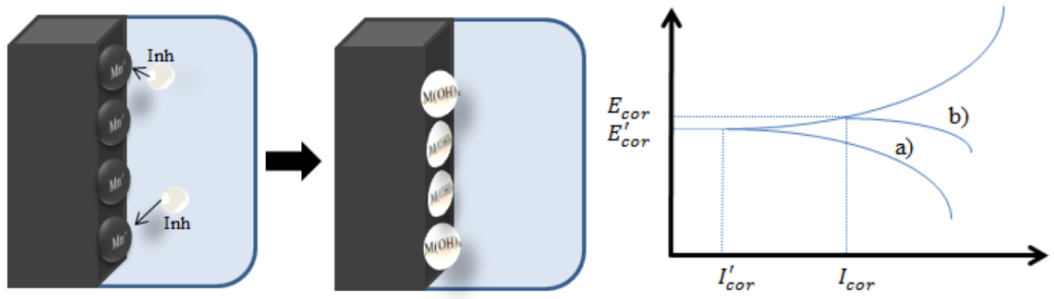


Figure 1.8 Illustration of the mechanism of the cathodic inhibitors and potentiostatic polarization diagram of the metal in (a) a solution with cathodic inhibitors and (b) same solution, without inhibitors.[20]

1.4.1.2 Anodic type corrosion inhibitors

Anodic inhibitors which are known as passivators, protect the metal surface from corrosion by reacting with the corrosion product and forming a protective oxide film on the surface of the metal (Figure 1.9). Hence, they cause a large anodic shift of the corrosion potential by blocking the anodic reaction and supporting the natural reaction of passivation of the metal surface. Chromates, nitrates, tungstate, molybdates are some examples of anodic inhibitors.[22-23] Figure 1.9 shows a potentiostatic polarization diagram of a solution with and without anodic inhibitor. It can be seen that the corrosion potential of the metal is moved to more positive values and the value of the current in the curve decreases with the presence of the corrosion inhibitor.

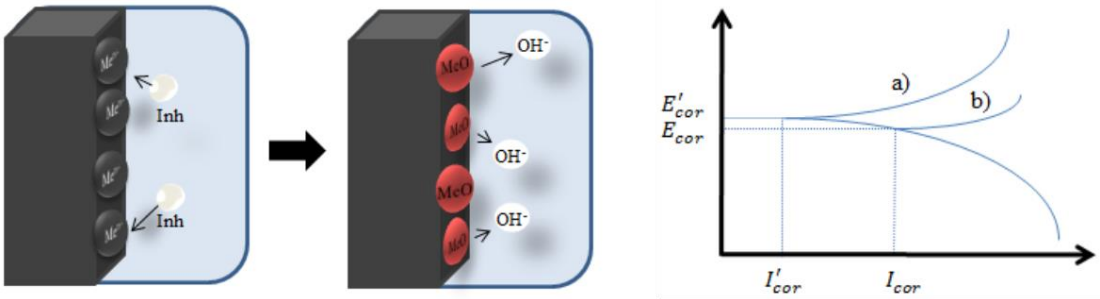


Figure 1.9 Illustration of the mechanism of the anodic inhibitors and potentiostatic polarization diagram of the metal in the presence of (a) anodic inhibitors solution and (b) same solution, without inhibitor.[20]

Although inorganic corrosion inhibitors have been found effective as inhibitors and are believed to exhibit good protection against corrosion, a major disadvantage is their toxicity, particularly those based on heavy metal ions such as chromium.

1.4.2 Organic inhibitors

1.4.2.1 Adsorption type corrosion inhibitors

Generally, the inorganic inhibitors are either cathodic or anodic inhibitors whereas; the organics inhibitors are adsorption or mixed inhibitors. Molecular organic inhibitors work by an adsorption mechanism in which the adsorption of the inhibitor molecule at the metal-solution interface result in a change of potential difference between the metal electrode and the solution. Thus, it forms the non-uniform distribution of electric charges at the interface. Subsequently, the resultant film of inhibitor molecules protects the surface from the corrosive environment either by physically blocking or by delaying the electrochemical processes. The metal-electrolyte interface is characterized by an electrical double layer. A schematic representation of the electrical double layer is given in Figure 1.3. Organic inhibitors generally contain heteroatoms (S, O, or N) and their efficiency is related to the presence of these atoms in the molecule as well as heterocyclic compounds and π electrons. This is due to the fact that O, N, and S are found to have higher basicity and electron density and are the key active centres for the adsorption process on the metal surface.[24]

Adsorption inhibitors protect the metal following three possible ways: 1) physical adsorption, 2) chemical adsorption and 3) film formation (Figure 1.7). Physical (or electrostatic) adsorption is a result of electrostatic attraction between the inhibitor and the metal surface. Physically adsorbed inhibitors interact rapidly, but they are also easily removed from the surface. The most effective inhibitors are those that chemically adsorbed (chemisorbed). Chemisorption occurs as a result of charge sharing or charge transfer between the inhibitor molecules and the metal surface. However, chemisorption is slower than physical adsorption process and is not completely reversible. The main functional groups that are able to form chemisorbed bonds with metal surfaces are amino ($-NH_2$), imine (-NH), carboxyl (-COOH), and phosphonate ($-PO_3H_2$), although other functional groups or atoms can also form co-ordinate bonds with metal surfaces.[20] Film formation mechanism is based on blocking both anodic and cathodic areas indirectly, a result of surface reactions of inhibitor molecules and producing thin films on the surface. In this process, inhibition is effective only when the films are adherent, not soluble, and prevent the access of metal to the solution. Figure 1.10 shows the potentiostatic polarization curve of the solution containing organic inhibitor on the

metal. It has been depicted that with the addition of the inhibitor, current decreases from I_{corr} to I'_{corr} while the corrosion potential remains the same. Organic inhibitors are able to form a protective hydrophobic film, adsorbed on the metal surface. In fact, the polar group of the organic molecule is directly attached to metal and the nonpolar end is oriented in a vertical direction to the metal surface. Thus, they can prevent diffusion of corrosive species and establish a barrier against chemical and electrochemical attack.[25]

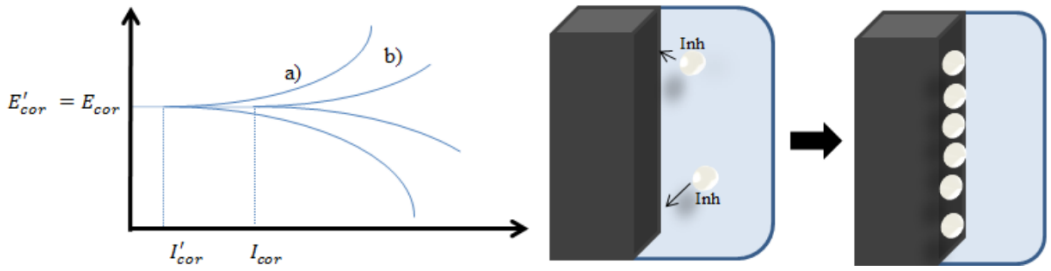


Figure 1.10 Electrochemical behaviour of a metal on a solution containing a (a) organic inhibitor compared to the (b) same solution without the inhibitor and mechanism of organic inhibitors through adsorption of the inhibitor on the metal surface. The Inh represents the inhibitor molecules.[20]

The efficiency of an organic inhibitor could be affected by chain length, size of the molecule, type of bonds, aromaticity/conjugation, and strength of bonding to the substrate, cross-linking ability, and solubility in the solvent environment. Inhibitor efficiency, E_I (%), is given as:[19]

$$I_{corr} = \frac{I_{corr} - I'_{corr}}{I_{corr}} \times 100 \qquad \text{Eq.6}$$

where I_{corr} and I'_{corr} are corrosion rate (corrosion current densities) in the absence and presence of inhibitor, respectively. Most organic inhibitors contain at least one functional group. The strength of adsorption of organic inhibitors relies on the charge on this group rather on the hetero atom present in the organic molecule. The structure of the rest of the molecule influences the charge density on the functional group.[25] Most common organic inhibitors belonging to different chemical families such as fatty amides,[26-27] pyridines,[28-29] imidazolines,[30-31] other 1,3-azoles[32-33] and polymers[34] have showed excellent performance as corrosion inhibitors (Table 1.2).[35]

Table 1.2 Most common organic corrosion inhibitors

Chemical family	Application
Primary amines and diamines	acid media
Secondary amines	carbon steel in acid media
Oximes	carbon steel in acid media
Nitriles	carbon steel in acid media
Amides & thioamides	carbon steel in acid media
Imidazoles	copper alloys and carbon steel in basic media
Benzoazoles	copper alloys and carbon steel in basic media
Imidazolines	carbon steel in acid media
Pyridines	carbon steel in acid media
Triazoles	copper alloys in basic media
Benzotriazoles	copper alloys in basic media
Tetrazoles	copper alloys in basic media
Polyvinyls	carbon steel in acid media
Polyesters	carbon steel in acid media

Despite large numbers of inorganic, organic, and polymeric compounds, which have shown good corrosion inhibition performances for different metals and alloys, many of these compounds are toxic. The final choice of the inhibitor for a particular application is restricted by several factors, including increased environmental awareness and the need to improve environmentally friendly processes.[36] Therefore, aspects that need to be taken into account in the development of corrosion inhibitors include their toxicity and impact on environmental pollution.

1.4.3 Environmentally friendly organic corrosion inhibitors (EFCIs)

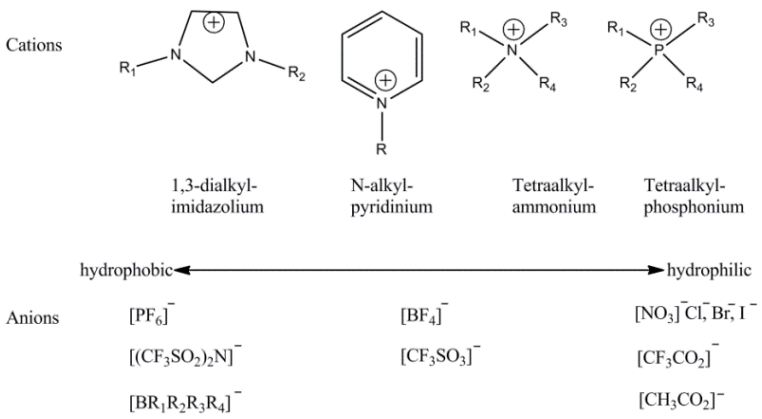
In the last decades, much attention has been focused on the need to design and develop synthetic, non-toxic, and relatively less expensive organic corrosion inhibitor to replace toxic ones. As example, 1,2-aminododecanoic acids have been investigated as “green” corrosion inhibitors for carbon steel.[37] Moreover, imidazole derivatives[38] and guanidine[39] have been reported as non-toxic corrosion inhibitors for copper in acid media. Several synthetic polymers have also been designed as efficient EFCIs for carbon steel in alkaline solution.[40-41] Most polymers are not easily biodegradable which,

to their advantage, allow for long time storage and usage on corrosion protection of metals and alloys. Among all the different types of synthetic materials, which could be used as EFCIs, new class of low toxicity organic compounds known as Ionic liquids (ILs) deserve particular attention due to their rapid grow in a number of applications, and particularly within the topic of synthetic EFCIs, they have shown effective performance as inhibitors for various metals and alloys.[42-44] In the following sections, an insight into ionic liquids will be discussed in detail.

1.5 Corrosion inhibition using Ionic liquids (ILs)

ILs are the low-melting organic salts that are composed of cations and anions that melt below 100 °C.[45-46] The first IL was investigated in 1914 by Paul Walden with his observation on ethylammonium nitrate ($[EtNH_3][NO_3]$) with very low melting point of 13-14 °C.[45] Due to the unique properties such as low toxicity, negligible vapour pressure, high thermochemical and electrochemical stabilities, non-flammability, and their ability to act as catalyst, ILs have been used in a large number of applications as an eco-friendly alternative to substitute volatile organic solvents including catalysis,[47] separation processes,[48-49] analytics,[50] lubricants,[51] and electrochemical applications.[52] The diagram of ionic liquid applications is represented in Figure 1.11.[46] Common ionic liquids are formed by an organic cation (i.e. ammonium, imidazolium, pyridinium, pyrrolidinium, phosphonium, sulfonium) in combination with a complex anion (Scheme 1.1).[53]

The common configuration of ILs consists of an amphiphilic group with a long chain, hydrophobic tail, and a hydrophilic polar head.[54] Therefore, their molecular configuration is able to form micelles and lowering interfacial tension of aggressive media, results in an enhancement in surface wetting and adsorption.[54-56] These properties of ILs have a useful effect on surface exposure and may be responsible for the corrosion inhibition of metals.



Scheme 1.1 Most commonly used cations and anions in the formation of ILs.[53]



Figure 1.11 The diagram of ionic liquid applications.[46]

The most extensively studied ILs is based upon the imidazolium cation. The Imidazolium compounds are reported to show corrosion resistant behaviour on copper,[55, 57-58] mild steel[43] and aluminium.[43] It has been observed that the high inhibition efficiency of such inhibitors depends on the specific interaction between the functional groups and the metal surface, due to the presence of the –C=N– group and electronegative nitrogen in the structure of the imidazolium.[59] One of the recent works in the application of ILs as corrosion inhibitors is the work by Guzám-Lucero.[60] The author investigated five types of imidazolium ionic liquids containing unsaturated and long alkyl saturated chains as cations with bromide as anion, which have been used for protection of carbon steel in aqueous 1.0 M H_2SO_4. The results showed that the

inhibition mechanism of ILs was attributed to the strong adsorption ability of ILs as surfactants to form a protective layer that isolates the mild steel surface from an aggressive environment. Therefore, the study of the relations between ILs' molecular structure, their counterion, the length of substituted alkyl chains, and the functional groups adsorbed on the metallic surface and corrosion inhibition is essential. In next section, the effect of ILs' structure on the inhibition performance has been presented with literature examples.

1.5.1 Effect of IL structure on corrosion inhibition

1.5.1.1 Cation effect

Among many kinds of ionic liquids, imidazolinium and pyridinium cations based ILs have been investigated intensively. Shi et al.[61] synthesized a series of new imidazolium ionic liquids and investigated the relationship between the alkyl connecting with $N_{(3)}$ of imidazolium ring and corrosion inhibition performance in acidic solution. The inhibition efficiency was found to increase with increasing the carbon chain length of the alkyl connecting with $N_{(3)}$ of imidazolium ring. In another study, the corrosion inhibition behaviour of three synthesized imidazolium ionic liquids with similar chemical structure (namely 1-butyl-3-methylimidazolium chlorides, 1-hexyl-3-methylimidazolium chlorides and 1-octyl-3-methylimidazolium chlorides) on aluminium in hydrochloric acid has been investigated.[59] It has been reported that corrosion of aluminium in aqueous solution depends on the concentration of anions in solution. A general mechanism for the dissolution of aluminium that reported in the literature is:[62]

$$Al_{(s)} + H_2O \rightleftharpoons ALOH_{ads} + H^+ + e \qquad \text{Eq.7}$$

$$ALOH_{ads} + 5H_2O + H^+ \rightleftharpoons Al^{3+} + 6H_2O + 2e \qquad \text{Eq.8}$$

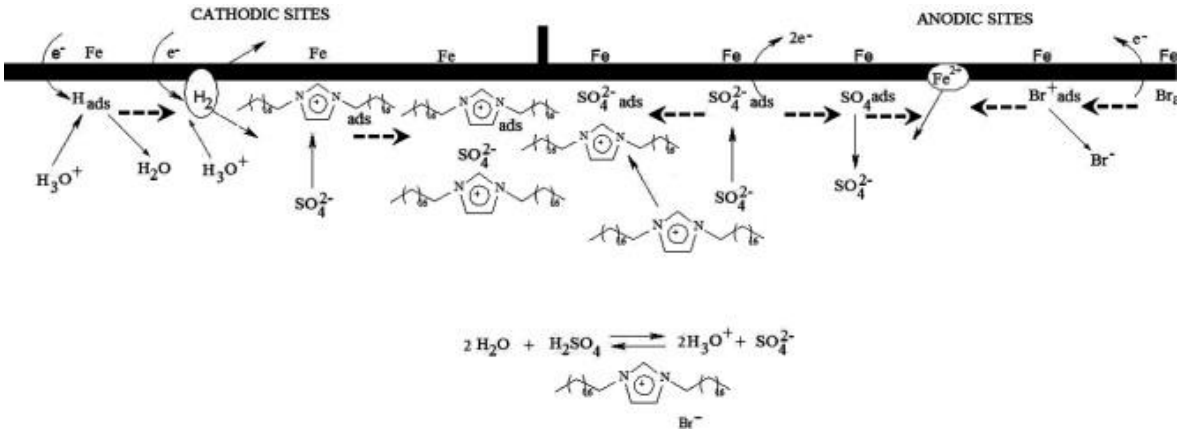
$$Al^{3+} + H_2O \rightleftharpoons [AlOH]^{2+} + H^+ \qquad \text{Eq.9}$$

In the presence of chloride ions the reaction will correspond to:

$$[AlOH]^{2+} + H^+ \rightarrow [AlOHCL]^+ \qquad \text{Eq.10}$$

It is well known that imidazolium group as well as nitrogen atom in heteroaromatic ring of imidazolium compounds can be protonated in acidic solutions.[63] Thus, the interaction of the protonated imidazolium ionic liquid molecules on the aluminium surface

competes with the interaction of the ions in the solution. The adsorption of inhibitors on the aluminium surface removes or depletes some of the water molecules originally adsorbed on to the surface, which blocks the formation of $AlOH_{ads}$. Thus both the oxidation reaction of $AlOH_{ads}$ to Al^{3+} and the complexation reaction between the hydrated cation $[AlOH]^{2+}$ species and chloride ions can be prevented. Moreover, these protonated molecules also compete with the hydrogen ions, thus reducing hydrogen evolution. In this case, adsorption would have occurred through polar centres of nitrogen atom in the –C=N– group. Meanwhile, the presence of the electron donating group (Cl) on the imidazolium base IL increases the electron density on the nitrogen of the –C=N– group, resulting in high inhibition efficiency.[43] This particular effect is more evident with increasing chain length of the alkyl connecting with $N_{(3)}$ of imidazolium cationic ring. Likhanova et al.[53] reported the inhibition action of imidazolium and pyridinium bromides ILs on mild steel in 1 M H_2SO_4 at room temperature. Since these ILs affected both anodic and cathodic reactions they are classified as mixed type inhibitor. Scheme 1.2 represents the inhibition mechanism, which is thought to act during the interaction of the ionic liquids with the metallic surface. The adsorption of hydronium (H_3O^+) ion and desorption of hydrogen gas (H_2) occurs on the cathodic sites whereas the adsorption and desorption of Br^- and SO_4^{2-} ions occur on the anodic sites. The protonated imidazolium or pyridinum molecules are electrostatically adsorbed on the cathodic sites in competition with the hydronium ions available to reduce hydrogen evolution.[64]



Scheme 1.2 Corrosion inhibition mechanism and adsorption model of experimental ionic liquids on mild steel surface in aqueous sulfuric acid medium.[64]

The cations of ILs are bigger than those of hydrogen. This way, alkyl chains and aromatic rings of the IL cover a large part of the metallic surface, which also displaces water molecules from the surface. In that study, both ILs show a fair corrosion inhibition with average corrosion efficiency within 82–88% at 100 ppm to protect mild steel from corrosion in an aqueous solution of sulphuric acid; their efficiencies increased with inhibitor concentration within the range 10–100 ppm. However, due to the larger steric effect of imidazolium in comparison to pyridinium, which results in a higher surface coverage area during the chemical adsorption process, imidazolium based IL provides a better inhibition effect than pyridinium.

1.5.1.2 Anion effect

In another study, Uerdingen et al.[65] investigated the behaviour of carbon steel, austenitic stainless steel, nickel-based alloy, copper, brass, and aluminium in seven ionic liquids (ILs) with different chemical structure under flow conditions at temperatures up to 90 °C. It was reported that for carbon steel and aluminium, the corrosivity of IL media strongly depends on the chemical structure of the cationic moiety and the nature of anion in the IL molecule. Specifically, the corrosion resistance of carbon steel in water-free ILs strongly depends on the IL anion. Depending on the type of IL, carbon steel may undergo severe corrosion in diluted IL media. Anions like tosylate and dimethyl phosphate generally trigger higher corrosivity specifically in water-diluted ILs.

Ashassi-Sorkhabi et al.[44] studied the effect of IL anions in corrosion inhibitor behaviour of two synthesized imidazolium ionic liquids with chlorides and hydrogen sulphate anion on mild steel in hydrochloric acid. In the structure of the imidazolium bases, the atoms of the imidazolium ring and the –C=N– group can form a π bond. The π* orbital can also accept the electrons from the d orbitals of iron to form bonds, which produces more than one centre of adsorption. Moreover, the presence of the Cl and S on the imidazolium structure, which are electron donating groups, increases the electron density on the nitrogen of the –C=N– group, resulting in high inhibition efficiency. Therefore, in this study hydrogen sulphate counter-anions showed better inhibiting effect for mild steel in HCl compare with chloride anion.

1.5.2 Synergistic corrosion inhibition using ILs

As described earlier, one of the proposed advantages of ILs is the ability to select both the anion and cation to have useful properties for a particular application. It is this feature of ILs and organic salts that could be generally exploited to find new organic inhibitors, ideally with synergistic effects. A number of publications have investigated the use of biologically safe anions and cations to produce a salt that could approach the performance of chromates, while being environmentally friendly.

Somers at al.[66] described such a family of ILs and organic salts that target dual activity by incorporating both anions and cations that have shown prior evidence of effective inhibition. These salts were based on the imidazolinium cation with carboxylate anions. The imidazolinium structure is similar to imidazolium, and the only difference being saturation of the C4−C5 double bond on the core ring of the imidazolinium. Depending upon the nature of the anion in the salts, these materials were found to have interesting physical properties such as facile ion transport, as well as demonstrating synergistic corrosion inhibition on mild steel. They also studied the influence of pH on the corrosion inhibiting performance of the organic salt for mild steel in chloride environments.

It has been shown that this environmentally friendly organic salt remains highly active at pH 2 and 8, which are common environments in which corrosion protection is required. Also, at higher pH the inhibition was controlled by the anion, and the solution showed a high level of protection. At low pH, even though both the components were largely ineffective on their own, the combined salt still had an inhibition efficiency of 72%, indicating a strong synergy between the two ionic species under these conditions. Figure 1.12 shows an optical microscope image of mild steel samples with corrosion product intact after immersion for 24 h in salt solutions at different pH.

As it has been shown at a pH of 8, Figure 1.12a and b shows much less corrosion product but still show some local attack on the sample in the inhibitor-containing solution. At a pH of 2 many bubbles have been observed due to the hydrogen gas evolution, where the sample at pH 2 with inhibitor does not show any bubbles, suggesting a significant reduction in the rate of reaction. The samples immersed in the

neutral condition show a similar trend to those at pH 8, where the inhibited solution showed much less corrosion product but still with signs of localized attack.

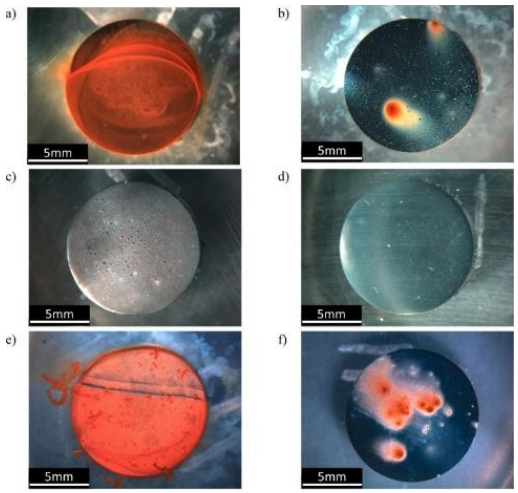


Figure 1.12 Optical images of the surfaces of mild steel samples after immersion for 24 h in (a) NaCl at pH 8; (b) NaCl and inhibitor at pH 8; (c) NaCl at pH 2; (d) NaCl and inhibitor at pH 2; (e) NaCl neutral; and (f) NaCl and inhibitor in neutral.[66]

Such synergy, however, is not always achievable due to some limitation of ILs. One main disadvantages of ILs is unfavourable transport properties of these solvents, which generally present higher viscosity and surface tension than conventional organic solvents.[67-68] Also, once ILs are applied into a coating, they pose problem of miscibility with a coating formulation. For these reasons polymerized ionic liquids or poly (ionic liquid)s (PILs) are considered more favourable than their monomers in the field of corrosion inhibitor. This is due to their low sensitivity to salts, high shear and thermal stability, high resistivity to strong acid and their efficiencies at lower concentrations. Moreover, such PIL could act as reservoir for IL with controlled release characteristics, such as microencapsulation of inhibitor which can prevent miscibility issue with other components of coating formulation. Also, they act as controlled release type inhibitor. In the following section detail study of PILs structure and chemistry will be investigated.

1.6 Introduction to polymerized ionic liquids (PILs)

A special type of polyelectrolytes which carry an IL species in each of the repeating units are referred to polymerized ionic liquids or poly (ionic liquid)s (PILs), and have been proposed as alternative inhibitor materials. Thus, PILs consist of the cationic or

anionic centres on their repeating units in the polymer chain (Figure 1.13).[53] Although ILs are in a liquid state near room temperature, PILs are in fact solid in most cases, with a couple of exceptions.[69] Nevertheless, opposite to solid polyelectrolytes, PILs have a reportable glass transition temperature in most cases, being well below usual ionic glasses. The major advantages of using a PIL instead of an IL are the enhanced mechanical stability, improved processability, durability, and spatial controllability over the IL species. The combination of properties of ionic liquids with the flexibility and properties of macromolecular structure results in the unique properties for PILs, which can be used in various applications including solid ionic conductor, powerful dispersant and stabilizer, absorbent, premises for carbon materials, permeable polymers, etc.[70-72] The initial research of PILs goes back to 1970's. The major design efforts towards developing novel PILs are focused on vinylimidazolium based PILs with diverse functional substitutes due to the positive charge being on an aromatic ring and adjacent to the vinyl groups.[73-76] Intensive studies on PILs significantly expanded the research scope of PILs. New structures, properties and applications have been spotted, which generate several valuable branches for researchers. Meanwhile, there is a number of reviews which discussed the synthesis of some PILs and introduced the application of PILs, especially imidazolium based PILs in the field of polymer science.[45, 70, 77] An insight into PILs synthesis, chemistry, characteristic features and their application is presented in the following sections.

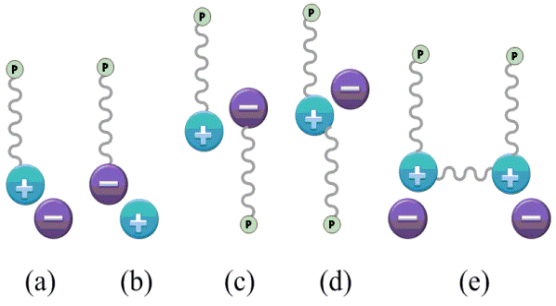


Figure 1.13 Basic polymerizable IL monomers. "p" represented of a polymerizing unit in an IL monomer.

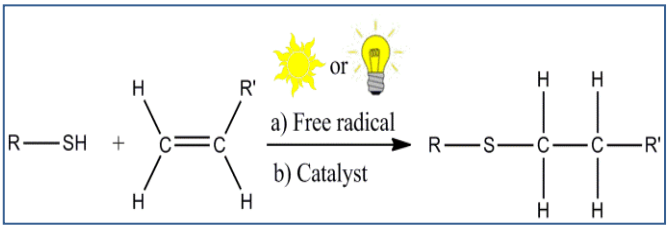
1.6.1 Insight into synthesis and chemistry of PILs

There are two general approaches for synthesizing PILs: (1) direct polymerization of polymerizable IL monomers (free radical polymerization, controlled radical or step growth polymerization), (2) chemical modification of existing polymers. Depending on

the targeted PIL, both methods can present some advantages/disadvantages. Most commonly used IL is the one with a polymerizable unit on the cation and the key approach to prepare PILs is free radical polymerization of IL monomers, which can be divided to two subclasses: homopolymerization and copolymerization.[78,79-81] Recently, several novel PIL structures with different properties for different applications have been investigated. Major efforts toward developing novel PILs are focused on using vinylimidazolium based PILs with diverse functional substitutes.[73-74, 82-83] However, there is very little information available in the literature on imidazolium based PILs for corrosion inhibition application. Thus, imidazolium based IL and corresponding PILs form the basis of this research work. From the viewpoint of synthetic techniques, recently the advantages of using the "click" chemistry concept with the benefits associated with the thiol-ene chemistry, has received remarkable attention in achieving new designs for PILs.[73-74] A more detailed description of the type of chemistry is given in the following section.

1.6.1.1 Application of Thiol-ene chemistry in synthesis of PIL

The thiol-ene reaction,[84] is the hydrothiolation of a C=C bond. In the field of polymer and materials science this reaction has been most widely employed as a tool of preparing near-perfect networks and films as exemplified by the work of Hoyle and co-workers[85] and Bowman et al.[86-87] The advantage of the ''click'' nature of thiol-ene reaction has recently attracted attention in other areas of polymer chemistry and materials development (Scheme 1.3).



Scheme 1.3 The thiol-ene reaction.

There are several features associated with the thiol-ene reaction that makes it a particularly attractive, facile and versatile process. Firstly, such thiol-ene reactions can proceed under a broad range of reaction conditions or solvents including through a radical pathway, via catalytic processes mediated by nucleophiles, acids, bases, and in the absence of any catalyst in highly polar solvents such as water or DMF.[88-89]

Secondly, due to the weak sulphur-hydrogen bond, the thiol-ene reaction could be initiated using a wide-range of starting materials. Finally, such reactions are generally simple with rapid synthesis strategies, which can be complete in a matter of seconds. Therefore, the thiol-ene reaction provides insensitivity to the presence of air/oxygen and proceeds with near quantitative formation for both linear and cross-linked polymer networks.[73, 90] Thiol-ene reaction attracted significant interest in broad range of areas associated with polymer and materials chemistry such as preparation and application of hydrogels, synthesis of crosslinked beads/polymeric nanoparticles, monomer synthesis, polymer side and end chain modification, synthesis of dendrimers, hyperbranched and star polymers, and organic-inorganic hybrid materials.[91]

As such, thiol-ene chemistry offers flexibility in terms of the variety of monomers available, reaction conditions that can be employed and properties of the resulting networks that can be attained. This makes thiol-ene chemistry an interesting novel synthetic approach for the facile preparation of cross-linked PILs in different forms. Drockenmuller et al. [92-93] applied a copper catalyzed azide-alkyne cycloaddition reaction towards the preparation of 1,2,3-triazolium-based main-chain PILs. In the synthetic route, α-azide-ω-alkyne monomer underwent polyaddition via a click chemistry route. In another work by Shaplov et al.[73] the radical thiol-ene addition was successfully applied for the synthesis of functional pyrrolidinium ILs. The synthesized ILs were consequently transformed into ILMs by the interaction with the methacrylates. Furthermore, the new PILs were obtained from free radical polymerization of ILMs with high molar masses.

Apart from these studies, there have been very few reports where the combination of thiol-mediated polyadditions with polymerizable ionic liquid has been employed and also few reports on application of synthesised PILs as corrosion inhibitors.

1.6.2 PIL structural diversity

There have been persistent efforts devoted to the preparation of PILs in various forms and dimension scales like spherical micro-/nanoparticles, micro/nanogels, vesicles, nanoworms, etc.[94] Therefore, PILs have a diverse chemical structure reservoir. The most recent forms of PILs which have been mostly used in different applications are

PIL colloidal particles and PIL gels. An insight into these types of PILs and their characteristic features is presented in the following sections.

1.6.2.1 PIL colloidal particles

Since colloidal systems have a close connection with nature and human life, PIL colloids are a new platform to investigate the unique properties of ILs with the rather small dimension and the superior dispersity of colloidal particles. Moreover, they setup a powerful platform for a variety of studies on PIL functions and applications. A colloidal system is defined as a state of subdivision dispersed in a medium with at least one dimension between approximately 1 nm and 1 μm.[95] Recently, nanostructured PILs, and especially colloidal nanoparticles, have received significant interest as functional polymer nanoparticles. This is due to the fact that small particle sizes increase surface effects on the interfacial interaction and mass/energy transport. Moreover, a small particle size and the charged character of PILs improve the colloidal stability in aqueous as well as non-aqueous dispersions. So far, some synthetic routes developed to prepare PIL nanoparticles including suspension polymerization,[96] water-in-oil concentrated emulsion polymerization,[97] and precipitation polymerization in water without stabilizers using ionic liquid monomers with long alkyl chains has been recently reported.[78, 98] Among PIL nanoparticles a new focus in this field is on the nanostructured imidazolium-type PILs.[72, 99] One of the examples of this type of applications is the work by Yang et al.[100] which reported the preparation of the crosslinked poly(1-butyl-3-vinylimidazolium bromide) microspheres with the diameter of about 200 nm synthesized via miniemulsion polymerization for application as metal ion scavenger and catalysis.

In another work by Zhou et al.[101] a thermosensitive type ionic microgels was obtained via the surfactant-free emulsion copolymerization of 1-vinylimidazole and 4-vinylpyridine with the thermosensitive monomer N-isopropylacrylamide. The obtained microgels were spherical in shape with narrow size distribution and exhibited thermosensitive behaviour plus the unique features of PILs in aqueous solution (Figure 1.14).

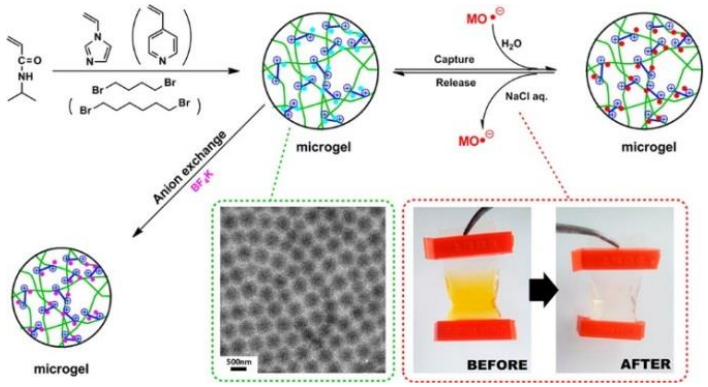


Figure 1.14 Schematic summary of the synthesis of thermosensitive ionic microgels via quaternized crosslinking reaction and their properties.[101]

One of the most common methods used for the fabrication of polymer nanoparticles with the droplet sizes typically in the range of 20-200 nm is miniemulsion. The use of water as the dispersion medium is one of the main advantages of this system, which makes it environmentally friendly and also allows excellent heat dissipation during the polymerization process.[102]

On the other hand, very recently, "click" polyaddition reactions in miniemulsions, specifically thiol-mediated chemistry (i.e. thiol-ene/yne, thiol-Michael); have attracted attention as one of the facile methods for synthesis of polymer nanoparticles, and nanocapsules dispersion in heterophase media with high efficiency.[85, 103-104] However, following examples of recent work in this area evidenced that there is no example of the combination of thiol-mediated polyadditions in dispersed systems with polymerizable IL, which could broaden their applications in different fields. For example, for the first time Jasinski and co-workers[105] reported the preparation of poly (thioether ester) latex nanoparticles using miniemulsion thiol-ene photopolymerization. Their synthesis was performed in water, at ambient temperature, and without the use of any organic solvent. The resultant linear poly (thioether ester) particles had an average diameter of 130 nm. In another recent work, sub-100 nm crosslinked polythioether nanoparticles were synthesized via thiol-ene photopolymerization in miniemulsion using high-energy homogenization (Figure1.15).[102]

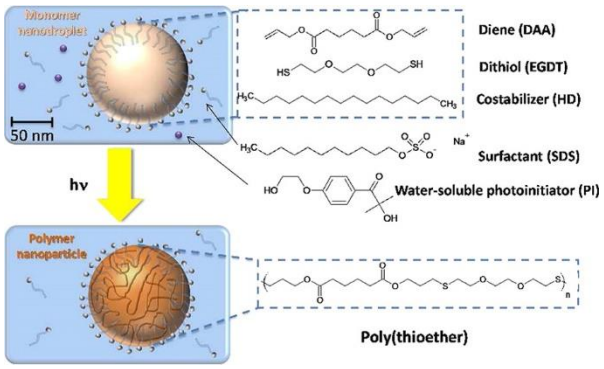


Figure 1.15 Schematic representation of a thiol-ene miniemulsion photopolymerization of stoichiometric diene and ethylene glycol dithiol.[102]

Despite the potential of both thiol-ene and miniemulsion in synthesis of PIL nanoparticle, to date there has not been any report of using combination of these two valuable techniques for the fabrication of PIL nanoparticles especially for fabrication of PIL based corrosion inhibitors.

1.6.2.3 PIL gels

As described above, PIL gels are one form of PILs which recently has been used in a number of applications such as electrolytes for batteries and supercapacitors,[106] drug delivery,[107] agriculture, and biomedical fields.[108] Indeed, they are showing a multitude of characteristics that make them very versatile materials with tuneable properties. Gordon and co-workers[96] pioneered the synthesis of large PIL beads in the micron size scale through the direct polymerizations of 1-butyl-3-vinylimidazoium TFSI in the presence of a 1,8-di(vinylimidazolium)-octane TFSI as a crosslinker. Furthermore, the resulting gel-type beads were swelled in acetone, and loaded with palladium nanoparticles to catalyze C–C coupling reactions. The authors suggested the application of such gel beads in catalysis, separation technology, and ion-exchange resins. Xiong and co-workers[109] reported a facile one-step synthetic strategy for the preparation of cross-linked polymeric nanogels by the conventional radical copolymerization of a phosphonium-based IL for use as catalysts. Recently, Rahman et al.[110] used a microfluidic method to fabricate monodisperse spherical PIL microgel beads. Authors showed anion exchange can enable fine-tuning of size and swell ability of these beads. By incorporating diverse anions, they were able to impart a multitude of functionalities to these beads, ranging from redox capabilities, controlled release of payload, magnetization, toxic metal removal, and robust, reversible pH sensing. These

chemically switchable stimulus-responsive PIL beads have potential applications in portable and preparative chemical analysis, separations, and spatially addressed sensing (Figure 1.16).

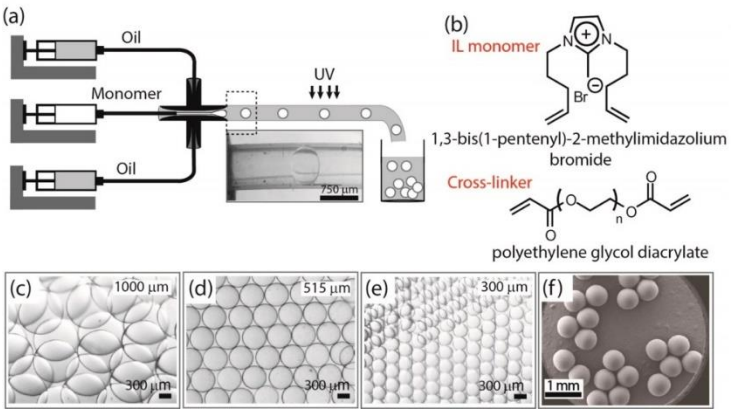


Figure 1.16 Schematics illustrating microfluidic method to generate switchable stimulus-responsive PIL microgels.[110]

A number of different methods have been employed to fabricate PIL gels, including crosslinked networks,[62] microfluidic devices, solvent evaporation, composite gels,[62] seeded polymerization,[63] etc. However, the formation of PIL gels that takes advantage of the thiol-ene chemistry has not been reported to date. Also, no investigation has been reported on such PIL micro gel for corrosion inhibitor.

Although, different forms of PILs such as gels and nanoparticles have been fully investigated in the literatures, there is a significant gap for the incorporation methods of PILs into the coating for application as corrosion inhibitor. In the case of inhibitors that adsorb on the metal surface and inhibit the corrosion, there are two main challenges: (1) metal-inhibitor interactions and (2) transport of the corrosion inhibitor from bulk solution to the surface of the metal. In order to address these issues further literature review on mechanism of adsorption following the methods of application of PIL into the corrosion protection system as corrosion inhibitors will be presented and discussed in following sections.

1.7. Mechanism of inhibitor adsorption on the carbon steel

Basic information on the interaction between the inhibitor and the mild steel surface can be obtained from adsorption study provided by the adsorption isotherm. Adsorption

isotherm is the relationships between corrosion rate, corrosion inhibition and concentration of inhibitor. Adsorption isotherms are often used to demonstrate the performance of organic adsorbent-type inhibitors.[111] In the case of corrosion inhibition performance of organic adsorbent-type inhibitors, the structure of the inhibitor plays an important role. Organic inhibitors such as amines (aliphatic amines, pyridines, imidazoles) and thiazoles form a coordinate bond with metals such as iron, copper, and zinc. Corrosion inhibition of metals by organic inhibitors containing electron donor atoms such as oxygen, nitrogen, sulfur, and selenium show a decreasing trend with the decreasing electronegativity order as shown here: O<N<S< Se.[111] Another form of the metal-inhibitor bond is with inhibitors containing electrons associated with triple bonds or aromatic rings.

As an example of the recent study on adsorption mechanism of corrosion inhibitors, Feng at al.[112] studied the effective behaviour of imidazoline based inhibitor in protecting carbon steel from corrosion in alkaline chloride solution. This inhibitor acts as a cathodic type inhibitor with the dominant suppression of cathodic reduction of oxygen. Density functional theory (DFT) calculations suggest that the N=C–N region in imidazoline ring is the most active reaction site for the inhibitor adsorption on metal surface, which can share electrons between the nitrogen atoms and iron atoms, in which involving the displacement of water molecules from the metal surface.

Figure 1.17 shows the highest occupied molecular orbital (HOMO) and lowest unoccupied molecular orbital (LUMO) distribution of imidazoline based inhibitor. It can be seen that due to the presence of lone pairs in the nitrogen atom in imidazoline structure and also delocalization of π electrons of the ring, HOMO mostly distributed over the imidazoline. Whereas, LUMO is mainly covered the N=C–N region of the imidazoline ring. Thus, it can be concluded that nitrogen atom around imidazoline ring is the active site for an electrophilic attack and N=C–N region is the active site for nucleophilic attack.[113] Since adsorption of inhibitor on metal surface occurs based on donor-acceptor interactions, unoccupied d orbital of iron atom can accept electrons from the inhibitor molecule to form coordinate bonds. Also, the inhibitor molecule can accept electrons from the iron atom.[114]

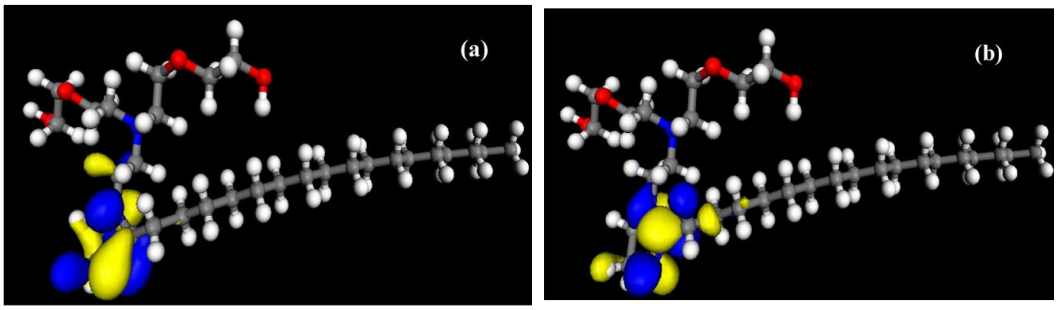


Figure 1.17 (a) HOMO and (b) LUMO orbital distribution of imidazoline based inhibitor.[112]

Obot et al.[115] reported the corrosion inhibition effect of ketoconazole for the corrosion of mild steel in 0.1 M H_2SO_4. Among several adsorption isotherm studies, Langmuir adsorption isotherm was found to be the best description of the adsorption behaviour of the inhibitor studied. Langmuir adsorption isotherm is described by the following equations:

$$S = \frac{1}{K_{ads}} + C \qquad \text{Eq.11}$$

where S is fractional surface covered by adsorption, K_{ads} is the equilibrium constant of the adsorption process and C the inhibitor concentration. Furthermore, the equilibrium constant of adsorption K_{ads} is related to the standard free energy of adsorption, ΔG^0_{ads}. It has been reported that the values of ΔG^0_{ads} up to -20 kJ/mol are adsorbed to the metal via physical adsorption while those around -40 kJ/mol or higher are associated with chemisorption as a result of sharing or transfer of electrons from organic molecules to the metal surface to form a coordinate type of bond (chemisorption).[116] The value of ΔG^0_{ads} in this study was less than -20 kJ/mol, suggesting physical adsorption of inhibitor on mild steel surface.

In another study, corrosion inhibition by triazole derivatives on mild steel in phosphoric acid solutions has been investigated by Lin Wang.[117] In this study, Langmuir behaviour was not observed, suggesting that surface attachment is not due to simple chemisorption. The mechanism of adsorption of triazole derivatives on the metal surface can be based on the donor-acceptor interactions between the π-electrons of the heterocycle compound and the vacant d-orbitals of iron surface atoms. Amines and heterocyclic nitrogen compounds may also adsorb through electrostatic interactions between the positively charged nitrogen atoms and negatively charged metal surface.

Therefore, the author suggested a mixed-type inhibitor mechanism for the inhibitor studied.

1.7.1 Mechanism of adsorption of ILs and PILs on metal surface

It has been reported that some ILs based on imidazolium, pyridinium and pyridazinium exhibited corrosion inhibition properties for various metals.[118] However, there is very limited investigation on the mechanism of adsorption of IL and PIL as corrosion inhibitors. Only a few studies have been reported on the mechanism of adsorption of PIL and IL based corrosion inhibitors into the metal. The corrosion inhibition behaviour of two synthesized imidazolium ionic liquids, namely 1-butyl-3-methylimidazolium chlorides (BMIC) and 1-butyl-3-methylimidazolium hydrogen sulfate ([BMIM]HSO_4) on mild steel in hydrochloric acid is reported by Zhang et al.[119] Results of this study indicated that the inhibition efficiencies decreased in the order of [BMIM]HSO_4 > BMIC. This is due to the fact that the presence of more electron donating groups on [BMIM]HSO_4 (with S rather than Cl atom) increases the electron density on the nitrogen of the –C=N– group, resulting in a higher inhibition efficiency than BMIC. In particular, sulfur atom is found to have excellent ability to offer free electrons. The corrosion mechanism of anodic dissolution of iron and the cathodic hydrogen evolution in hydrochloric acid was proposed as below:[120]

$$Fe + Cl^- \rightleftharpoons (FeCl^-)_{ads} \quad \text{Eq.12}$$

$$(FeCl^-)_{ads} \rightleftharpoons (FeCl)_{ads} + e^- \quad \text{Eq.13}$$

$$Fe + H^+ \rightleftharpoons (FeH^+)_{ads} \quad \text{Eq.14}$$

$$(FeH^+)_{ads} + e^- \rightarrow (FeH)_{ads} \quad \text{Eq.15}$$

$$(FeH)_{ads} + H^+ + e^- \rightarrow Fe + H_2 \quad \text{Eq.16}$$

Based on this mechanism, Cl^- anion is first adsorbed onto the positively charged metal surface by columbic attraction. Then, the inhibitor molecules can be adsorbed through electrostatic interactions between the positively charged molecules and the negatively charged metal surface.[121] Furthermore, these adsorbed molecules interact with $(FeCl^-)_{ads}$ species to form protective mono layers (by forming a complex) on the steel surface. Also, at cathodic sites protonated imidazolium molecules are adsorbed in competition

with hydrogen ions that going to reduce hydrogen evolution. On the other hand, the atoms of the imidazolium ring and the –C=N– group can form a π bond. Then, not only can the π electron of the imidazolium bases enter unoccupied orbitals of iron, but the π * orbital can also accept the electrons of d orbitals of iron to form back bonds to produce more than one center of adsorption.[122]

Olivares-Xometl and co-workers reported PILs derived from imidazole with different alkylic chain lengths for corrosion inhibition of aluminium alloy in diluted sulfuric acid.[123] Figure 1.18 shows the likely mechanism of PILs' interaction with both the metallic surface and the aggressive environment. The interaction among the hydrophobic parts of the PILs molecules is a possible explanation for the protective action. However, it is more likely that the main chains of the polymer form an obstacle, which may have a supportive action on inhibition, as they hinder the passage of water and aggressive ions, in agreement with their hydrophobic nature. When the alkyl side chain is composed of 12 carbons a more effective steric hindrance can be seen as it can interact with the other lateral alkylic groups to slow down molecular diffusion.

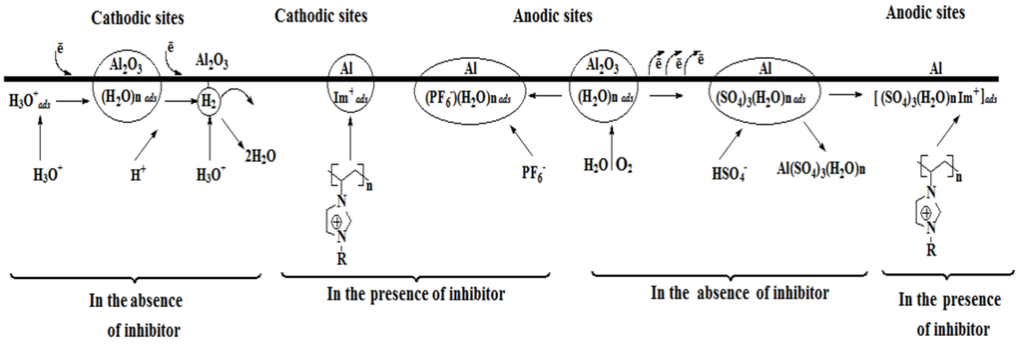


Figure 1.18 Schematic representation of corrosion and inhibition of aluminium alloy before and after PIL addition in diluted sulfuric acid.[123]

However, in this study the PILs displayed a short protection range for the alloy. Thus, these PILs are not suitable to be applied in acidic media, as they are not easily adsorbed due to ionic competition, which leads to the formation of a non-uniform corrosion inhibitor film on the aluminium alloy surface. In another study by Ayman et al.[124-125], PIL based on 2-acrylamido-2 methylpropane sulfonic acid showed an excellent corrosion inhibition performance for steel in 1 M HCl medium. The adsorption of IL on steel surface blocked the active centres, which lowered the corrosion rate of steel. It has been reported that introducing oxyethylene ammonium counter ion into the ionic liquid

polymer system promotes the wetting characteristics to form anticorrosion protective layer at the solid surfaces.[124] Also, it has been indicated that PIL in this system behaved as a mixed type inhibitor and acted via adsorption on steel surface by hindering and retarding the active centres from the corrosion reaction.

Another challenging step after the adsorption mechanism of corrosion inhibitors is the transport of corrosion inhibitors from bulk solution to the surface of the metal. Thus, there is an ongoing study on different methods of incorporation of corrosion inhibitors into the corrosion protection coating formulation, which will be discussed in following section.

1.8 Incorporation of corrosion inhibitors into the coating

Corrosion inhibitors can be incorporated into the coating formulation through different ways. One of the most commonly used methods is the direct addition of inhibitors in the primer or topcoat. However, a too high concentration or low solubility of the inhibitors often results in a deterioration of the integrity and physical barrier properties of the matrix of the protection system.[126] In addition, the existing interaction of the inhibiting agents with the protective matrix often leads to significantly reduced stability of the protective layer and the deactivation of the inhibitors. Recently, different new methods for inhibitor incorporation have emerged to prevent the direct interaction of inhibitor with the matrix. One of the most common methods is application of inhibitor loaded coatings. Coatings based on inhibitor loaded containers protect the metal by releasing corrosion inhibitor in response to changes in the coating integrity (cracks) or local environment (pH shift) caused by corrosion attack. These systems have been extensively investigated because they represent a potential replacement for the banned chromate-based coatings. Various types of containers for inhibitor encapsulation have been reported so far. These differ in their size (nano- and microcontainers), chemical nature (organic, inorganic), shape (spheres, tubes, platelets) and structure (core-shell, porous, layered).[118]

The coating may consist of: (i) another metal, e.g. zinc or tin coatings on steel, (ii) a protective coating derived from the metal itself, e.g. aluminium oxide on “anodised” aluminium, (iii) organic coatings including hybrid organic-inorganic sol gel coatings. In recent years, the sol-gel derived polymers are presented as a promising green alternative

to chromate surface treatments.[43, 53] The sol-gel process is a chemical synthesis method consisting of hydrolysis and condensation of appropriate metal alkoxides, $M(OR)_n$, where R represents an organic group and M a metal.[127] In principle, alkoxysilanes are used as the only or one of the precursors and the organic groups are introduced into the inorganic network through the silicon-carbon bond in an alkoxysilane.[43, 128] One of the main advantages of the sol-gel process is that it enables the preparation of numerous types of new organic-inorganic (hybrid) materials with improved thermal, mechanical, optical, and electrical properties.[126] Combination of organic polymers and inorganic materials in a sol-gel coating provides exceptional possibilities to tailor electrical, optical, anticorrosive, and mechanical properties of this material. The advantages of using sol-gel as a matrix for inhibitors is that it is environmentally friendly, cheap to produce and requires little preparation. The reason for the high inhibition efficiency of sol-gel coating is the excellent adhesion of this material to the substrate and its suitability to protect against corrosion by creating a chemically inert barrier between the metal and the aggressive environment.[64] Generally, the sol-gel method used to obtain hybrid materials consists of four steps: (1) a hydrolysis reaction where the metal alkoxide groups (–OR) are replaced by hydroxyl groups (–OH); (2) condensation and polymerization of monomers to form chains and particles; (3) growth of the particles; and (4) agglomeration of the polymer structures followed by the formation of networks that extend throughout the liquid medium resulting in a gel.[129] Since this process uses materials that do not introduce impurities into the end product, it is waste-free, and is an environmentally friendly.[118] Additionally, in this process hybrid materials with high specific porosity and specific surface area can be easily obtained, which also allows for encapsulation or incorporation of substances, such as inhibitors. The numerous applications of these materials include scratch and abrasive-resistant hard coatings and special coatings for polymeric materials, metal specifically for mild steel and aluminium alloys, and glass surfaces.[126]

However, a pure sol-gel coating contains imperfections, such as micropores, cracks and areas of low cross-link density, which provides a path for diffusion of corrosive species such as water, oxygen and chloride ions to the coating/ metal interface. Therefore, sol-gel coating without the addition of corrosion inhibitors cannot provide sufficient corrosion protection to a metal substrate and it acts only as a barrier coating.[130] Incorporation of inorganic or organic inhibitors into sol-gel coating can significantly

improve the corrosion protection. There is a significant research on sol-gel coatings doped with inhibitor for corrosion protection of aluminium alloys. For example, Quinet et al.[131] studied the effect of addition of organic redox active corrosion inhibitor (chloranil) into sol-gel matrix. Addition of high content of chloranil did not provide an adequate corrosion protection due to the immiscibility of the sol-gel system. Incorporation of lower concentrations resulted in homogeneous structures, increasing the protective properties of the sol-gel coatings.

Also there are number of studies on addition of environmental friendly inorganic type corrosion inhibitors such as trivalent chromium, molybdate ions, permanganate ions and cerium salts into the sol-gel coating for aluminium alloys, that were found to have a significant inhibiting action on corrosion process.[132] Some of the most effective and environmentally friendly inhibitors are thiazole based inhibitors.[133-134] However, it has been reported that when the inhibitors are freely dispersed in the sol-gel matrix above a certain limit, it has an unfavourable effect in the long-term chemical stability and barrier properties of the coatings.[135-136] As a result, significant research efforts in this field have focused on the development of micro- and nanocontainers compatible with hybrid sol-gel coatings (Figure 1.19).

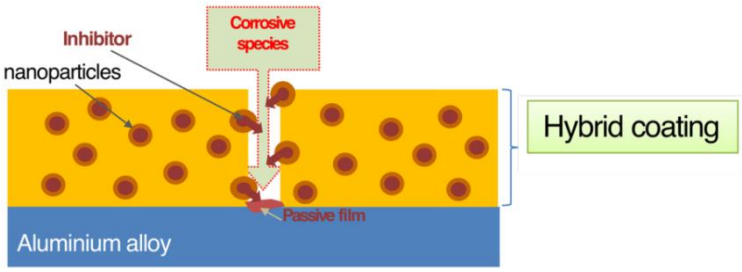


Figure 1.19 Schematic illustration showing the corrosion protection mechanism of a hybrid sol-gel coating containing inhibitor loaded nanoparticles.[135]

Sol-gel coating can be applied into the metal surface using various techniques such as spraying on a surface, dipping or spinning through a set of rotating nozzles (Figure 1.20).[125]

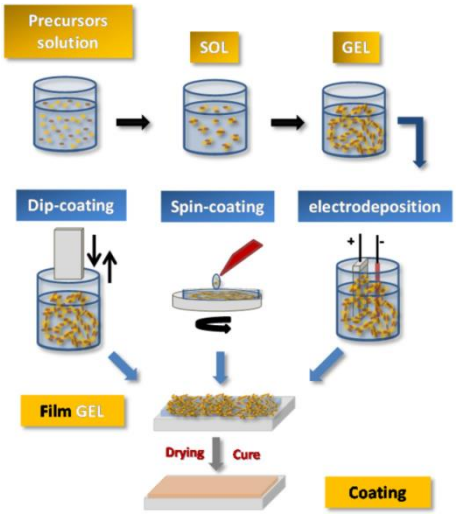


Figure 1.20 Different methods of applying Sol-gel coating on metal.[125]

Messadeq et al.[137] for the first time showed that using hybrid coatings prepared by dispersion of poly(methyl methacrylate), into a zirconia sol improved the corrosion resistance of stainless steel. However, the authors showed that in long term phase separation and subsequent delamination caused the failure of the film. Therefore, the use of hybrid materials, in which the organic and inorganic components are linked by covalent bonds, could reduce the phase separation and delamination as well as increase resistance. Therefore, the research in this area focused on organo-functional alkoxysilanes which have been extensively used in the last decade to prepare hybrid coatings. Recently, Figueira et al.[135] published a review of the most recent and relevant achievements on the development of hybrid sol-gel coatings for corrosion mitigation of metallic substrates. Most common hybrid silica coatings on mild steel which have been recently reported are tetraethylorthosilicate (TEOS), 3-glycidoxypropyltrimethoxysilane (GPTMS), 3-methacryloxypropyltrimethoxysilan (MPTS), and methyltriethoxysilane (MTES).[64]

On the other hand, different organic groups also have been used to reach the required properties of the sol-gel coatings including compatibility with organic paints systems. Among them the application of amine based cross-linking agents in the sol-gel synthesis of hybrid coatings allows the enhancement of the organic network formation at low temperature. For example, Vreugdenhil et al.[138] and Davis et al.[139] studied the corrosion behaviour of amine-cured epoxy-silane sol-gel coatings using diethylenetriamine (DETA). Khramov et al.[140] studied epoxy-silane sol-gel coatings crosslinked with

amino-silanes curing agent which showed significant improvement in these coating's corrosion performance in comparison to those of DETA crosslinked ones.

Although addition of organic components in sol-gel films results in thicker crack-free coatings with improved corrosion protection performances, it also decreases wear resistance and mechanical properties, making them more sensitive to physical damage. To overcome this drawback, several strategies have been studied, such as the addition of inorganic nanoparticles of silica, aluminium oxide, and other oxides to the sols,[140-141] or the formation of nanostructured films or particles achieved by in situ synthesis during the sol-gel process through controlled hydrolysis/condensation of sol-gel precursors.[142-143] The latter approach has the advantage of providing chemical bonds between a hybrid matrix and nanoparticles. Examples of such coatings are those reported by Donley et al. through the self-assembled nanophase particle (SNAP) process using TMOS and GPTMS.[140] Furthermore, hybrid coatings with incorporated zirconia nanoparticles have also been prepared first by Zheludkevich et al.[143], and later by Fontinha[144] and by Lamaka et al.[143] However, it should be noted that these coatings still cannot offer an adequate protection for a long term due to the presence of micro-pores, cracks and permeable areas with in their structure. These zones favour the diffusion of aggressive species to the coating/substrate interface and are preferential sites of corrosion initiation.[145-146] Therefore, doping the hybrid sol-gel coatings with corrosion inhibitors offers a very important route in improving the sol-gel coatings' corrosion performance.

It is worth nothing that number of research has been carried out in this field for the protection of aluminium using sol-gel coatings, whereas inhibition protection of steel by applying sol-gel coating loaded inhibitors is still a comparatively untouched area with a large scope for further exploration. Also, there is no published investigation of the application of PIL based corrosion inhibitors into the sol-gel protection system, which has a potential to enhance the corrosion protection performance of metal.

1.9 Evaluation of corrosion inhibitors using advanced characterization techniques

1.9.1 Evaluation of corrosion performance of IL based corrosion inhibitors using electrochemical techniques

As corrosion is an electrochemical process, electrochemical analysis methods are the most commonly used techniques for the evaluation of the efficiency of corrosion inhibitors. The advantages of electrochemical methods are short measurement time and mechanistic information that they provide which help not only in the design of corrosion protection strategies but also in the design of new inhibitors. Although several electrochemical techniques may be used to study the performance of corrosion inhibitors, potentiodynamic polarization method and electrochemical impedance spectroscopy (EIS) can provide significant information, which makes them the most useful and widely used method in this regard. In order to obtain a better understanding of the application of these methods for the evaluation of corrosion inhibitor efficiency, a detailed discussion of the recent application of these methods for study of corrosion efficiency of inhibitors is presented in this section. Amongst many studies, the recent study of Likhanova et al.[147] presented the use of five imidazolium-type ionic liquids (IL1-IL5) containing N1 unsaturated and N3 long alkyl saturated chains (cation) and bromide (anion) for the protection of carbon steel in aqueous 1.0M H_2SO_4. The polarization curves for carbon steel obtained at various inhibitor concentrations of IL4 and chemical structure of the ILs are shown in Figure 1.21. Results of this study indicated that the presence of ILs produced a positive shift to more noble values of E_{corr} when the concentration was increased, which is the indication of the formation of a protective layer on the metal surface. Moreover, the presence of ILs affected the E_{corr} by the displacement of the polarization curves to anodic potentials. The IL4 displayed the maximum reduction in corrosion current density, and the compounds follow the order IL4 > IL3 > IL1 > IL2 > IL5. The inhibition mechanism of ILs were attributed to the strong adsorption ability of these surfactants to form a protective layer that isolates the mild steel surface from an aggressive environment.

ILs	Cation	Anion	Molecular weight
IL1		Br^-	231.14
IL2		Br^-	287.24
IL3		Br^-	343.35
IL4		Br^-	427.51
IL5		Br^-	483.62

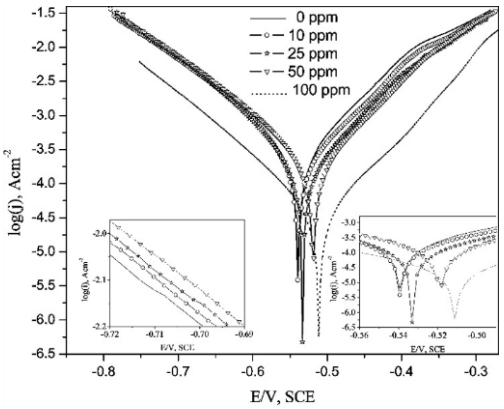


Figure 1.21 Chemical structure of the ILs and polarization plots of steel electrode obtained in 1.0M H_2SO_4 containing various concentrations of IL4.[147]

In another recent work by Atta et al.[148] the use of new hydrophobic IL derivatives, namely octadecylammonium tosylate (ODA-TS) and oleylammonium tosylate (OA-TS) for corrosion protection of steel in 1 M hydrochloric acid solution has been reported. They investigated the effect of the OA-TS and ODA-TS concentrations on the impedance behaviour of steel in acidic solution using EIS (Figure 1.22 (a) and (b)). The size of capacitive loop of impedance diagrams, increased with increasing inhibitor concentration. The capacitive loop was related to charge transfer in the corrosion process.[149] They reported the electrical equivalent circuit for fitting the data composed of solution resistance (Rs), charge transfer resistance (Rct) and double layer capacitance (Cdl), as shown in Figure 1.22 (c).

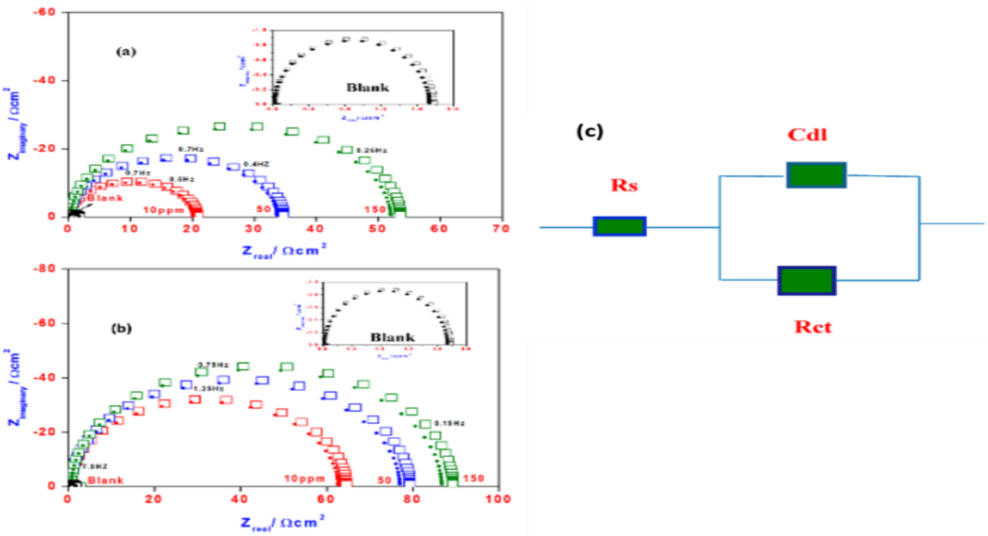


Figure 1.22 Nyqusit plots of steel electrode containing various concentrations of: (a) ODA-TS and (b) OA-TS and (c) equivalent circuit employed for fitting EIS data.[148]

Apart from these studies with IL based inhibitors, there have been no reports on investigation of the efficiency of PIL based inhibitors through different electrochemical techniques. A greater understanding of the PILs based corrosion inhibitors would certainly allow for the use of these unique polyelectrolytes for a range of corrosion inhibitor applications.

1.9.2 Advanced method for evaluation of adsorption behaviour of corrosion inhibitors

The quartz crystal microbalance with dissipation (QCM-D) is a simple, cost effective, high-resolution mass sensing technique, which could be used to obtain deeper insight into the mechanism of corrosion inhibitors by monitoring the adsorption of inhibitor and dissolution of metal over time. However, this unique technique has rarely been used in corrosion related adsorption studies and the number of reports, which used this method for the study of corrosion inhibition performance is limited. More detailed description is given below in the following section.

In a recent study, Otmacic Curkovic et al.[150] studied the mechanism of the protective action of three imidazole-based (4-Methyl-1-(p-tolyl)-imidazole, 4-methyl-1-(o-tolyl)-imidazole, and 4-methyl-1-phenyl imidazole) corrosion inhibitors on copper in 3% NaCl, using quartz crystal microbalance measurements. This study confirmed that even slight changes in the molecular structure induce a significant effect on the inhibition properties. Both tolyl-substituted 4-methyl imidazoles rapidly adsorbed onto the copper surface and decreased the copper corrosion rate while the phenyl-substituted 4-methyl imidazole slowly formed a protective 3D layer. On the other hand, the inhibiting effect of o-tolyl-substituted compound did not improve with time, while the inhibiting efficiency of the phenyl-substituted inhibitor increased with immersion time. Figure 1.23 presents the mass and the corrosion potential changes with respect to immersion period measured by QCM-D in the presence of (a) 4-methyl-1-(o-tolyl)-imidazole and (b) 4-methyl-1-phenyl imidazole. When the better inhibitor (phenyl based imidazole) was used, the increase of the mass of the electrode has been observed due to the formation of a protective layer on the copper surface. Firstly, an inhibitor monolayer is formed, upon which grows the protecting layer. Therefore, at the very initial stage, the rate of the mass gain increases with the increase of the surface area covered by inhibitor

until the whole surface is covered by inhibitor. Then, growth of the 3D layer continues on constant area, and therefore the rate of mass growth is constant.

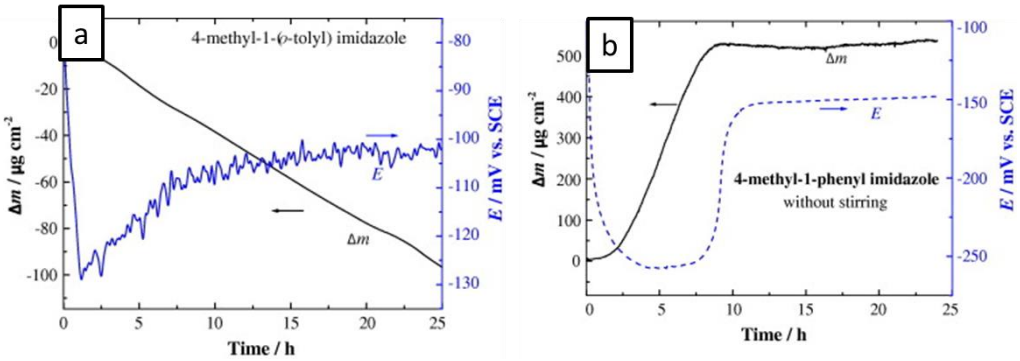


Figure 1.23 Mass and potential change of copper electrode in 3% NaCl with the addition of (a) 4-methyl-1-(p-tolyl)-imidazole and (b) 4-methyl-1-phenyl imidazole.[150]

As can be seen, QCM-D is a unique technique which has not yet been harnessed as a useful tool for in-depth understanding of the corrosion inhibitor mechanism. Thus, a fundamental understanding of the corrosion inhibition process of ILs and PILs based inhibitors using QCM-D has a potential to give new insight into the mechanism and form the basis of achieving a high level of control over the performance of corrosion inhibitors.

1.9.3 Advanced method for understanding the interfacial properties of the coatings

The measurement of electrochemical reactions at the interface becomes a matter of particular interest for the prediction of the service life times of coating. To achieve such information, new techniques that perform local measurements, such as scanning kelvin probe (SKP) are increasingly applied.[151-152] This method is a non-destructive, non-contact mode technique based on a vibrating capacitor to measure the surface work function (WF) distribution on surface. Surface work function is an extremely sensitive indicator of the surface condition and can be used to track changes in the surface such as surface contamination and corrosive adhesion of polymers on metal substrates.[153] Amongst many studies, Choudhury at al.[154] recently presented the sol-gel derived hybrid coatings containing three different compositions of methacrylate-phosphosilicate on mild steel substrates where SKP microscopy was used to evaluate the adhesion and corrosion protection properties. Phosphorus containing methacrylate hybrids were synthesized from 2-(methacryloyloxy)ethyl phosphate (EGMP) and 3-[(methacryloyloxy)-propyl] trimethoxysilane (MEMO) via dual-cure process involving

sol-gel reaction and addition polymerization. Similar experimental procedures were used to synthesize hybrids at other composition namely M:E – 3:7.[155] Figure 1.24 illustrates the SKP maps of the gold-coated aluminium (reference), bare metal substrate (MS), MEMO, EGMP, M:E – 1:1 and 3:7 coated samples. The average WF values of the samples shift positively towards noble potential in the order of bare MS < EGMP < MEMO < M:E – 1:1 < M:E – 3:7. The following equation can be used to correlate the absolute WF measured using SKP to the corrosion potential:[156]

$$V_{KP} = E_{corr} + \text{const.} \qquad \text{Eq.17}$$

The deviation in WF values can be correlated to the interfacial interaction between the coating and the substrate. The SKP measurements showed the presence of strong interfacial interaction, which is attributed to the interaction of phosphate group with the metallic substrate.[157]

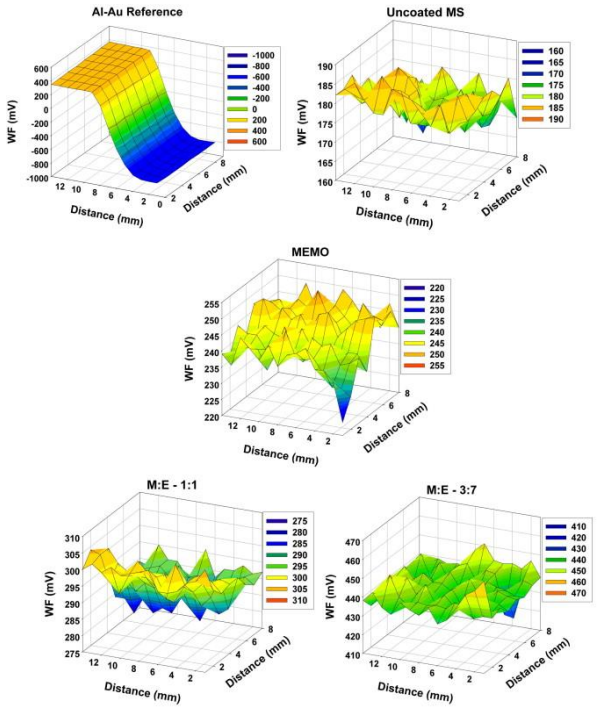


Figure 1.24 SKP maps of pristine gold on aluminum reference, bare MS, MEMO, M:E – 1:1 and M:E – 3:7 coated samples, respectively.

Although SKP could be used to obtain valuable information relating to the adhesion and corrosion protection properties of the coating, there are very few reports on application of SKP for understanding the interfacial properties of the coatings on steel surface.

1.10 Aims and scope of the project

In light of the above discussion it is evident that significant work has been carried out in the area of ionic liquids as environmentally friendly corrosion inhibitors. Due to the molecular configuration of ILs, they are able to form micelles and lowering interfacial tension of aggressive media, which results in an enhancement in surface wetting and adsorption. These properties have useful effect on exposed surfaces and may be responsible of the corrosion inhibition of metals. However, they generally demonstrate poor transport properties due to their high viscosity and surface tension and are not ideal for corrosion inhibition applications that require high mobility of corrosion inhibitors for protecting the metal. Therefore, the combination of the unique properties of ILs with the macromolecular architecture provides a method for the development of polymerized ionic liquids or poly (ionic liquid)s (PILs) with the enhanced mechanical stability, high shear and thermal stability, high resistivity to strong acid, durability, and spatial controllability over the IL species. Despite the very interesting properties of PILs for corrosion inhibition, there have been very few reports on their application for corrosion protection of metals. On the other hand, in spite of the considerable progress made in the chemistry of inhibitors, the problem of inhibition in a corrosion system presents the same challenges today as it did in the past. The transport of the corrosion inhibitor from bulk solution to the surface of the metal and the active inhibitor species that is available to interact with the metal are the fundamental factors governing corrosion inhibition. Therefore, there is a significant need to develop new corrosion inhibitors with effective morphology that provide rapid transportation of inhibitors, whilst possessing the desired interaction with metal.

Despite the extensive work on the different forms of PIL for different applications, there is no report on use of corrosion inhibitors based PIL and the application of PIL with different morphologies like gel particles and nanoparticles for corrosion inhibition application. Thus, there is a distinct need to achieve facile and rapid formation of novel PIL based corrosion inhibitors combining various heteroatoms and heterocyclic rings that possess effective corrosion inhibition properties.

The hypothesis of this work is that PIL based corrosion inhibitors formed by click-chemistry are promising for fabricating advanced coatings with improved barrier function and corrosion protection. Therefore, the specific aims of this research include:

1. Facile preparation of PIL based corrosion inhibitors in different forms such as gel particles, nanoparticles and films, using thiol-ene click chemistry
2. Evaluate the corrosion inhibition performance of the PIL based corrosion inhibitors in all three forms
3. In-depth understanding of the adsorption and inhibition performance of polymerizable ILs and PILs
4. Understanding the inhibition performance of PIL based coating

The scope of this work has been shown schematically in Figure 1.25. The fundamental in-depth understandings and the breakthroughs from this study will enable not only a facile design of PIL based corrosion inhibitors, but also guide their subsequent application in development of anticorrosion coatings.

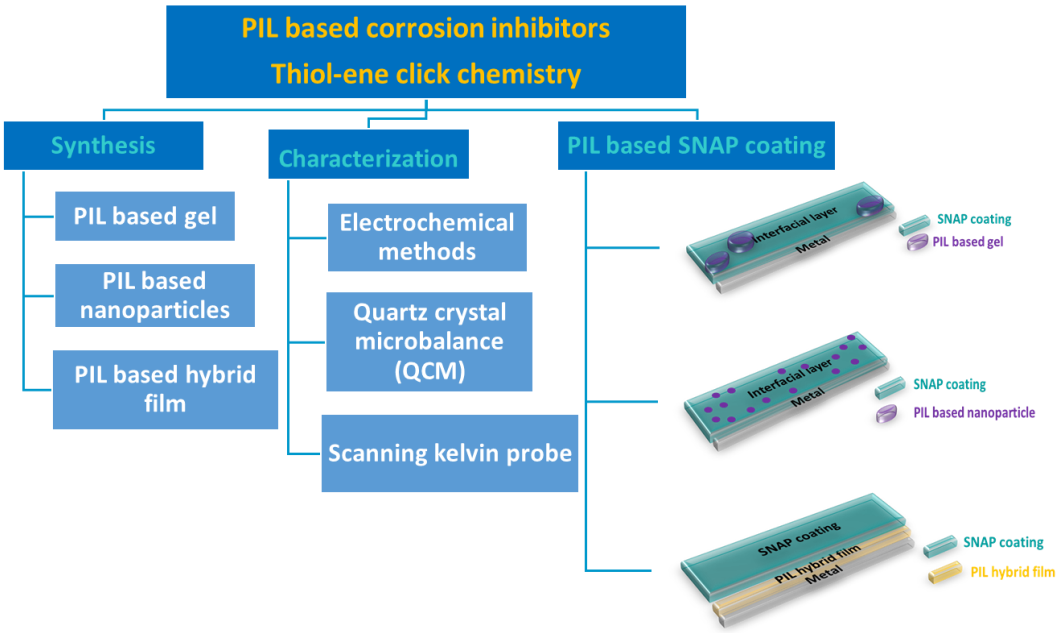


Figure 1.25 Scope of the work

1.11 References

1. Koch, G. H.; Brongers, M. P.; Thompson, N. G.; Virmani, Y. P.; Payer, J. H. *Corrosion cost and preventive strategies in the United States*; 2002.
2. Ratcliff, S. Research shows corrosion costs the local economy. *Curtin news* 2009.
3. Düdükcü, M.; Yazici, B.; Erbil, M. *Mater. Chem. Phys.* **2004,** *87* (1), 138-141.
4. Galal, A.; Atta, N. F.; Al-Hassan, M. H. S. *Mater. Chem. Phys.* **2005,** *89* (1), 28-37.
5. Al-Otaibi, M. S.; Al-Mayouf, A. M.; Khan, M.; Mousa, A. A.; Al-Mazroa, S. A.; Alkhathlan, H. Z. *Arabian J. Chem.* **2014,** *7* (3), 340-346.
6. de Souza, F. S.; Spinelli, A. *Corros. Sci.* **2009,** *51* (3), 642-649.
7. Cao, H.; Yuan, J. P.; Zhang, R.; Huang, C. M.; He, Y.; Sandreczki, T. C.; Jean, Y. C.; Nielsen, B.; Suzuki, R.; Ohdaira, T. *Macromolecules* **1999,** *32* (18), 5925-5933.
8. Pospíšil, J.; Nešpurek, S. *Prog. Polym. Sci.* **2000,** *25* (9), 1261-1335.
9. Trethewey, K. R.; Chamberlain, J. *Corrosion for Science and Engineering*. 2nd ed.; Longman: UK, 1995.
10. Pérez, N. *Electrochemistry and corrosion science*. Kluwer Academic Publishers: 2004.
11. Ahmad, Z. Chapter 1 - Introduction to Corrosion. In *Principles of Corrosion Engineering and Corrosion Control*, Butterworth-Heinemann: Oxford, 2006; pp 1-8.
12. Chawla, S. L. *Materials selection for corrosion control*. ASM international: 1993.
13. Lyon, S. *Int. Mater. Rev.* **2013**.
14. Evans, U. R. *An introduction to metallic corrosion*. Edward Arnold Ltd.: 1981.
15. Bockris, J. O. M.; Reddy, A. K. *Modern Electrochemistry 2B: Electrodics in Chemistry, Engineering, Biology and Environmental Science*. Springer Science & Business Media: 2001; Vol. 2.
16. Revie, R. W. *Corrosion and corrosion control*. John Wiley & Sons: 2008.
17. Sørensen, P. A.; Kiil, S.; Dam-Johansen, K.; Weinell, C. E. *J Coat Technol Res* **2009,** *6* (2), 135-176.

18. Rahimi, S. K.; Potrekar, R.; Dutta, N. K.; Choudhury, N. R. *Surf. Innovations* **2013,** *1* (2), 112-137.
19. Messaadia.L; El mouden.O. ID; Anejjar. A; Messali.M; Salghi.R; Benali.O; Cherkaoui.O; Lallam.A. *J. Mater. Environ. Sci.* **2015,** *6* (2), 598-606.
20. Dariva, C. G.; Galio, A. F. *Corrosion Inhibitors – Principles, Mechanisms and Applications, Developments in Corrosion Protection*. InTech: 2014
21. Talbot, D.; Talbot, J. *Corrosion science and technology*. CRC Press: Florida, 2000.
22. Roberge, P. R. *Handbook of Corrosion Engineering*. Mc Graw Hill Handbook: New York, 1999.
23. Bardal, E. *Corrosion and protection*. Springer: London, 2004.
24. El-Haddad, M. N. *Int. J. Biol. Macromol.* **2013,** *55,* 142-149.
25. Yaro, A. S.; Khadom, A. A.; Wael, R. K. *Alexandria Eng. J.* **2013,** *52* (1), 129-135.
26. Olivares, O.; Likhanova, N. V.; Gomez, B.; Navarrete, J.; Llanos-Serrano, M. E.; Arce, E.; Hallen, J. M. *Appl. Surf. Sci.* **2006,** *252* (8), 2894-2909.
27. Olivares-Xometl, O.; Likhanova, N. V.; Domínguez-Aguilar, M. A.; Arce, E.; Dorantes, H.; Arellanes-Lozada, P. *Mater. Chem. Phys.* **2008,** *110* (2–3), 344-351.
28. Abd El-Maksoud, S. A.; Fouda, A. S. *Mater. Chem. Phys.* **2005,** *93* (1), 84-90.
29. Noor, E. A. *Mater. Chem. Phys.* **2009,** *114* (2–3), 533-541.
30. Martínez-Palou, R.; Rivera, J.; Zepeda, L. G.; Rodríguez, A. N.; Hernández, M. A.; Marín-Cruz, J.; Estrada, A. *Corrosion* **2004,** *60* (5), 465-470.
31. Olivares-Xometl, O.; Likhanova, N. V.; Martínez-Palou, R.; Domínguez-Aguilar, M. A. *Mater. Corros.* **2009,** *60* (1), 14-21.
32. Popova, A.; Christov, M.; Zwetanova, A. *Corros. Sci.* **2007,** *49* (5), 2131-2143.
33. Antonijević, M. M.; Milić, S. M.; Petrović, M. B. *Corros. Sci.* **2009,** *51* (6), 1228-1237.
34. Tallman, D. E.; Spinks, G.; Dominis, A.; Wallace, G. G. *J. Solid State Electrochem.* **2001,** *6* (2), 73-84.
35. Clubley, B. G. *Chemical inhibitors for corrosion control*. 1990; p Medium: X; Size: Pages: (150 p).
36. Sastri, V. S. Environmentally Friendly Corrosion Inhibitors. In *Green Corrosion Inhibitors*, John Wiley & Sons, Inc.: 2011; pp 257-303.

37. Ghareba, S.; Omanovic, S. *Corros. Sci.* **2010,** *52* (6), 2104-2113.
38. Palomar, M. E.; Olivares-Xometl, C. O.; Likhanova, N. V.; Pérez-Navarrete, J.-B. *J. Surfactants Deterg.* **2010,** *14* (2), 211-220.
39. Khaled, K. F. *Appl. Surf. Sci.* **2008,** *255* (5, Part 1), 1811-1818.
40. Juhaiman, L. A. A.; Mustafa, A. A.; Mekhamer, W. K. *Anti-Corros. Methods Mater.* **2013,** *60* (1), 28-36.
41. Liu, G.; Huang, J.; Zhou, Y.; Yao, Q.; Yang, Y.; Ling, L.; Wang, H.; Wu, W.; Sun, W.; Hu, Z. *Des. Monomers Polym.* **2013,** *16* (1), 89-98.
42. Martínez-Palou, R.; Sánche, P. F. *Perspectives of Ionic Liquids Applications for Clean Oilfield Technologies, Ionic Liquids: Theory, Properties, New Approaches*. InTech: 2011.
43. Zhang, Q. B.; Hua, Y. X. *Electrochimica Acta* **2009,** *54* (6), 1881-1887.
44. Ashassi-Sorkhabi, H.; Es'haghi, M. *Mater. Chem. Phys.* **2009,** *114* (1), 267-271.
45. Yuan, J.; Antonietti, M. *Polymer* **2011,** *52* (7), 1469-1482.
46. Plechkova, N. V.; Seddon, K. R. *Chem. Soc. Rev.* **2008,** *37* (1), 123-150.
47. Olivier-Bourbigou, H.; Magna, L.; Morvan, D. *Appl. Catal., A* **2010,** *373* (1–2), 1-56.
48. Han, X.; Armstrong, D. W. *Acc. Chem. Res.* **2007,** *40* (11), 1079-1086.
49. Bara, J. E.; Carlisle, T. K.; Gabriel, C. J.; Camper, D.; Finotello, A.; Gin, D. L.; Noble, R. D. *Ind. Eng. Chem. Res.* **2009,** *48* (6), 2739-2751.
50. Anderson, J. L.; Armstrong, D. W.; Wei, G.-T. *Anal. Chem.* **2006,** *78* (9), 2892-2902.
51. Ye, C.; Liu, W.; Chen, Y.; Yu, L. *Chem. Commun.* **2001,** *0* (21), 2244-2245.
52. Kuang, D.; Wang, P.; Ito, S.; Zakeeruddin, S. M.; Grätzel, M. *J. Am. Chem. Soc.* **2006,** *128* (24), 7732-7733.
53. Likhanova, N. V.; Domínguez-Aguilar, M. A.; Olivares-Xometl, O.; Nava-Entzana, N.; Arce, E.; Dorantes, H. *Corros. Sci.* **2010,** *52* (6), 2088-2097.
54. Łuczak, J.; Hupka, J.; Thöming, J.; Jungnickel, C. *Colloids Surf., A* **2008,** *329* (3), 125-133.
55. Espinosa, T.; Sanes, J.; Jiménez, A.-E.; Bermúdez, M.-D. *Appl. Surf. Sci.* **2013,** *273*, 578-597.
56. Elachouri, M.; Hajji, M. S.; Kertit, S.; Essassi, E. M.; Salem, M.; Coudert, R. *Corros. Sci.* **1995,** *37* (3), 381-389.

57. Gašparac, R.; Martin, C. R.; Stupnišek - Lisac, E. *J. Electrochem. Soc.* **2000,** *147* (2), 548-551.
58. Zhang, D.-Q.; Gao, L.-X.; Zhou, G.-D. *Appl. Surf. Sci.* **2006,** *252* (14), 4975-4981.
59. Zhang, Q.; Hua, Y. *Mater. Chem. Phys.* **2010,** *119* (1–2), 57-64.
60. Guzmán-Lucero, D.; Olivares-Xometl, O.; Martínez-Palou, R.; Likhanova, N. V.; Domínguez-Aguilar, M. A.; Garibay-Febles, V. *Ind. Eng. Chem. Res.* **2011,** *50* (12), 7129-7140.
61. Shi, S.; Yi, P.; Cao, C.; Wang, X.; Su, J.; Liu, J. *Chin. J. Chem. Eng.* **2005,** *56* (6), 1112.
62. Ford, F.; Burstein, G.; Hoar, T. *J. Electrochem. Soc.* **1980,** *127* (6), 1325-1331.
63. Quraishi, M. A.; Rafiquee, M. Z. A.; Khan, S.; Saxena, N. *J. Appl. Electrochem.* **2007,** *37* (10), 1153-1162.
64. Saleh, M. M. *Mater. Chem. Phys.* **2006,** *98* (1), 83-89.
65. Uerdingen, M.; Treber, C.; Balser, M.; Schmitt, G.; Werner, C. *Green Chem.* **2005,** *7* (5), 321-325.
66. Chong, A. L.; Mardel, J. I.; MacFarlane, D. R.; Forsyth, M.; Somers, A. E. *ACS Sustainable Chem. Eng.* **2016,** *4* (3), 1746-1755.
67. Zhang, H.; Hong, K.; Mays, J. W. *Macromolecules* **2002,** *35* (15), 5738-5741.
68. Woecht, I.; Schmidt-Naake, G.; Beuermann, S.; Buback, M.; García, N. *J. Polym. Sci., Part A: Polym. Chem.* **2008,** *46* (4), 1460-1469.
69. Ricks-Laskoski, H. L.; Snow, A. W. *J. Am. Chem. Soc.* **2006,** *128* (38), 12402-12403.
70. Green, O.; Grubjesic, S.; Lee, S.; Firestone, M. A. *Polym. Rev.* **2009,** *49* (4), 339-360.
71. Anderson, E. B.; Long, T. E. *Polymer* **2010,** *51* (12), 2447-2454.
72. Green, M. D.; Long, T. E. *Polym. Rev.* **2009,** *49* (4), 291-314.
73. Shaplov, A. S.; Vlasov, P. S.; Lozinskaya, E. I.; Shishkan, O. A.; Ponkratov, D. O.; Malyshkina, I. A.; Vidal, F.; Wandrey, C.; Godovikov, I. A.; Vygodskii, Y. S. *Macromol. Chem. Phys.* **2012,** *213* (13), 1359-1369.
74. Shaplov, A. S.; Goujon, L.; Vidal, F.; Lozinskaya, E. I.; Meyer, F.; Malyshkina, I. A.; Chevrot, C.; Teyssie, D.; Odinets, I. L.; Vygodskii, Y. S. *J. Polym. Sci., Part A: Polym. Chem.* **2009,** *47* (17), 4245-4266.

75. Allen, M. H.; Green, M. D.; Getaneh, H. K.; Miller, K. M.; Long, T. E. *Biomacromolecules* **2011,** *12* (6), 2243-2250.
76. Qiu, B.; Lin, B.; Si, Z.; Qiu, L.; Chu, F.; Zhao, J.; Yan, F. *J. Power Sources* **2012,** *217*, 329-335.
77. Mecerreyes, D. *Prog. Polym. Sci.* **2011,** *36* (12), 1629-1648.
78. Yuan, J.; Soll, S.; Drechsler, M.; Müller, A. H. E.; Antonietti, M. *J. Am. Chem. Soc.* **2011,** *133* (44), 17556-17559.
79. Earle, M. J.; Esperanca, J. M. S. S.; Gilea, M. A.; Canongia Lopes, J. N.; Rebelo, L. P. N.; Magee, J. W.; Seddon, K. R.; Widegren, J. A. *Nature* **2006,** *439* (7078), 831-834.
80. Gordon, C. M. *Appl. Catal., A* **2001,** *222* (1–2), 101-117.
81. Endres, F.; Zein El Abedin, S. *Phys. Chem. Chem. Phys.* **2006,** *8* (18), 2101-2116.
82. Chen, X.; Zhao, J.; Zhang, J.; Qiu, L.; Xu, D.; Zhang, H.; Han, X.; Sun, B.; Fu, G.; Zhang, Y.; Yan, F. *J. Mater. Chem.* **2012,** *22* (34), 18018-18024.
83. Döbbelin, M.; Azcune, I.; Bedu, M.; Ruiz De Luzuriaga, A.; Genua, A.; Jovanovski, V.; Cabañero, G.; Odriozola, I. *Chem. Mater.* **2012,** *24* (9), 1583-1590.
84. Posner, T. *Ber. Dtsch. Chem. Ges.* **1905,** *38* (1), 646-657.
85. Hoyle, C. E.; Lee, T. Y.; Roper, T. *J. Polym. Sci., Part A: Polym. Chem.* **2004,** *42* (21), 5301-5338.
86. Rydholm, A. E.; Reddy, S. K.; Anseth, K. S.; Bowman, C. N. *Polymer* **2007,** *48* (15), 4589-4600.
87. Carioscia, J. A.; Stansbury, J. W.; Bowman, C. N. *Polymer* **2007,** *48* (6), 1526-1532.
88. Chan, J. W.; Hoyle, C. E.; Lowe, A. B. *J. Am. Chem. Soc.* **2009,** *131* (16), 5751-5753.
89. Kakwere, H.; Perrier, S. *J. Am. Chem. Soc.* **2009,** *131* (5), 1889-1895.
90. Durham, O. Z.; Krishnan, S.; Shipp, D. A. *ACS Macro Lett.* **2012,** *1* (9), 1134-1137.
91. Lowe, A. B. *Polym. Chem.* **2014,** *5* (17), 4820-4870.
92. Dimitrov-Raytchev, P.; Beghdadi, S.; Serghei, A.; Drockenmuller, E. *J. Polym. Sci., Part A: Polym. Chem.* **2013,** *51* (1), 34-38.

93. Abdelhedi-Miladi, I.; Obadia, M. M.; Allaoua, I.; Serghei, A.; Romdhane, H. B.; Drockenmuller, E. *Macromol. Chem. Phys.* **2014,** *215* (22), 2229-2236.
94. Men, Y.; Kuzmicz, D.; Yuan, J. *Curr. Opin. Colloid Interface Sci.* **2014,** *19* (2), 76-83.
95. Stepto Robert, F. T. Dispersity in polymer science (IUPAC Recommendations 2009). In *Pure and Applied Chemistry*, 2009; Vol. 81, p 351.
96. Muldoon, M. J.; Gordon, C. M. *J. Polym. Sci., Part A: Polym. Chem.* **2004,** *42* (15), 3865-3869.
97. Marcilla, R.; Sanchez-Paniagua, M.; Lopez-Ruiz, B.; Lopez-Cabarcos, E.; Ochoteco, E.; Grande, H.; Mecerreyes, D. *J. Polym. Sci., Part A: Polym. Chem.* **2006,** *44* (13), 3958-3965.
98. Yuan, J.; Antonietti, M. *Macromolecules* **2011,** *44* (4), 744-750.
99. Weber, R. L.; Ye, Y.; Schmitt, A. L.; Banik, S. M.; Elabd, Y. A.; Mahanthappa, M. K. *Macromolecules* **2011,** *44* (14), 5727-5735.
100. Yang, J.; Qiu, L.; Liu, B.; Peng, Y.; Yan, F.; Shang, S. *J. Polym. Sci., Part A: Polym. Chem.* **2011,** *49* (21), 4531-4538.
101. Zhou, X.; Zhou, Y.; Nie, J.; Ji, Z.; Xu, J.; Zhang, X.; Du, B. *ACS Appl. Mater. Interfaces* **2014,** *6* (6), 4498-4513.
102. Amato, D. V.; Amato, D. N.; Flynt, A. S.; Patton, D. L. *Polym. Chem.* **2015,** *6* (31), 5625-5632.
103. Hoyle, C. E.; Bowman, C. N. *Angew. Chem., Int. Ed. Engl.* **2010,** *49* (9), 1540-1573.
104. Hoyle, C. E.; Lowe, A. B.; Bowman, C. N. *Chem. Soc. Rev.* **2010,** *39* (4), 1355-1387.
105. Jasinski, F.; Lobry, E.; Tarablsi, B.; Chemtob, A.; Croutxé-Barghorn, C.; Le Nouen, D.; Criqui, A. *ACS Macro Lett.* **2014,** *3* (9), 958-962.
106. Raghavan, P.; Manuel, J.; Zhao, X.; Kim, D.-S.; Ahn, J.-H.; Nah, C. *J. Power Sources* **2011,** *196* (16), 6742-6749.
107. Murata, Y.; Sasaki, N.; Miyamoto, E.; Kawashima, S. *Eur. J. Pharm. Biopharm.* **2000,** *50* (2), 221-226.
108. Kashyap, N.; Kumar, N.; Kumar, M. N. V. R. *Crit. Rev. Ther. Drug Carrier Syst.* **2005,** *22* (2), 107-149.
109. Xiong, Y.; Wang, H.; Wang, R.; Yan, Y.; Zheng, B.; Wang, Y. *Chem. Commun.* **2010,** *46* (19), 3399-3401.

110. Rahman, M. T.; Barikbin, Z.; Badruddoza, A. Z. M.; Doyle, P. S.; Khan, S. A. *Langmuir* **2013,** *29* (30), 9535-9543.
111. Sastri, V. S. Adsorption in Corrosion Inhibition. In *Green Corrosion Inhibitors*, John Wiley & Sons, Inc.: 2011; pp 103-138.
112. Feng, L.; Yang, H.; Wang, F. *Electrochimica Acta* **2011,** *58*, 427-436.
113. Ashassi-Sorkhabi, H.; Shaabani, B.; Seifzadeh, D. *Electrochimica Acta* **2005,** *50* (16), 3446-3452.
114. Obot, I.; Obi-Egbedi, N. *Corros. Sci.* **2010,** *52* (2), 657-660.
115. Obot, I. B.; Obi-Egbedi, N. O. *Corros. Sci.* **2010,** *52* (1), 198-204.
116. Ebenso, E. E.; Alemu, H.; Umoren, S. A.; Obot, I. B. *Int. J. Electrochem. Sci.* **2008,** *3* (12), 1325-1339.
117. Wang, L. *Corros. Sci.* **2006,** *48* (3), 608-616.
118. Shchukin, D. G.; Grigoriev, D. O.; Mohwald, H. *Soft Matter* **2010,** *6* (4), 720-725.
119. Li, S.; Wang, Y.; Chen, S.; Yu, R.; Lei, S.; Ma, H.; Liu, D. X. *Corros. Sci.* **1999,** *41* (9), 1769-1782.
120. El-Mahdy, G. A.; Atta, A. M.; Al-Lohedan, H. A.; Tawfik, A. M.; Abdel-Khalek, A. A. *Int. J. Electrochem. Sci* **2015,** *10*, 151-161.
121. Quraishi, M.; Rafiquee, M.; Khan, S.; Saxena, N. *J. Appl. Electrochem.* **2007,** *37* (10), 1153-1162.
122. Yurt, A.; Balaban, A.; Kandemir, S. U.; Bereket, G.; Erk, B. *Mater. Chem. Phys.* **2004,** *85* (2), 420-426.
123. Arellanes-Lozada, P.; Olivares-Xometl, O.; Guzmán-Lucero, D.; Likhanova, N.; Domínguez-Aguilar, M.; Lijanova, I.; Arce-Estrada, E. *Materials* **2014,** *7* (8), 5711.
124. Atta, A. M.; El-Mahdy, G. A.; Allohedan, H. A.; Abdullah, M. M. *Int. J. Electrochem. Sci* **2015,** *10*, 10389-10401.
125. Borisova, D.; Akçakayıran, D.; Schenderlein, M.; Möhwald, H.; Shchukin, D. G. *Adv. Funct. Mater.* **2013,** *23* (30), 3799-3812.
126. Borisova, D.; Möhwald, H.; Shchukin, D. G. *ACS Nano* **2011,** *5* (3), 1939-1946.
127. Fang, J.; Li, J. *J. Mol. Struct.: THEOCHEM* **2002,** *593* (1), 179-185.
128. Mona Taghavikish; Surya Subianto; Naba Kumar Dutta; Liliana de Campo; Jitendra P. Mata; Christine Rehm; Choudhury, N. R. *ACS Omega* **2016**.

129. Zheng, Z.; Huang, X.; Schenderlein, M.; Borisova, D.; Cao, R.; Möhwald, H.; Shchukin, D. *Adv. Funct. Mater.* **2013,** *23* (26), 3307-3314.
130. Suleiman, R.; Khaled, M.; Wang, H.; Smith, T. J.; Gittens, J.; Akid, R.; Mohamad El Ali, B.; Khalil, A. *Corros. Eng., Sci. Technol.* **2014,** *49* (3), 189-196.
131. Quinet, M.; Neveu, B.; Moutarlier, V.; Audebert, P.; Ricq, L. *Prog. Org. Coat.* **2007,** *58* (1), 46-53.
132. Moutarlier, V.; Neveu, B.; Gigandet, M. P. *Surf. Coat. Technol.* **2008,** *202* (10), 2052-2058.
133. Lamaka, S.; Zheludkevich, M.; Yasakau, K.; Montemor, M.; Ferreira, M. *Electrochimica Acta* **2007,** *52* (25), 7231-7247.
134. Bera, S.; Rout, T.; Udayabhanu, G.; Narayan, R. *Prog. Org. Coat.* **2015,** *88*, 293-303.
135. Figueira, R.; Silva, C.; Pereira, E. *J Coat Technol Res* **2015,** *12* (1), 1-35.
136. Figueira, R. B.; Silva, C. J.; Pereira, E. V.; Salta, M. M. *J. Electrochem. Soc.* **2013,** *160* (10), C467-C479.
137. Zhang, X.-F.; Chen, R.-J.; Liu, Y.-H.; Hu, J.-M. *J. Mater. Chem. A* **2016,** *4* (2), 649-656.
138. Vreugdenhil, A.; Balbyshev, V.; Donley, M. *J. Coat. Technol.* **2001,** *73* (915), 35-43.
139. Davis, S. R.; Brough, A. R.; Atkinson, A. *J. Non-Cryst. Solids* **2003,** *315* (1), 197-205.
140. Donley, M. S.; Mantz, R. A.; Khramov, A.; Balbyshev, V.; Kasten, L. S.; Gaspar, D. J. *Prog. Org. Coat.* **2003,** *47* (3), 401-415.
141. Zheludkevich, M.; Salvado, I. M.; Ferreira, M. *J. Mater. Chem.* **2005,** *15* (48), 5099-5111.
142. Voevodin, N.; Grebasch, N.; Soto, W.; Kasten, L.; Grant, J.; Arnold, F.; Donley, M. *Prog. Org. Coat.* **2001,** *41* (4), 287-293.
143. Lamaka, S. V.; Zheludkevich, M. L.; Yasakau, K. A.; Montemor, M. F.; Cecílio, P.; Ferreira, M. G. *Electrochem. Commun.* **2006,** *8* (3), 421-428.
144. Fontinha, I. R. **2012**.
145. Metroke, T. L.; Parkhill, R. L.; Knobbe, E. T. *Prog. Org. Coat.* **2001,** *41* (4), 233-238.

146. Zandi-Zand, R.; Ershad-Langroudi, A.; Rahimi, A. *Prog. Org. Coat.* **2005,** *53* (4), 286-291.
147. Guzmán-Lucero, D.; Olivares-Xometl, O.; Martínez-Palou, R.; Likhanova, N. V.; Domínguez-Aguilar, M. A.; Garibay-Febles, V. *Ind. Eng. Chem. Res.* **2011,** *50* (12), 7129-7140.
148. Atta, A.; El-Mahdy, G.; Al-Lohedan, H.; Ezzat, A. *Molecules* **2015,** *20* (6), 11131.
149. Deyab, M.; El-Rehim, S. A. *Corros. Sci.* **2012,** *65*, 309-316.
150. Otmacic Curkovic, H.; Stupnisek-Lisac, E.; Takenouti, H. *Corros. Sci.* **2009,** *51* (10), 2342-2348.
151. Dornbusch, M. *Prog. Org. Coat.* **2008,** *61* (2-4), 240-244.
152. Nazarov, A.; Prosek, T.; Thierry, D. *Electrochimica Acta* **2008,** *53* (25), 7531-7538.
153. Wapner, K.; Stratmann, M.; Grundmeier, G. *Silicon Chem.* **2005,** *2* (5), 235-245.
154. Kannan, A. G.; Choudhury, N. R.; Dutta, N. K. *J. Electroanal. Chem.* **2010,** *641* (1–2), 28-34.
155. Kannan, A. G.; Choudhury, N. R.; Dutta, N. K. *Polymer* **2007,** *48* (24), 7078-7086.
156. Stratmann, M. *Corros. Sci.* **1987,** *27* (8), 869-872.
157. Pepe, A.; Galliano, P.; Aparicio, M.; Durán, A.; Ceré, S. *Surf. Coat. Technol.* **2006,** *200* (11), 3486-3491.

Chapter 2: Experimental: materials and methodology

This chapter is presented in four sections: (a) chemicals and materials; (b) chemistry of synthesis and fabrication methods; (c) preparation of corrosion inhibitors loaded coating and surface preparation of steel and (d) background to the instrumental techniques that have been used in this research. In the first part the main materials used in the work are included, while chapter specific materials are highlighted in each chapter. The second part of the chapter covers the different chemistries that have been used in the entire work for synthesis and fabrication of inhibitors, while chapter specific synthesis methods of corrosion inhibitors are highlighted in each chapter. In the third part of this chapter, preparation of corrosion inhibitors loaded coating and surface preparation of steel are described. In the fourth part, various instrumental techniques that are used for the characterization of various prepared samples and coatings are discussed such as various spectroscopic, microscopic, electrochemical, thermal and mechanical techniques.

2.1 Chemicals, solvents and materials

Table 2.1 summarises the details of the chemicals and solvents used for synthesis and preparation of the ionic liquids (ILs), polymerized ionic liquids (PILs), gels, nanoparticles, hybrid film for inhibitor loaded coatings, and to perform all chemical and physical characterisations. Also, the details of metals that have been used as a substrate for all the electrochemical studies are provided. All chemicals are of laboratory and/or analytical grade and were used without further purification. In the case of use of water, double distilled water (DDW) was used for all experiments.

Table 2.1 List of chemicals, solvents and materials used in this research work.

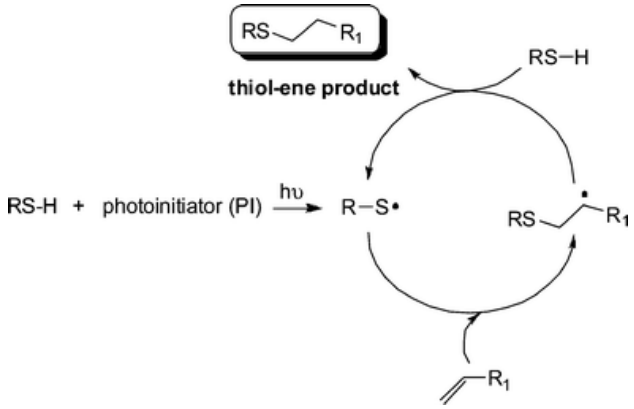
Name	Supplier
Solvents and chemicals for synthesis of IL and PIL based inhibitors and properties study	
Pentaerythritol tetrakis(3-mercaptopropionate)(PETKMP)	Sigma-Aldrich, Australia
1-Vinylimidazole	Sigma-Aldrich, Australia
1,4-dibromobutane	Sigma-Aldrich, Australia

Benzophenone (BP)	Sigma-Aldrich, Australia
1-butyl-3-methylImidazolium hexafluorophosphate	Sigma-Aldrich, Australia
Azobis(isobutyronitrile) (AIBN)	Sigma-Aldrich, Australia
Methyl red	Sigma-Aldrich, Australia
Diethyl ether	Sigma-Aldrich, Australia
Methanol(analytical grade)	Sigma-Aldrich, Australia
Sodium dodecyl sulfate (SDS)	Sigma-Aldrich, Australia
3-Amino propyl)triethoxysilane	Sigma-Aldrich, Australia
Sorbitan monostearate	Sigma-Aldrich, Australia
Toluene	Sigma-Aldrich, Australia
Acetone	Sigma-Aldrich, Australia
1,6-dibromohexane	Sigma-Aldrich, Australia
1,8-dibromooctane	Sigma-Aldrich, Australia
Acetonitrile	Sigma-Aldrich, Australia
Ethyl acetate	Sigma-Aldrich, Australia
Hexane	Sigma-Aldrich, Australia
Solvents and chemicals for inhibitor loaded coatings	
3-glycidoxypropyltrimethoxysilane(GPTMS)	Sigma-Aldrich, Australia
(3-mercaptopropyl)trimethoxysilane(MPTS)	Sigma-Aldrich, Australia
3-aminopropyltriethoxysilane	Sigma-Aldrich, Australia
Tetraethylorthosilicate(TEOS)	Sigma-Aldrich, Australia
Fluorosurfactant FC-4432	3M Advanced Materials
Acetic acid	Sigma-Aldrich, Australia
Sodium hydroxide (NaOH)	Sigma-Aldrich, Australia
Sodium chloride (NaCl)	Sigma-Aldrich, Australia
Metal substrate properties	
Mild steel, CA3SN-G cold rolled, 0.08 % carbon contents, thickness~0.6 mm of 1.7 cm×1.7 cm	BlueScope Steel, Australia
QCM sensor	
Sensor crystal SS2343(similar to us standard) stainless steel, 50 nm	ATA Scientific Pty Ltd

2.2 Chemistry of synthesis and fabrication methods

2.2.1 Thiol-ene chemistry

The thiol-ene reaction, known for over 100 years,[1] is the hydrothiolation of a C=C bond. In the field of polymer and materials science this reaction has been most widely employed as a tool of preparing near-perfect networks and films as exemplified by the work of Hoyle and co-workers[2] and Bowman et al.[3-4] The advantage of the ‘‘click’’ nature of thiol-ene reaction has recently attracted researchers in other areas of polymer chemistry and materials development. Generally, the thiol-ene reaction has been processed under radical conditions, which is often photochemically induced. Therefore, the reaction proceeds via a step-growth free-radical polymerization mechanism and includes two main reactions, a propagation step and a chain transfer step, that are outlined in Scheme 2.1.[5]



Scheme 2.1 The mechanism of thiol-ene reaction.[5]

By the employment of a difunctional ene and a difunctional thiol a linear polymer chain is obtained whereas by the employment of a thiol-ene pair with average functionality of greater than two, a polymer network is formed.[6]

The initiation step involves a proton abstraction from a thiol-functional compound by using photoinitiator and under irradiation, resulting a thiyl radical RS•, plus other by-products. Thus, the thiol-ene chemistry can take place at room temperature under the influence of ultraviolet (UV) radiation. At higher temperatures, the thiol-ene reaction takes place using thermal initiation of the S–H bond to generate thiyl radicals. Propagation is a two-step process involving first the direct addition of the thiyl radical across the ene double-bond followed by chain transfer to a second molecule of thiol to

give the thiol-ene addition product, with the subsequent formation of a thiyl-radical. Because thiol-ene chemistry involves a free-radical polymerization process, the species involved are capable of undergoing typical radical–radical termination reactions. The reactivity of the radical thiol-ene reaction depends on the chemical structure of the ene and thiol components. Usually three types of thiol-compounds are used in thiol-ene chemistry, namely alkyl 3-mercaptopropionates, alkyl thioglycolates and alkanethiols. The reactivity of the ene decreases in the order:[5-6]
norbornene > vinylether > Alkene > Vinyl ester > Allyl ether > Acrylate >Methacrylate > Styrene > Conjugated diene and the reactivity of the thiol decreases in the order:
Alkyl (3-mercaptopropionate) > Alkyl thioglycolate > Alkanethiol.

Thiol-ene reaction has been attracted significant interest in broad range of areas associated with polymer and materials chemistry such as preparation and application of hydrogels, the synthesis of crosslinked beads/polymeric nanoparticles, as well as the monomer synthesis and polymer side and end chain modification, the synthesis of dendrimers, hyperbranched and star polymers and the organic–inorganic hybrid materials.[6] In entire work of this thesis, thiol-ene chemistry has been employed for the synthesis of PIL based corrosion inhibitors in three forms including: gel, nanoparticle, and hybrid film using two different thiols (tetra thiol and single thiol). Details of synthesis and experimental process are included in each chapter.

2.2.2 Emulsion polymerization

An emulsion polymerization is a hetero-phase polymerization technique in which a monomer is dispersed in a continuous phase, usually water, and stabilized by surfactant molecules against coalescence. The monomer phase is dispersed in the continuous phase via mechanical agitation, and the size distribution of the monomer droplets is broad. Generally, particle sizes obtained via emulsion polymerization range from about 50 nanometers to a few microns. Harkins' theory gives valuable insight into the mechanism of emulsion polymerization.[7] As shown in Figure 2.1, the majority of monomer is present as big monomer droplets in the aqueous phase and they are stabilized by surfactant molecules.[7-8] The majority of surfactant molecules are however present as aggregates, known as micelles, that are formed above a certain concentration (the critical micelle concentration, cmc). These micelles contain a small amount of monomer (monomer swollen micelles) and a small fraction of the surfactant molecules

exist as single molecules in the aqueous phase, the amount of which is dependent, for example, on the solubility, type of surfactant and the temperature. Finally, the polymerization is started by means of an initiator. [2, 8-9]

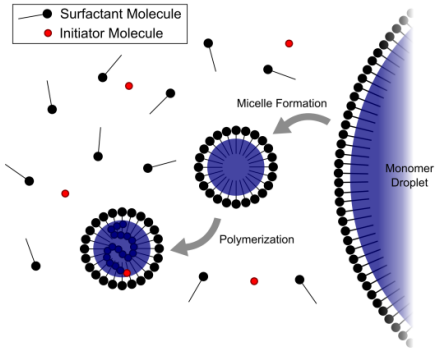


Figure 2.1 Mechanism of emulsion polymerization.[10]

One of the most common methods used for the fabrication of polymer nanoparticles with the droplet sizes typically in the range of 20-200 nm is miniemulsion. In chapter 5, combination of thiol-ene chemistry with miniemulsion has been employed for synthesis of PIL based corrosion inhibitors in the form of nanoparticles. Details of the synthesis method are shown in Chapter 5.

2.3 Preparation of inhibitor loaded coating and surface preparation of steel

2.3.1 Surface preparation of steel

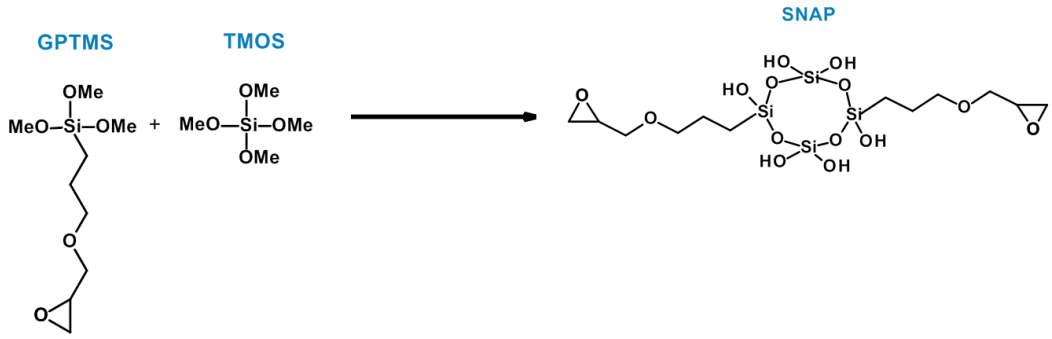
The mild steel substrates were sequentially polished using abrasive papers with grit numbers 800, 1000 and 1200 prior to cleaning by sequential immersion for 10 min each in acetone, hexane and ethanol solutions (to remove surface oils). The substrates were then rinsed with distilled water and dried between each solvent wash and after the final solvent wash. Finally, the dried substrates were treated with a commercial alkaline cleaner rinsed with distilled water and dried with N_2 purge. Figure 2.2 illustrates the schematic diagram of the surface preparation process.



Figure 2.2 Schematic of surface preparation of mild steel.

2.3.2 Synthesis of self-assembled nanoparticle phase (SNAP) coating

Self-assembled nanoparticle phase (SNAP) solution was synthesised following the method proposed by Donley et al.[11] The SNAP solution was prepared by drop wise addition of 42 ml (0.19 mol) 3-glycidoxypropyltrimethoxysilane (GPTMS) and 13.4 ml (0.06 mol) of tetraethylorthosilicate (TEOS) to 64.8 ml solution of 0.05M acetic acid in doubly distilled water (DDW) water in inert atmosphere. The solution was continuously stirred for 1h during addition. The TEOS: GPTMS molar ratio used was (1:3 mol ratio) respectively. Hydrolysis and condensation of silanes were conducted at high water/silane ratio of 15. After all of the silanes had been added and hydrolysed, the solution was aged in a closed container for 3 days under continued stirring at ambient temperature. Scheme 2.2 shows the reaction of synthesis of SNAP.



Scheme 2.2 Reaction scheme for synthesis of SNAP.

Generally, SNAP coating solution, for applying into the metal is prepared by diluting the aged SNAP solution with water by a factor of 1.75 and subsequent addition of crosslinking agent (aminosilane) and surfactant (3M FC-4432, 0.04wt/ v %). The molar ratio of crosslinking agent to GPTMS was kept constant

at 6.5. The details of the SNAP coating formulation is summarised in Table 2.2. The final mixture was vigorously stirred and applied to cleaned panels by dip coating at a withdrawal speed of 10 cm/min. The coating was made within a time frame of 10-30 min, counting from the point of addition of the crosslinking agent. The coated samples were dried at room temperature for 24 hours to allow solvent evaporation. The coating was thermally cured at 80 °C, 60% humidity for overnight in humidity oven. Figure 2.3 illustrates the SNAP coating preparation process.

Table 2.2 General formulation for preparation of SNAP coating.

Components	Quantities
SNAP	7 ml
DDW	12.25 ml
FC-4432	4.4 ml
Aminosilane (Crosslinking agent)	8 mg (0.04 wt%)

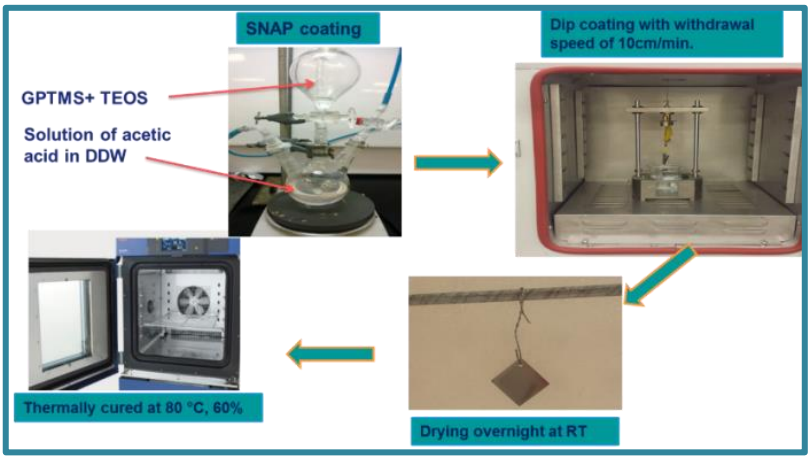


Figure 2.3 Preparation process of SNAP coating.

2.3.3 Preparation of SNAP loaded PIL gel and nanoparticle based inhibitors

The SNAP loaded with PIL gels were prepared using similar experimental procedure and formulation to the SNAP coating (Table 2.2) while 20 mg (0.2 wt %) fine grinded gels in micron size were added to the solution and ultrasonicated for 5 min. PIL nanoparticle inhibitor loaded coatings were prepared following similar experimental procedure using the formulation given in Table 2.3. The

mixtures were ultrasonicated at 50% rpm for 5 min to obtain homogenous solutions.

Table 2.3 Formulation of 0.8 wt% PIL nanoparticle inhibitor loaded SNAP coating

Components	Quantities
SNAP	7 ml
DDW	8.75 ml
FC-4432	4.4 ml
Aminosilane (Crosslinking agent)	8 mg (0.04 wt%)
Emulsion (0.8 wt%)	3.5 ml

2.4 Characterization techniques

2.4.1 Spectroscopic techniques

2.4.1.1 Photo-acoustic fourier transform infrared (PA-FTIR) Spectroscopy

Photo-acoustic spectroscopy is based on the photo-acoustic effect, which was discovered by Alexander Graham Bell in 1880. In photo-acoustic effect, intermittent light is irradiated onto a substrate, which then emits waves of the same frequency as the light pulse frequency (Figure 2.4).[12] During operation, a modulated infrared beam from the FTIR spectrometer strikes the sample. The light is absorbed and produces heat that alters the pressure of the surrounding gas (Helium). The change in pressure is detected as sound by a microphone and is then converted to an acoustic interference waves and Fourier transformation is applied to produce a spectrum. In this study, experiments were conducted using the Nicolet Magna-IR Spectrometer 750 in photo-acoustic mode using a carbon black as reference. Spectra were obtained in the range of 400 to 4000 cm^{-1} and the data was processed using the Omnic computer program.

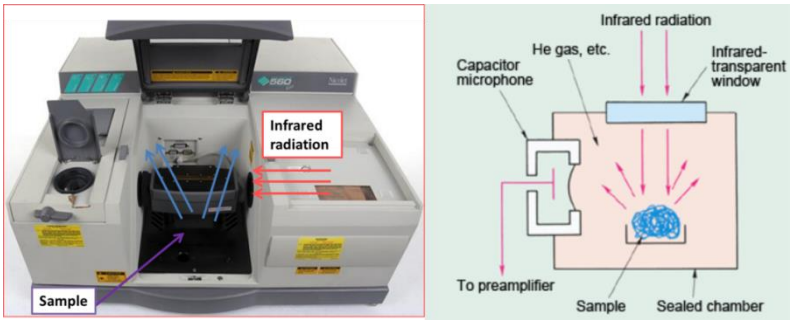


Figure 2.4 Thermo / Nicolet Magna-IR 750 Spectrometer and principle of PA-FTIR spectroscopy.[13]

2.4.1.2 Nuclear magnetic resonance (NMR) spectroscopy

NMR spectroscopy is a common technique that is used to analyse the properties and chemical environment of molecules which involves electromagnetic radiation interacting with a sample of matter contained in a homogenous magnetic field. The principle of the technique is that when a sample is placed in a magnetic field, NMR active nuclei, such as ^{1}H or ^{13}C, absorb electromagnetic radiation at a frequency characteristic of the isotope. Spectra are obtained by excitation of a sample with radio frequency pulse and a NMR response obtained. A Fourier transform is performed to extract the frequency-domain spectrum and is presented in terms of the chemical shift. The chemical shift provides information about the structure of a molecule. In this study, NMR was used to characterise the DVIMBr, $[C_6(VIm)_2][Br]_2$ and $[C_8(VIm)_2][Br]_2$ structures. All samples were dissolved in deuterated water (D_2O) for NMR experiments. ^{1}H NMR spectra were obtained on a 300 MHz Bruker Avance spectrometer operating at 300.138 MHz and the spectra were referenced relative to TMS (0 ppm).

2.4.2 Scattering techniques

2.4.2.1 Dynamic light scattering (DLS)

DLS is one of the most widely used methods to characterize size of various particles including polymers and nanoparticles in solution. In DLS, the sample is irradiated with light (usually a laser), repeatedly at short time intervals and the scattered light due to particles is measured using a detector at a fixed angle over time. Small particles or molecules in solution undergo Brownian motion, thereby causing fluctuations in scattered light intensity. The collected intensity fluctuations yield the velocity of the Brownian motion of particles in solution and their relative size, using the Stokes-Einstein relationship.[14]

In this study, the Zetasizer Nano ZS was employed to measure PIL nanoparticles and SNAP coating size distribution. The measured values were calculated from cumulative analysis (three cycles) using the Zetasizer software. The algorithm used by the software is based upon a non-negative least-squares fit. Schematic of DLS is shown in Figure 2.5.

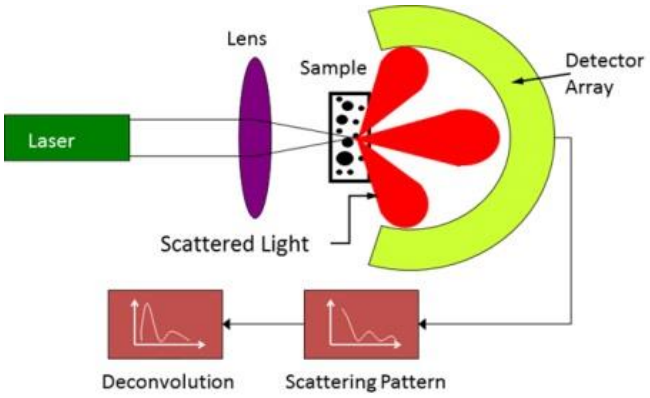


Figure 2.5 Schematic of dynamic light scattering system.[15]

2.4.3 Morphological investigation

2.4.3.1 Scanning electron microscopy (SEM)

SEM is an electron microscopic technique widely used to obtain images of a range of different sample types to provide information of their surface topology. In SEM, a focused beam of electrons (primary electrons) is scanned over the sample surface in vacuum (to avoid the collision of electrons with air molecules) and the secondary electrons, backscattered electrons, Auger electrons, and X-rays generated by the atoms of the sample by irradiation are collected by a detector and an image of the surface is created. The collected electrons provide information about the sample topography and composition. Schematic of SEM is shown in Figure 2.6. The most common mode of surface morphology and composition detection of a sample are by secondary electrons emitted by the sample excited by the primary electron beam.[16] In this study, the size and morphology of the PIL nanoparticles were analysed by field emission scanning electron microscopy (FE-SEM) using Philips XL30 FEG instrument operated at an acceleration voltage of 15 kV where surface compositions were obtained using energy dispersive spectroscopy (EDS) module (OXFORD instruments) attached to the microscope. Sample material was placed on an Indium tin oxide (ITO) coated glass as a conducting surface and images were taken without any further coating. Also, the surface of the metal after application of corrosion inhibitors loaded coatings were visualized using SEM in chapter 4, 5 and 7, where metal was coated with another layer of carbon coating.

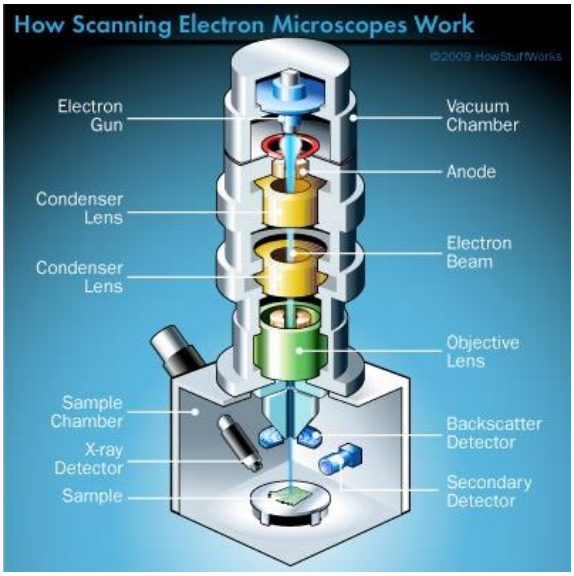


Figure 2.6 Schematic representation of a SEM instrument.[17]

2.4.3.2 Transmission electron microscopy (TEM)

TEM is a commonly used electron microscopic technique to image and analyses the morphology, crystal structure and defects of a wide range of sample materials. TEM operates by transmitting an electron beam through a vacuum, which is then focused using electromagnetic lenses and is transmitted through a thin sample of interest. The density of the material dictates whether the electrons are scattered or disappear from the beam. At the bottom of the microscope the unscattered electrons hit a fluorescent screen, which generates an image that can be captured with a camera. The contrast between different materials in the TEM micrograph is due to the differences in composition, while thicker regions or samples regions with a higher atomic number appear darker. Schematic of TEM is shown in Figure 2.7.[18-19] In this study, the size, and morphology of PIL nanoparticle were examined using a JEOL 2100F TEM operated at 200 kV with a resolution ~2 Å. The analysis was performed using the 'Digital Micrograph' software (Gatan Inc.). For sample preparation, a well dispersed drop of emulsion was dropped on carbon coated copper grid and allowed to adsorb to the grid for 1 min.

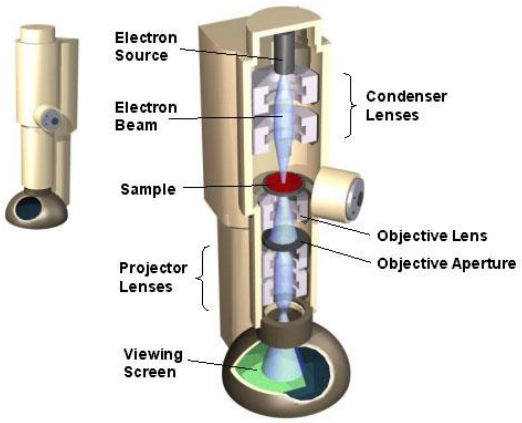


Figure 2.7 Schematic representation of a TEM instrument.[18]

2.4.4 Thermal analysis techniques

2.4.4.1 Differential scanning calorimetry (DSC)

DSC is a thermoanalytical technique commonly used to study the heat effects associated with phase transitions and chemical reactions as a function of temperature. In a DSC the difference in heat flow to the sample and a reference at the same temperature is recorded as a function of time and temperature. Figure 2.8a shows the principle of DSC instrument and Figure 2.8b shows the instrument used. The measured difference in heat flow between the sample and reference provides information about the exothermic and endothermic reaction occurring in the sample, and the thermal phase transition.[20] In this study, Discovery DSC analyser (TA Instruments) has been used in two different applications. In one application DSC was used to measure the glass transition temperature of PIL corrosion inhibitors in the form of gel, nanoparticle and hybrid film as a function of temperature. The samples were sealed in hermetic aluminium pans for use in the DSC experiment, and an empty pan was used as the reference. The temperature range for the experiment was from −70 to 200 °C, with a heating rate of 10 °C/min and under controlled nitrogen gas flow rate of 50 mL/min. In the other application, it has been used for kinetic study. In this study, the samples were held isothermally at 125, 135, and 145 °C for 45 min under a flow of nitrogen. The heat capacity and its derivative were measured as a function of heating and cooling (with constant rate) under controlled nitrogen atmosphere. The instrument was calibrated for baseline and cell constant prior to running the experiments. The analysis was performed using TA Instrument's software

'TRIOS'. The temperature range for the experiment was from −70 to 200 °C, with a heating rate of 10 °C/min and under controlled nitrogen gas flow rate of 50 mL/min.

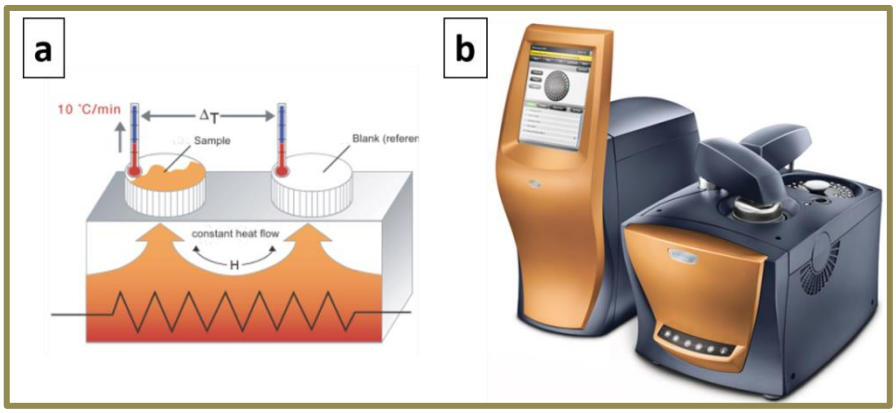


Figure 2.8 (a) Schematic principle of DSC measurement and (b) Image of the TA Instruments Discovery DSC.[21]

2.4.4.2 Thermogravimetric analysis (TGA)

TGA is a commonly used thermal analysis method to measure thermal phase transitions and decomposition of material as a function of temperature, time, and atmosphere. In a thermo gravimetric analyser, a precision balance with a pan loaded with the sample measures the sample weight in a heating chamber at a constant heating rate and controlled gas atmosphere.[22] In this study, a Discovery TGA analyser (TA Instruments) was used to study the thermal behaviour of all synthesised PIL corrosion inhibitors in three forms: gel, nanoparticle and hybrid film as a function of temperature. In all studies, samples were subjected to a 10 °C/min ramp rate from 100 to 600 °C under a nitrogen atmosphere. The weight loss pattern and its derivative were measured as a function of increasing temperature (with constant heating rate) under controlled nitrogen atmosphere. The analysis was performed using the TA Instrument's software 'TRIOS'. Figure 2.9a shows the principle of TGA instrument and Figure 2.9b shows the instrument.

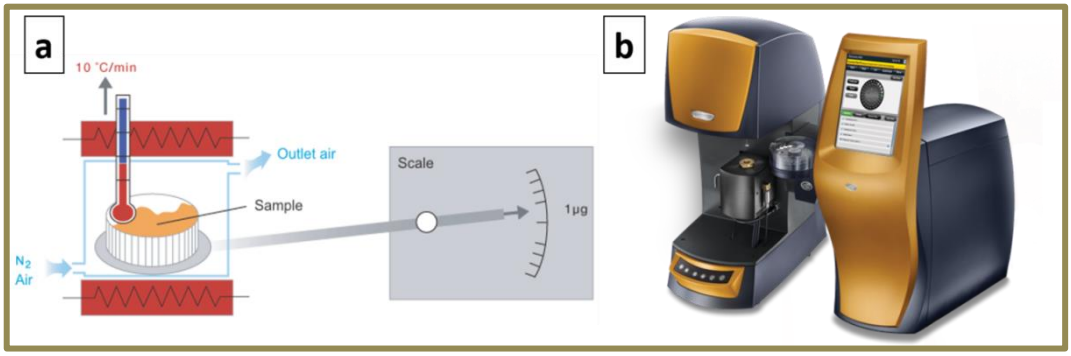


Figure 2.9 (a) Schematic principle of TGA measurement and (b) Image of the TA Instruments Discovery TGA.[22]

2.4.5 Mechanical testing

2.4.5.1 Dynamic mechanical analysis (DMA)

DMA is used to analyze the viscoelastic properties of polymer materials. The mechanical properties of a sample are measured as a function of time, temperature and frequency. The DMA applies a sinusoidal stress to a sample and measures the resulting strain. For a perfectly elastic material, the resulting strain and stress will be perfectly in phase; however for a purely viscous material, there will be a phase lag (δ) of strain with respect to stress of 90 degrees. Viscoelastic materials display characteristics somewhere in between and thus when the strain is applied there is some lag in the stress. DMA measurements determine the storage and loss modulus of a material, where the storage modulus is a measure of the stored energy and represents the elastic portion, and the loss modulus measures the energy dissipated as heat and represents the viscous portions. Tan δ is measured as the ratio of the loss modulus to storage modulus and is a measure of the viscoelasticity of a material.

In this study, DMA of the PIL gel with different mole ratios was performed in tension mode using the DMA Q800 (TA Instruments) equipped with a humidity accessory. The storage and loss moduli of the PIL gel were determined under controlled humidity. The PIL gel strips of thickness of 1.3 mm and width of 9.3 mm were mounted using a tension clamp and run at ambient temperature with amplitude of 10 µm and a preload force of 0.0100 N. The DMA run was conducted with the humidity ramped to 75 % and held for the duration of half an hour with isothermal temperature.

2.4.6 Wettability study - sessile drop technique

The contact angle measurement is a quantitative measurement of wetting of a solid by a liquid. It is defined geometrically as the angle formed by a liquid at the three phase boundary where a liquid, gas and solid intersect, which is used for the characterization of dynamic wettability of the surface, and is relevant for coating applications. Contact angle hysteresis is the difference between the advancing and receding contact angles. Contact angle hysteresis arises from the chemical and topographical heterogeneity of the surface, solution impurities absorbing on the surface, swelling, rearrangement or alteration of the surface by the solvent.[23] Dynamic Wilhelmy method is a method for calculating average advancing and receding contact angles on solids of uniform geometry (Figure 2.10). Both sides of the solid must have the same properties. Wetting force on the solid is measured as the solid is immersed in or withdrawn from a liquid of known surface tension. In this study the contact angle is used to evaluate the dynamic wetting behaviour and interaction of the PIL nanoparticle, SNAP solution and SNAP/PIL nanoparticle with the metal surface.

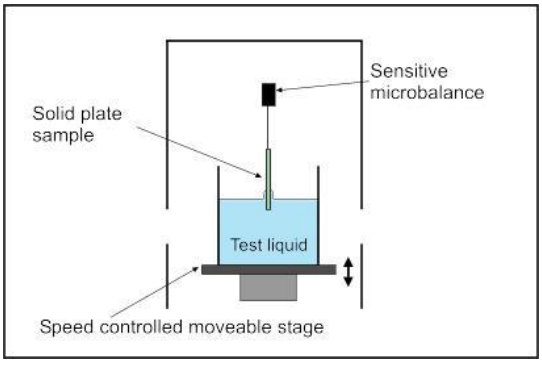


Figure 2.10 Schematic showing the Wilhelmy method to determine the contact angle.

2.4.7. Electrochemical analysis

2.4.7.1. Potentiodynamic

Since corrosion occurs via electrochemical reactions, electrochemical techniques are ideal for the study of the corrosion processes. In electrochemical studies, a metal sample with a surface area of a few square centimetres is used to model the metal in a corroding system. The metal sample is immersed in a solution typical of the metals' environment in the system being studied which in this study is 3.5 wt% salt solution. Additional electrodes are immersed in the solution, and all the

electrodes are connected to a device called a potentiostat. A potentiostat allows changing the potential E of the metal sample in a controlled manner and measuring the current (I) that flows as a function of applied potential. A plot of log I versus E is called a Tafel plot. The corrosion current, I_{corr}, is obtained from a Tafel plot by extrapolating the linear portion of the curve to E_{corr}, as shown in Figure 2.11.[24]

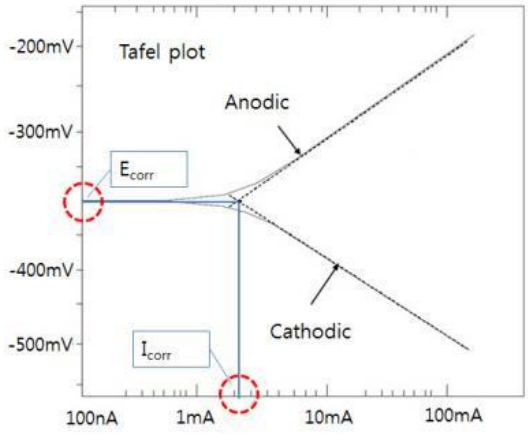


Figure 2.11 Tafel plot analysis.[22]

In this study electrochemical characterization of the uncoated and the coated samples (SNAP/PIL loaded nanoparticles, gel, SNAP, PIL hybrid film) was carried out using a standard corrosion cell (1 L, Pine Research Instrumentation) with conventional three electrode set-up. A saturated calomel electrode (SCE, Pine Research Instrumentation, +0.24 V vs. Normal Hydrogen Electrode, NHE) was employed as the reference electrode, a graphite rod of 2 mm diameter as counter electrode and the sample under test as the working electrode. The sample holder is made of Teflon and a platinum sheet and a platinum wire was used for electrical connection. Potentiodynamic polarization equipment was studied at a scan rate of 1 mVs^{-1} in the potential range of ±300 mV. The electrochemical experimental set up used is shown in Figure 2.12.

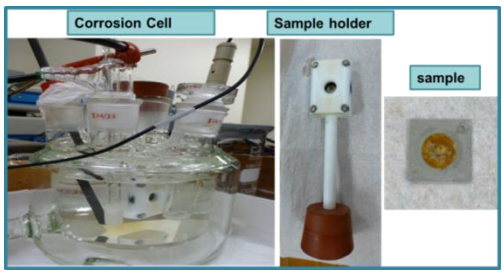


Figure 2.12 Electrochemical setup used for Potentiodynamic measurements

2.4.7.2. Impedance spectroscopy

Electrochemical impedance spectroscopy (EIS) has been successfully applied to the study of corrosion systems for thirty years and been proven to be a powerful and accurate method for measuring corrosion rates.[25] An important advantage of EIS over other laboratory techniques is the possibility of using very small amplitude signals without significantly disturbing the properties being measured. To make an EIS measurement, a small amplitude signal, usually a voltage between 5 to 100 mV, is applied to a specimen over a range of frequencies of 0.001 Hz to 100,000 Hz. The EIS instrument records the real (resistance) and imaginary (capacitance) components of the impedance response of the system. In order to access the charge transfer resistance or polarization resistance that is proportional to the corrosion rate at the monitored interface, EIS results have to be interpreted with the help of a model of the interface (Figure 2.13). Depending on the shape of the EIS results, a circuit model and initial circuit parameters are assumed.[26] Then the best fit of the frequency response of the given EIS spectra is measured by the program, to obtain fitting parameters. The quality of the fitting is judged by how well the fitting curve overlaps the original spectra. By fitting the EIS data it is possible to obtain a set of parameters which can be correlated with the coating condition and the corrosion of the steel substrate.

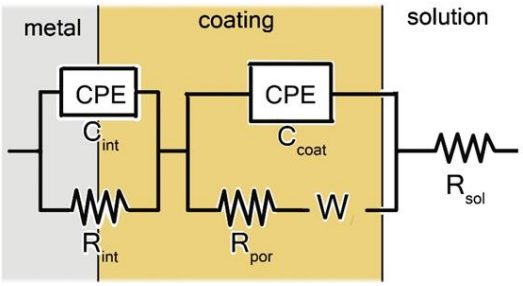


Figure 2.13 Circuit model of the metal-coating interface.[26]

In this study, the EIS measurements were performed using a Solartron 1260 impedance/gain-phase analyser in combination with a Solartron 1280B electrochemical interface. The impedance measurements were carried out in a 1 MHz to 10 kHz frequency range with 40 steps per decade. All the spectra were recorded at open circuit potential with applied 10 mV sinusoidal perturbation. In this study Nyquist diagram and the Bode plot of impedance modulus vs frequency, and phase angle vs frequency for all the coated samples were used to analyse the deterioration process.

2.4.7.3 Scanning kelvin probe (SKP)

SKP measures two-dimensional distributions of contact potential difference (CPD) between the tip and the sample with resolution in the nanometre range. The CPD can be converted to the work function of the sample if the measurement is performed under thermo equilibrium state; and it is the electrical potential when the sample is illuminated or a bias is applied to the sample. SKP microscopy has been applied to evaluate the adhesion and corrosion protection properties of the coating along with its electrochemical performance.[27] This technique was used in this project to measure the surface work function of the cleaned substrate and the freshly coated and salt immersed samples.[28] Work function is the minimum amount of energy required to remove an electron from the surface of a metal. Figure 2.14 illustrates the Scanning Kelvin Probe instrument set up.

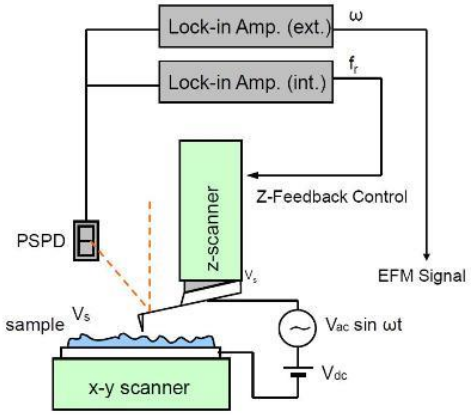


Figure 2.14 Instrument set up of SKP.[29]

2.4.8 Quartz crystal microbalance (QCM)

QCM is a simple, cost effective, high-resolution mass sensing technique that measures a mass variation per unit area by measuring the change in frequency of a quartz crystal resonator. The technique possesses a wide detection range. At the low mass end, it can detect monolayer surface coverage by small molecules or polymer films. At the upper end, it is capable of detecting much larger masses bound to the surface. In addition, the QCM can provide information about the viscoelastic properties of bound surface mass.[30] In principle, QCM relies on the piezoelectric properties of quart; by applying an alternating electric field across the quartz crystal through upper and lower metal electrodes covering the quartz surface, a mechanical oscillation of characteristic frequency, f, is produced in the crystal. In an AT-cut quartz plate, an oscillating voltage applied to electrodes on opposite surfaces will excite resonant through-thickness shear modes, if the frequency of the driving voltage matches that of one of these modes.[31-32] Mass loading of the crystal surface will change the resonant frequencies. Sauerbrey derived a relationship (Eq.1)) between frequency change (Δf) and mass change per unit area (Δm) for a rigidly adsorbed uniform elastic thin film:[33]

$$\Delta m = -\frac{c\Delta f}{n} \qquad \text{Eq.1}$$

where C = 17.7 ng Hz^{-1} cm^{-2} for a 5 MHz quartz crystal, n is the overtone number and Δf is the frequency change induced by adsorption. To validate the Sauerbrey relationship the adsorbed layer needs to be deemed sufficiently rigid which is generally considered when the ratio of ΔD/(-Δf/n) is less than 4 x 10^{-7}. In this study, QCM has been used to investigate the corrosion inhibition performance of the ILs with different spacer on steel surface. For this study, quartz crystal microbalance with dissipation (QCM-D) (E4, Q-sense, Sweden) and AT-cut quartz crystals with a fundamental resonant frequency of 5 MHz were used. One side of each diaphragm crystal was coated by the manufacturer with 100 nm of gold and then 50 nm of stainless steel (SS). Figure 2.15 illustrates the typical quartz crystal microbalance.

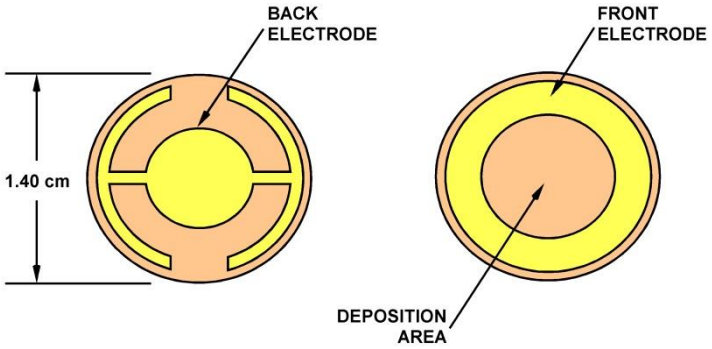


Figure 2.15 The Schematic of typical quartz crystal microbalance.[34]

The crystals were cleaned by sonicating for at least 10 minutes in a 2% Hellmanex solution before being rinsed with DDW and dried with nitrogen gas. The quartz crystal was mounted in a flow cell with the steel surface exposed to the solution. For adsorption of IL based inhibitors onto a bare surface, the 0.1, 0.2, 0.3, 0.4 and 0.5 wt% solutions of each ILs (butyl, hexyl, octyl) were pumped through the flow cell by a peristaltic pump at a flow rate of 50 μL / min. A baseline was established for 1 h in the DDW and inhibitors adsorption was allowed to proceed for 1 h to 2 h. Inhibitors solution was pumped through starting from lowest concentration, followed by higher concentration without rinsing the surface between additions. The kinetics of sample adsorption and desorption were followed by changes in the resonant frequency of the crystal and dissipation of the crystal vibrations. All measurements were done with the system temperature stabilized at 23±0.5 °C. Multiple overtones (3rd, 5th, 7th, 9th, 11th and 13th) were recorded. The 5th overtone was selected and analysed for all sensors. The mass of the adsorbed inhibitors was estimated using the Sauerbrey relationship.

2.5 References

1. Posner, T. *Ber. Dtsch. Chem. Ges.* **1905,** *38* (1), 646-657.
2. Hoyle, C. E.; Lee, T. Y.; Roper, T. *J. Polym. Sci., Part A: Polym. Chem.* **2004,** *42* (21), 5301-5338.
3. Rydholm, A. E.; Reddy, S. K.; Anseth, K. S.; Bowman, C. N. *Polymer* **2007,** *48* (15), 4589-4600.
4. Carioscia, J. A.; Stansbury, J. W.; Bowman, C. N. *Polymer* **2007,** *48* (6), 1526-1532.
5. Lowe, A. B. *Polym. Chem.* **2010,** *1* (1), 17-36.
6. Lowe, A. B. *Polym. Chem.* **2014,** *5* (17), 4820-4870.
7. Harkins, W. D. *J. Am. Chem. Soc.* **1947,** *69* (6), 1428-1444.
8. Hoyle, C. E.; Bowman, C. N. *Angew. Chem., Int. Ed. Engl.* **2010,** *49* (9), 1540-1573.
9. Hoyle, C. E.; Lowe, A. B.; Bowman, C. N. *Chem. Soc. Rev.* **2010,** *39* (4), 1355-1387.
10. Amato, D. V.; Amato, D. N.; Flynt, A. S.; Patton, D. L. *Polym. Chem.* **2015,** *6* (31), 5625-5632.
11. Donley, M. S.; Mantz, R. A.; Khramov, A. N.; Balbyshev, V. N.; Kasten, L. S.; Gaspar, D. J. *Prog. Org. Coat.* **2003,** *47* (3-4), 401-415.
12. Peter R. Griffiths; Haseth, J. A. D. *Fourier Transform Infrared Spectrometry*. 2nd Edition ed.; John Wiley & Sons, Inc.: 2007.
13. Bentiss, F.; Lagrenee, M.; Traisnel, M.; Hornez, J. *Corros. Sci.* **1999,** *41* (4), 789-803.
14. Miller, C. C. *Proc. R. Soc. London, Ser. A* **1924,** *106* (740), 724-749.
15. Laser Diffraction. (accessed 10 July 2016).
16. Goodhew, P. J.; Humphreys, F. J.; Beanland, R. *Electron Microscopy and Analysis*. Taylor and Francis: London, 2000.
17. Atteberry, J. How Scanning Electron Microscopes Work. (accessed 4 February 2016).
18. Williams, D. B.; Carter, C. B. The transmission electron microscope. In *Transmission electron microscopy*, Springer: 1996; pp 3-17.
19. Goodhew, P. J.; Humphreys, J.; Beanland, R. *Electron microscopy and analysis*. CRC Press: 2000.

20. Höhne, G. W. H.; Hemminger, W. F.; Flammersheim, H.-J. *Differential Scanning Calorimetry*. SpringerLink: Springer: Berlin, Heidelberg, 2003.
21. Spink, C. H. *Methods Cell Biol.* **2008,** *84*, 115-141.
22. Coats, A. W.; Redfern, J. P. *Analyst* **1963,** *88* (1053), 906-924.
23. Gao, L.; McCarthy, T. J. *Langmuir* **2006,** *22* (14), 6234-6237.
24. Research, P. A. Basics of Corrosion Measurements. (accessed 15 Febuary 2016).
25. Schütze, M. *Mater. Corros.* **2002,** *53* (4), 284-284.
26. Lvovich, V. F. Fundamentals of Electrochemical Impedance Spectroscopy. In *Impedance Spectroscopy*, John Wiley & Sons, Inc.: 2012; pp 1-21.
27. Kannan, A. G.; Choudhury, N. R.; Dutta, N. K. *J. Electroanal. Chem.* **2010,** *641* (1–2), 28-34.
28. Łosiewicz, B.; Popczyk, M.; Szklarska, M.; Smołka, A.; Osak, P.; Budniok, A. In *Application of the Scanning Kelvin Probe Technique for Characterization of Corrosion Interfaces*, Solid State Phenomena, Trans Tech Publ: 2015; pp 369-382.
29. Bhushan, B.; Marti, O. Scanning probe microscopy–principle of operation, instrumentation, and probes. In *Springer handbook of nanotechnology*, Springer: 2010; pp 573-617.
30. Reipa, V.; Purdum, G.; Choi, J. *J. Phys. Chem. B* **2010,** *114* (49), 16112-16117.
31. Reviakine, I.; Johannsmann, D.; Richter, R. P. *Anal. Chem.* **2011,** *83* (23), 8838-8848.
32. Ferreira, G. N. M.; da-Silva, A.-C.; Tomé, B. *Trends Biotechnol.* **2009,** *27* (12), 689-697.
33. Sauerbrey, G. *Zeitschrift für Physik 155* (2), 206-222.
34. Janata, J. *Principles of chemical sensors*. Springer Science & Business Media: 2010.

Chapter 3: Facile fabrication of polymerizable ionic liquid based-gel beads via thiol–ene chemistry

This chapter of the thesis is presented as a research article “Taghavikish, M.; Subianto, S.; Dutta, N. K.; Choudhury, N. R. Facile fabrication of polymerizable ionic liquid based-gel beads via thiol-ene chemistry. ACS Applied materials & Interfaces 2015, 7 (31), 17298-17306”, published and reproduced by permission of the American Chemical Society, Copyright 2016.

3.1 Research article

ACS APPLIED MATERIALS & INTERFACES

Research Article

www.acsami.org

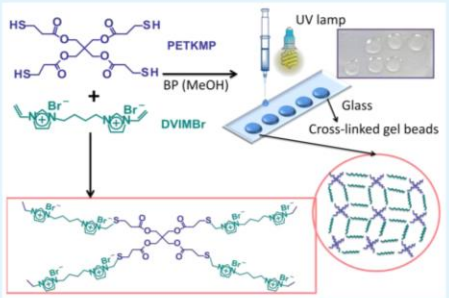
Facile Fabrication of Polymerizable Ionic Liquid Based-Gel Beads via Thiol−ene Chemistry

Mona Taghavikish, Surya Subianto, Naba Kumar. Dutta,* and Namita Roy Choudhury*

Ian Wark Research Institute, Mawson Lakes Campus, University of South Australia, Mawson Lakes, Adelaide, South Australia 5095, Australia

Supporting Information

ABSTRACT: Multipurpose gel beads prepared from natural or synthetic polymers have received significant attention in various applications such as drug delivery, coatings, and electrolytes because of their versatility and unique performance as micro- and nanocontainers.[1] However, comparatively little work has been done on poly(ionic liquid)-based materials despite their unique ionic characteristics. Thus, in this contribution we report the facile preparation of polymerizable ionic liquid-based gel beads using thiol−ene click chemistry. This novel system incorporates pentaerythritol tetra (3-mercaptopropionate) (PETKMP) and 1,4-di(vinylimidazolium) butane bisbromide in a thiol−ene-based photopolymerization to fabricate the gel beads. Their chemical structure, thermal and mechanical properties have been investigated using Fourier transform infrared spectroscopy (FTIR), differential scanning calorimetry (DSC), thermogravimetric analysis (TGA), and dynamic mechanical analysis (DMA). The gel beads possess low T_g and their ionic functionalities attribute self-healing properties and their ability to uptake small molecules or organic compounds offers their potential use as pH sensing material and macrocontainers.



KEYWORDS: *polymerizable ionic liquid, gel beads, thiol−ene chemistry, self-healing, pH sensing material*

INTRODUCTION

Poly(ionic liquids) or polymerized ionic liquids (PIL) are a special class of polyelectrolyte with an ionic species in each of its repeating units. They have attracted significant interest because of the unique combination of properties of ionic liquids (IL) with a macromolecular architecture.[2,3] As polyelectrolyte gels, they have shown potential not only in more obvious applications such as electrolytes for batteries and super-capacitors,[4] but also where immobilization of active ingredients and their subsequent release in controlled fashion is desired, such as in drug delivery,[5] agriculture, and biomedical fields.[6] Indeed, they are showing a multitude of characteristics that make them very versatile materials with tunable properties.

Another characteristic of these PILs, that has not been well investigated is their potential self-healing capability: upon damage, the self-healing process requires either a suitable chemistry to trigger at the crack plane or exploit the in-built ability of the polymer network structure to repair macroscopic defects. This can occur via a molecular mechanism such as hydrogen bond or ionic interactions combined with physical processes such as viscoelastic flow (chain mobility and entanglement).[7,8] All these requisite characteristics for self-healing are found in PILs, as they are soft, polymeric materials that may have sufficient viscoelastic flow and also secondary ionic interactions to hold them together. However, very few investigations have been reported so far into the self-healing characteristics of PILs, and most of these studies have been directed toward the use of microcapsule or nanocontainers,[9] with scant reports on polymerizable ionic liquid-based gel beads.

Such gel beads have several attractive features for use in applications such as multifunctional additives: they are able to uptake liquids and active organic compounds, are chemically inert and stable, and possess tunable properties. One potential application for such PIL-based gel beads would be in anticorrosion coatings. Imidazolium-based ILs exhibit excellent inhibition performance on copper, steel and aluminum.[10,11] The actions of such inhibitors are correlated to the specific interaction of the −C═N− group of ILs and electronegative nitrogen in the molecule.[12] However, the main challenges in the use of IL are the risk of gradual loss over time and lack of miscibility. Xiong and co-workers[13] reported a facile one-step synthetic strategy for the preparation of cross-linked polymeric nanogels by the conventional radical copolymerization of a phosphonium-based IL for use as catalysts, whereas Muldoon and Gordon[14] reported the synthesis of polymer microgel by emulsion polymerization. However, no investigation has been reported on PIL micro gel beads for sensing and inhibition of corrosion.[15]

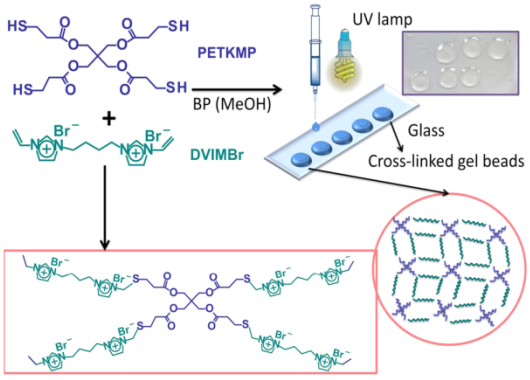
Received: May 21, 2015
Accepted: July 14, 2015
Published: July 14, 2015

ACS Publications © 2015 American Chemical Society

DOI: 10.1021/acsami.5b04405
ACS Appl. Mater. Interfaces 2015, 7, 17298−17306

With a view to prepare such multipurpose gel beads with inhibitor or pH sensing (indicator) characteristics, we have chosen in this work thiol−ene based click chemistry to prepare PIL gel beads. The use of thiol−ene chemistry offers the desirable features of a click-type reaction and is frequently photo initiated.[16,17] This inherent versatility of thiol−ene chemistry allows for the reaction between a large variety of compounds that contains thiols with those containing unsaturated C═C groups, allowing a large degree of control on the macromolecular structure.[18] We herein report a thiol−ene photopolymerization using vinyl-containing imidazolium ionic liquids to prepare cross-linked gel beads under mild reaction conditions (Scheme 1). Combining the functionalities of thiol−ene and PIL chemistry, our aim is to create unique polymeric networks possessing multiple functionalities that are applicable toward anticorrosion coatings.

Scheme 1. Schematic of the Thiol−ene Photopolymerized Gel Beads Fabricated in This Study



EXPERIMENTAL SECTION

Materials. Pentaerythritol tetrakis(3-mercaptopropionate) (PETKMP), 1-Vinylimidazole, 1,4-dibromobutane, benzophenone (BP), 1-butyl-3-methylImidazolium hexafluorophosphate, Azobis-(isobutyronitrile) (AIBN), methyl red, diethyl ether and methanol (analytical grade) were all obtained from Sigma-Aldrich, Australia and used without further purification. Double distilled water was used for all experiments.

Synthesis of 1,4-Di(vinylimidazolium)butane Bisbromide. 1,4-di(vinylimidazolium)butane bisbromide (DVIMBr) was synthesized by stirring a mixture containing 2:1 molar ratio of 1-vinylimidazole to 1,4-dibromobutane in methanol at 60 °C for 15 h. After cooling, the reaction mixture was added dropwise into 1 L of diethyl ether. The white precipitate was filtered off and dried at room temperature until constant weight with a yield of 68%.[19]

^{1}H NMR (300 MHz, D_2O, δ, ppm): 8.98 (2H), 7.69 (2H), 7.49 (2H), 7.04 (2H), 5.75 (2H), 5.33 (2H), 4.21 (4H), 1.87 (4H) (Figure S1).

Fabrication of Gel Beads. Gel beads were prepared using the slow solvent evaporation method using different ratio of precursors. In a typical synthesis method, a 1:2 mol ratio of pentaerythritol tetrakis(3-mercaptopropionate) (PETKMP) (0.5 mmol, 0.24g) and DVIMBr (1 mmol, 0.4 g) were dissolved in the minimum volume of methanol (0.2 mL) and small amount of BP (18.2 mg, 5 wt % with respect to monomer concentration). The reaction mixture was stirred for approximately 30 min in 4 mL vial while protecting from light and then ultrasonicated in the ice bath for 10 min with amplitude of 50%. The solution was then degassed in the degassing vacuum chamber while stirring for 1 h. Photopolymerization was initiated using an UV lamp in a dark hood. The gel beads were disposed drop by drop on a glass slide using a flat end needle (17 gauge, 1.07 mm inner diameter) syringe and beads were formed by exposure to UV light (365 nm wavelength). Transparent gel particles with an average size of 5 mm formed within 5 min. The beads were washed with water and methanol to remove any unreacted monomer; afterward, they were dried under a high vacuum. Elemental analysis shows: C, 40.6; S, 9.1; N, 7.9%. Calcd: C, 41.5; S, 9.8; N, 8.6%). Using this procedure, gel beads were also synthesized at two other 1:1 and 1:4 stoichiometric ratios of PETKMP:DVIMBr.

Characterization. ^{1}H NMR analysis was performed on a 300 MHz Bruker Avance spectrometer at room temperature using D_2O as the solvent. Infrared spectra of the gels were acquired using Nicolet Magna-IR Spectrometer 750 in photoacoustic mode, with 256 scans and using a carbon black reference. Differential scanning calorimetry (DSC) measurement was conducted using TA Instruments Discovery DSC (model 2920). The instrument was calibrated for baseline and cell constant prior to running the experiments. The samples were sealed in hermetic aluminum pans for use in the DSC experiment, and an empty pan was used as the reference. The temperature range for the experiment was from −70 to 200 °C, with a heating rate of 10 °C/min and under controlled nitrogen gas flow rate of 50 mL/min. For kinetic study the samples were held isothermally at 125, 135, and 145 °C for 45 min under a flow of nitrogen. Thermogravimetric analysis (TGA) was performed using a TA Instruments Discovery TGA with an

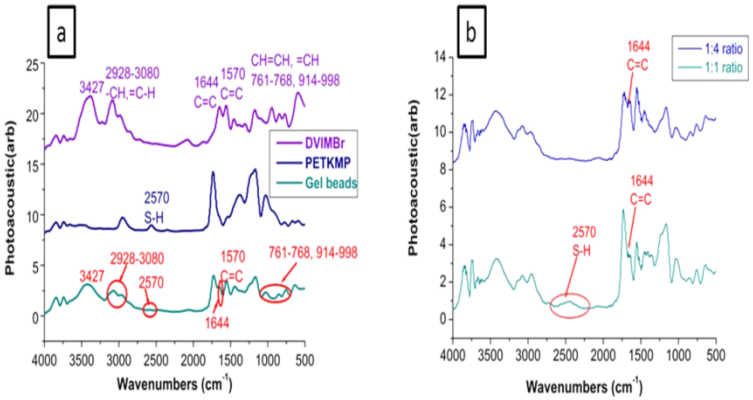


Figure 1. (a) FTIR spectra of the cured gel beads with stoichiometric (1:2) ratio of the monomers used, (b) FTIR spectra of 1:1 and 1:4 ratios.

DOI: 10.1021/acsami.5b04405
ACS Appl. Mater. Interfaces 2015, 7, 17298−17306

aluminum pan. The samples were subjected to a 10 °C/min ramp rate from 100 to 550 °C under a nitrogen atmosphere. The UV−vis experiment was carried out with Evolution 201 UV/vis spectrophotometer. Qsonica ultrasonicator was used for ultrasonication. Elemental analysis was performed using a LECO Trumac CNS analyzer. DMA was conducted using the TA Instruments Q800 DMA equipped with a humidity accessory. The storage and loss moduli of the gel samples were determined under controlled humidity. The gel strips of thickness of 1.3 mm and width of 9.3 mm were mounted using a tension clamp and run at ambient temperature with amplitude of 10 μm and a preload force of 0.0100 N. The DMA run was conducted with the humidity ramped to 75% and held for the duration of half an hour with isothermal temperature. Rheometric measurements were performed on an ARES (TA Instruments) AR-1000 Rheometer using parallel plate geometry. All tests were done at room temperature with light intensity around 90 mW cm^{-2}. The rheometer was operated at a frequency of 0.3 Hz with average strain amplitude of 1%.

RESULTS AND DISCUSSION

Thiol−ene Photopolymerization. FTIR analysis of the cured gel beads with stoichiometric ratio shows the disappearance of the reactants after photo polymerization for 5 min. As can be seen in Figure 1a, the spectra of the monomers (DVIMBr and PETKMP) show distinct differences with the cured gel beads. The spectrum of DVIMBr shows various characteristic peaks associated with the ionic liquids structure and the unsaturated vinyl moiety. It shows two bands at 3080 (=C−H stretching) cm^{-1} and at 2928 cm^{-1} representing the stretching of −CH groups of the imidazole ring of the IL, a peak for the C=C double bonds of the imidazole ring around 1570 cm^{-1}, and another for the C=C stretching of the vinyl group at 1644 cm^{-1}. It also shows the presence of bands attributed to the vinyl group between 914 and 998 (out-of-plane =C−H bending) and at 761−768 cm^{-1} (H−C=C−H wagging). The spectrum of the other monomer, PETKMP, shows presence of a peak attributed to thiol groups at 2570 cm^{-1}(S−H stretching). The cured PIL gel beads, on the other hand, show no detectable amount of the peak due to sulfur−hydrogen stretching around 2570 cm^{-1} as well as the absence of the C=C vinyl peak at 1644 cm^{-1}, which indicates that the thiol and vinyl groups have fully reacted. A reduction in intensity at 3080 cm^{-1} and around 761−768, 914−998 cm^{-1} regions in gel beads spectra in comparison with the DVIMBr spectra also confirms the consumption of vinyl groups. Additionally, there is also a band at 3427 cm^{-1} in the spectra of the PIL gel (which was also present in the DVIMBr spectra) which is attributed to strongly bound water. This analysis was supported by elemental analysis, which confirmed a 1:2 ratio of sulfur to nitrogen in cured gel beads, which is in agreement with the stoichiometry used for the fabrication of these gel beads.

In PIL gels, conversion rate and the extent of cross-linking is important as the toughness of such material depends on these parameters. As such, the stoichiometry between the thiol and vinyl groups (monomer ratio) and polymerization time (extent of cross-linking) are the vital factors for controlling the material's properties through achieving a high monomer conversion and preventing side reactions.[20] Thus, in addition to the 1:2 ratio, we have fabricated samples with a 1:1 (excess thiol groups) and 1:4 (excess vinyl groups) ratio of PETKMP:DVIMBr to investigate the effect of stoichiometry on the PIL gel formation. As can be expected, FTIR spectrum of sample with 1:1 ratio (Figure 1b) shows an extra S−H group but full consumption of the C=C vinyl peak because there are extra thiol groups available, whereas in the sample with a 1:4 ratio where excess vinyl groups were used, there is no evidence of unreacted thiol groups (Figure 1b) but evidence of excess, unreacted vinyl group. This indicates that although in principle homopolymerization of DVIMBr could occur as a competing reaction to the thiol−ene reaction, the FTIR spectrum shows that the thiol−ene reaction occurs in preference and thus the excess vinyl groups did not lead to extensive homopolymerization of DVIMBr after all the thiol have been consumed. This approach offers us the advantage to prepare either excess thiol functionalized or excess vinyl functionalized (off-stoichiometry) thiol−ene-based gel beads (e.g oligomeric IL gel with excess vinyl group) for further modification.

Kinetics of Thiol−ene Reaction. *In Situ Dynamic Rheology during Photopolymerization.* Direct monitoring of the thiol−ene reaction and cross-linking was done by in situ rheology. Under UV light exposure, the shear modulus changes were followed as reaction progressed to understand the effect of stoichiometry on the thiol−ene reaction. When the stoichiometric amounts (1:2) were used, it can be seen that the elastic modulus G' and the viscous modulus G'' increase significantly after 30 s and starts to plateau after 2 min, indicating a very rapid reaction (Figure 2). As observed in Figure 2, the step

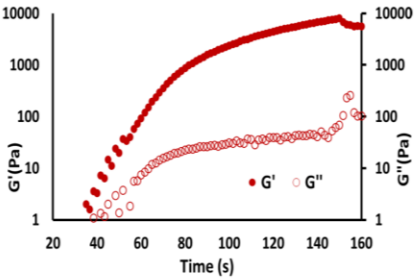


Figure 2. In situ rheology study during photopolymerization of the PETKMP:DVIMBr system (1:2 ratio).

growth polymerization proceeds rapidly achieving a modulus value of ~10 kPa within 3 min of light exposure. Also, both the G' and G'' increased at about the same point in time, however the crossover point could not be seen as expected for a fully gelled sample, but noise appeared in data after 2 min, with the values fluctuating strongly after 140s due to drying of the solvent. A plateau in G' curve gives an indication of approximate reaction time for the photopolymerization of the system. This seems to indicate that under shear conditions, although the thiol−ene reaction took place the applied shear may have prevented the formation of a solid, cohesive gel, but rather a loosely attached dispersion of gelled material within the solvent (methanol). Nevertheless, it confirmed that the thiol−ene reaction occurred rapidly at room temperature under UV irradiation.

As can be seen from Figure 3, increasing either the DVIMBr or PETKMP content (excess vinyl or thiol) resulted in a slower gelation compared to the stoichiometric ratio sample (1:2). The addition of excess thiol (1:1) resulted in a material with a lower modulus compared to the stoichiometric ratio, while increasing the vinyl content resulted in a material which ultimately may have greater modulus; however the polymerization was slower and more gradual as it is likely to be a

DOI: 10.1021/acsami.5b04405
ACS Appl. Mater. Interfaces 2015, 7, 17298−17306

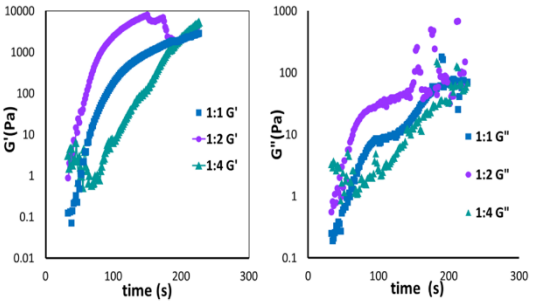


Figure 3. In situ rheology study during photopolymerization of PETKMP/DVIMBr of varying stoichiometry showing evolution of mechanical properties.

mixture of thiol−ene reactions and free radical polymerization. In each case, it led to the formation of polymer or oligomer with excess thiol or vinyl groups.

Kinteic Study of Photopolymerization Using Differential Scanning Calorimetry. On the basis of the above results, the stoichiometric amount of 1:2 of PETKMP:DVIMBr was chosen as an optimal composition for further kinetic study. In this case the kinetics of the thiol−ene reaction was further studied using differential scanning calorimetry (DSC) by both a temperature-ramp and isothermal methods.[21] In this work, a thermal initiator (AIBN) was used for a comparative study with photoinitiated system. However, as thiol−ene chemistry proceeds through a radical step-growth mechanism, it was expected that experiments with thermal initiator would yield similar trends to the photoinitiated system.

To do this, first two conventional DSC experiments (with a temperature ramp) were performed to find the effective thiol−ene curing temperature: first using the divinyl monomer only (DVIMBr) with thermal initiator (AIBN) (to find the divinyl polymerization temperature range) and second using the full stoichiometric polymerization system with monomers, solvent, and thermal initiator (DVIMBr/PETKMP/MeOH/AIBN). In the first experiment, the DVIMBr polymerization reaction was detected at 396 K, whereas in the second experiment, a broad peak from 398 to 423 K indicates the occurrence of thiol−ene reaction.

On the basis of these results, the kinetics of the thiol−ene reaction was then studied using an isothermal method where the samples were quickly brought to a temperature above which the reaction starts and held isothermally, monitoring the course of polymerization over time. Thus, the sample is quickly brought to one of three different temperatures within the appropriate temperature range (398, 408, and 418 K) at a fast heating rate of 20 K/min (the fast ramp rate was used to minimize the effect of the heating ramp), and then held at that temperature for a fixed time (45 min). The time duration and the enthalpy (ΔH) were then determined from the DSC isothermal exotherm for all three temperatures. As shown in Figure 4a, the peak maximum occurs more rapidly with increasing temperatures. The presence of the maximum in the reaction curve indicates that the reaction follows an autocatalytic mechanism, while the heat evolved during polymerization reaction at a particular time is directly proportional to the degree of conversion ($x = \Delta H_1/\Delta H$).

From these data, the values can then be converted to a reaction rate (k), $d\alpha/dt$, using an isothermal conversion (%) vs time (min) graph. The calculated values were then used to plot $\ln[k(T)]$ versus $1/T$ (Arrhenius plot), which indicates that the thiol−ene reaction is a zero order reaction as the plot was linear (Figure 4b). Because the fit of the line follows the equation $\ln K = \ln Z - E_a/RT$, the value of the reaction constant K can be determined from the y value of the fitted experimental data, whereas the slope of the fit is equal to E_a/R (as $1/T$ is set as the x values) and the intercept is equal to Ln Z. Using this equation the activation energy (E_a) of 8.54 kJ/mol and pre-exponential factor (Z) of 107.5 S^{-1} are obtained from the slope and intercept of this plot, respectively. Previously, Cook and co-workers[22] reported the activation energy for photopolymerization of thiol−ene reaction is 7.6 kJ/mol, which is in very good agreement with the results reported here. This low value of activation energy for free radical polymerization corresponds to the fact that the thiol−ene reaction is a very fast reaction with the activation energy of the initiation step being close to zero.

Thermal and Mechanical Study. *Thermal Behavior Using Thermogravimetric Analysis.* Thermogravimetric analysis was done on the gel beads to confirm the formation of the polymer and study the properties of the gel beads. The TGA of the cured gel beads (Figure 5) showed one main degradation (around 70 wt %) with an onset temperature of around 265 °C and peak degradation temperature of 313 °C, with the gradual weight loss above 360 °C likely due to sulfur-containing residues. Previous literature on similar, nonpolymerized imidazolium ionic liquid with Br^- counterion reported an onset of degradation at around 253−259 °C. Comparatively, this 10 °C increase in thermal stability of the PIL gel beads is

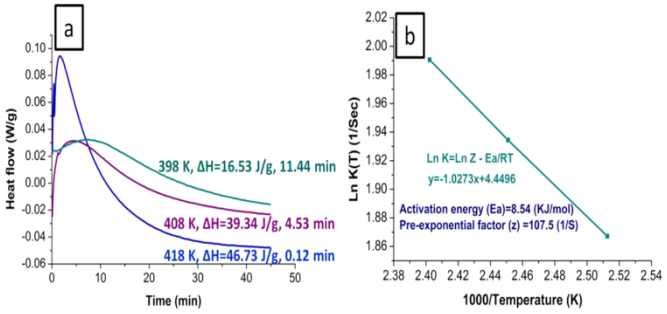


Figure 4. (a. Isothermal exotherm of PETKMP/DVIMBr system at three different temperatures measured using DSC, (b) Arrhenius plot of the DVIMBr/PETKMP system.

DOI: 10.1021/acsami.5b04405
ACS Appl. Mater. Interfaces 2015, 7, 17298−17306

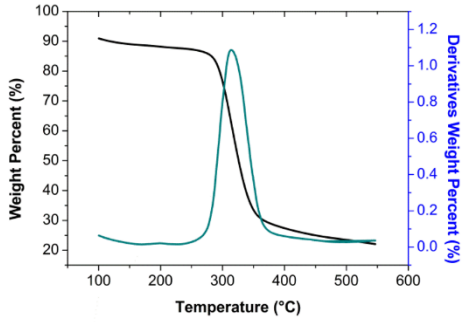


Figure 5. TGA thermogram of the gel beads (1:2 ratio) showed in black and first derivatives vs temperature presented in dark cyan.

ascribed to the photopolymerised PIL.[23] This is supported also by the higher range of temperature at which the main degradation occurs, with gel beads showing the thermal degradation over 265−350 °C, whereas free ionic liquid was completely degraded at around 330 °C. The existence of only a single degradation peak also indicates that there are unlikely to be unreacted reagents or small molecular weight oligomers present (as this would show a lower onset degradation temperature, resulting in a second mass loss earlier than the main degradation). The TGA also indicates that there is trace amount of water present in the gel beads as there is a gradual mass loss at 100−150 °C, which confirms our previous FTIR results showing a peak for tightly bound water molecules.

The thermal degradation properties were also affected by the stoichiometry. Comparing the TGA thermograms in Figure 6

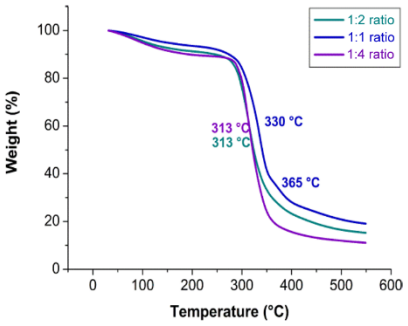


Figure 6. TGA thermogram showing the peak degradation temperature of three samples with different stoichiometric ratios of PETKMP:DVIMBr (1:2, 1:1, 1:4).

of samples with different stoichiometry (1:1, 1:2, 1:4 molar ratios of PETKMP and DVIMBr), samples with a 1:1 ratio show an earlier onset of degradation that is ascribed to the unreacted thiols (which is a liquid) volatizing at their boiling point of around 275 °C. Also, two peak degradation temperatures were observed in the 1:1 ratio sample at 330 and 365 °C, whereas the 1:2 and 1:4 ratio samples show only one peak degradation around 313 °C. This confirms our assignment of the main degradation to the degradation of the PIL gel and the second one to the degradation of sulfur-containing residues, as this second degradation increases with increasing amount of thiols (1:1 > 1:2 > 1:4 stoichiometry). The excess thiols may have reacted at these temperatures to form other compounds which resulted in the slight shift of the peak degradation temperature in this sample (1:1 ratio). On the other hand, 1:2 and 1:4 showed almost same degradation profile as a result of the same kind of product in their structure because of the thiol−ene reaction, as further homopolymerization of DVIMBr in 1:4 ratios is unlikely to significantly affect the thermal degradation temperature.

Phase Behavior Study Using Differential Scanning Calorimetry. In this type of gel material, another parameter of interest is the glass transition temperature (T_g). This is because self-healing in this type of material occurs through a combination of intermolecular diffusion and reversible, dynamic noncovalent bonds. DSC thermogram of samples with varying stoichiometry is shown in Figure 7. DSC results in Figure 7

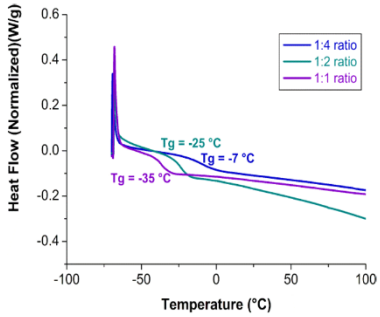


Figure 7. DSC thermogram showing the glass transition temperature of three samples with varying stoichiometry of PETKMP:DVIMBr (1:1, 1:2, 1:4) under a temperature ramp of 10 °C/min.

show that sample containing excess thiol (1:1 ratio) has the lowest T_g around −35 °C which is almost same as the Tg of the DVIMBr monomer. This shows that there were insufficient amount of cross-linkable vinyl groups to form an extensive thiol−ene network and thus only low molecular weight oligomers were formed where they are likely to be held together by ionic interaction rather than extensive physical entanglement. It is worth noting that this sample disintegrated when immersed in water, which indicates a loose network formation. On the other hand, increasing the PETKMP:DVIMBr ratio to the required stoichiometric amounts or to an excess in vinyl groups increases the T_g, with a T_g of −25 °C for the 1:2 ratio sample and increasing to around −7 °C in the 1:4 ratio sample, indicating strong network formation. The higher T_g for the sample with excess vinyl group (1:4) compared to the stoichiometric one (1:2) indicates the occurrence of some homopolymerization of the vinyl monomer; however, as was shown in the FTIR results previously, the main process for the network formation was the thiol−ene reaction.

Nevertheless, low T_g materials allow interchain diffusion and entanglement at room temperature,[24] resulting in a degree of self-healing based on two mechanisms; reconstruction of noncovalent bond by hydrogen bonding or reassociation of the molecular chain as proposed by Wool and O'Connor.[25] In this mechanism, diffusion of polymer chains near the surface results in the displacement and entanglement of mobile chains followed by interpenetration into the matrix material, healing the initial defect or rupture. Previous studies on elastomers show that this occurs mainly at temperatures above the bulk

DOI: 10.1021/acsami.5b04405
ACS Appl. Mater. Interfaces 2015, 7, 17298−17306

polymer glass transition temperature (T_g), and Scheltjens et al.[26] reported that with increasing mobility (by reducing T_g) the self-healing properties can be improved.

To investigate the autonomous self-healing properties of this composition at ambient environment, we cut the gel beads (1:2 ratios) using scalpel and the healing process was observed with a high speed camera. Figure 8 inset shows the time laps optical image of healing behavior of cut sample surface. It is clear that upon the occurrence of microcracks at room temperature, the gel beads have sufficient chain mobility, allowing them to flow into and fill small gaps to recover the surface in a healing process. This is evidenced by time lapse images of a scratch on the surface of the gel beads, which show that the material is capable of viscoelastic flow into such defects (Figure 8), and thus demonstrating a degree of self-healing behavior in the bulk material. As such, the gel beads are an intrinsic type of self-healing materials with an internal ability for repair to occur through molecular-scale mechanisms, such as polymer-chain mobility and entanglement. Such a mechanism is reversible, making multiple healings possible.

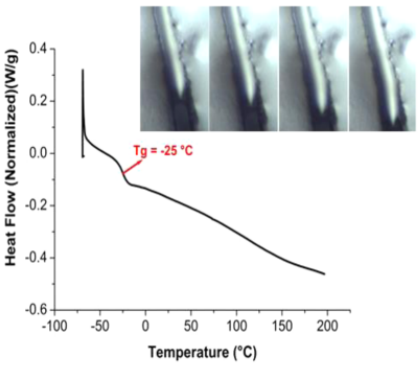


Figure 8. DSC thermogram of the cured gel beads (1:2 ratios). Inset: time-lapse optical image of healing on a cut on the surface of a gel bead.

Mechanical Properties of the Gels by Dynamic Mechanical Analysis (DMA). DMA is a useful tool to obtain the viscoelastic properties of these ionic gels. Generally, it has been reported that thermal and mechanical parameters are directly related to features inherent to the chemical structure of both the thiol and ene functional groups.[27] To provide corroborative evidence for the DSC results and provide an interpretation of those results, the dynamic mechanical test was conducted. Figure 9 shows the storage modulus (E) data at different ratios and at two different humidity levels (40 and 60% relative humidity) at room temperature. It shows a significant increase in the storage modulus from 0.054 MPa for 1:1 ratio to 7.7 MPa for 1:2 and 19.88 MPa for 1:4 ratios at 40% humidity. The low modulus for the sample with 1:1 ratio confirms the lack of network formation in this sample, while the increase between the 1:2 and 1:4 also shows some homopolymerization of DVIMBr can occur after the thiols have been reacted. At 60% humidity level, an increase in modulus was detected with increasing DVIMBr content but in the case of 1:4 ratio samples, breakage occurred. This is consistent with the DSC results in Figure 8, where increased T_g for this sample may make it more brittle.

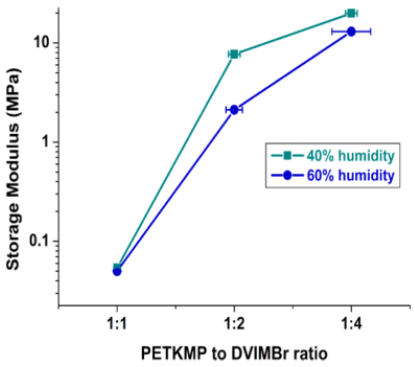


Figure 9. Storage modulus of three different ratios of thiol−ene reaction in two different humidity levels. The sample with 1:4 ratio did not fully maintain its mechanical integrity and broke during measurement so the value for 1:4 ratio at 60% is the last record.

The DSC and DMA results indicate that in the 1:1 ratio, the structure is likely that of a loosely bound network with greater coordinated segmental motion and as a result has the least mechanical strength and lowest T_g. The sample with 1:2 ratio appears to have optimized full network formation, resulting in higher T_g and modulus. This sample also shows more stable mechanical properties, which is decreased slightly with increasing humidity but remained intact, whereas the sample with a 1:4 ratio (with the highest modulus) breaks because of its brittle nature.

On the basis of the previous results, it is clear that three different precursor ratios lead to different compositions of polymer with different characteristics. The 1:1 system mostly showed oligomeric type behavior, whereas 1:2 was a fully cross-linked network and 1:4 was more brittle, with a mixture of both thiol−ene and vinyl polymerized systems.

Thus, the stoichiometric ratio of 1:2 of PETKMP:DVIMBr was considered optimal as it provides a material that is thermally and mechanically more stable and robust. This material is then selected for studying further for its use as a reservoir for controlled release or delivery.

Poly(Ionic Liquid) Gels as pH Sensing Material. Although it has not been widely studied in anticorrosion applications, another characteristic of PILs is that they contain ionic functionalities which can bind ionic compounds through ion exchange. Similar materials have been shown in the literature[10] to be able to act as corrosion indicators; when loaded with pH sensing molecule and incorporated into coatings, this adds significant value and a diagnostic aspect to the coating. It is expected that this PIL gel would be able to perform similar task, and thus a preliminary sorption study was done using these gels. In this study a pH indicator, methyl red (MR), was incorporated into the gel through ion exchange. The synthesized gels are placed into a solution containing 0.3 wt % of MR and the uptake of dye into the gel was monitored by UV−vis spectroscopy through the decrease in the color intensity of the dye solution. After 9 days, no further reduction in color intensity was observed, which indicates that the dyes have been absorbed into the beads (Figure S2). The unbound dyes were then washed from the beads by soaking the beads in ultrapure water (Figure S3). The release of unbound dyes during 16 days was also monitored through UV−vis (Figure

DOI: 10.1021/acsami.5b04405
ACS Appl. Mater. Interfaces 2015, 7, 17298−17306

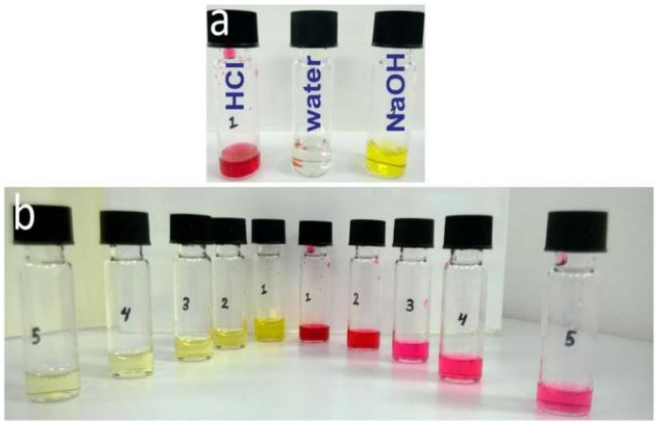


Figure 10. (a) Indicator (MR) release from the gel beads due to pH changes; (b) successive leaching showing that after 5 repetitions, leaching of MR was still observed.

S4), and after 16 days, the peak intensity in the UV−vis spectra reached a plateau (Figure S5), indicating all the unbound dyes have been washed out. Since the gel beads themselves remained strongly colored after washing, this indicates that the remaining dye within the gel is bound through ionic interaction with the vinylimidazolium moiety.

This was confirmed by the fact that when the washed, MR loaded−beads were exposed to ultrapure water at neutral pH, no visible leaching of MR was observed. However, as soon as the pH of the surrounding aqueous medium was lowered (pH ~ 0.5) by adding 0.1 M HCl (pK_a of methyl orange is 5.1), slow release of MR into water was observed by changing of the solution color to pink (Figure 10a). This was confirmed through UV−vis measurements (Figure S6) that show a quick release of MR into solutions of 0.1 M HCl or 0.1 M NaOH; however, there was no release detected in deionized water over 24 h. This shows that unlike a container that relies on physical entrapment, the PIL gel acts as an active, environmental sensing container where the release of the indicator dye is controlled by the pH of the solution. This is because the MR is bound in the PIL gel through ion exchange, and a lowering in pH changes the nature of the MR by protonating the carboxylate ion and, disrupting the ionic bond between the MR and the imidazolium group of the PIL and releasing the MR into the solution. Similarly, exposure to higher pH by adding 0.1 M NaOH releases MR into water through anion exchange with the hydroxyl ions, changing the solution color to yellow. This shows that the unique property of PIL gels enables both acidic and basic conditions to induce a slow release of pH indicators,[28] making it a versatile pH sensing material. The speed of the release is also suitable for the intended application in corrosion, as this would mean that the indicator would be released readily only when corrosion occurs.

Furthermore, although this release mechanism was pH sensitive, it was also sufficiently gradual to be repeatable several times. The leaching through pH change (by repeated washing and exposure to low/high pH) was repeated 5 times and even after this further release of bound MR could still be detected (Figure 10b), indicating that despite the rapid release of MR under acidic or basic conditions, sufficient MR was still retained in the PIL gel beads for sustained release. This may offer advantages in longevity compared to indicators directly incorporated in coatings,[10] as repeated use is possible, while still offering the advantages of mobility of the indicator molecules as opposed to immobilized approaches such as with covalently bound[29] or sol−gel-based systems.[30] These experiments show the potential of these gel beads as pH sensing indicators for applications such as environmentally friendly coatings, which will be investigated in future studies.

Ionic Liquid Gel as Macrocontainer for IL. To investigate whether these PIL gels have the potential to be used as macrocontainers for other compounds, we have examined them as containers for ionic liquid for potential anticorrosion application.[31−33] Unlike other encapsulation methods, these PIL-based macrocontainers may solve some of the drawbacks of traditional (nonpolymerized) IL gels such as phase mixing, phase separation, leakage of ionic liquids as well as the high viscosity of ionic liquids. Till now, studies have been conducted with ionic liquids in polymeric or inorganic macrocontainers, but there is little study on the use of PIL macrocontainers.[34]

In terms of potential applications in anticorrosion coatings, loading of corrosion inhibitors onto macrocontainers have shown promising results for corrosion protection.[35] Free ILs have been shown to act as corrosion inhibitors,[11] and PIL gel beads would be an ideal reservoir for ILs since they would have a high compatibility. Thus, the loading capacity of the PIL gel was investigated with respect to the feasibility of this approach. For this experiment, 1-butyl-2,3-dimethylimidazolium hexafluorophosphate ionic liquid (IL) was dissolved in tetrahydrofuran (THF) and preweighted PIL gel beads was added to the solution, and the mass uptake was monitored over 40 days through the weight changes of the gel beads. As can be seen in Figure 11, under ambient conditions the PIL gel beads gradually uptake free IL during 30 days, reaching a plateau after around 25% mass uptake. This uptake is quite linear for most of this time period, indicating a straightforward diffusion-controlled uptake of IL from solution. This uptake result is also supported by FTIR in Figure 12, which shows extra peaks at 852−559 cm^{-1} indicating the presence of the hexafluorophosphate of the free IL in the PIL gel beads. This 25% loading is relatively low compared to some encapsulation methods where IL acts as a solvent to a gelling agent,[36] but is comparable to IL uptake of materials with similar macromolecular structures such as polyelectrolyte membranes,[37] and this is attributed to the IL

DOI: 10.1021/acsami.5b04405
ACS Appl. Mater. Interfaces 2015, 7, 17298−17306

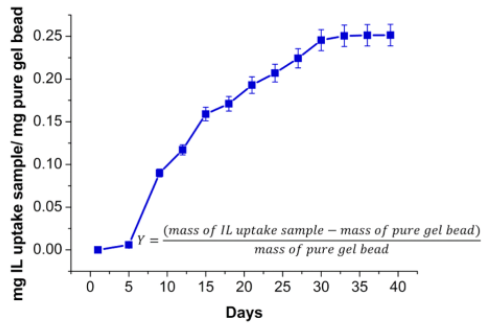


Figure 11. IL uptake of the gel beads where the *Y* axis is calculated using the above formulation and the *X* axis presents the number of days.

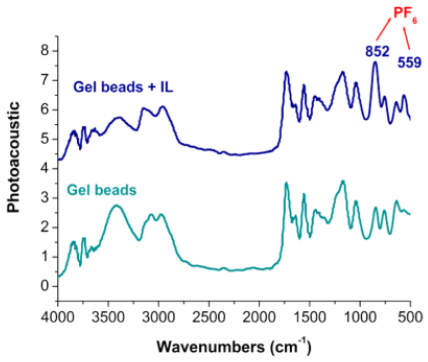


Figure 12. FTIR spectra of the IL-loaded gel beads.

being uptaken after synthesis rather than present during network formation.

In this study, the PIL gel beads are formed as a cross-linked network with methanol as the solvent, and this limits the maximum sorption of the bulky IL molecules post-synthesis. It is likely that reducing the cross-link density or having the IL acting as the polymerization solvent would significantly increase IL loading; however this is beyond the scope of the current study. This result does show that the PIL gel beads are able to act as macrocontainers for IL, with potential use in various applications such as anticorrosion coating.[11] Currently work is underway to investigate those behaviors and will be communicated in our future work.

CONCLUSION

In this work, we have shown the fabrication of poly(ionic liquid) gel beads through click-type reactions using thiol−ene chemistry. The use of thiol−ene chemistry allows for a very rapid and efficient formation of gel beads suitable for large scale synthesis. The formation of gel beads is confirmed through FTIR, thermal analysis, and kinetic studies. These gel beads also show self-healing characteristics, capable of reassociation of chains through viscoelastic flow into small defects, because of their rubbery nature. The beads also demonstrate the ability to uptake active molecules such as corrosion inhibitors or as macrocontainers for sensing molecules through ion exchange, with the ability to pH sensing or controlled release of active anticorrosion agents. Overall, these results show that these gel beads are multipurpose promising materials suitable for pH sensing or anticorrosion applications.

ASSOCIATED CONTENT

Supporting Information

The Supporting Information is available free of charge on the ACS Publications website at DOI: 10.1021/acsami.5b04405.

^{1}H NMR and experimental details of dye uptake and release study with UV−vis data (PDF)

AUTHOR INFORMATION

Corresponding Authors

*E-mail: naba.dutta@unisa.edu.au. Tel.: +6188302 3546.
*E-mail: namita.choudhury@unisa.edu.au. Tel.: +6188302 3719.

Notes

The authors declare no competing financial interest.

ACKNOWLEDGMENTS

The authors gratefully acknowledge the financial support of the Australian Research Council's Linkage grant for carrying out this work and also the industry partner Wave rider Energy for financial support of this work. The authors thank Mr. Steve Shamis of TA Instruments for assistance with the Photo-rheology work.

REFERENCES

(1) Priya James, H.; John, R.; Alex, A.; Anoop, K. R. Smart Polymers for the Controlled Delivery of Drugs − a Concise Overview. *Acta Pharm. Sin. B* **2014**, *4*, 120−127.
(2) Yuan, J.; Antonietti, M. Poly(Ionic Liquid)S: Polymers Expanding Classical Property Profiles. *Polymer* **2011**, *52*, 1469−1482.
(3) Shaplov, A. S.; Vlasov, P. S.; Lozinskaya, E. I.; Shishkan, O. A.; Ponkratov, D. O.; Malyshkina, I. A.; Vidal, F.; Wandrey, C.; Godovikov, I. A.; Vygodskii, Y. S. Thiol-Ene Click Chemistry as a Tool for a Novel Family of Polymeric Ionic Liquids. *Macromol. Chem. Phys.* **2012**, *213*, 1359−1369.
(4) Raghavan, P.; Manuel, J.; Zhao, X.; Kim, D.-S.; Ahn, J.-H.; Nah, C. Preparation and Electrochemical Characterization of Gel Polymer Electrolyte Based on Electrospun Polyacrylonitrile Nonwoven Membranes for Lithium Batteries. *J. Power Sources* **2011**, *196*, 6742−6749.
(5) Murata, Y.; Sasaki, N.; Miyamoto, E.; Kawashima, S. Use of Floating Alginate Gel Beads for Stomach-Specific Drug Delivery. *Eur. J. Pharm. Biopharm.* **2000**, *50*, 221−226.
(6) Kashyap, N.; Kumar, N.; Kumar, M. N. V. R. Hydrogels for Pharmaceutical and Biomedical Applications. *Crit. Rev. Ther. Drug Carrier Syst.* **2005**, *22*, 107−149.
(7) Xing, X.; Li, L.; Wang, T.; Ding, Y.; Liu, G.; Zhang, G. A Self-Healing Polymeric Material: From Gel to Plastic. *J. Mater. Chem. A* **2014**, *2*, 11049−11053.
(8) Cui, J.; Campo, A. D. Multivalent H-Bonds for Self-Healing Hydrogels. *Chem. Commun.* **2012**, *48*, 9302−9304.
(9) Blaiszik, B. J.; Sottos, N. R.; White, S. R. Nanocapsules for Self-Healing Materials. *Compos. Sci. Technol.* **2008**, *68*, 978−986.
(10) Maia, F.; Tedim, J.; Bastos, A. C.; Ferreira, M. G. S.; Zheludkevich, M. L. Nanocontainer-Based Corrosion Sensing Coating. *Nanotechnology* **2013**, *24*, 415502.
(11) Ibrahim, M. A. A.; Messali, M.; Moussa, Z.; Alzahrani, A. Y.; Alamry, S. N.; Hammouti, B. Corrosion Inhibition of Carbon Steel by Imidazolium and Pyridinium Cations Ionic Liquids in Acidic Environment. *Port. Electrochim. Acta* **2011**, *29*, 375−389.

DOI: 10.1021/acsami.5b04405
ACS Appl. Mater. Interfaces 2015, 7, 17298−17306

(12) Baskar, R.; Kesavan, D.; Gopiraman, M.; Subramanian, K. Synthesis of Novel Photosensitive Polymers for the Protection of Mild Steel from Acid Corrosion. *RSC Adv.* **2013**, *3*, 17039−17047.
(13) Xiong, Y.; Wang, H.; Wang, R.; Yan, Y.; Zheng, B.; Wang, Y. A Facile One-Step Synthesis to Cross-Linked Polymeric Nanoparticles as Highly Active and Selective Catalysts for Cycloaddition of Co2 to Epoxides. *Chem. Commun.* **2010**, *46*, 3399−3401.
(14) Muldoon, M. J.; Gordon, C. M. Synthesis of Gel-Type Polymer Beads from Ionic Liquid Monomers. *J. Polym. Sci., Part A: Polym. Chem.* **2004**, *42*, 3865−3869.
(15) Men, Y.; Kuzmicz, D.; Yuan, J. Poly(Ionic Liquid) Colloidal Particles. *Curr. Opin. Colloid Interface Sci.* **2014**, *19*, 76−83.
(16) Hoyle, C. E.; Lee, T. Y.; Roper, T. Thiol−Enes: Chemistry of the Past with Promise for the Future. *J. Polym. Sci., Part A: Polym. Chem.* **2004**, *42*, 5301−5338.
(17) Hoyle, C. E.; Bowman, C. N. Thiol−Ene Click Chemistry. *Angew. Chem., Int. Ed.* **2010**, *49*, 1540−1573.
(18) Gokmen, M. T.; Brassinne, J.; Prasath, R. A.; Du Prez, F. E. Revealing the Nature of Thio-Click Reactions on the Solid Phase. *Chem. Commun.* **2011**, *47*, 4652−4654.
(19) Yuan, J.; Antonietti, M. Poly(Ionic Liquid) Latexes Prepared by Dispersion Polymerization of Ionic Liquid Monomers. *Macromolecules* **2011**, *44*, 744−750.
(20) Storha, A.; Mun, E. A.; Khutoryanskiy, V. V. Synthesis of Thiolated and Acrylated Nanoparticles Using Thiol-Ene Click Chemistry: Towards Novel Mucoadhesive Materials for Drug Delivery. *RSC Adv.* **2013**, *3*, 12275−12279.
(21) Joraid, A. A.; Abu-Sehly, A. A.; Alamri, S. N. A Study on Isothermal Kinetics of Glassy Sb9.1te20.1se70.8 Alloy. *J. Taibah Univ Med. Sci.* **2009**, *2*, 106−117.
(22) Cook, W. D.; Chausson, S.; Chen, F.; Le Pluart, L.; Bowman, C. N.; Scott, T. F. Photopolymerization Kinetics, Photorheology and Photoplasticity of Thiol−Ene−Allylic Sulfide Networks. *Polym. Int.* **2008**, *57*, 469−478.
(23) Awad, W. H.; Gilman, J. W.; Nyden, M.; Harris, R. H., Jr; Sutto, T. E.; Callahan, J.; Trulove, P. C.; DeLong, H. C.; Fox, D. M. Thermal Degradation Studies of Alkyl-Imidazolium Salts and Their Application in Nanocomposites. *Thermochim. Acta* **2004**, *409*, 3−11.
(24) Garcia, S. J. Effect of Polymer Architecture on the Intrinsic Self-Healing Character of Polymers. *Eur. Polym. J.* **2014**, *53*, 118−125.
(25) Wool, R. P.; O'Connor, K. M. A Theory Crack Healing in Polymers. *J. Appl. Phys.* **1981**, *52*, 5953−5963.
(26) Scheltjens, G.; Diaz, M. M.; Brancart, J.; Van Assche, G.; Van Mele, B. A Self-Healing Polymer Network Based on Reversible Covalent Bonding. *React. Funct. Polym.* **2013**, *73*, 413−420.
(27) Li, Q.; Zhou, H.; Hoyle, C. E. The Effect of Thiol and Ene Structures on Thiol−Ene Networks: Photopolymerization, Physical, Mechanical and Optical Properties. *Polymer* **2009**, *50*, 2237−2245.
(28) Rahman, M. T.; Barikbin, Z.; Badruddoza, A. Z. M.; Doyle, P. S.; Khan, S. A. Monodisperse Polymeric Ionic Liquid Microgel Beads with Multiple Chemically Switchable Functionalities. *Langmuir* **2013**, *29*, 9535−9543.
(29) Vasylevska, G. S.; Borisov, S. M.; Krause, C.; Wolfbeis, O. S. Indicator-Loaded Permeation-Selective Microbeads for Use in Fiber Optic Simultaneous Sensing of Ph and Dissolved Oxygen. *Chem. Mater.* **2006**, *18*, 4609−4616.
(30) Dong, S.; Luo, M.; Peng, G.; Cheng, W. Broad Range Ph Sensor Based on Sol−Gel Entrapped Indicators on Fibre Optic. *Sens. Actuators, B* **2008**, *129*, 94−98.
(31) Spath, A.; Minami, H.; Suzuki, T.; Fink, R. H. Morphology Changes of Ionic Liquid Encapsulating Polymer Microcontainers Upon X-Ray Irradiation. *RSC Adv.* **2014**, *4*, 3272−3277.
(32) Yang, W. W.; Lu, Y. C.; Xiang, Z. Y.; Luo, G. S. Monodispersed Microcapsules Enclosing Ionic Liquid of 1-Butyl-3-Methylimidazolium Hexafluorophosphate. *React. Funct. Polym.* **2007**, *67*, 81−86.
(33) Rana, R. K.; Murthy, V. S.; Yu, J.; Wong, M. S. Nanoparticle Self-Assembly of Hierarchically Ordered Microcapsule Structures. *Adv. Mater.* **2005**, *17*, 1145−1150.
(34) Xiang, Z. Y.; Lu, Y. C.; Zou, Y.; Gong, X. C.; Luo, G. S. Preparation of Microcapsules Containing Ionic Liquids with a New Solvent Extraction System. *React. Funct. Polym.* **2008**, *68*, 1260−1265.
(35) Wei, H.; Wang, Y.; Guo, J.; Shen, N. Z.; Jiang, D.; Zhang, X.; Yan, X.; Zhu, J.; Wang, Q.; Shao, L.; Lin, H.; Wei, S.; Guo, Z. Advanced Micro/Nanocapsules for Self-Healing Smart Anticorrosion Coatings. *J. Mater. Chem. A* **2015**, *3*, 469−480.
(36) Ohno, H.; Yoshizawa, M.; Ogihara, W. Development of New Class of Ion Conductive Polymers Based on Ionic Liquids. *Electrochim. Acta* **2004**, *50*, 255−261.
(37) Subianto, S.; Mistry, M. K.; Choudhury, N. R.; Dutta, N. K.; Knott, R. Composite Polymer Electrolyte Containing Ionic Liquid and Functionalized Polyhedral Oligomeric Silsesquioxanes for Anhydrous Pem Applications. *ACS Appl. Mater. Interfaces* **2009**, *1*, 1173−1182.

DOI: 10.1021/acsami.5b04405
ACS Appl. Mater. Interfaces 2015, 7, 17298−17306

3.2 Supplementary information

Supporting Information

for

Facile fabrication of polymerizable ionic liquid based-gel beads via thiol-ene chemistry

Mona Taghavikish, Surya Subianto, Naba Kumar Dutta, and Namita Roy Choudhury

Ian Wark Research Institute, Mawson Lakes Campus, University of South Australia, Mawson Lakes, Adelaide, SA 5095, Australia

Corresponding Author

*E-mail: namita.choudhury@unisa.edu.au, Tel.: +61883023719

*E-mail: naba.dutta@unisa.edu.au, Tel.: +61883023546

Experimental details for the synthesis of PIL gel beads with non-stoichiometric ratio of PETKMP and DVIMBr:

In the case of the sample with 1:1 mole ratio of pentaerythritol tetrakis(3-mercaptopropionate) (PETKMP) (1 mmol, 0.5g) and DVIMBr (1 mmol, 0.4g), both monomers were dissolved in the minimum volume of methanol (0.2 ml) and a small amount of BP (18.2 mg, 5 wt% with respect to monomers concentration) added to the solution. For the sample with 1:4 ratio, 0.25 mmol, 0.12g of PETKMP and 1 mmol, 0.4g of DVIMBr have been used. In both cases the same process of fabrication compared to gel beads with 1:2 ratio have been followed, with the same reaction time considered. However, rather than an elastic gel as per the 1:2 ratio a sticky film was obtained for the 1:1 ratio sample while hard films were obtained for the 1:4 ratio.

^{1}H NMR of 1,4-Di(vinylimidazolium)butane Bisbromide:

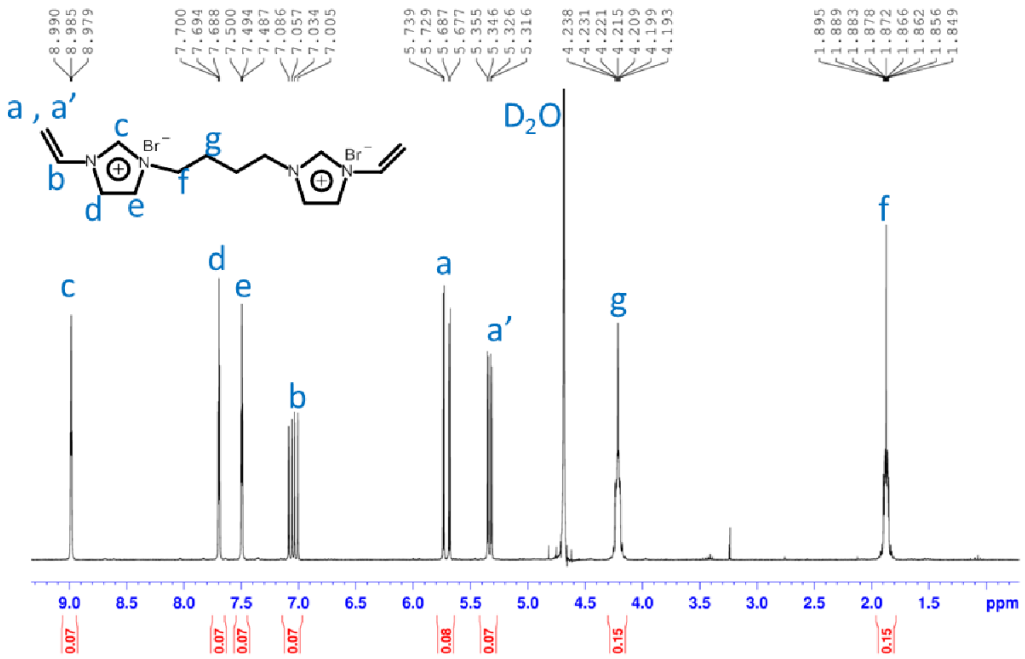


Figure S1. ^{1}H NMR of 1,4-Di(vinylimidazolium)butane Bisbromide in D_2O.(a and a' are due to the cis and trans protons of the vinyl group)

Dye uptake experiment

Washed and dried gel beads have been soaked in 0.05 wt% solution of MR. Colour change in the solution was monitored for 9 days as visible decrease in intensity of the solution colour from dark orange to lighter orange indicated that some of the dye was absorbed into the gel bead (S2). Then the gel beads were washed several times with double distilled water (DDW) and then immerseing in DDW in order to leach out all the excess and unbounded dyes. This process was monitored for 16 days under ambient conditions (S3) and UV-vis of this leaching solutions during 16 days has been investigated (S4). As expected, UV-vis results show the peak intensity for MR increasing from day 1 to day 16 and become closer to the a reference solution of MR.

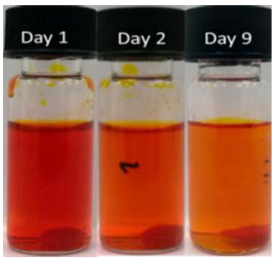


Figure S2. Dye absorption during 9 days

After 16 days a plateau in peak intensity was reached showing that at this stage all the unbounded dyes have been removed as S5 and all the dye remaining in the gel beads are bound through ion-exchange with the PIL matrix. Using elemental analysis of both gel baed and gel beads with MR, the content of methyl red in gel beads calculated around 20% based nitrogen.

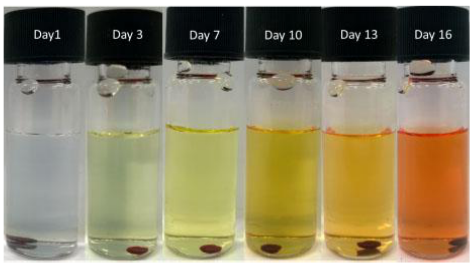


Figure S3. Unbounded dyes leached out during 16 days

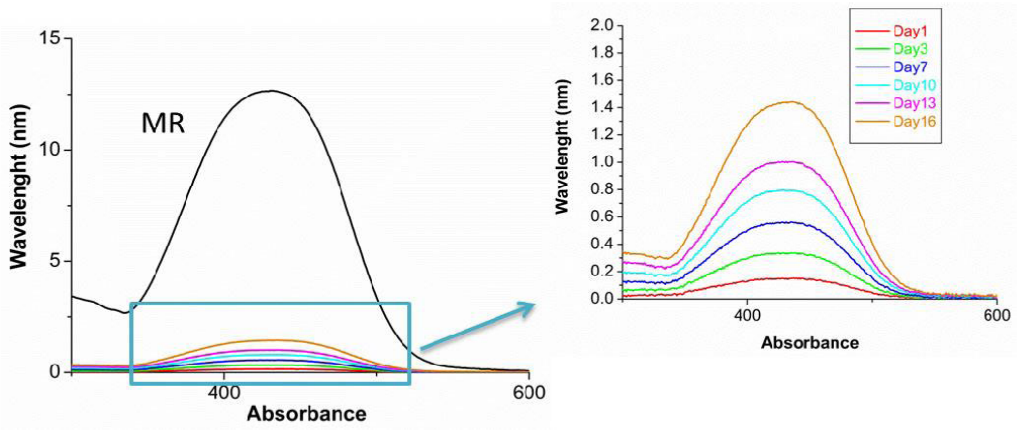


Figure S4. UV-vis of the washing solution on successive days showing unbound dyes released during 16 days

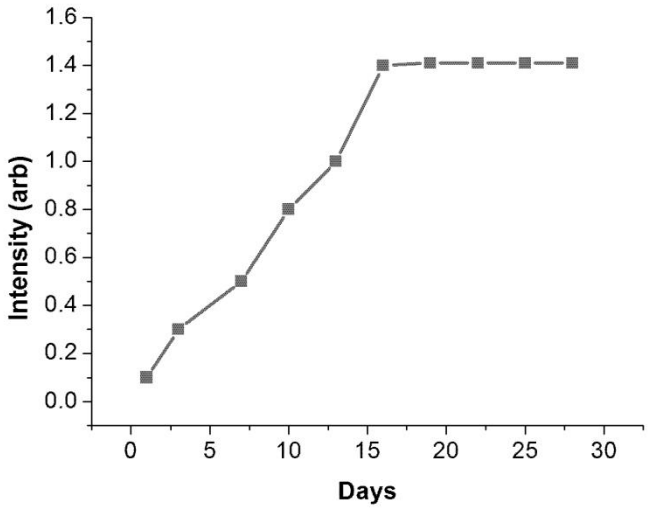


Figure S5. UV-Vis peak intensity of MR showing that after 16 days, a plateau was reached indicating no further release of dye into the solution.

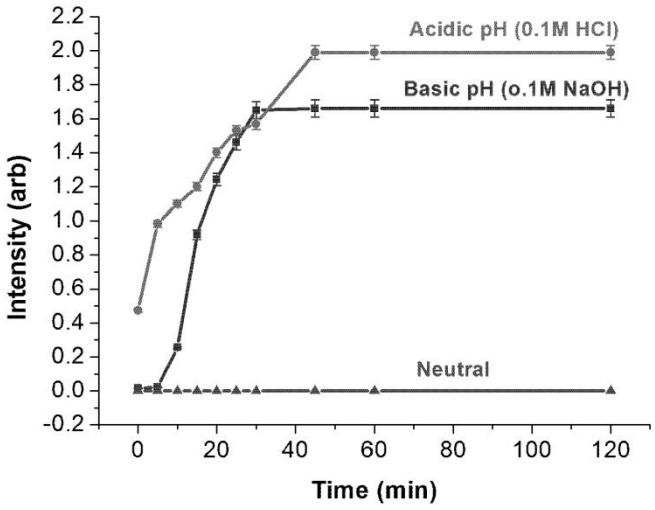


Figure S6. UV-vis of the gel beads in three different pH showing the release of MR in solutions under acidic, basic, and neutral conditions.

Chapter 4: Electrochemical performance of polymerized ionic liquid (PIL) based gel inhibitor in sol-gel coating

This chapter of the thesis is presented as a research manuscript “Mona Taghavikish, Surya Subianto, Naba K. Dutta, Namita Roy Choudhury. Electrochemical performance of polymerized ionic liquid (PIL) based gel inhibitor in sol-gel coating”, to be submitted to ACS, Industrial & Engineering Chemistry Research for peer review publication.

4.1 Abstract

The corrosion process is a surface reaction that can be controlled by the addition of corrosion inhibitors, which adsorb on the reacting metal surface. The inhibitors could be applied to a metal surface in many different ways. In this chapter, carbon steel samples coated with the sol-gel derived Self-assembled nanophase particle (SNAP) coating containing polymerized ionic liquid (PIL) was characterised using potentiodynamic polarization, electrochemical impedance spectroscopy and scanning kelvin probe techniques. The inhibition efficiency of the coating increases with the addition of PIL as observed from potentiodynamic polarization and electrochemical impedance spectroscopy (EIS) measurements. In addition, scanning kelvin probe (SKP) measurements provides further understanding on the strong interfacial properties of the modified coating compared to that of SNAP

4.2 Introduction

In recent years, the emergence of Ionic liquids (ILs) and their polymeric analogues, the polymerized ionic liquids (PILs), have attracted significant interest due to their low toxicity, good electrical conductivity, high thermal stability, high viscosity and low volatility. Many IL and PILs are based on heterocycles and thus contain heteroatoms such as sulphur, phosphorus and nitrogen, which make them highly suitable as corrosion inhibitors to reduce or arrest corrosion.[1-4] With regards to corrosion inhibitors, another class of material that is of interest is polymeric materials, which are often used as corrosion inhibitors because they possess a large number of functional groups, leading to effective interfacial interaction through complexation with metal or by physical or chemisorption.[5] The performance of such polymeric inhibitors depends on their chemical structure and physico-chemical properties, which are based on factors such as their functional group, the electron density of the donor atom, and also the electronic structure of their heterocycle or aromatic components, which serve as the major active component for any interaction or adsorption with the metal surface. ILs and PILs possess such characteristics which are desirable for a corrosion inhibitor, and therefore offer new opportunities in the field of corrosion inhibition and metal protection due to their structural diversity.

Several approaches can be used to incorporate the ILs and PILs into the coating, such as electrodeposition, conversion plating solution and dip/spray coating to mitigate material corrosion.[6-7] However, some of these methods may cause damage to metal substrates themselves depending on the method of application.[8] Therefore, it is crucial to explore new strategies for incorporating PIL inhibitors into coatings to minimise such risks and also to improve the ease of processing while maximising its anticorrosion potential. Later in chapter 5, it will be shown that the PIL in the form of nanoparticles demonstrates potential for use as a corrosion inhibitor in an interfacial coating layer.[9]

Previously in chapter 3 it has been shown that the PIL gels synthesised using click-chemistry also show a strong potential for use as corrosion inhibitors for the corrosion protection of steel.[10] However, their application as corrosion inhibitors was not thoroughly presented in that chapter. Thus, in this chapter the PIL gel based inhibitors were incorporated in a coating in order to establish their potential application as corrosion inhibitors. Among the existing coatings, inorganic sol-gel coatings based on self-assembled nanophase particles (SNAP) have been widely used in combination with other functional additives for the protection of aluminium alloys against corrosion due to the chemical bonding between the SNAP coating and the natural oxide of aluminium.[11-12] Such inorganic coatings show great potential especially when used as the interfacial layer due to their ability to chemically bond to the metal surface; however, to date there has been little study on the application of SNAP coating for metals that corrode more easily, such as carbon steel. In this regard, this chapter will focus on the addition of PIL gel particles to improve the corrosion resistance of such SNAP coating on steel surfaces. Unlike aluminium with its native oxide layer, mild carbon steel is more susceptible to corrosion and thus corrosion inhibitors may play a large role in the lifetime of such materials. This study aims to investigate the corrosion inhibition performance PIL gel particles loaded SNAP coating using electrochemical impedance spectroscopy (EIS) and potentiodynamic polarisation measurements performed at different time period in a 3.5% NaCl solution (to simulate marine environments). Furthermore, scanning kelvin probe (SKP), which performs local measurements, is also used as a complementary technique to understand the stability and protection properties of the corrosion inhibitors.

4.3 Experimental

4.3.1 Materials

3-glycidoxypropyltrimethoxysilane (GPTMS), (3-mercaptopropyl)trimethoxysilane (MPTS), 3-aminopropyltriethoxysilane, tetraethylorthosilicate (TEOS), acetic acid were all obtained from Sigma-Aldrich and used without further purification. Fluorosurfactant FC-4432 was obtained from 3M. Double distilled water (DDW) was used for all experiments. PIL based gel were prepared according to the method described in previous chapter.[10]

4.3.2 Preparation of SNAP, SNAP loaded PIL gel inhibitor (SNAP/PIL)

SANP coating has been used as a matrix to incorporate PIL gel particle as inhibitor. The SNAP solution was prepared with drop-wise addition of 42 ml (0.19mol) 3-glycidoxypropyltrimethoxysilane (GPTMS) and 13.4 ml (0.06mol) tetraethylorthosilicate (TEOS) to 64.8 ml solution of 0.05M acetic acid in doubly distilled water (DDW) in inert atmosphere. The solution was continuously stirred for 1h during addition. The TEOS: GPTMS molar ratio used was (1:3 mol ratio) respectively. Hydrolysis and condensation of silanes were conducted at high water/silane ratio of 15. After all the silanes had been added and hydrolysed, the solution was aged in closed container for 3 days under continued stirring at ambient temperature.

PIL gel loaded SNAP coating was prepared with the following method; the coating solutions with total volume of 20 ml were prepared by diluting 7 ml SNAP solution with DDW by a factor of 1.75 with considering the amount of DDW. Then 20 mg (0.2 wt %) finely ground gel particle in micron size (1µ) were added to the SNAP solution followed by addition of surfactant (3M FC-4432, 0.04 wt/v %). The mixtures were ultrasonicated at 50% rpm for 5 min to obtain homogenous solutions. At the end (3-amino propyl)triethoxysilane crosslinking agent was added into the solutions and the final mixture was vigorously stirred and applied to cleaned metal substrates by following experimental procedures.

SNAP, SNAP loaded PIL gel particle were applied on steel substrates via the following procedure: The mild steel (Mild Steel CA3SN-G, 0.08 % carbon contents, thickness~0.6 mm of 1.7 cm×1.7 cm) substrates were sequentially polished using abrasive papers with grit numbers 800, 1000 and 1200 prior to cleaning by sequential immersion for 10 min

each in acetone, hexane and ethanol solutions to remove surface oils. The substrates were rinsed with distilled water and dried with N_2 purge between each solvent wash and after the final solvent wash. Finally, the dried substrate was treated with a commercial alkaline cleaner and rinsed with distilled water and dried. The SNAP coating solutions were prepared by diluting the aged SNAP solution with water by a factor of 1.75 and subsequent addition of crosslinking agent (aminosilane) and surfactant (3M FC-4432, 0.04 wt/v %). The final mixture was vigorously stirred and applied to cleaned metal substrates by dip coating at a withdrawal speed of 10cm/min. The coating was made within a time frame of 10-30 min, counting from point of addition of the crosslinking agent. The coated sample was dried at room temperature for 24 h to allow solvent evaporation. The coating was thermally cured at 80 °C, 60% humidity for overnight in humidity oven (ESPEC-model SH-241).

4.3.3 Electrochemical measurements

Electrochemical characterization of the uncoated and the coated samples was carried out using a standard corrosion cell (1 L, Pine Research Instrumentation) with conventional three electrode set-up in non-deaerated 3.5 wt% NaCl solution prepared from analytical grade chemicals (ChemSupply, Australia) and distilled water (Milli Q). A saturated calomel electrode (SCE, Pine Research Instrumentation, +0.24 V vs. Normal Hydrogen Electrode, NHE) was employed as the reference electrode, a graphite rod of 2 mm diameter as counter electrode and the sample under test as the working electrode. All reported potentials in this work (determined using electrochemical techniques) are with reference to SCE. The open circuit potential (OCP) of the specimens was monitored as a function of time and samples were allowed to stabilize at their OCP for at least 1 h (until a stable OCP was achieved) before measurements. In this regard, all the measurements marked as ‘initial’ without time notation were done after a minimum of 1 hour stabilization time, and the measurements marked as ‘sample-1h’ were done 1 hour after the initial measurement (and thus after stabilization).

Mild steel coupons (thickness ~ 0.6 mm) of 1.7 cm × 1.7 cm (both coated and uncoated) were used as sample coupons for electrochemical testing. The sample holder is made of Teflon and a platinum sheet and a platinum wire was used for electrical connection. The area exposed to the electrolyte solution is controlled using an inner and outer ‘O’ rings for an electrode area of 0.785 cm^2. Measurements were done in duplicates.

Potentiodynamic polarization experiments were performed at a scan rate of 1 mVs^{-1} in the potential range of ±300 mV relative to OCP. The Electrochemical Impedance Spectroscopy (EIS) measurements were performed using a Solartron 1260 impedance/gain-phase analyzer in combination with a Solartron 1280B electrochemical interface. The impedance measurements were carried out in a 1 MHz to 10 kHz frequency range with 40 steps per decade. All the spectra were recorded at open circuit potential with applied 10 mV sinusoidal perturbation. The EIS data were analysed and fitted using the ZView software. The EIS data fitting and equivalent circuit modelling were done in the ZView software, and the model was fitted to the experimental data with a maximum allowable variation (error) of 5%. In addition, morphologies of the coated surfaces were observed using field emission scanning electron microscopy (FE-SEM) using Philips XL30 FEG instrument operated at an acceleration voltage of 15 KV where coating compositions were obtained using energy dispersive spectroscopy (EDS) module (OXFORD instruments) attached to the microscope.

Scanning kelvin probe (SKP) microscopy (KP Technology Ltd), was used to measure surface work function of the cleaned substrate and the freshly coated samples. Each sample was mounted on the sample holder and lightly held in place by conductive putty placed around the edges. A 2 mm diameter tipped Kelvin Probe was used with the tip to sample spacing of within 1–2 µm throughout the scans. Measurements were taken at ambient conditions before and after the scans on a pristine gold reference sample to determine the absolute tip work function. The average measurement for gold was 50 mV giving a tip work function (WF) of 5.05 eV. For each sample the scanned area is 2×2 mm, consisting of 20 × 20 points spaced 1µm apart.

4.4 Results and discussion

4.4.1 Electrochemical studies

In this study, the gel beads were used as particulate corrosion inhibitors by mechanically grinding the gel in liquid nitrogen to produce micrometre-sized particles. The use of such micrometre-sized inhibitors in SNAP coating have been previously reported in the literature,[13-14] and the PIL gel loading for this study was based on those optimised parameters.[15] In the literature, such inhibitors are expected to improve the anticorrosion performance of the coating through several potential mechanisms, including improved barrier properties and also the corrosion inhibition properties of the

inhibitors themselves. In order to evaluate the corrosion inhibition performance and mechanism of the PIL gel particles in the SNAP coating (which will be referred to here as SNAP/gel), potentiodynamic polarization and EIS measurements were carried out on these samples.

4.4.1.1 Potentiodynamic polarization studies

In order to study the inhibition performance of PIL gel particle loaded SNAP coating, potentiodynamic polarisation measurements of the modified samples (SNAP/gel) were carried out and compared with SNAP coated samples. Previous studies have shown that ionic liquids act as corrosion inhibitors on metal surfaces through both physical and chemical interactions.[16] Physically, they form a barrier when adsorbed on the metal surface, while chemically they provide redox protection by acting as a scavenger for reactive ions. This combined mechanism is what gives ILs their unique potential as corrosion inhibitors. To investigate the effect of the PIL in a coating, firstly the coatings were analysed by potentiodynamic polarisation (Tafel) measurements. Figure 4.1 shows a comparison of the Tafel plot obtained for SNAP/gel, SNAP and blank metal in 3.5 wt% salt solution. The corrosion current density (I_{corr}) and corrosion potential (E_{corr}) values of the PIL based coated samples were evaluated by fitting the anodic and cathodic polarization curves using CORR view software and are presented in Table 4.1.

The results of the potentiodynamic study show that the addition of the gel particle to the SNAP coating significantly shifted the E_{corr} to a more noble potential compared to the unmodified SNAP, with an initial E_{corr} of -0.144 V compared to -0.402 V for unmodified SNAP. This shift is indicative of specific interactions between the PIL and the metal coating resulting in a reduced tendency to corrode for the SNAP/gel coating. Furthermore, after 24 hours in the salt solution it can be seen that the E_{corr} value of SNAP/gel showed a slight shift towards more noble potentials, with an E_{corr} of -0.074 V; whereas the unmodified SNAP and the uncoated blank metal samples showed a shift towards more negative potentials with E_{corr} values of -0.723 and -0.934 V, respectively.

Table 4.1 Corrosion potential and current determined from potentiodynamic polarisation study of the SNAP, and SNAP/gel coated samples before and after immersion in 3.5 % wt/v NaCl solution for 24 hours.

Sample	Condition	I_{corr} (A.cm^{-2})	E_{corr} (V)
Blank Metal	Before	1.01 x 10^{-5}	-0.698
	After	4.86 x 10^{-6}	-0.937
SNAP	Before	3.46 x 10^{-7}	-0.402
	After	4.16 x 10^{-6}	-0.723
SNAP/Gel	Before	1.35 x 10^{-7}	-0.144
	After	1.92 x 10^{-7}	-0.074

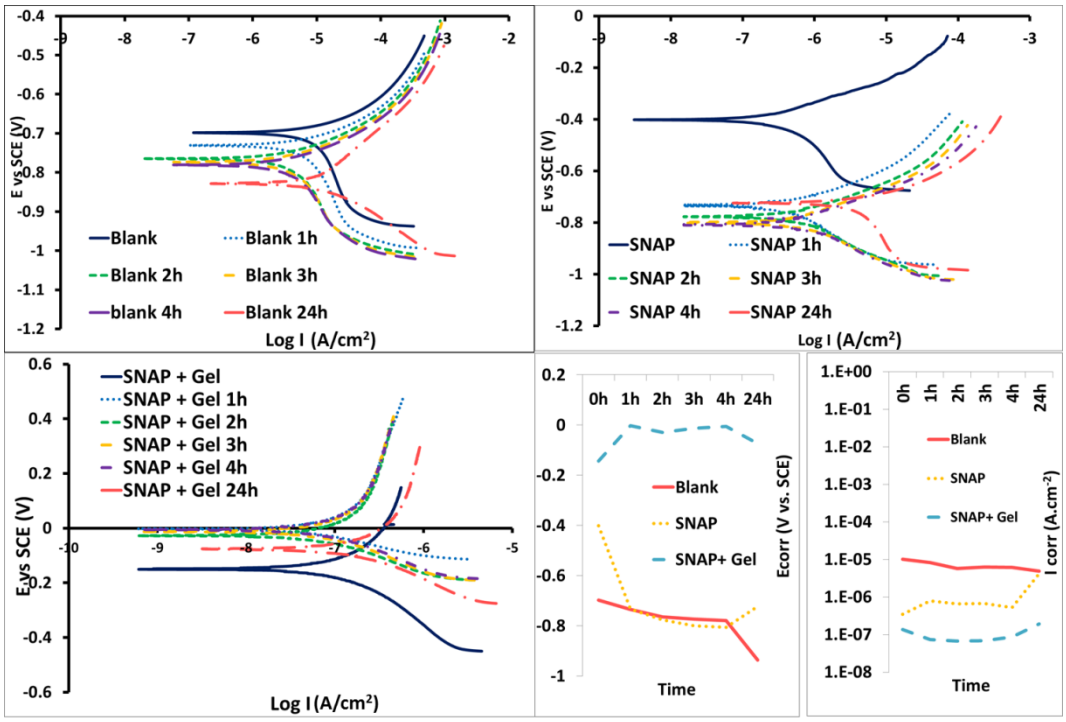


Figure 4.1 Potentiodynamic analysis of the SNAP, SNAP/gel and blank metal in 3.5 wt% NaCl solution and the profile of E_{corr} and I_{corr} over time.

Compared to the SNAP/gel coating, for the SNAP coating the shift of E_{corr} to lower potentials indicates that although initially the SNAP coating provides a resistance to corrosion (with an E_{corr} value of -0.402V compared to -0.698 V for uncoated metal), it is still susceptible to diffusion of electrolyte and thus it shows a reduction in E_{corr} over time. This indicates a semi-permeable coating where electrolyte diffusion onto the metal substrate over time results in corrosion on the metal/coating interface. This permeability of the coating will be further discussed later in the EIS analysis. Regardless, the more noble potential of the PIL gel based coating compared with the unmodified SNAP can be correlated to the strong interfacial interaction between the PIL in the coating and the substrate, due to the presence of the PIL based particles with a combination of the SNAP coating.

It has been reported that imidazolium compounds show corrosion inhibition behaviour on steel due to the specific interaction between the –C=N– group and the electronegative nitrogen in the molecule with the metal surface.[17] Therefore, such interactions can also result in the observed reduction in the changes of E_{corr} of SNAP/gel in comparison to pristine SNAP.

The I_{corr} of the samples coated with SNAP showed a reduction of two orders of magnitude compared to that of the blank metal, which indicates that the SNAP coating in general acts as an efficient barrier coating. In particular, the I_{corr} of the SNAP/gel also showed a smaller value compared to SNAP alone, indicating that the presence of the gel particles enhances the properties of the SNAP coating, which resulted in better protection of the metal. After 24 hours, the I_{corr} of the pristine SNAP showed an increase of nearly an order of magnitude in the value, which indicates increased diffusion of electrolyte, while the PIL gel based coating demonstrated only a very slight increase. The increase in I_{corr} for the SNAP coating may indicate a degree of delamination or physical degradation of the SNAP coating, resulting in increased permeability and flow of electrolytes onto the metal surface. This is due to the SNAP formulation, which uses amino silane in the coating formulation at a 6.5 molar ratio excess to the epoxy groups in the SNAP, resulting in an excess of amino groups making the SNAP coating itself quite hydrophilic. When immersed in water, adsorption and diffusion of water through the coating over time may result in additional mechanical strain due to

swelling. In a rigid, inorganic based material this swelling may cause mechanical degradation, which deteriorates the coating and compromises its integrity.

In contrast, the lack of such increase in I_{corr} for the SNAP/gel coating shows that the presence of the gel particles significantly enhances the integrity of the SNAP coating, making it less susceptible to degradation. This can be attributed to the presence of the elastic PIL gel particles reinforcing the SNAP structure, making it less porous and more rigid and thus preventing it from suffering morphological changes, which would result in the coating becoming more permeable as corrosion progresses. Thus, it can be seen that the rubbery nature of the PIL gel will improve the barrier properties and reduce the brittleness of these SNAP coatings, improving their overall inhibition efficiency and performance.[18]

The low corrosion current densities and more noble corrosion potentials of the SNAP/gel coated samples indicate the formation of well-adhered interfacial coatings with good barrier and inhibition properties. Although corrosion still occurs to some degree due to the edge effect in the metal, this study demonstrates that PIL gel loaded SNAP coatings are suitable as an interfacial layer on the metal coating interface, and also that the PIL gel corrosion inhibitors act as both a structural reinforcement, which improves the barrier properties of the metal (lower I_{corr}), as well as corrosion inhibitors that have a specific interaction with the metal, which reduces the likelihood of corrosion (more noble E_{corr}).

4.4.1.2 EIS investigation

Electrochemical Impedance analysis of the gel-bead containing SNAP coating also showed significant differences compared to SNAP alone (Figure 4.2). Bode plots of the impedance modulus (Zmod) and phase angle (θ) versus frequency generally show two time constants for SNAP-coated samples, one at a higher frequency due to the coating-metal interface and one at a lower frequency due to the coating layer. Both of the SNAP coated samples exhibited significantly higher impedance modulus compared to the blank metal; however, the SNAP/gel sample showed an additional order of magnitude resistance at most frequencies compared to SNAP alone. The blank metal showed mostly resistive behaviour as expected, but in the majority of the frequency range analysed, both coatings also exhibited

resistive rather than capacitive behaviour, as indicated by a phase angle of lower than 45 degrees (Figure 4.2b). Moreover, the gel particle containing SNAP coating showed a significantly different profile compared to SNAP alone (Figure 4.2b).

As mentioned, the SNAP/gel sample exhibits an additional time constant compared to the SNAP and blank metal sample. The first time-constant, observed in all three samples at low and middle frequencies observed is commonly associated with diffusion of electrolytes and corrosion activity on the metal surface (Figure 4.2b). The similarities between the SNAP/gel and SNAP sample (as well as their shift to lower frequencies compared to the blank metal) shows that this may be attributed to diffusion of charged species through the SNAP coating. This indicates that SNAP coatings, being intended to be used as interfacial layers, are still permeable to electrolyte diffusion. However, the presence of another time-constant at middle frequencies in the impedance spectra of the SNAP/gel sample indicates changes at the coating-metal interface due to an intermediate layer formed by the interaction of the PIL with the metal surface, as this time constant is most likely due to charge transfer between the metal surface and the ionic species in the PIL gel (as this was not observed in SNAP alone). This could be facilitated by the imidazolium functional groups on the PIL that can form complexes with either the metal surface or metal ions. This is supported by the impedance modulus of the SNAP/gel sample, which is an order of magnitude greater than the SNAP alone.

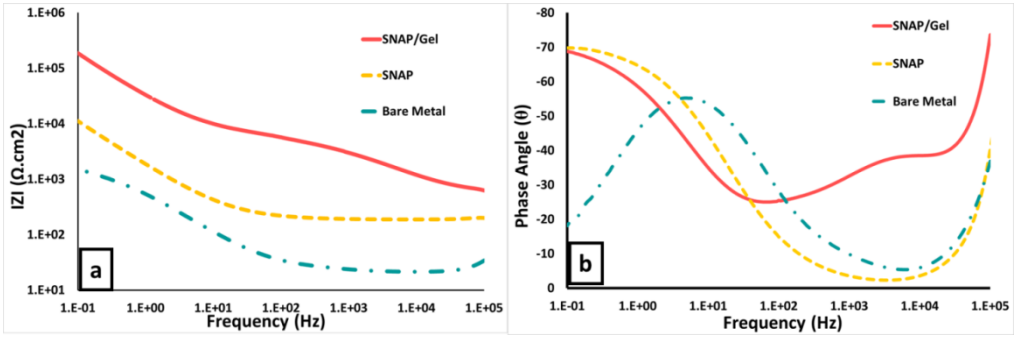


Figure 4.2 (a) Impedance modulus and (b) phase angle of the SNAP, SNAP/gel coated samples and blank metal.

The impedance data were fitted according to the general model for an imperfect, semi-permeable coating, chosen based on the number of time constants and its fit of the experimental results (Figure 4.4).[19] The model is depicted in Figure 4.3, and it consists of resistive elements (due to solution resistance R_s, coating resistance R_{coat}, and interfacial resistance R_{int}) and constant phase elements (to represent imperfect capacitors due to coating capacitance CPE_{coat} and interfacial capacitance CPE_{int}) where the parameters obtained from the constant phase elements can be used to calculate the capacitance using the relationship $C = R^{([1-n]/n)} \times Q^{(1/n)}$, where R is the resistance parallel to the constant phase elements, Q is the pseudo capacitance and n is the phase change value obtained from fitting. The results of the fitting show that the coating resistances exhibit very similar values of 180 Ω for the SNAP/gel coating compared to 174 Ω for the SNAP alone after 1 hour of equilibration in salt solution. After 24 hours, a similar value of around 173 Ω was obtained for the SNAP/gel sample whereas the SNAP alone has shown a reduction to 156 Ω. This indicates that the presence of the gel particles offer an inhibition effect which improves the integrity of the SNAP coating. The inhibition effect is related to the chemical structure (containing heteroatoms S and N) and physico-chemical properties of the PIL gel particle inhibitor arising from their heterocyclic functional group. The use of organic inhibitors containing O, S and N has been shown to reduce corrosion on steel.[20] Such inhibitors form compact barrier films through the transfer of electrons from the available lone pair of electron in the inhibitor to the metal surface. The strength of such an interaction depends on the electron density of the donor atom in the functional group of the inhibitor and the polarizability of this group.

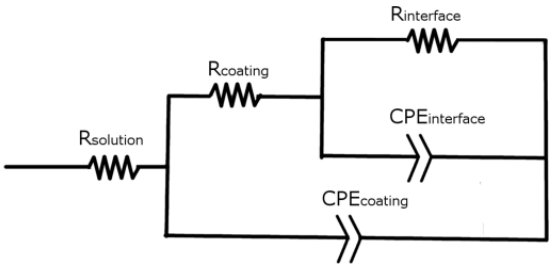


Figure 4.3 The equivalent circuit for semi-permeable coating used to model the electrochemical impedance result of SNAP-coated samples

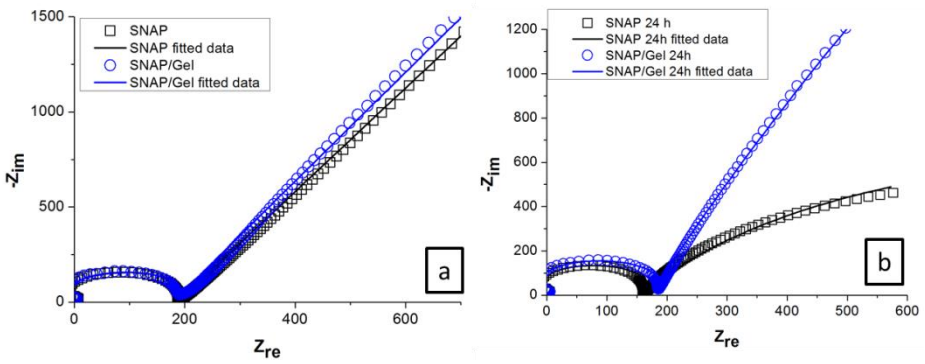


Figure 4.4 Nyquist plot and EIS modelling result for the SNAP and SNAP/Gel samples (a) before and (b) after 24h immersion in salt solution.

Table 4.2 Parameters obtained from modelling of impedance results

Sample	R_s (Ω)	R_{coat} (Ω)	R_{int} (Ω)	C_{coat} (F)	C_{int} (F)
SNAP	7	180	578320	6.71×10^{-9}	5.317×10^{-4}
SNAP 24h	8	156	1305	7.98×10^{-9}	2.01×10^{-3}
SNAP/Gel	6	174	421420	6.65×10^{-9}	6.64×10^{-6}
SNAP/Gel 24h	7	173	35387	7.21×10^{-9}	5.32×10^{-6}

In the SNAP sample, the initial coating has a very high interfacial resistance which degraded significantly after 24 hours from 578 kΩ to 1.3 kΩ (Table 4.2). This reduction of interfacial resistance was accompanied by an increase in the interfacial capacitance from 0.5 µF to 2 µF, indicating corrosion on the SNAP-metal interface and potential delamination or blister formation. Meanwhile, the coating resistance and capacitance remains quite similar, and thus the degradation on the interface indicates that the SNAP coating, being an interfacial layer rather than a barrier layer, was still permeable to electrolytes, which allows corrosion to occur at the SNAP-metal interface.

The SNAP/gel sample showed similar initial values to the SNAP sample, with a similar coating resistance and capacitance as well as similar interfacial resistance. After 24 hours it also showed relatively unchanged coating resistance and capacitance values, indicating the integrity of the bulk coating. However, a clear difference can be seen between the SNAP/gel sample and the SNAP, with the SNAP/gel sample showing a

marginal change in interfacial capacitance values despite the reduction in the interfacial resistance. Moreover, the SNAP/gel sample showed the highest interfacial resistance value at 35 kΩ, which is significantly higher than the SNAP sample. The interfacial capacitance of the SNAP/gel sample also remained relatively unchanged at around 5 μF, which indicates that the SNAP/gel sample resists delamination better than the SNAP alone.

Furthermore, the parameters obtained from EIS modelling can also be used together with the previously obtained E_{corr} values (Table 4.1) to calculate the porosity (P) of the SNAP and SNAP/gel from the following equation;[21]

$$P = \frac{R_{ps}}{R_p} \times 10^{-\left|\frac{\Delta Ecorr}{\beta}\right|} \times 100 \qquad \text{Eq.1}$$

where Rp and R_{ps} are the polarization resistances of the coating (Table 4.2) and the uncoated steel, respectively, and β is the anodic Tafel slope determined from the linear part of the anodic polarization curve (Figure 4.1). The experimentally determined polarization resistances of uncoated steel SNAP and SNAP/gel coated samples are 9.57×10^{-2}, 180 and 174 Ω, respectively (Table 4.2). Thus, the porosity values of the SNAP and SNAP/gel coatings determined using the above equation are 0.5% and 5.5×10^{-4} %, respectively.

The porosity calculations show that the SNAP/gel coating is intact and almost free from electrochemically active sites in comparison with the SNAP alone. As an inorganic primer intended for use as an interfacial layer, this result is not unexpected as this type of hydrophilic sol-gel coating would not be fully dense and thus would be permeable to water and salt, as demonstrated in the porosity calculation.[22] This is consistent with our previous observation on the I_{corr} of these coatings, where the SNAP/gel coating showed a lower I_{corr} indicative of improved barrier properties and retained its mechanical integrity over 24 hours of immersion in the salt solution; whereas the SNAP coating alone showed good barrier properties initially, but this degrades over time due to electrolyte permeation.

4.4.2 Microscopy Analysis

The morphology of the coating was also investigated by scanning electron microscopy. Figure 4.5 shows the SEM micrographs of the blank metal, SNAP and SNAP/gel surfaces before and after immersion in 3.5 wt% salt solution. As can be seen, the surface morphology of the metal showed significant damage in the absence of any coating, with increased roughness and features indicative of corrosion. In the SNAP and SNAP/gel coated samples the damage was considerably diminished, which demonstrates the protective effect of the coating. However, the SNAP/gel coated sample after immersion in the salt solution showed a more defect-free morphology after immersion compared with the unmodified SNAP. The unmodified SNAP showed signs of roughening on its surface, with the presence of some pits and cracks showing deterioration of the coating morphology. However, the SNAP/gel sample did not show such significant roughening of the surface, which indicates that the SNAP/gel coating is more rigid and tougher than the unmodified SNAP due to the presence of the PIL gel particles. In addition, when the PIL gel particles were added into the SNAP coating (Figure 4.5c), spherical uniform clusters were observed on the surface at higher magnifications. As the PIL gel particles were prepared by mechanical grinding in liquid nitrogen, it is evident that these spherical formations are not the PIL gel particles themselves. Rather, they are likely silica particles formed during the ultrasonication of the SNAP solution, as the SNAP solution contains a surfactant and thus during ultrasonication it is possible that some of the SNAP particles prematurely form these spherical particles. However, EDS analysis of these particles show high content of Si (Figure 4.6c), which indicates that these silicon particles attached to the coating surface and not embedded within the coating itself, and thus are unlikely to play a major role in the corrosion inhibition performance of the coating.

The elemental analysis obtained from EDS indicated that the blank metal before salt solution test is mainly composed of Fe, as is expected for carbon steel (Figure 4.6a), while after immersion in the salt solution a relatively high concentration of oxygen was detected as a result of formed oxyhydroxides from iron in salt solution (Figure 4.6b).

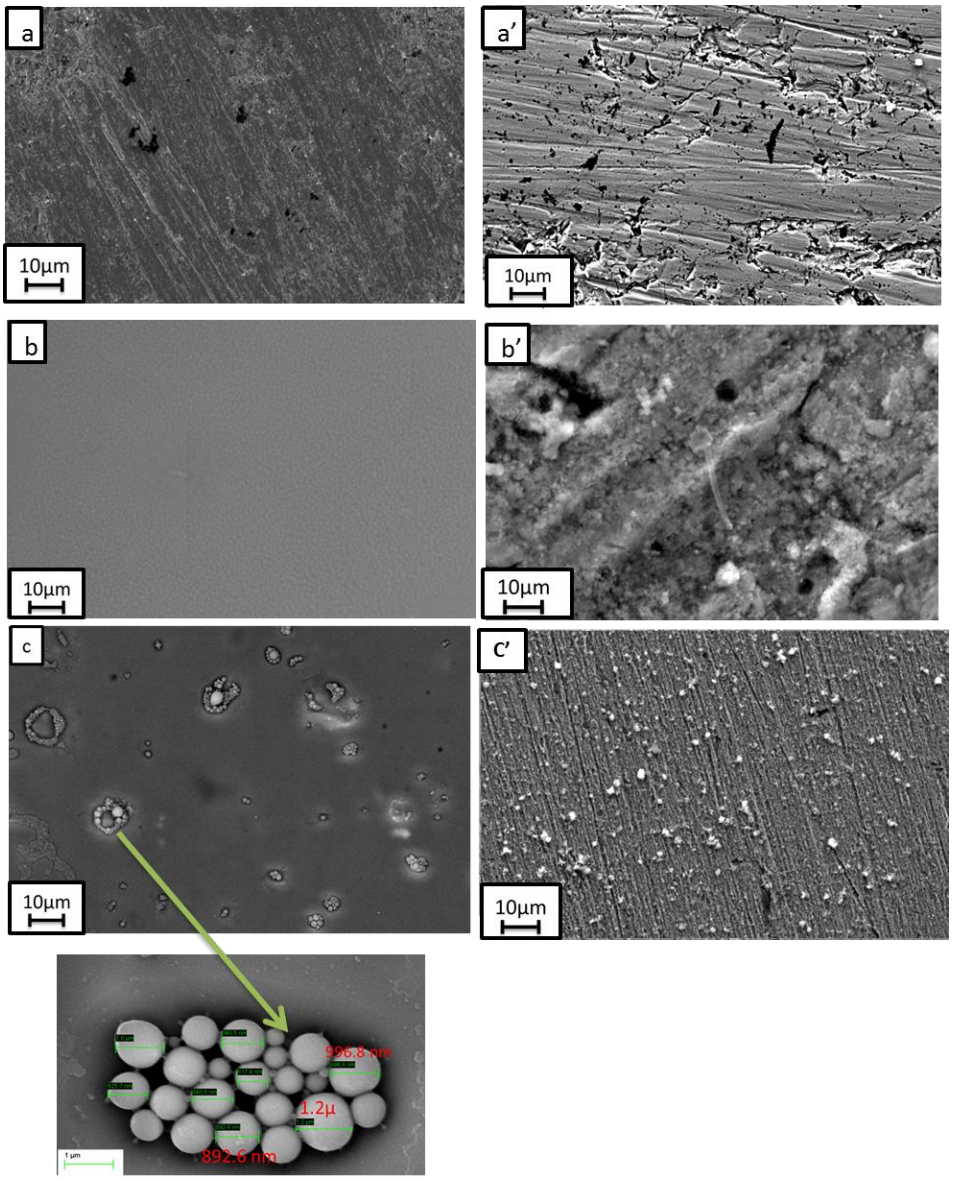


Figure 4.5 SEM image of (a) and (a') blank metal, (b) and (b') SNAP and (c) and (c') SNAP/gel before and after immersion in 3.5 wt% salt solution

In contrast, a considerable reduction in the content of silicon and oxygen was detected on the SNAP/gel after immersion in the salt solution (Figure 4.6d), despite the increase in Fe detected. Since the SNAP coating itself contains oxygen atoms in its chemical bonds, this increase in Fe accompanied by reduction in Si, C, and O indicates the presence of Fe ions adsorbed on the surface masking the detectable elements of the SNAP coating itself. However, unlike in the blank metal, these ions are unlikely to be in the form of oxides or hydroxides as per the blank metal (as there was a reduction in oxygen) and thus it is most likely due to Fe ions adsorbed or complexed on the SNAP

surface. This indicated that the SNAP/gel coating may inhibit the formation of corrosion products, such as oxides, through scavenging of the metal ions produced during corrosion.

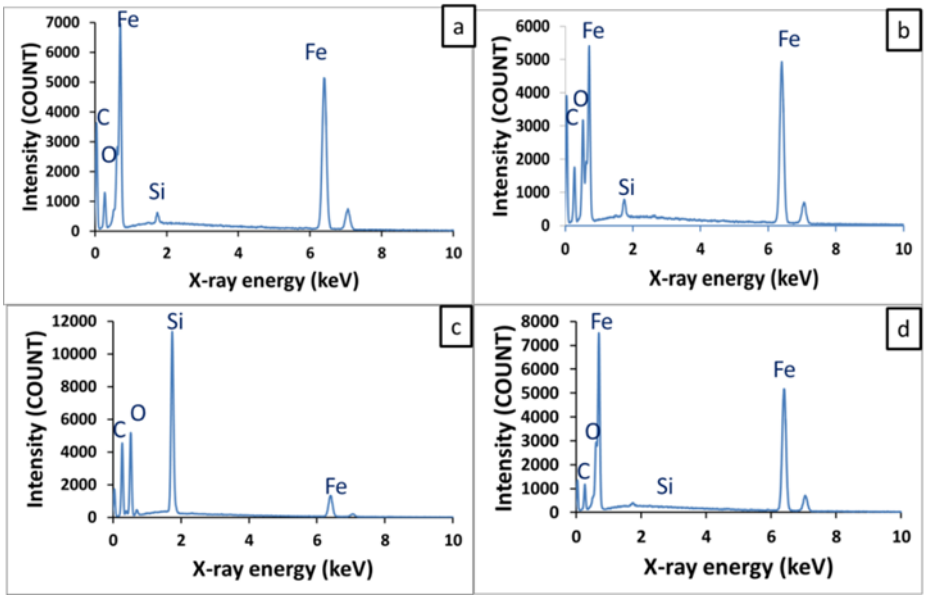


Figure 4.6 EDS analysis of (a), (b) blank metal and (c), (d) SNAP/gel before and after 24 h in salt solution, respectively.

4.4.3 SKP measurements

SKP measurements were carried out to establish a further understanding of the interfacial properties of the coatings. SKP is a non-destructive, non-contact mode technique based on a vibrating capacitor, which is used to evaluate the adhesion and corrosion protection properties of the coatings by measuring the surface work function distribution on the sample surface. Surface work function is an extremely sensitive indicator of the surface condition and can be used to track changes in the surface, such as surface contamination and corrosive adhesion of polymers on metal substrates.[23-24] The SKP maps of the blank metal, SNAP and SNAP/gel coated samples are shown in Figure 4.7. The average work function (WF) and absolute WF values of these samples before and after immersing in salt solution for 24 hours are given in Table 4.3. The absolute WF was calculated using equation 4.2, where the WF of the tip is 5.05 eV (determined via calibration with a reference gold surface) and the CPD is the contact potential difference between the samples and the tip measured experimentally using SKP.

WF of sample = WF of Tip + CPD Eq.2

Table 4.3 Absolute WF values and measured CPD for blank, SNAP and SNAP/gel coated samples before and after immersing in salt solution determined using SKP

Samples	Average CPD (meV) Before salt test	Absolute WF(eV)	Average CPD (meV) After salt test	Absolute WF(eV)
Blank metal	-250 ± 13	4.80	36 ± 20	5.08
SNAP	-97 ± 7	4.95	-355 ± 20	4.70
SNAP/gel	-84 ± 7	4.96	-157 ± 20	4.90

The absolute WF values of the samples shifted towards more noble potential values in the order of blank metal < SNAP < SNAP/gel samples before immersion in the salt solution for 24 hours, which was consistent with our electrochemistry data. After 24 hours immersion in salt solutions, the blank metal showed significant changes to positive values; however, this is due to the formation of an oxide layer on the metal (as WF is a measure of the energy required to remove electrons from the surface, metal oxides generally show higher WF than pure metals), which is not comparable with the coated samples. SNAP/gel showed higher WF values in comparison to the unmodified SNAP, which can be correlated with the interfacial interaction between the inhibitor molecule and the metal. Also, the WF of the SNAP after 24 hours significantly decreased to a lower value compare with the before salt solution test, which could be correlated to the weaker interaction of the coating with the metal and some sort of degradation of the coating. Although the WF values for SNAP/gel slightly decreased to lower values, this change was very small compared with the SNAP alone. Furthermore, the work function map of the surface showed large variations in unmodified SNAP after 24 hours, which further indicates that corrosion has resulted in inhomogeneity in the coating and possibly a degree of delamination of the interface. This shows that the SNAP/gel coating exhibits stronger interactions with the substrate compared to the

unmodified SNAP. Based on these experimental results, it can be concluded that the primary protection provided by the SNAP/gel coating is through both the interfacial adhesion and improvement of the barrier characteristics.

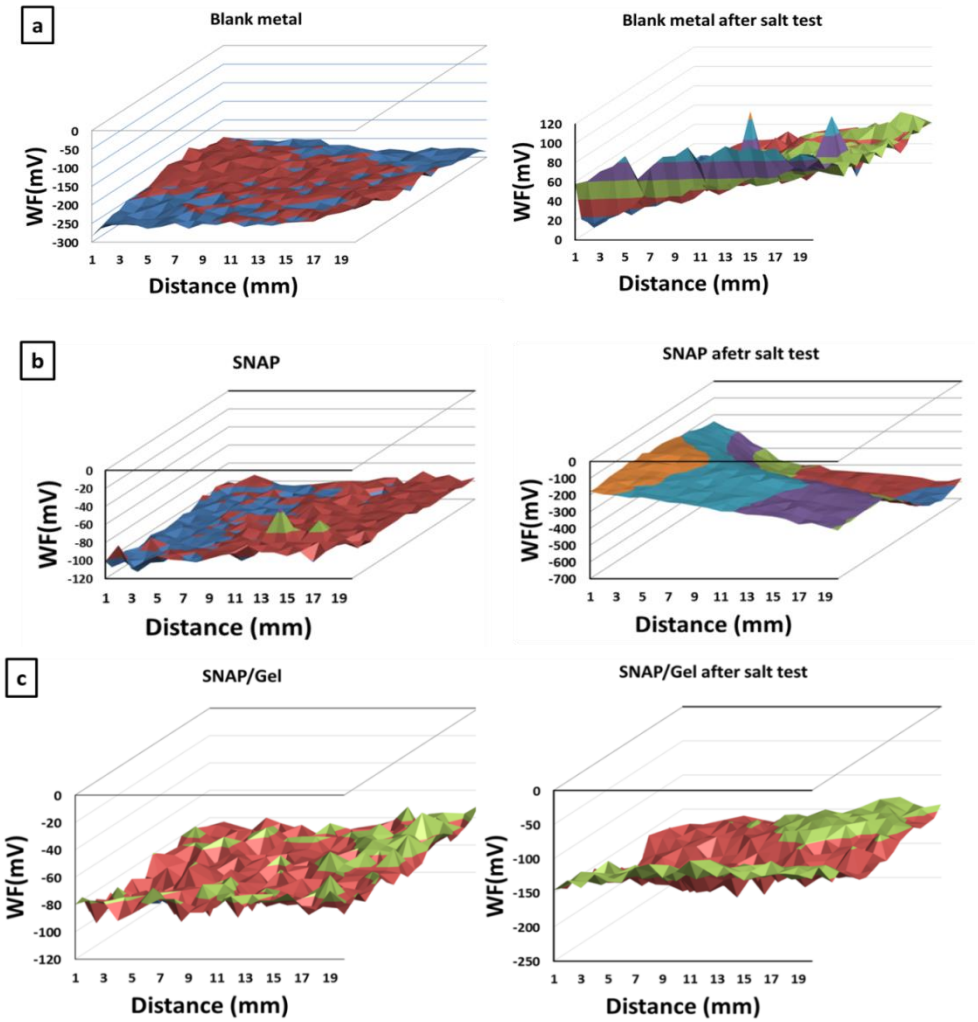


Figure 4.7 SKP maps of (a) blank metal, (b) SNAP and (c) SNAP/gel coated samples before and after salt solution test.

The absolute WF measured using SKP can be correlated to the corrosion potential using the equation 4.3:[25]

$$Vp = E_{corr} + \text{constant} \qquad \text{Eq.3}$$

In order to determine the constant, the absolute WF values are plotted against E_{corr} obtained from potentiodynamic measurements of blank, SNAP and SNAP/PIL gel and the plot is shown in Figure 4.8.

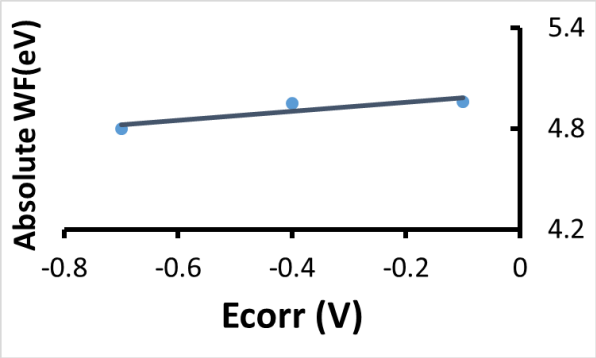


Figure 4.8 Correlation plot between corrosion potential determined from electrochemical methods and the absolute WF obtained from SKP measurements.

The plot shows a linear correlation between the absolute WF and the E_{corr} where the intercept of the plot determined as 5.01 eV. This value indicates the constant in the equation. Using this equation, corrosion potential of a metal could be determined indirectly and without being in contact with the electrolyte.

4.5 Conclusion

The polymerizable ionic liquid (PIL) containing the imidazolium group in the form of a gel showed corrosion inhibition properties for protection of carbon steel when incorporated into the SNAP coating, as confirmed by potentiodynamic polarization and electrochemical impedance spectroscopy (EIS) measurements. The inhibition mechanism of PIL was attributed to the strong adsorption ability of this inhibitor to form a protective layer that isolates the mild steel surface from an aggressive environment. Indeed, the presence of S and N in the structure of the PIL provides a free electron pair that promoted the chemical adsorption on the metallic surface and protects the metal from corrosion. Furthermore, the surface work function distributions on the sample surface were measured using Scanning Kelvin Probe (SKP), which showed stronger surface interactions of the SNAP loaded with PIL gel particles compared to SNAP alone.

4.6 References

1. Tüken, T.; Demir, F.; Kıcır, N.; Sığırcık, G.; Erbil, M. *Corros. Sci.* **2012,** *59*, 110-118.
2. Likhanova, N. V.; Domínguez-Aguilar, M. A.; Olivares-Xometl, O.; Nava-Entzana, N.; Arce, E.; Dorantes, H. *Corros. Sci.* **2010,** *52* (6), 2088-2097.
3. Zhou, X.; Yang, H.; Wang, F. *Electrochimica Acta* **2011,** *56* (11), 4268-4275.
4. Ashassi-Sorkhabi, H.; Es'haghi, M. *Mater. Chem. Phys.* **2009,** *114* (1), 267-271.
5. Zhang, Q. B.; Hua, Y. X. *Electrochimica Acta* **2009,** *54* (6), 1881-1887.
6. Chuang, M.-H.; Chang, J.-K.; Tsai, P.-J.; Tsai, W.-T.; Deng, M.-J.; Sun, I. W. *Surf. Coat. Technol.* **2010,** *205* (1), 200-204.
7. A. M. Atta; H. A. Al-Lohedan; A. O. Ezzat. *Int. J. Electrochem. Sci.* **2015,** *10*, 5812.
8. Lin, P.-C.; Sun, I. W.; Chang, J.-K.; Su, C.-J.; Lin, J.-C. *Corros. Sci.* **2011,** *53* (12), 4318-4323.
9. Taghavikish, M.; Subianto, S.; Dutta, N. K.; de Campo, L.; Mata, J. P.; Rehm, C.; Choudhury, N. R. *ACS Omega* **2016,** *1* (1), 29-40.
10. Taghavikish, M.; Subianto, S.; Dutta, N. K.; Choudhury, N. R. *ACS Appl. Mater. Interfaces* **2015,** *7* (31), 17298-17306.
11. Figueira, R. B.; Silva, C. J. R.; Pereira, E. V. *J Coat Technol Res* **2014,** *12* (1), 1-35.
12. Donley, M. S.; Mantz, R. A.; Khramov, A. N.; Balbyshev, V. N.; Kasten, L. S.; Gaspar, D. J. *Prog. Org. Coat.* **2003,** *47* (3-4), 401-415.
13. Lvov, Y.; Wang, W.; Zhang, L.; Fakhrullin, R. *Adv. Mater.* **2016,** *28* (6), 1227-1250.
14. Riza Erdogan, A.; Kaygusuz, I.; Kaynak, C. *Polym. Compos.* **2014,** *35* (7), 1350-1361.
15. Lvov, Y. M.; Shchukin, D. G.; Möhwald, H.; Price, R. R. *ACS Nano* **2008,** *2* (5), 814-820.
16. Guzmán-Lucero, D.; Olivares-Xometl, O.; Martínez-Palou, R.; Likhanova, N. V.; Domínguez-Aguilar, M. A.; Garibay-Febles, V. *Ind. Eng. Chem. Res.* **2011,** *50* (12), 7129-7140.
17. Xu, A.; Zhang, F. Z.; Jin, F.; Zhang, R.; Luo, B.; Zhang, T. *Int. J. Electrochem. Sci.* **2014,** *9*, 5116 - 5125.

18. Huang, P.; Latham, J.-A.; MacFarlane, D. R.; Howlett, P. C.; Forsyth, M. *Electrochimica Acta* **2013,** *110* (0), 501-510.
19. Pepe, A.; Galliano, P.; Aparicio, M.; Durán, A.; Ceré, S. *Surf. Coat. Technol.* **2006,** *200* (11), 3486-3491.
20. Sastri, V. S. Adsorption in Corrosion Inhibition. In *Green Corrosion Inhibitors*, John Wiley & Sons, Inc.: 2011; pp 103-138.
21. Creus, J.; Mazille, H.; Idrissi, H. *Surf. Coat. Technol.* **2000,** *130* (2-3), 224-232.
22. Asadi, N.; Naderi, R.; Saremi, M.; Arman, S. Y.; Fedel, M.; Deflorian, F. *J Sol-Gel Sci Technol* **2014,** *70* (3), 329-338.
23. Nazarov, A.; Thierry, D. *Electrochimica Acta* **2007,** *52* (27), 7689-7696.
24. Choudhury, N. R.; Kannan, A. G.; Dutta, N. K.; Klaus, F.; Alois, K. Novel nanocomposites and hybrids for lubricating coating applications. Elsevier, 2008.
25. Stratmann, M. *Corros. Sci.* **1987,** *27* (8), 869-872.

Chapter 5: Polymeric ionic liquid nanoparticle emulsion as corrosion inhibitor in anticorrosion coating

This chapter of the thesis is presented part of a research manuscript “Taghavikish, M.; Subianto, S.; Dutta, N. K.; de Campo, L.; Mata, J. P.; Rehm, C.; Choudhury, N. R. ACS Omega 2016, 1 (1), 29-40. Polymeric ionic liquid nanoparticle emulsion as corrosion inhibitor in anticorrosion coating”, published and reproduced by permission of the American Chemical Society, Copyright 2016.

5.1 Abstract

In this chapter, we report the facile preparation of cross-linked polymerized ionic liquid (PILs) based nanoparticles via thiol-ene photo-polymerization in miniemulsion. The synthesised PIL nanoparticles with a diameter of about 200 nm are fully characterized for chemical structure, morphology and properties using different techniques such as Fourier transform infrared spectroscopy (FTIR), Thermogravimetric analysis (TGA), Scanning Electron Microscopy (SEM) and Transmission Electron Microscopy (TEM). Furthermore, PIL nanoparticle emulsion is utilised as inhibitor into the self-assembled nanophase particle (SNAP) coating. The corrosion protection performance of the resultant coating was examined using potentiodynamic polarization experiment and electrochemical impedance spectroscopy (EIS). Results show the PIL nanoparticle emulsion in the SNAP coating acts as inhibitor and is promising for fabricating advanced coatings with improved barrier and corrosion protection.

KEYWORDS: Polymerized ionic liquid, thiol-ene chemistry, miniemulsion, nanoparticles, corrosion protection.

5.2 Introduction

Recently, polymerized ionic liquid (PIL) based nanoparticles have received significant interest as a new class of functional polymer that combines both the properties of ionic liquids (ILs) with polyelectrolyte characteristics and improved mechanical durability and dimensional control. Polymer nanoparticles have been conveniently prepared either from preformed polymers, by methods including precipitation, solvent evaporation, dialysis, and supercritical fluid expansion, or by direct polymerization of monomers using classical polymerization, including micro-emulsion, mini-emulsion, surfactant-free emulsion and interfacial polymerization.[1] The preparation of PILs as nanoparticles via suspension polymerization,[2] water-in-oil concentrated emulsion polymerization,[3] and precipitation polymerization in water without stabilizers using ionic liquid monomers with long alkyl chains has been recently reported.[4-5] Due to the dense charge and the ionic liquid functionality, the PIL nanoparticles have an important role in the practical design of various functional materials, such as catalyst support, binders, coatings, and sensors.[6] One of the examples of this type of applications is the work by Yang et al. [7] which reported the preparation of crosslinked PIL microspheres with a

diameter of about 200 nm synthesized via miniemulsion polymerization for application as potential scaffolds to immobilize metal nanoparticles for electrocatalysis and heterogeneous catalysis.

Miniemulsion, with droplet sizes typically in the range of 20-200 nm, is one of the most common methods used for the fabrication of polymer nanoparticles in the water-borne system. The use of water as the dispersion medium is one of the main advantages of this system, which makes it environmentally friendly and also allows excellent heat dissipation during the polymerization process.[8]

Recently, "click" polyaddition reactions in miniemulsions, specifically thiol-mediated chemistry (i.e. thiol-ene/yne, thiol-Michael), have attracted attention as one of the facile methods for the synthesis of polymer microparticles, nanoparticles, and nanocapsules dispersion in heterophase media with high efficiency.[9-11] The earliest example of using thiol-ene reaction in miniemulsion system was reported by Berkel et al.[12] This involved thiol-ene chemistry for facile surface functionalization of composite nanoparticles dispersed in a wide variety of solvents. On the other hand, a recent example of incorporation of thiol-ene chemistry into a water-borne system by Shipp and co-workers reported water-borne thiol-ene photo-polymerization that yields dispersions of polymer particles.[13] In another work by the same group, the effect of surfactant on the particle size and stability was investigated where they found that during water-borne thiol-ene photo-polymerization the use of emulsifying agents is crucial to prevent particle aggregation.[14] Similarly, Amato et al. reported the synthesis of small, sub-100 nm crosslinked poly thioether nanoparticles using miniemulsion thiol-ene photo-polymerization. The authors studied the effect of miniemulsion formulation including inhibitor, surfactant concentration and monomer weight fraction and process parameters such as ultrasonication time and amplitude on nanoparticle size.[8]

Considering the synergistic properties of PILs and thiol-ene photo-polymerization, combining the two certainly broadens their application potentials.[15] The relatively few examples of the combination of thiol-mediated polyadditions in dispersed systems with polymerizable ionic liquids (PIL) offer a significant opportunity to exploit thiol-mediated polyadditions in miniemulsions using PIL for the fabrication of crosslinked, functional polymer nanoparticles. In chapter 3, we have reported the facile preparation of polymerizable ionic liquid based gel beads using thiol-ene click chemistry and

illustrated their unique properties as multipurpose materials suitable for pH sensing or anti-corrosion applications.[16]

Since ILs are known to inhibit corrosion in metals, the PIL emulsion system is expected to exhibit corrosion inhibition properties when incorporated into inorganic sol-gel coatings such as self-assembled nanophase particle (SNAP) coating. Unlike free IL, they would be immobilised within the coating, and thus should provide a better protection against leaching of the free IL from the SNAP coating, which has shown good anti-corrosion properties on materials such as aluminium alloys.[17] However, its potential for metals has not been fully explored with respect to low carbon steel. Unlike polymer-based paints, inorganic coatings are prone to crack formation and hence become more permeable, but their ability to bond with surface oxides and hydroxides makes them promising materials for use as interfacial layers.

In this chapter, we demonstrate the fabrication of crosslinked PIL based nanoparticle via thiol-ene photo-polymerization in miniemulsion. Combining the functionalities of thiol-ene and PIL in water based system; we demonstrate the application of these nanoparticles in anti-corrosion coatings. This is the first report on the application of PIL based nanoparticles in anticorrosion coatings, where particles have been characterised for their size, shape, electrochemical performance etc using neutron scattering, microscopy and electrochemical techniques.

5.3 Experimental

5.3.1 Materials

Pentaerythritol tetrakis(3-mercaptopropionate) (PETKMP), 1-vinylimidazole, 1,4-dibromobutane, benzophenone (BP), Triton™ X-100 , Azobisisobutyronitrile (AIBN), sodium dodecyl sulfate (SDS), (3-Amino propyl)triethoxysilane, Sorbitan monostearate, Toluene, acetone, hexane diethyl ether and methanol (analytical grade) were obtained from Sigma-Aldrich and used without further purification. Fluorosurfactant FC-4432 was obtained from 3M. Double distilled water (DDW) was used for all experiments.

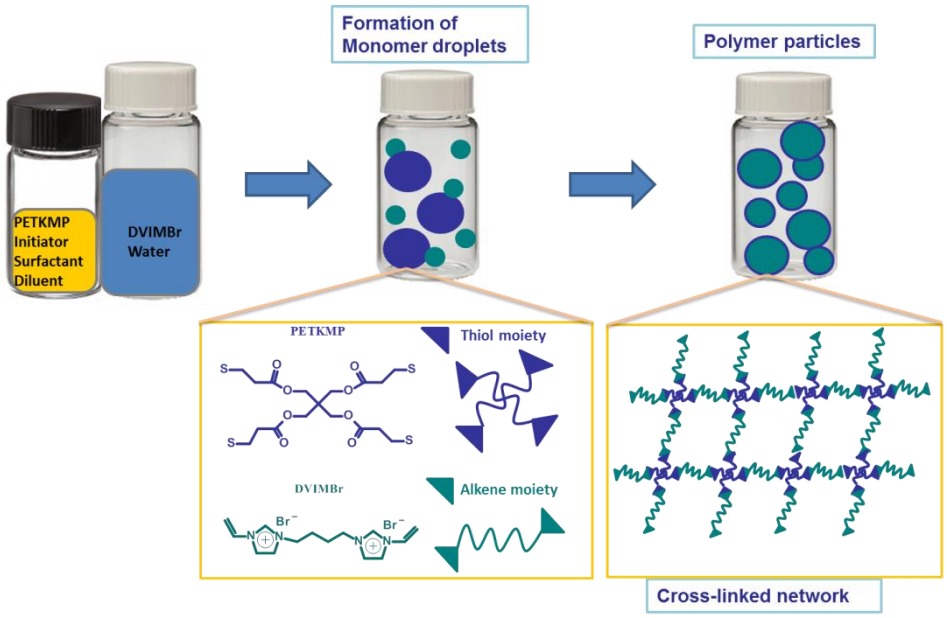
5.3.2 Synthesis of 1,4-Di(vinyl imidazolium)butane Bisbromide

1,4-di(vinyl imidazolium)butane bisbromide (DVIMBr) was synthesized by stirring a mixture of 2:1 molar ratio of 1-vinylimidazole to 1,4-dibromobutane in methanol at 60 °C for 15 h. Upon cooling, the reaction mixture was poured dropwise into 1 L of diethyl ether. The white precipitate was filtered off and dried at room temperature until constant weight with a yield of 68%.[4]

^{1}H NMR (300MHz, D_2O, δ, ppm): 8.98 (2H), 7.69 (2H), 7.49 (2H), 7.04 (2H), 5.75 (2H), 5.33 (2H), 4.21 (4H), 1.87 (4H).

5.3.3 Miniemulsion thiol-ene photopolymerization

A typical miniemulsion photo-polymerization reaction for the synthesis of PIL nanoparticle involves the mixing of two separate phases, an organic phase and an aqueous phase. The organic phase consists of 0.24g PETKMP dissolved in 0.1 ml toluene and mixed with 0.1g triton surfactant (2.5 wt% with respect to monomer) and 18.2 mg benzophenone (BP) photoinitiator (5 wt% with respect to monomers concentration). Separately, an aqueous phase was prepared by dissolving 0.4g of DVIMBr in 9 ml double distilled water. The organic phase was added to the aqueous solution drop-wise using the syringe needle and the reaction mixture was stirred for approximately 5-10 minutes and then ultrasonicated in an ice bath for 10 minutes with an amplitude of 50% to emulsify the organic phase in the aqueous phase and to create nanodroplets. Finally, photo-polymerization was performed in the presence of ultraviolet light (365 nm wavelength) inside a black box for another 1hr with continuous stirring, resulting in cross-linked polymer nanospheres and a stable emulsion (Scheme 5.1). Before and after photopolymerization the solution was degassed to remove any bubble.



Scheme 5.1 General reaction scheme for development of water-borne thiol-ene polymer nanoparticles.

The emulsion solution was centrifuged at 5000 rpm for 30 minutes at room temperature. As a result, two fully separated phases formed: one phase containing unstable particles and unreacted monomers and the other phase with stable PIL particles was collected in the water phase (Figure 5.1). PIL nanoparticles were washed with methanol and toluene to remove any trace of impurities. The concentration of PIL nanoparticles before centrifugation was 35 mg/ml, which has been decreased to 23 mg/ml after removing all the unreacted monomers. Collecting PIL nanoparticles in water phase has an advantage for easier characterization.



Figure 5.1 Fabrication of PIL nanoparticles through thiol-ene photopolymerization

5.3.4 Preparation of the PIL nanoparticles based coating

The coatings have been prepared using the self-assembled nanophase particle (SNAP) as a matrix for coating and addition of different concentrations of the emulsion to improve the barrier and protective properties of SNAP coating. The SNAP coating was prepared by the method proposed by Donley et al.[17] The Mild Steel CA3SN-G, 0.08 % carbon contents, thickness~0.6 mm of 1.7 cm×1.7 cm substrates were cleaned using process which has been reported by our group.[18] The coating solutions with total volume of 20 ml were prepared by diluting the 7 ml SNAP solution with DDW by a factor of 1.75 with considering the amount of DDW. In order to find an optimized concentration of PIL nanoparticle emulsion, three different concentrations (0.4, 0.8 and 1.6 wt%) of emulsion were added the SNAP solution followed by addition of surfactant (3M FC-4432, 0.04 wt/ v%). Then the mixtures were ultrasonicated at 50% rpm for 5 min to obtain homogenous solutions. At the end (3-amino propyl)triethoxysilane crosslinking agent was added into the solutions and the final mixture was vigorously stirred and applied to cleaned metal substrates by dip coating at a withdrawal speed of 10 cm/min. The coated sample was dried at room temperature for 24 h to allow solvent evaporation. Finally, the coating was thermally cured at 80 °C, 60% humidity for overnight in humidity oven (ESPEC-model SH-241).

5.3.5 Characterization

^{1}H NMR analysis was performed on a 300 MHz Bruker Avance spectrometer at room temperature using deuterium oxide (D_2O) as the solvent. Infrared spectra of the gels were acquired using Nicolet Magna-IR Spectrometer 750 in photo-acoustic mode with 256 scans and a carbon black reference.

Quantitative analysis of particle size was done via Dynamic Light Scattering (DLS) using a Nano ZS Zetasizer (Malvern Instruments Ltd.) equipped with a 633 nm He-Ne laser to measure the hydrodynamic size distribution of PIL nanoparticles in aqueous solutions. The differential scanning calorimetry (DSC) measurement was conducted using TA Instruments Discovery DSC. The instrument was calibrated for baseline and cell constant prior to running the experiments. The samples were sealed in hermetic aluminium pans for use in the DSC experiment, and an empty pan was used as the reference. The temperature range for the experiment was from -70 °C to 200 °C, with a

heating rate of 10 °C/min and under controlled nitrogen gas flow of 50 ml/min. Thermogravimetric analysis was performed using a TA Instruments Discovery TGA with an aluminium pan. The samples were subjected to a 10 °C/min ramp rate from 100 °C to 550 °C under a nitrogen atmosphere. The size and morphology of the particles were analysed by optical microscopy (Prism optical microscope) and field emission scanning electron microscopy (FE-SEM) using Philips XL30 FEG instrument operated at an acceleration voltage of 15 kV. For electron microscopic analysis, the sample was placed on an Indium tin oxide (ITO) coated glass as a conducting surface and images were taken without any further coating. In addition, morphologies of the coatings surface were observed using SEM where composition were obtained by the energy dispersive spectroscopy (EDS) module (OXFORD instruments) attached to the microscope.

Also, JEOL 2100F Transmission Electron Microscopy (TEM) was used for size characterization; which was operated at 200 kV with a resolution ~2 Å. Utilizing a technique based on the Wilhelmy balance principle, advancing and receding contact angles were measured by Dynamic contact angle analyser at a constant velocity (100 µm/s) and 23 °C (42% relative humidity in a clean room). The advancing and receding contact angles were determined using the scanning Wilhelmy plate method for the SNAP, emulsion and SNAP/0.8 wt% emulsion (optimized concentration). The substrates used for these contact angle investigations were clean steel metal plates with 12.7 mm length and 0.12 mm thickness. The plates were cleaned with acetone, ethanol and dried with nitrogen flow before each experiment. The surface tension of the coatings was also measured by the Wilhelmy plate using a platinum plate with 19.9 mm lengths and 0.2 mm thickness. The advancing and receding contact angles were calculated from the scanning Wilhelmy plate result.

Electrochemical characterization of the uncoated and the coated samples was carried out using a standard corrosion cell (1 L, Pine Research Instrumentation) with conventional three electrode set-up in non-deaerated 3.5 wt% NaCl solution prepared from analytical grade chemicals (ChemSupply, Australia) and distilled water (Milli-Q). A saturated calomel electrode (SCE, Pine Research Instrumentation, +0.24 V vs. Normal Hydrogen Electrode, NHE) was employed as the reference electrode, a graphite rod of 2 mm diameter as a counter electrode and the sample under test as the working electrode. All reported potentials in this paper (determined using electrochemical techniques) are with

reference to the saturated calomel electrode (SCE). Initially, the open circuit potential (OCP) of the specimens was determined as a function of time and the samples were allowed to stabilize at their OCP for 1 hour before measurements. In this regard, all the measurements marked as 'initial' without time notation were done after a minimum of 1 hour stabilization time, and the measurements marked as 'sample-1h' were done 1 hour after the initial measurement (and thus after stabilization). Potentiodynamic polarization study was conducted at a scan rate of 1 mVs^{-1} in the potential range of ±300 mV relative to OCP. The Electrochemical Impedance Spectroscopy (EIS) measurements were performed using a Solartron 1260 impedance/gain-phase analyzer in combination with a Solartron 1280B electrochemical interface. The impedance measurements were carried out in a 1 MHz to 10 kHz frequency range with 40 steps per decade. All the spectra were recorded at open circuit potential with applied 10 mV sinusoidal perturbation. The impedance data was fitted using the Zview software and a model for permeable coating consisting of resistive elements (due to solution resitance R_s, coating resistance R_{coat}, and interfacial resistance R_{int}) and constant phase elements (to represent imperfect capacitors due to coating capacitance CPE_{coat} and interfacial capacitance CPE_{int}) where the parameters obtained from the constant phase elements are used to calculate the capacitance using the relationship $C = R^{([1-n]/n)} \times Q^{(1/n)}$ where R is the resistance parallel to the constant phase elements, Q is the pseudo capacitance and n is the phase change value obtained from fitting. The EIS data fitting and equivalent circuit modelling were done in the ZView software, and the model was fitted to the experimental data with a maximum allowable variation (error) of 5%.

5.4 Result and discussion

5.4.1 PIL nanoparticles by miniemulsion photo-polymerization

Polymerized ionic liquid (PILs) based nanoparticles were synthesized via thiol-ene photo-polymerization in miniemulsion. Thiol-ene miniemulsions were prepared using an organic phase of PETKMP, a photoinitiator, Triton, and solvent, which was then added to an aqueous phase consisting of water and DVIMBr. The precursors PETKMP to DVIMBr were chosen at a stoichiometric ratio. A water-immiscible solvent such as toluene was used to facilitate emulsification, and also for lowering the viscosity of the dispersed phase. The organic phase once mixed was then emulsified in the aqueous phase via ultrasonication to create PIL

nanoparticles (1:10 oil to water ratio). Centrifugation has been used as a means for isolation of PIL nanoparticles. The use of a centrifuge for separation of microcapsules was reported in the literature by Szabo et al.[19] The stability and size of polymer nanoparticles obtained from heterogeneous miniemulsion photo-polymerizations are strongly influenced by several process parameters, including surfactant structure and initiators. To examine this effect on the stability of the emulsion, effects of different surfactants and initiators have been studied. When the thermal initiator (AIBN) was replaced with BP, this resulted in colloidally unstable latexes and significant coagulum formation. However, the same system in the bulk form has been prepared using either thermal or photoinitiators polymerization and the behaviour of the synthesized polymer is similar.[16] Additionally, two reaction systems each with different surfactant were examined in order to obtain the most stable emulsion. In one system anionic surfactant SDS was used in the water phase and in another system non-ionic surfactant sorbitan was replaced with triton. In the presence of an anionic surfactant, we observed a phase separation and the settling of the PIL nanoparticles to the bottom of the aqueous phase. When the attractive forces between surfactant molecule and particles are dominant, the particles will adhere; however if the repulsive forces are stronger then the particles will remain suspended separately.[20] In this system, the attractive van der Waals interactions between Br^- group in PIL and Na^+ in SDS lead to the phase separation.[21] Whereas using a non-ionic surfactant like sorbitan, the surfactant layer provides steric stabilization to keep the nanoparticles from aggregating. However, weak adsorption of surfactant on particles (in the case of sorbitan) resulted in the coalescence of emulsion droplets after couple of hours.

In the case of using triton, long term stability of emulsion system can be achieved due to the fact that nonionic surfactants (such as triton X-100) do not ionize in an aqueous solution because their hydrophilic groups are nondissociable.[22] Therefore, there will be no ions to interact with Br^- in IL and destabilize the system. Thus, Triton was chosen for the rest of the studies presented here.

5.4.2 Structure and morphology study of PIL nanoparticles

To investigate the chemical composition of the emulsion and characteristics of each layer after centrifugation, FTIR analysis of the sample before and after centrifugation was performed and the spectra are presented in Figure 5.2. As discussed earlier, after centrifugation, the solution was separated into two layers. As can be seen in Figure 5.1, before centrifugation the emulsion is a white, milky colour which after centrifugation separates into a clear stable top layer and an unstable white bottom layer. In the stable top layer, FTIR spectrum does not show any band due to sulphur-hydrogen stretching around 2570 cm^{-1}, along with an absence of the C=C vinyl peak at 1644 cm^{-1}. This observation confirms that the thiol and vinyl groups have fully reacted in this layer. Furthermore, further comparison of the spectrum of the unstable layer with PETKMP also confirms that bottom layer contains unreacted thiol groups. However, in both layers, there was a reduction in the intensity of the peaks due to vinyl groups at 3080 cm^{-1} and around 761-768, 914-998 cm^{-1} regions (in comparison with the DVIMBr spectra), which confirms the consumption of vinyl groups in both layers. Since it appears that the main difference between the two layers is unreacted thiol groups, these results suggest that fully cured, stoichiometric particles are well dispersed and stable in the stable layer (unaffected by centrifugation) due to the hydrophilicity of the PIL, whereas any unreacted reagents and those with non-stoichiometric (less than 1:2 DVIMBr:PETKMP) composition formed unstable aggregates that settle into the bottom layer after centrifugation due to the more hydrophobic nature of the thiol component (PETKMP).

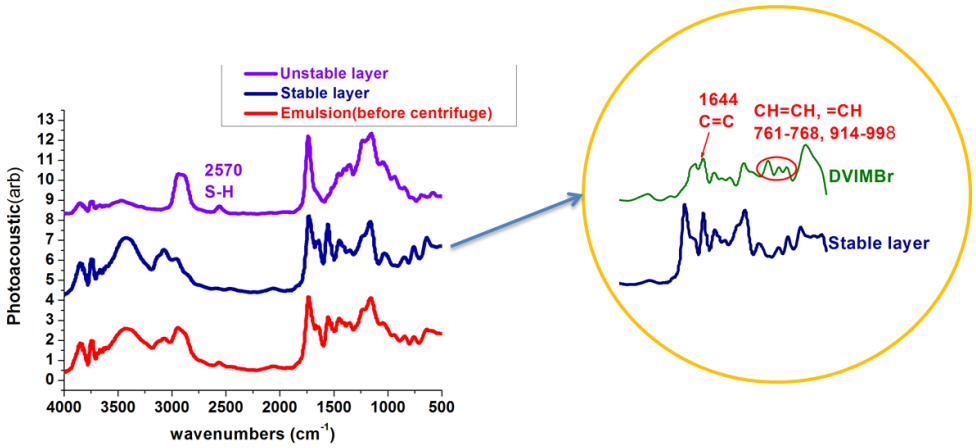


Figure 5.2 FTIR spectra of Emulsion before and after centrifugation and comparison of spectra of stable layer with DVIMBr.

Analysis of the PIL particle size was performed using an optical microscope, SEM and dynamic Light Scattering (DLS) (Figure 5.3). For optical microscopy, samples were prepared by air-drying or drying in a vacuum oven on glass slides, while for SEM due to the need for a conductive substrate for improved resolution the emulsion was dried on ITO glass. DLS results of the particle dispersion in water showed hydrodynamic particles size (diameter) around 200 nm, which is in a very good agreement with SEM results (Figure 5.3c); however, the optical images of dried samples show fairly larger particle size around 20 µm (Figure 5.3b). This is attributed to the difference in the substrates used for optical and SEM microscopy, in that by drying the sample for optical image some of these particles are aggregating and becoming larger as illustrated in Figure 5.3b. Interestingly, although the same aggregation phenomenon is seen to happen in some part of the ITO glass (as seen in SEM images), this is significantly reduced. This may be due to comparative rough nature of ITO surface 'trapping' some of the individual emulsion particles and, thus preventing them from coalescing to form larger aggregates as the solvent dries.

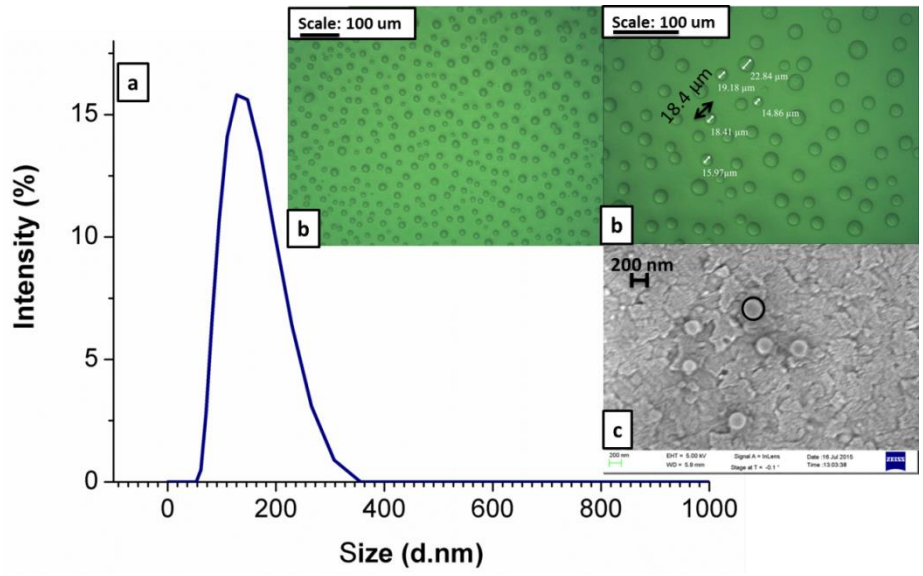


Figure 5.3 (a) Size distribution of PIL nanoparticles in dilute solutions as determined by DLS, (b) microscopy images of dried PIL nanoparticles on glass slides, (c) SEM image of dried PIL nanoparticles on ITO coated the glass.

Considering the significant role that the surfactants play in particle size and stabilization, we investigated the effect of surfactant concentration on particle formation. In this investigation, emulsions were made with varying triton surfactant concentrations of 0.2, 0.4, and 0.8 wt%. DLS and TEM were used to compare the results of this study, and the results are shown in Figure 5.4. As can be seen from the TEM images, at the lowest surfactant concentration (Figure 5.4a), the particles are small and spherical but there appears to be a greater variation in particle size. DLS analysis also indicates a dual distribution centred at around 150 and 700 nm, which indicates aggregation of the particles in solution due to low surfactant concentration. The larger particles were not observed in the TEM images. Increasing the surfactant concentration to 0.4 wt% (Figure 5.4b) results in particles that are similar in size but with a narrower distribution. DLS analyses of the particles show a single distribution with a particle size of around 200 nm, which corresponds well with the microscopy results. Further increasing the surfactant concentration to 0.8 wt% resulted in much broader particle size distributions and larger particles (as observed in TEM images, Figure 5.4c), which may be due to excess surfactant material affecting particle formation. This is because an excess of surfactant may lead to an attraction between multiple particles in solution, causing the polymer particles to undergo destabilization and aggregation. Thus, the

surfactant concentration of 0.4 wt% was considered to be optimum and used for all the investigation.

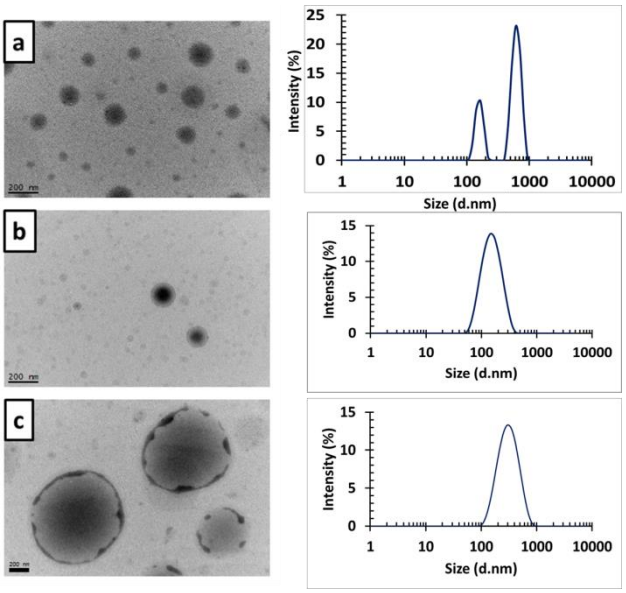


Figure 5.4 Size distribution and TEM image of PIL nanoparticles using (a) 0.2 wt % (b) 0.4 wt % and (c) 0.8 wt % surfactant.

5.4.3 Phase behaviour of PIL nanoparticles

In order to investigate phase behaviour and glass transition temperature of the PIL nanoparticle emulsion, different thermal techniques have been employed. Differential scanning calorimetry (DSC) analysis of dried nanoparticle emulsion sample revealed a glass transition temperature (Tg) at −53 °C for the PIL nanoparticles obtained using miniemulsion method (Figure 5.5a), while in our previous study the bulk PIL gel obtained using a solvent evaporation method showed a Tg of -23 °C (Figure 5.5b),[16] indicating that the composition and network structure of the polymer produced in the water-borne system was more elastic than that obtained using the more traditional solvent evaporation system. The DSC results also show that the glass to rubber transition occurs over a relatively narrow temperature range indicating a homogeneous network structure, which is typical of thiol-ene polymers.

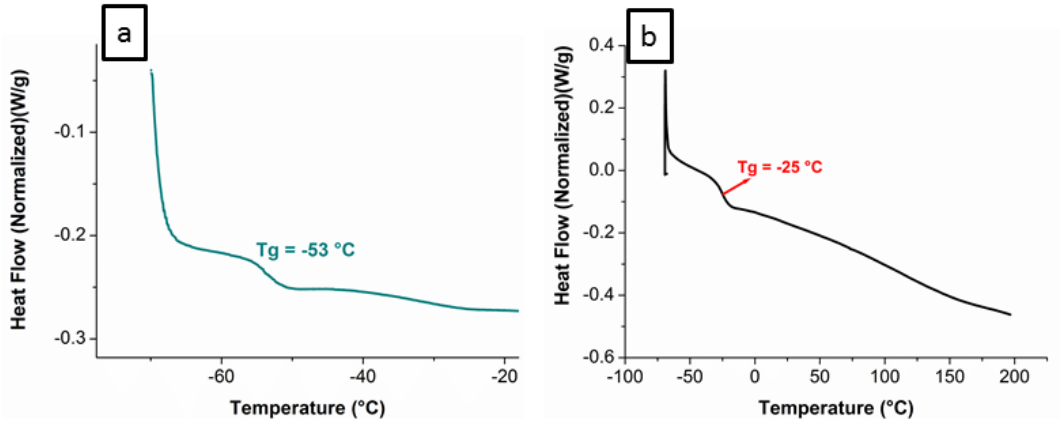


Figure 5.5 DSC thermograms showing the glass transition temperature of (a) PIL nanoparticles (b) PIL gel bead under a temperature ramp of 10 °C/min.

Thermogravimetric analysis of both the stable dispersion and the non-stoichiometric precipitate layer after centrifugation showed that the well-dispersed PIL nanoparticles in the top layer were thermally stable up to 305 °C under nitrogen, which was similar to the bulk PIL gel (Figure 5.6). However, the precipitate showed two degradation temperatures around 350 and 450 °C, which correlate to free ionic liquid and some unreacted thiols, which indicates that any unreacted thiols and vinyl monomers were not stable in the dispersion and thus was selectively removed by centrifugation.

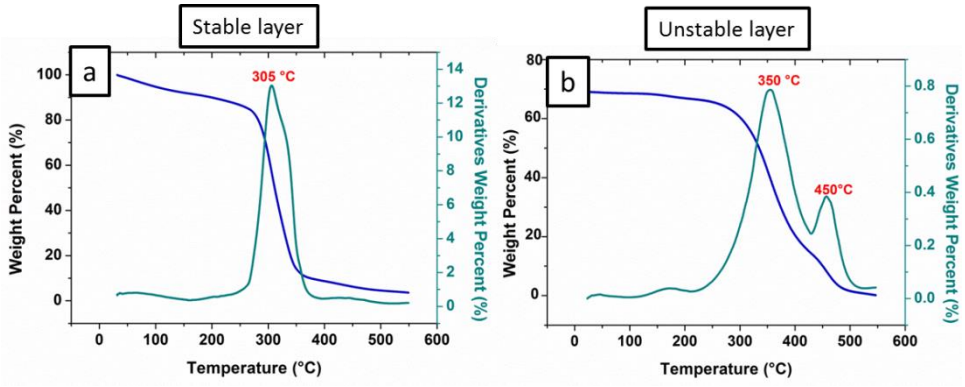


Figure 5.6 TGA thermograms of a (a) stable and (b) unstable layer of PIL nanoparticles after centrifuging showing different degradation temperatures for each layer.

Additionally, the phase behaviour of the SNAP/emulsion coating was investigated using TGA and DSC. TGA analysis of SNAP (Figure 5.7a) only has one degradation temperature around 430 °C, which altered to two temperature (400 °C and 500°C) in SNAP with PIL nanoparticles. This could attribute to the structure change of emulsion

due to the addition of SNAP, which also proved with DSC results. DSC of both the SNAP and SNAP/emulsion samples didn't show any Tg, which is due to the inorganic SNAP coating (which is inorganic and thus show no glass transition) being the major component and since the PIL emulsion nanoparticle was only present in small quantities (0.8 wt%) their Tg was not detected in the DSC analysis (Figure 5.7b).

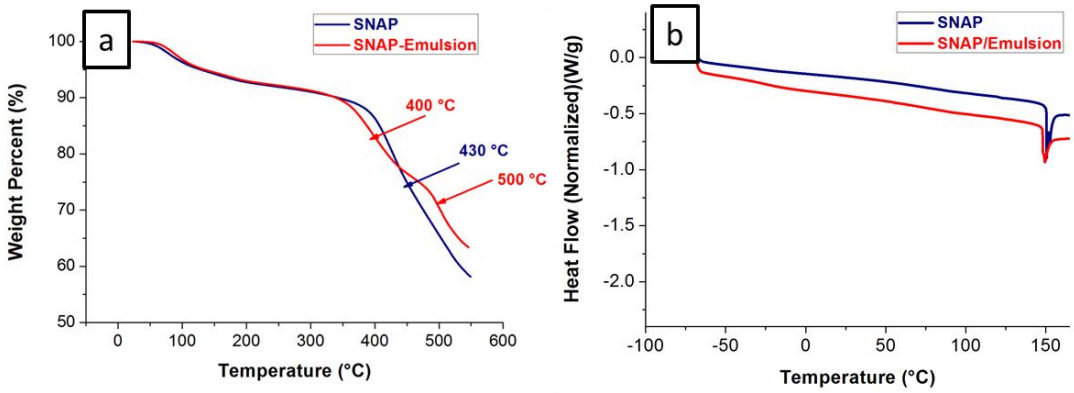


Figure 5.7 Comparison of (a) TGA and (b) DSC of SANP and SNAP/PIL nanoparticles

5.5 Evaluation of corrosion resistance

5.5.1 Potentiodynamic polarization studies

To evaluate and understand the corrosion protection mechanism of PIL emulsion loaded SNAP coating (which will be referred to here as SNAP/emulsion for simplicity) potentiodynamic polarization measurements were carried out. The PIL loading for this study was initially chosen based on previous results using micro containers such as halloysite.[23] To find the optimum concentration of PIL nanoparticle emulsion to be used for achieving better efficiency on an interfacial layer of the coating, the potentiodynamic polarization study of SNAP, SNAP with three different concentrations of emulsion (PIL nanoparticles) (0.4, 0.8 and 1.6 wt%) and blank metal was carried out and the results are shown in Figure 5.8 for the coated samples for both initial and after 24 hr measurements in aqueous salt solution (3.5 wt% NaCl). The corrosion current density (I_{corr}) and corrosion potential (E_{corr}) values were then estimated by fitting the anodic and cathodic polarization curves using CORRVIEW software and the values are presented in Table 5.1.

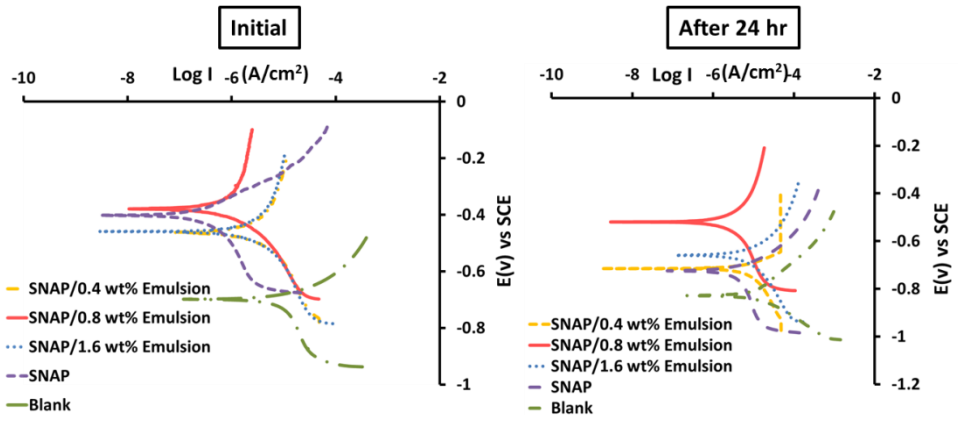


Figure 5.8 Potentiodynamic analysis of SNAP PIL emulsion coated samples at three different emulsion concentrations, blank metal and SNAP coating alone at the beginning of the experiment and after 24 hr immersion in 3.5 wt% NaCl solution.

Initially, the I_{corr} value of SNAP/0.8 wt% emulsion coated samples is lower by two orders of magnitude in comparison with blank metal and is very close to the I_{corr} for SNAP coated sample as would be expected for a barrier coating. However, after 24 hr there was an order of magnitude increase in I_{corr} for pristine SNAP compared to the SNAP/0.8 wt% emulsion coated sample. On the other hand, the SNAP coatings containing 0.4 wt% and 1.6 wt% emulsions showed higher I_{corr} compared to pristine SNAP. After 24 hours immersion in the salt solution, all the emulsion containing samples show significantly less increase in I_{corr} compared to pristine SNAP, with the best-performing system being the SNAP/0.8 wt% emulsion sample. This can be attributed to the presence of the optimum concentration of PIL nanoparticle reinforcing the SNAP structure, and preventing it from corrosion progresses. Where less or more concentration of emulsion had been used, I_{corr} increased compared to SNAP which indicates that at these concentrations emulsion particles are not acting synergistically interfering with SNAP coating and weakening the efficiency of SNAP coating. Therefore, the reason for better protection of SNAP/0.8 wt% emulsion could be attributed to the fact that this amount of emulsion has better miscibility with SNAP structure and enhance the performance of the SNAP coating and provide a better protection of the metal surface.

Table 5.1 Corrosion potential and current determined from potentiodynamic polarisation the SNAP and SNAP with 0.4, 0.8 and 1.6 wt% emulsion nanoparticle coated samples before and after immersing in a 3.5 % wt/v NaCl solution for 24 hours.

Sample	Condition	I_{corr} (A.cm^{-2})	E_{corr} (V)	E_I(%)
SNAP/0.4wt%	Before	3.75×10^{-6}	-0.4608	
Emulsion	After	7.03×10^{-6}	-0.7151	43. 3
SNAP/0.8wt%	Before	3.60×10^{-7}	-0.3769	
Emulsion	After	1.05×10^{-6}	-0.5192	78.6
SNAP/1.6wt%	Before	3.12×10^{-6}	-0.46	
Emulsion	After	6.07×10^{-6}	-0.658	23.9
SNAP	Before	3.46×10^{-7}	-0.4015	
	After	4.16×10^{-6}	-0.7234	16.3

Moreover, inhibition efficiency E_I (%) is calculated from the values of I_{corr} using following equation:[24]

$$E_I\,(\%) = \frac{I\,corr - I'corr}{I_{corr}} \times 100 \qquad \text{Eq.1}$$

Where I_{corr} and I'_{corr} are uninhibited and inhibited corrosion current densities, respectively. These results are also indicative of better E_I of SNAP/0.8 wt % emulsion with highest value of 78.6% (Table 5.1).

SNAP/0.8 wt% emulsion also shows the best corrosion protection based on the E_{corr} values, showing a more noble E_{corr} (-0.3769 V) amongst the samples and remaining at more noble potentials (-0.5192) after 24 hours. The shifting of the E_{corr} values to the noble potential indicates the enhanced corrosion resistance due to the inhibition effect of the coatings. In the case of the 0.4 wt% and 1.6 wt% samples, the E_{corr} is shifted to more negative values, as it can be seen that the final Ecorr values are very similar with pristine SNAP, indicating that structurally these concentrations are not optimal.

It has been reported that imidazolium compounds show corrosion resistant behaviour on steel due to the specific interaction between the –C=N– group and electronegative nitrogen in the molecule with the metal surface.[25] Therefore, such interaction is highly

likely in the present system and, can also result in the observed reduction in the changes in E_{corr} of SNAP/emulsion in comparison to pristine SNAP due to the use of imidazolium-based ionic liquid emulsion particles in this formulation.

5.5.2 EIS investigation

Electrochemical Impedance Spectroscopy was used to investigate the nature of the coatings. Figure 5.9 shows the Bode plot of impedance modulus vs frequency and phase angle vs frequency for the coated samples. The impedance modulus for SNAP and SNAP/emulsion coated samples at three different concentrations decreases in the following order: |Z| (SNAP/0.8 wt% emulsion) > |Z| (SNAP) > |Z| (SNAP/1.6 wt% emulsion) > |Z| (SNAP/0.4 wt% emulsion). This is in agreement with the inhibiting efficiency demonstrated by Tafel plot in Figure 5.8 where SNAP/0.8 wt% emulsion coated sample shows the lowest I_{corr} which correlates to higher impedance of this type of coating.

As it has been illustrated in Figure 5.9a the SNAP and SNAP/emulsion coated samples exhibit similar profile except for SNAP/0.8 wt% emulsion coated sample which exhibits an additional time constant at middle frequencies, which is reminiscent of the SNAP/gel coatings investigated in chapter 4. As in the SNAP/gel sample, the first time-constant at low frequency observed in all samples is commonly associated with diffusion of electrolyte through the SNAP coating and corrosion activity on the substrate surface. However, the presence of another time-constant at middle frequencies in the impedance spectrum of the SNAP/0.8 wt% emulsion indicates the presence of another interface due to an intermediate layer formed by the interaction of the emulsion with the metal surface, which could be due to the presence of the imidazolium groups on the PIL. Such a behaviour (an increase in phase angle in middle frequencies) can be indicative of the presence of ionic species at the metal-coating interface[26], which indicates that similarly to the SNAP/gel sample, the SNAP/0.8 wt% emulsion sample facilitates the formation of a PIL/metal interface and this time constant likely indicates charge transfer between the PIL and the metal surface. Since this was not observed in the other two emulsion samples, it is likely that the lower or higher concentration did not facilitate PIL-metal interaction, which may be due to insufficient concentration (SNAP/0.4 wt% emulsion) or aggregation due to excess emulsion nanoparticle concentration (SNAP/1.6 wt%). In this case since the EIS measurements were done after only a short equilibration (and

thus this increase in phase angle is unlikely to be due to corrosion), this extra time constant can be attributed to an emulsion interface between the SNAP coating and the metal surface, which indicates a preferential migration of the emulsion particle at the metal surface during the dip-coating process as it will be further confirmed with wettability study.

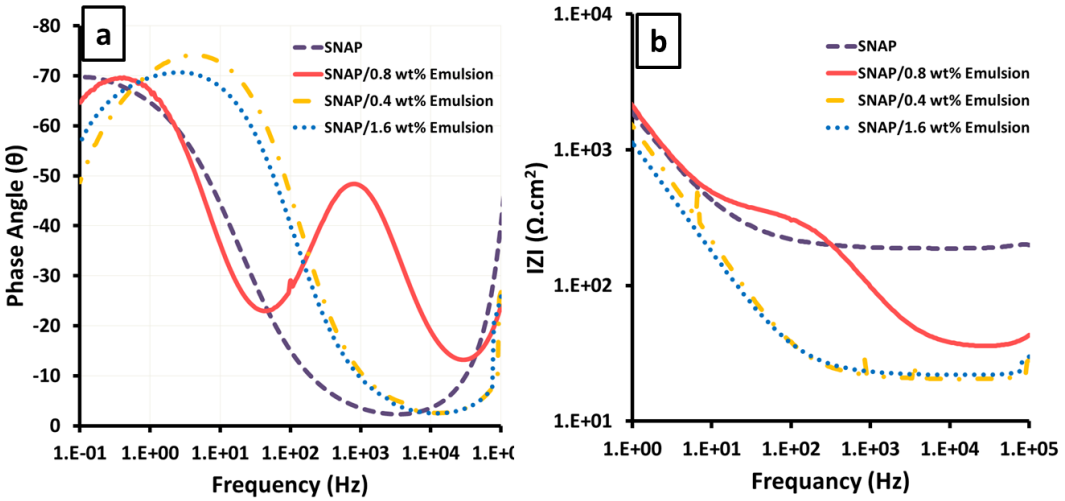


Figure 5.9 (a) Phase angle and (b) Bode plot as a function of frequency for SNAP with emulsion coated samples at three different concentrations in compare with SNAP alone.

In order to better understand this phenomenon, an electrical equivalent circuit has been used to analyse and model the impedance data. In general, semi-permeable coatings can be modelled by the equivalent circuit displayed in Figure 5.10, which takes into account the resistance of the solution, coating, and interface, with capacitive elements due to the bulk coating and the metal/coating interface.[26-27] The impedance spectra of SNAP and SNAP/0.8 wt% emulsion samples were fitted using this model. Modelling of the impedance results as shown on the Nyquist plot in Figure 5.11a show that the coating resistance increases but the interfacial resistance decreases for the SNAP/ emulsion sample compared to pristine SNAP, with the coating resistance increasing from 180 Ω to 348 Ω and the interfacial resistance decreases from 578 kΩ to 61 kΩ. The presence of the emulsion particles in the SNAP coating also increases the coating and interfacial capacitance, which could be due to the ionic nature of these emulsion particles resulting in greater amount of charges in both the bulk coating and on the metal-coating interface. After 24 hours, clear differences can be observed in the behaviour of the samples with and without the PIL emulsion. In the SNAP-only sample, the initial coating has a very high interfacial resistance which has decreased significantly after 24 hours from 578 kΩ

to 1.3 kΩ. This reduction of interfacial resistance is accompanied by an increase in the interfacial capacitance from 0.5 mF to 2 mF, indicating corrosion on the SNAP-metal interface and potential delamination or blister formation. The coating resistance and capacitance, meanwhile, remain quite similar, and thus this change in the properties of the interface indicates that the SNAP coating, being an interfacial layer rather than a barrier layer, was still permeable to electrolyte which allows corrosion to occur at the SNAP-metal interface. Similarly to the SNAP samples, the SNAP/emulsion sample after 24 hours also shows a significant reduction in interfacial resistance from 61 kΩ to 8 kΩ but accompanied only by a slight increase in the interfacial capacitance from 0.12 mF to 0.24 mF (while the coating resistance and capacitance remains relatively unchanged), indicating a similar corrosion process to the SNAP sample (Table 5.2). However, the interfacial resistance remains higher than SNAP alone (8 kΩ for SNAP/emulsion compared to 1.3 kΩ for SNAP alone) which indicates that the presence of the emulsion helps protecting the interface.

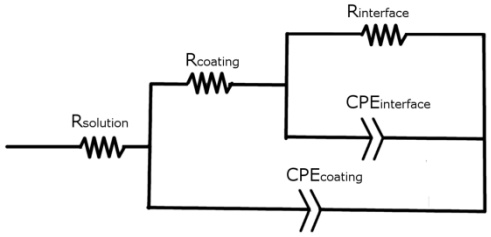


Figure 5.10 Electrical equivalent circuit used to model the impedance data of a permeable coating

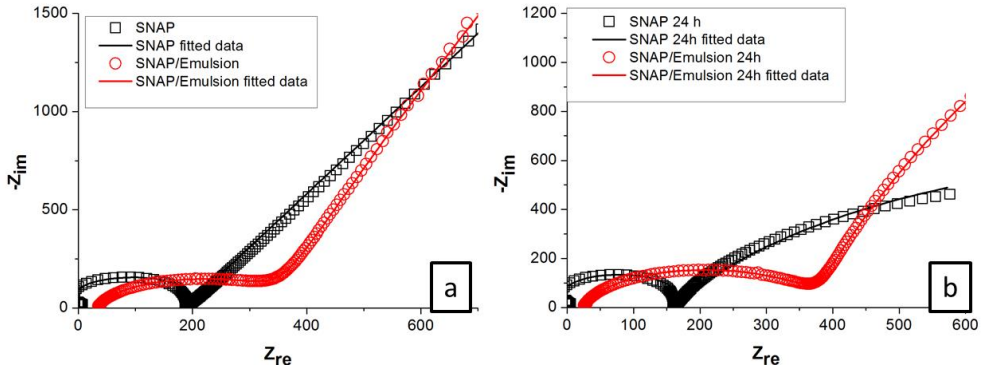


Figure 5.11 Nyquist plot and fitting result for SNAP and the SNAP/0.8 wt% emulsion coated sample in 3.5% NaCl solution. Impedance measurement was done after (a) 1h equilibration and after 24h immersion (b).

Table 5.2 Values obtained from fitting of the impedance data

Sample	$R_{solution}$ (Ω)	$R_{coating}$ (Ω)	$C_{coating}$ (F)	$R_{interface}$ (Ω)	$C_{interface}$ (F)
SNAP only	7	180	6.71×10^{-9}	578320	5.31×10^{-4}
SNAP only 24 h	8	156	7.98×10^{-9}	1305	2.01×10^{-3}
SNAP/emulsion	33	348	2.24×10^{-6}	61499	1.26×10^{-4}
SNAP/emulsion 24 h	22	365	2.15×10^{-6}	8925	2.40×10^{-4}

The results show that the PIL emulsion slightly increased coating resistance, which indicates that the PIL emulsion attributed some improvement in the barrier properties of the SNAP coating. Furthermore, some of the emulsion particles may be present at the SNAP-metal interface due to the emulsion particles acting like a surfactant which adheres to the metal surface during coating, resulting in an interfacial layer which contributes to the anti-corrosion properties of the coating.

5.6 Surface characterization

Figure 5.12 shows the SEM surface morphology of blank metal, SNAP and SNAP/emulsion before and after 1 day of immersion in 3.5 wt% NaCl solution. Before immersion, the SNAP and SNAP/emulsion coated samples show very smooth, homogeneous surface, with some visible particles in the SNAP/emulsion coating. After 24 hr immersion in the salt solution, the image of the blank metal surface (Figure 5.12a′) show a surface that strongly corroded, resulting in a porous, rough, and heterogeneous surface with visible corrosion products. The SNAP and SNAP/emulsion coated samples (Figures 5.12b′ and 12c′) also show a roughening of their surface after immersion in the salt solution, with the coating showing a rougher surface after immersion. However, it is evident that the SNAP/emulsion coated sample has retained a smoother and more uniform surface than the SNAP-only sample, which indicates the beneficial effect of the PIL emulsion on the integrity of the SNAP coating.

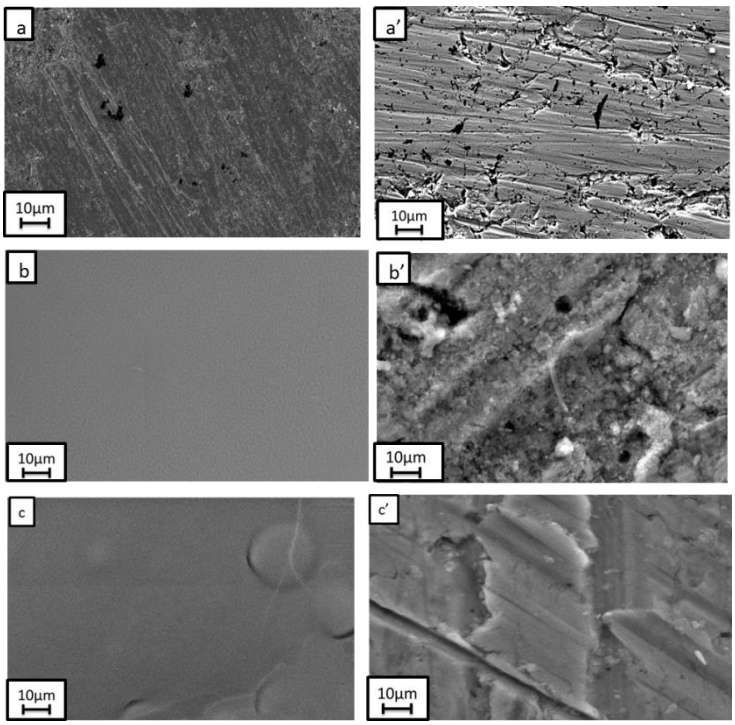


Figure 5.12 SEM images of (a) and (a') blank metal, (b) and (b') SNAP and (c) and (c') SNAP/emulsion before and after 24h in salt solution, respectively.

The EDS data of the surface analysis of the blank metal SNAP and SNAP/emulsion coated samples are summarised in Table 5.3. The EDS analysis performed on the surface of the blank metal (Figure 5.13) shows mostly the presence of peaks attributed to Fe and C, specific elements of the steel. After immersing in salt solution (Figure 5.13), the blank metal surface which contains mainly Fe and C (with small quantities of Si contaminants) now also show the presence of oxygen which indicates the corrosion of iron through the formation of iron oxides. On the other hand, the EDS for the surface of SNAP and SNAP/emulsion coatings were initially showing only carbon, oxygen, and silicone due to the SNAP coating (the oxygen is due to the Si-O in the SNAP composition). The appearance of low content of oxygen but an large amount of iron after immersion in the salt solution in the EDS profile of SNAP and SNAP/emulsion coatings shows that SNAP coating may adsorb ferric and ferrous ions, however the low oxygen content indicates that these species are present as ions and not as oxides. The lower Si content of the coating after immersion supports this as this indicates the presence of ferrous ions that is adsorbed on the surface and as EDS is predominantly a surface technique this presence of surface ions would masked the silicon from the SNAP coating underneath the adsorbed ions. This result indicates that the SNAP

coating strongly binds to ionic species which may inhibit corrosion through the blocking the formation of oxides and scavenging of released ions.

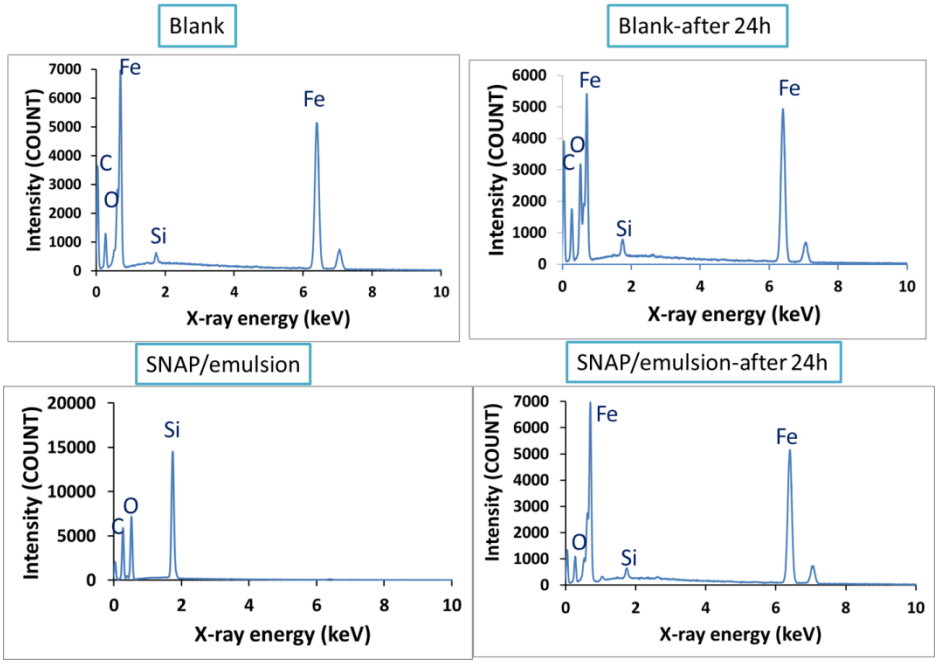


Figure 5.13 EDS gragh of blank metal and SNAP/emulsion before and after 24 in salt solution

Table 5.3 Summary of EDS data of the surface analysis before and after immersion in 3.5 wt% salt solution for 24 h

Samples	Element contents (atom %)			
	C	O	Fe	Si
Blank metal	39.49	0.00	59.42	1.09
Blank metal 24 h	38.62	17.53	42.50	1.35
SNAP	56.68	31.84	0.33	11.15
SNAP 24 h	34.42	6.40	58.23	0.94
SNAP/emulsion	57.41	30.79	0.27	11.53
SNAP/emulsion 24 h	34.01	5.10	59.51	1.38

5.7 Wettability study on coated substrate with Wilhelmy Balance technique

To support our hypothesis from electrochemical analysis results such as potentiodynamic polarization studies and EIS investigations which revealed that the PIL nanoparticle emulsion migrates to intersurface during the dip-coating process and lead

to better protection mechanism in SNAP coating, dynamic wettability study with contact angle measurement has been undertaken using the Wilhelmy technique at 23 ºC. A wetting cycle with the SNAP system is shown in Figure 5.14. In a typical dynamic contact angle measurement, the sample moves against the liquid when the sample is immersed to the liquid and the advancing contact angle is recorded. When the sample emerges, the receding contact angle is measured. It comprises of forced and spontaneous movement regions. At the metal-coating interface, the SNAP solution wets the surface well with the force decreasing marginally. Contact angle hysteresis is also recorded as the difference between the advancing and receding contact angles.[28]

The contact angle data is used to evaluate the dynamic wetting behaviour and interaction of the PIL emulsion with the metal surface. Generally, a lower contact angle corresponds to a higher adhesion per unit area and wetting of the surface is very favourable, and the fluid will spread over a large area of the surface. The work of adhesion was also calculated from the contact angle as follows:

$$\omega_a = \Upsilon_1(1 + \cos\theta) \qquad \text{Eq.2}$$

where Υ_1 is the surface tension of the liquid, and θ is the contact angle.[29] Table 5.4 shows the physical properties such as viscosity and surface tension of the probe liquids plus work of adhesion and contact angle.

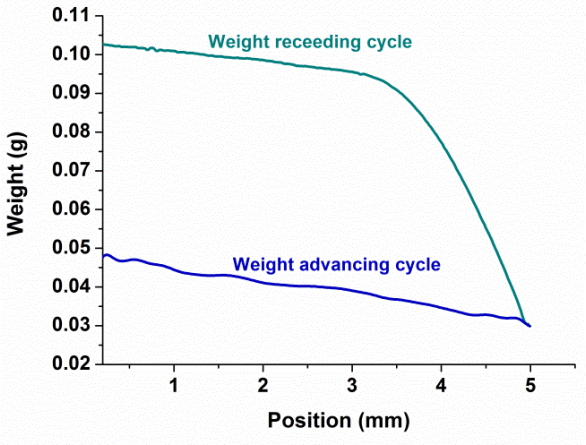


Figure 5.14 Wetting cycle of SNAP coating

Table 5.4 Summary of the physical properties of the probe liquids and wettability study of metal with SNAP, emulsion and SNAP/0.8 wt% emulsion.

Sample name	Viscosity (mPas)	Surface tension (mN/m)	Advancing contact angle (°)	Work of adhesion (mN/m)
SNAP	2.1	37.6	65.2 ± 2	53.4
0.8wt% Emulsion	1.0	31.9	52.4± 1.6	51.4
SNAP/0.8wt %Emulsion	1.9	37.5	52.3 ± 1.9	60.4

It is interesting to note that the viscosity of the emulsion (1mPas) is half compared to SNAP solution and also the surface tension is lowest compared to all samples. One of the important criteria of good adhesion is that the coating should wet the surface.[30-31] Therefore, the surface energy of the substrate has to be higher than that of the organic coating, which is in agreement with the data obtained in this study. The surface tension of all coatings is far below the surface tension value for steel, which ranges from 700 to 1100 mN/m depending on the cleaning process.[32] Results indicate that the lower the angle, the higher the surface polarity, so the better work of adhesion.

Moreover, the contact angle value of the emulsion containing samples is in the range of ~52.4° indicating the emulsion samples used in this study wet the surface very well compared to stand alone SNAP (Table 5.4). This could be attributed to the fact that applying emulsion to the SNAP increases the interaction with the metal surface with high wettability. The contact angle data of the PIL nanoparticle emulsion (31.9 vs 37.5 mN/m) compared to SNAP nanoparticle solution indicates a strong affinity and preferential diffusion and adsorption of the PIL nanoparticle emulsion onto the metal surface. As a result, it could act as inhibitor layer with improved barrier performance against diffusion of oxygen and moisture into the metal surface by the adsorbed layer. Figure 5.15 illustrates the diffusion pathway into the metal surface using SNAP and SNAP with emulsion coating. The strong affinity of the PIL nanoparticle emulsion to the metal substrate leads to a stronger interfacial layer at the interface, which illustrates its potential to be used as an organic inhibitor in the SNAP or other coatings.

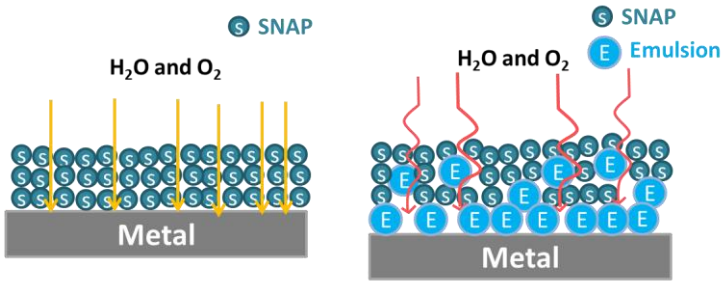


Figure 5.15 Schematic illustration of diffusion pathway into the metal surface using SNAP and SNAP with emulsion coating.

5.8 Conclusion

In conclusion, we report facile preparation of cross-linked polymerizable ionic liquid (PILs) based nanoparticles via thiol-ene photo-polymerization in miniemulsions. The utilization of this method offers great potential for the development of cross-linked polymer nanoparticles in the water phase. The synthesised PIL nanoparticles have been fully characterized for chemical structure, morphology and properties. Furthermore, in this study, we applied PIL nanoparticles at different concentrations into a SNAP-based interfacial layer on mild steel surfaces. Potentiodynamic polarization and EIS investigations show that the sample containing 0.8 wt% of the emulsion offers improved inhibitor properties to the coating. EIS and contact angle wettability studies also reveal that these nanoparticles offers improvement of the corrosion resistance in the SNAP-metal interface by preferentially migrating to the metal surface during coating as it shows a strong affinity between the PIL nanoparticle emulsion and the metal surface. This shows the potential for these PIL nanoparticle emulsion to enhance corrosion protection in SNAP-based coatings.

5.9 Reference

1. Rao, J. P.; Geckeler, K. E. *Prog. Polym. Sci.* **2011,** *36* (7), 887-913.
2. Muldoon, M. J.; Gordon, C. M. *J. Polym. Sci., Part A: Polym. Chem.* **2004,** *42* (15), 3865-3869.
3. Marcilla, R.; Sanchez-Paniagua, M.; Lopez-Ruiz, B.; Lopez-Cabarcos, E.; Ochoteco, E.; Grande, H.; Mecerreyes, D. *J. Polym. Sci., Part A: Polym. Chem.* **2006,** *44* (13), 3958-3965.
4. Yuan, J.; Antonietti, M. *Macromolecules* **2011,** *44* (4), 744-750.
5. Yuan, J.; Soll, S.; Drechsler, M.; Müller, A. H. E.; Antonietti, M. *J. Am. Chem. Soc.* **2011,** *133* (44), 17556-17559.
6. Men, Y.; Kuzmicz, D.; Yuan, J. *Curr. Opin. Colloid Interface Sci.* **2014,** *19* (2), 76-83.
7. Yang, J.; Qiu, L.; Liu, B.; Peng, Y.; Yan, F.; Shang, S. *J. Polym. Sci., Part A: Polym. Chem.* **2011,** *49* (21), 4531-4538.
8. Amato, D. V.; Amato, D. N.; Flynt, A. S.; Patton, D. L. *Polym. Chem.* **2015,** *6* (31), 5625-5632.
9. Hoyle, C. E.; Lee, T. Y.; Roper, T. *J. Polym. Sci., Part A: Polym. Chem.* **2004,** *42* (21), 5301-5338.
10. Hoyle, C. E.; Bowman, C. N. *Angew. Chem., Int. Ed. Engl.* **2010,** *49* (9), 1540-1573.
11. Hoyle, C. E.; Lowe, A. B.; Bowman, C. N. *Chem. Soc. Rev.* **2010,** *39* (4), 1355-1387.
12. Van Berkel, K. Y.; Hawker, C. J. *J. Polym. Sci., Part A: Polym. Chem.* **2010,** *48* (7), 1594-1606.
13. Durham, O. Z.; Krishnan, S.; Shipp, D. A. *ACS Macro Lett.* **2012,** *1* (9), 1134-1137.
14. Durham, O. Z.; Shipp, D. A. *Polymer* **2014,** *55* (7), 1674-1680.
15. Wei, H.; Wang, Y.; Guo, J.; Shen, N. Z.; Jiang, D.; Zhang, X.; Yan, X.; Zhu, J.; Wang, Q.; Shao, L.; Lin, H.; Wei, S.; Guo, Z. *J. Mater. Chem. A* **2015,** *3* (2), 469-480.
16. Taghavikish, M.; Subianto, S.; Dutta, N. K.; Choudhury, N. R. *ACS Appl. Mater. Interfaces* **2015,** *7* (31), 17298-17306.

17. Donley, M. S.; Mantz, R. A.; Khramov, A. N.; Balbyshev, V. N.; Kasten, L. S.; Gaspar, D. J. *Prog. Org. Coat.* **2003,** *47* (3-4), 401-415.
18. Taghavikish, M.; Subianto, S.; Dutta, N.; Roy Choudhury, N. *Coatings* **2016,** *6* (2), 17.
19. Szabó, T.; Molnár-Nagy, L.; Bognár, J.; Nyikos, L.; Telegdi, J. *Prog. Org. Coat.* **2011,** *72* (1–2), 52-57.
20. Diane, J. B. Physical Stability of Dispersed Systems. In *Injectable Dispersed Systems*, CRC Press: 2005; pp 1-37.
21. Ahualli, S.; Iglesias, G. R.; Wachter, W.; Dulle, M.; Minami, D.; Glatter, O. *Langmuir* **2011,** *27* (15), 9182-9192.
22. Samiey, B.; Cheng, C.-H.; Wu, J. *J. Chem.* **2014,** *2014*, 14.
23. Lvov, Y. M.; Shchukin, D. G.; Möhwald, H.; Price, R. R. *ACS Nano* **2008,** *2* (5), 814-820.
24. Daoud, D.; Douadi, T.; Issaadi, S.; Chafaa, S. *Corros. Sci.* **2014,** *79*, 50-58.
25. Xu, A.; Zhang, F. Z.; Jin, F.; Zhang, R.; Luo, B.; Zhang, T. *Int. J. Electrochem. Sci.* **2014,** *9*, 5116 - 5125.
26. Wang, H.; Akid, R. *Corros. Sci.* **2007,** *49* (12), 4491-4503.
27. Banerjee, P.; Woo, R.; Grayson, S.; Majumder, A.; Raman, R. *Materials* **2014,** *7* (8), 6092.
28. Gao, L.; McCarthy, T. J. *Langmuir* **2006,** *22* (14), 6234-6237.
29. Ginic-Markovic, M.; Choudhury, N. R.; Dimopoulos, M.; Matisons, J.; Kumudinie, C. *J. Appl. Polym. Sci.* **2001,** *80* (14), 2647-2661.
30. Wicks, Z. W.; Jones, F. N.; Pappas, S. P.; Wicks, D. A. Adhesion. In *Organic Coatings*, John Wiley & Sons, Inc.: 2006; pp 121-136.
31. Feldman, D. *J. Polym. Sci., Part A: Polym. Chem.* **1991,** *29* (12), 1834.
32. Davim, J. P. *Sustainable Manufacturing*. 1st ed.; John Wiley & Sons: 2013; p 79-105.

Chapter 6: Fundamental understanding of inhibitive effect and adsorption behaviour of various ILs and PILs

This chapter of the thesis is presented as a research manuscript “Mona Taghavikish, Surya Subianto, Mikael Larsson, Naba K. Dutta, Namita Roy Choudhury. Fundamental understanding of inhibitive effect and adsorption behaviour of various ILs and PILs.”, to be submitted for peer review publication.

6.1 Abstract

A new class of heterocyclic ionic liquids (ILs) and polymerized ionic liquids (PILs) have been synthesised and their potential as corrosion inhibitors for steel surface immersed in aqueous solution has been investigated using quartz crystal microbalance with dissipation (QCM-D) and polarization study. In particular, the adsorption behaviour of the ILs has been investigated both in-situ and in real time using a quartz crystal microbalance. The QCM-D studies of the synthesised ILs show that all of the ILs are able to be adsorbed onto steel surface, which forms the basis of their corrosion inhibition properties. The heterocyclic IL in this study has a unique structure containing two imidazole groups separated by an n-alkyl spacer, wherein the spacer length was varied from C_4 to C_8. The effect of the spacer length on the inhibitor efficiency is observed to change with the longer chain length spacer (octyl) showing highest adsorption. This adsorption can be expected to result in corrosion inhibition on mild steel surface through blocking of the corrosion sites. Moreover, the PIL gels that are fabricated from these ILs using thiol-ene chemistry also show even greater inhibition efficiency through sustained release of ions for a prolonged period of time. This efficiency of the PIL in terms of their corrosion inhibition effect is attributed to the different structure of the IL and PIL. The presence of N, S and the heterocyclic group in the PIL due to the thiol-based crosslinker and their polymeric form providing greater interaction appears to increase the inhibition effect of the PIL compared to the unpolymerized IL.

Keywords: polymerized ionic liquids (PILs), adsorption, quartz crystal microbalance with dissipation (QCM-D)

6.2 Introduction

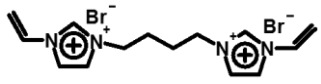
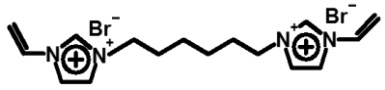
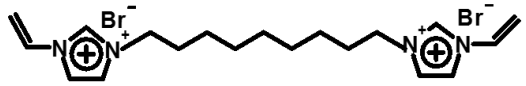
One of the most economical and effective ways to mitigate corrosion is through the use of organic corrosion inhibitors. Among various types of organic corrosion inhibitors, imidazolium type ionic liquids containing N, unsaturated chains, and N3-long alkyl chain on their cations have received significant research attention. This is due to the fact that these heteroatom-containing moieties can act as effective inhibitors via adsorption of these molecules on the metal surface creating a barrier against corrosion attack. In chapter 3, it has also been shown that these types of compounds can be polymerized with sulphur containing thiol compounds using thiol-ene photochemistry. Such

polymerized ionic liquids (PILs) present an extended molecular structure with multiple nitrogen and sulphur atoms that can be readily adsorbed on metallic surfaces via specific interactions between the functional groups and the metal surface, which is due to the presence of the –C=N– group and the electronegative nitrogen and sulphur atoms in the molecule.[1-2] Recent studies have shown that the inhibition efficiency of heterocycles such as imidazoles can be improved significantly by substituting different alkyl or aryl groups in the imidazole moiety.[3] Otmačić et al. observed an increase in inhibition efficiency for phenyl-substituted imidazoles for the corrosion inhibition on copper.[4-5] This effect is due to the electron-donating effect of the phenyl ring, which increases the electron density of the imidazole ring. Indeed, many studies have shown that even a slight difference in molecular structure yields a significantly different protective effect.[6-7] In another study, the inhibition efficiency of five imidazolium-types of polymerizable ionic liquids containing unsaturated and long saturated alkyl chains (as the cation) with bromide counterions has been investigated for the protection of carbon steel in aqueous 1.0M sulfuric acid. The results showed that increasing the carbon chain length of the alkyl spacer connecting the imidazolium rings increased their inhibition performance.[3] However, most of these studies focused on mono vinyl imidazolium based ILs, whereas using the divinyl functionalized imidazolium compounds (which can be used to form gels with a stable, highly crosslinked network structure) with varying spacer chain length between two imidazolium groups can even offer better corrosion inhibitor performance due to the presence of multiple imidazolium moieties.

Furthermore, these divinyl-diimidazolium type molecules can be fabricated into different forms and size such as nanoparticles (nm size) and gel particles (μm size). Previous chapters (chapter 3 and chapter 5) have presented the synthesis of difunctional PIL based nanoparticles and gel particles via thiol-ene reaction and demonstrated the potential use of such nanoparticles as corrosion inhibitors for the protection of steel.[8]

In this study, three difunctional-imidazolium type polymerizable ionic liquids (IL1-IL3) were synthesised and evaluated for their adsorption behaviour on steel in aqueous media using quartz crystal microbalance with dissipation (QCM-D) (Table 6.1). Furthermore, two sets of gels using two different thiols (tetra and single thiols) were fabricated by a thiol-ene reaction in order to investigate the effect of difunctional PILs as corrosion inhibitors (Scheme 6.1). This is the first work, to our knowledge, that delves into the adsorption behaviour of these ILs and the inhibition performance of these PILs.

Table 6.1 Chemical structure of ILs used as corrosion inhibitors

ILs	Chemical structure	Molecular weight (g/mol)
IL1		404.14
IL2		436.23
IL3		464.28

6.3 Experimental

6.3.1 Materials

Pentaerythritol tetrakis(3-mercaptopropionate) (PETKMP), 1-vinylimidazole, 1,4-dibromobutane, 1,8-dibromooctane, 1,6-dibromohexane, (3-mercaptopropyl)trimethoxysilane (MPTS), benzophenone (BP), acetonitrile, ethyl acetate, diethyl ether and methanol (analytical grade) were obtained from Sigma-Aldrich and used without further purification.

6.3.2 Synthesis of 1,4-di(vinyl imidazolium)butane bisbromide (IL1)

1,4-di(vinyl imidazolium)butane bisbromide (DVIMBr) was synthesised by reacting a mixture of 2:1 molar ratio of 1-vinylimidazole to 1,4-dibromobutane in methanol at 60 °C for 15 h. Upon cooling, the reaction mixture was poured dropwise into 1 L of diethyl ether. The white precipitate was filtered off and dried at room temperature until constant weight with a yield of 68%.[9]

^{1}H NMR (300MHz, D_2O, δ, ppm): 8.98 (2H), 7.69 (2H), 7.49 (2H), 7.04 (2H), 5.75 (2H), 5.33 (2H), 4.21 (4H), 1.87 (4H).

6.3.3 Synthesis of 1,6-di-(3-vinylimidazolium) hexane dibromide $[C_6(VIm)_2][Br]_2$ (IL2)

$[C_6(VIm)_2][Br]_2$ was prepared as follows. 1-vinylimidazole (5 ml, 0.05 mol) and 1,6-dibromohexane (4.1 mL, 0.027 mol) were dissolved in acetonitrile (12.5 mL)

in a round-bottom flask fitted with a condenser under slow N_2 atmosphere.[10-11] After 72 h under reflux at 70 °C, the solvent was removed under vacuum. The traces of the starting material and the monoquaternized impurity were washed with ethyl acetate at 70 °C under reflux for 2 h and with acetonitrile for 2 h at the same temperature. The desired product was collected as a white solid by filtration with a Buchner funnel and dried under reduced pressure (75% yield).

^{1}H NMR (300 MHz, D2O, δ, ppm): 7.74 (s, 2H), 7.55 (s, 2H), 7.11 (dd, 2H), 5.79 (dd, 2H), 5.41 (dd, 2H), 4.21 (t, 4H), 1.88 (t, 4H), 1.36 (m, 4H).

6.3.4 Synthesis of 1,8-di-(3-vinylimidazolium) octane dibromide $[C_8(vim)_2][Br]_2$ (IL3)

1-vinylimidazole (5 mL, 0.0.0 mol) was added to 1,8-dibromooctane (5 mL, 0.02 mol) dissolved in 12 ml acetonitrile. After 72 h under reflux at 70 °C, the solvent was removed under vacuum yielding a white solid.[10] In order to eliminate the residual reactants, the mixture was washed with ethyl acetate at 70 °C under reflux for 2 h and with acetonitrile for 2 h at the same temperature, the solvents being removed by filtration. A yield of 81% of the white solid was collected.

^{1}H NMR (300 MHz, D2O, δ, ppm): 7.73 (d, 2H), 7.54 (d, 2H), 7.10 (dd, 2H), 5.76 (dd, 2H), 5.39 (dd, 2H), 4.19 (t, 4H), 1.85 (t, 4H), 1.28 (m, 8H).

6.3.5 Fabrication of different chain length PILs

In a typical synthesis method, PIL (PIL1-PIL3) gel samples were prepared using a stoichiometry 1:2 mole ratio of PETKMP (tetrathiol) and imidazolium ILs (IL1-IL3) and 2:1 MPTS (single thiol) and imidazolium ILs. Solution mixtures were dissolved in the minimum volume of methanol and a small amount of BP. The reaction mixtures were stirred for approximately 30 minutes in the vial while protected from light and then ultrasonicated in an ice bath for 10 minutes with amplitude of 50%. Then the solution mixtures were poured into Teflon containers and photopolymerization was initiated using a UV lamp in a dark hood (Figure 6.1).

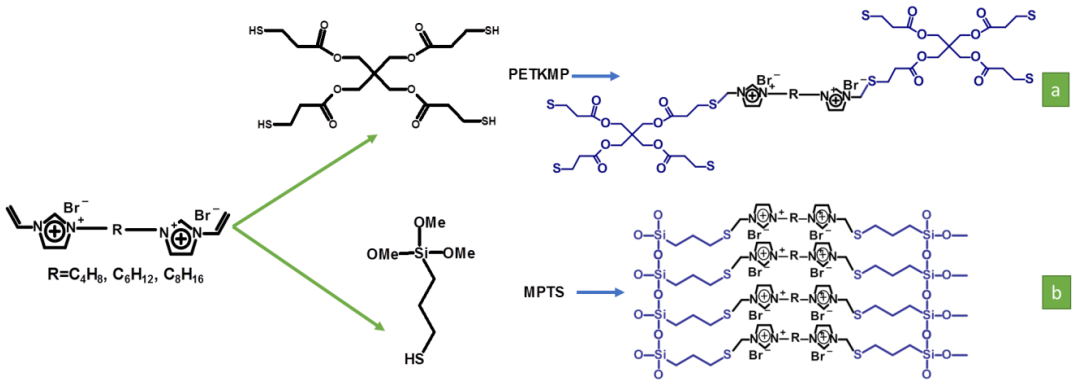


Figure 6.1 Schematic representation of thiol-ene reaction for fabrication of (a) PETKMP and (b) MPTS based PIL gels

6.4 Characterizations

An E4 quartz crystal microbalance with dissipation (QCM-D) unit from Q-Sense was used for the adsorption experiments. Stainless steel coated AT-cut quartz crystals were used as the model substrate. The crystals were cleaned by sonicating for at least 10 minutes in a 2% Hellmanex solution before being rinsed with distilled water and dried with nitrogen gas. All experiments on IL samples (IL1-IL3) were performed at 22 °C and the flow rate of 50 µL/min. ^{1}H-NMR analysis was performed on a 300 MHz Bruker Avance spectrometer at room temperature using D_2O as the solvent. Differential scanning calorimetry (DSC) measurement was conducted using TA Instruments Discovery DSC. The instrument was calibrated for baseline and cell constant prior to running the experiments. The samples were sealed in hermetic aluminium pans for use in the DSC experiment, and an empty pan was used as the reference. The temperature range for the experiment was 70 °C to 200 °C with a heating rate of 10 °C/min under controlled nitrogen gas flow rate of 50 mL/min. Thermogravimetric analysis (TGA) was performed using a TA Instruments Discovery TGA with an aluminium pan. The experimental samples were subjected to a 10 °C/min heating rate from 100 °C to 550 °C under a nitrogen atmosphere. Potentiodynamic polarization analysis was conducted at a scan rate of 1 mV/s in the potential range of ±300 mV relative to OCP. Elemental analysis was performed using a LECO Trumac CNS analyzer.

6.5 Results and discussion

6.5.1 Characterization of the effect of various spacer chain length of IL on PIL gels: Compositional and phase behaviour

6.5.1.1 Compositional analysis by TGA

One of the main advantages of ILs containing unsaturated vinyl groups is that they can be used to form a stable gel through their polymerizable functionality. In this study, the ILs are crosslinked using thiol-ene chemistry to form a crosslinked gel as previously discussed in chapter 3. Two types of crosslinkers were used to form the gels. PETKMP is an organic crosslinker while MPTS is an organo-silane type crosslinker where dual crosslinking is achieved through both the thiol-ene bond and condensation of the inorganic silane groups. The chemical structure of PIL1-PETKMP and PIL1-MPTS gels were shown in Chapters 3 and 7 using FTIR. Therefore, the main focus of this chapter is to study the effect of the spacer chain length between the imidazolium groups on the compositional and phase behaviour of these PIL gels. As such crosslinked gels are insoluble in many common solvents, which make it difficult for spectroscopic or chromatographic analysis in liquid form, and thus thermal analysis methods such as TGA were used for compositional analysis of the synthesised gels.

Thermogravimetric analysis was utilised on the gels to compare the effect of both the spacer length of the ILs and the type of crosslinker on the compositional and thermal stability of the gels. Figures 6.2a and 6.2b illustrate the TGA thermograms of the PETKMP and MPTS gels, respectively. The PETKMP gels show one main degradation peak (75 wt%) with an onset temperature of around 265 °C and a peak degradation temperature of around 310 °C, with further gradual weight loss above 360 °C, which was attributed to sulphur-containing residues. This behaviour is consistent with what has been previously observed for the PIL1-PETKMP gel beads in preceding studies (chapter 3).[12] The TGA thermograms also indicates an initial weight loss at 100–250 °C, which could be attributed to the presence of a trace amount of solvent and water as the PIL contains hydrophilic moieties. Moreover, the presence of only one main degradation peak in the thermogram of PETKMP gels can be correlated with one main component of the gels and also to the purity of the gels without presence of

any unreacted reagents. On the other hand, the TGA thermograms of MPTS gels showed very similar behaviour but with higher degradation temperature peaks of around 320 °C and more residue compared with PETKMP gels due to the presence of inorganic components (Si) in the mercaptosilane structure. The difference between the degradation temperatures (10 °C) of these two sets of gels indicates that the additional inorganic network of the MPTS gels results in a higher thermal stability compared with PETKMP gels (Figure 6.2), with the inorganic crosslinker also resulting in a higher residue due to the Si content.

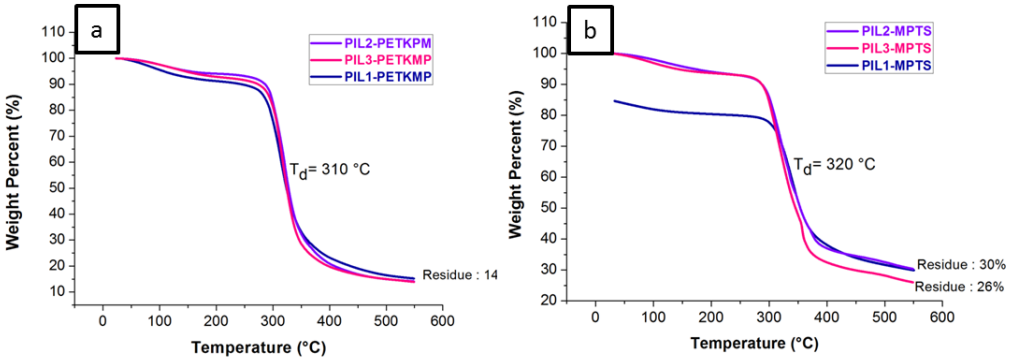


Figure 6.2 TGA curves of (a) PETKMP and (b) MPTS PIL gels with different chain lengths

In contrast, for the same crosslinker there were no significant differences in terms of thermal stability with the varying spacer chain length, with all three chain lengths showing the same onset degradation temperatures. Thus, the inorganic crosslinker resulted in a higher thermal stability, but an increase in the chain length did not result in significant changes in thermal stability. Overall, the TGA results indicate that all materials are synthesised with thiol-ene based crosslinkers as a homogenous network.

6.5.1.2 Phase behaviour of various gels

The glass transition temperature (Tg) of the gel is another critical parameter, which correlates to the phase behaviour and structure of the crosslinked network, and has been determined from differential scanning calorimetry (DSC). Due to their polymeric nature, these polymerized ionic liquids (PILs) are solid at ambient temperature but have a Tg in contrast to some conventional polyelectrolytes. DSC thermograms of the gels with different alkyl spacer chain lengths and organic

(PETKMP, 6.3a) or inorganic (MPTS, 6.3b) crosslinkers are shown in Figure 6.3. The PETKMP-crosslinked gels show a Tg value below room temperature indicating their amorphous rubbery nature, which has also been noticed during the fabrication process. In addition, increasing the spacer chain length from butyl to octyl increases the Tg from -25 °C to around -2 °C, indicating rigid network formation and a more ordered structure with higher spacer chain length and a subsequent decrease in rubbery nature. This likely indicates that the ordering of the network structure may increase with the higher chain length, whereas with the shorter chain length the structure may be more disordered and thus show a lower Tg. In contrast, the Tg of the MPTS gels are found to be above zero and no Tg was detected for the PIL3-MPTS gel. This positive shift in Tg could be explained due to dual network formation as a result of the inorganic crosslinker, which limits segmental mobility of the chains and makes a more rigid structure at room temperature. No melting or crystallization peak was observed in the DSC curve. Therefore, both TGA and DSC show that MPTS gels form a rigid network structure, which is due to the dual crosslinking through both the thiol-ene reaction between the vinyl groups with the thiol in mercaptosilane and also the condensation of the sol-gel network due to the silane group.

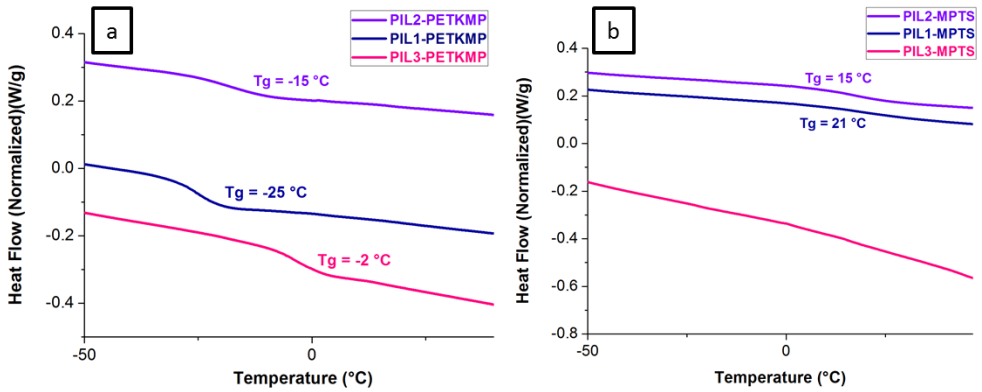


Figure 6.3 DSC thermograms showing the glass transition temperature, Tg of (a) PETKMP and (b) MPTS PIL gels with different chain lengths.

6.5.2 Adsorption study of various ILs using QCM-D

In order to investigate the ability of various monomeric ILs (which were further used for thiol-ene reaction), as corrosion inhibitors for metal surface, an adsorption study was carried out using QCM-D. In the adsorption of organic molecules onto a surface, there is an optimal chain length which promotes

adhesion. A shorter chain length than the optimal length may result in a less ordered packing, and similarly if the alkyl chain spacers are too long it will hinder their ability to form an ordered layer on the surface. Since a more ordered layer would be denser than a less ordered one, such parameters can be evaluated using QCM-D, which studies the mass uptake of the adsorbed layer.

In this study, experimental measurements consisted of first initializing the system in air and allowing the QCM-D to equilibrate for several minutes. Water was then circulated over the sensor crystal and the system was allowed to equilibrate until a stable signal was maintained. Once a stable baseline was obtained, measurements of the Δf and ΔD values were taken during the adsorption of ILs solution. Imidazolium based ILs (IL1-IL3) with different chain length spacers were studied separately at 5 different concentrations (0.1, 0.2, 0.3, 0.4 and 0.5 wt%) to investigate the effect of concentration on the adsorption behaviour. ILs solutions of increasing concentrations were then injected into the measurement cell, leading to a step-by-step change in frequency caused by adsorption of the IL molecule onto the surface of the sensor. The variations of frequency for the ILs solutions were recorded for multiple overtones and the fifth overtone was selected and analysed for all samples. The mass adsorbed can then be determined using the Sauerbrey relation. [13]

$$\Delta m = -\frac{c\Delta f}{n} \qquad \text{Eq.1}$$

where Δm is the adsorbed mass, Δf is the variation in frequency observed at overtone n, and C = 17.7 ng cm^{-2}, which is a constant characteristic of the equipment. The Sauerbrey relation is only valid in cases of sufficiently rigid, evenly distributed and for thin films. This could typically be verified as true if the ratio of $\Delta D/(-\Delta f_n/n)$ is less than 4×10^{-7} Hz^{-1} (ΔD represents dissipation changes).[14-15] In the present study, the ratio ΔD/Δf was always lower than 10^{-7} for all of the studied inhibitor concentrations, indicating that the adsorbed layer was rigid. Consequently, the mass of adsorbed molecules on the QCM sensor surface was calculated from the Δf using the Sauerbrey equation. In a typical case, when a material is adsorbed to the sensor surface, the frequency decreases and the dissipation increases. Figure 6.4 illustrates the adsorption behaviour IL1, IL2, and IL3 with (a) butyl, (b) hexyl and (c) octyl spacers, respectively. The adsorption behaviour was observed to be similar for each inhibitor on the steel surface, as can be seen in Figure 6.4, with some exceptions for IL1 adsorption at the

beginning, where at low concentrations the adsorption shows an irregular behaviour. Generally, the adsorption of the ILs increased with increasing concentration, showing a strong affinity of the IL inhibitors for steel. At each concentration for all three ILs, the adsorbed mass slowly increased and then gradually levelled off to a quasi-steady state. At higher concentrations, the mass adsorption followed the same pattern. This increase of the mass of the electrode is due to the formation of an inhibitor layer on the steel surface. However, the rate of mass gain decreased with an increase in the inhibitor bulk concentration where at very high concentrations of around 0.4 and 0.5 wt% it is difficult to detect the mass gain and quasi-steady state for all three ILs.

The decrease in the rate of mass adsorption at higher concentration suggests that the intermolecular interactions with the already adsorbed inhibitor molecules inhibit further adsorption from the solution through steric hindrance and saturation is attained.

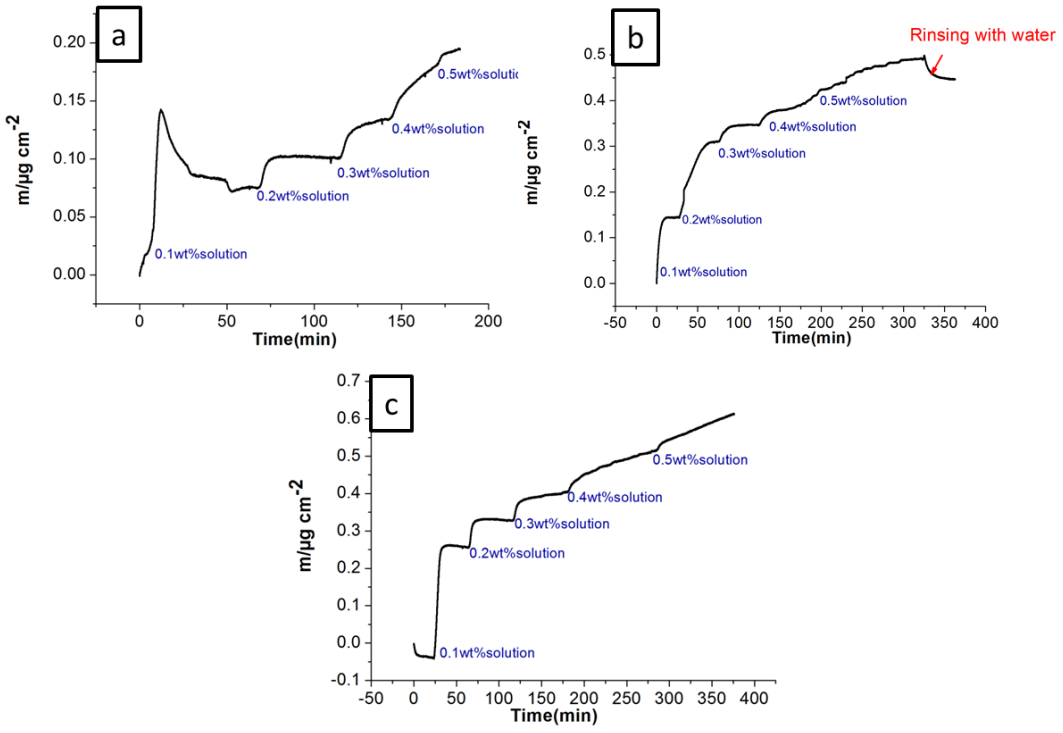


Figure 6.4 Adsorption of (a) butyl, (b) hexyl and (c) octyl IL based inhibitors with different concentrations on a stainless steel surface.

In general, the first inhibitor monolayer is formed upon which a multilayer grows. Therefore, at the very initial stage, the rate of the mass gain increases significantly with the increase of the surface area covered by the inhibitor molecule until the whole surface area is covered by the inhibitor. Then, the growth of the inhibitor layer

continues on a constant area, and therefore the rate of mass growth is constant. The results demonstrate that with an increase in spacer chain length, the mass adsorption also increases.

In case of IL1, significant mass increase with the addition of the first concentration was observed; however, after approximately 30 min, the mass increase stopped and a marginal decrease was observed. The mass decrease fluctuated with time, which was induced by the competition between the adsorption-desorption of the inhibitor and reorientation of the adsorbed layer. It is also possible that some metal dissolution may occur due to the corrosion reaction. However, after addition of the second concentration, the mass adsorption followed the same pattern as with the other spacer ILs. In order to quantify the adsorption behaviour, the packing density of the molecules (the number of chains) adsorbed on the metal surface was then calculated in relation to the number of molecules per area by dividing the mass adsorbed per unit area by the molecular weight of each IL and multiplying this by Avogadro's number (6.023×10^{23} molecules.mol^{-1}). The number of molecules per unit area is found to be 1, 1.9 and 3 for IL1, IL2 and IL3, respectively. As expected, the highest IL chain density was achieved using IL3, of about 3 molecules/nm^2. This packing density result is in line with the expected number of chains per unit area based on the literature for other materials adsorbed on steel or gold using QCM-D or other techniques. For example, previous work by Ngadi et al.[16] showed that the number density of protein molecules (β-casein and Lysozyme) adsorbed onto stainless steel was about 0.5 chains /nm^2. In another study, the number of cationic gemini surfactants with a series of alkane spacers per nm^2 adsorbed on gold was calculated to be between 0.9 to 1.9.[17]

Based on this calculation, it can be seen that the IL3 shows the best packing density when adsorbed on the steel surface. Also, the chain density of the butyl species is relatively low. Thus, the conformations of IL1 chains are relatively sparse and loose, as indicated by its irregular adsorption profile and low mass of the adsorbed species. The regularity of the adsorption profile improves with the hexyl spacer; however, it is the octyl spacer that results in the largest mass adsorption and a uniform adsorption profile with a regular mass increase of up to 0.3 wt%, after which it appears that saturation has been achieved and further addition of IL species were not as readily adsorbed onto the surface. This indicates that the octyl spacer resulted in the most uniform packing of the IL species, and thus allows for better packing between the molecules compared to the

hexyl and butyl spacers, although all ILs are expected to form a tightly packed monolayer or closely aligned layers on steel surface. Considering the geometry and packing density of the IL chains, the orientation of the molecules on the metal surface is predicted. Figure 6.5 illustrates the two possible orientations (mushroom and pancake-like conformations) for the ILs and the size of the IL molecules.

Higher chain length results in larger excluded volumes, and more pronounced steric repulsion; however, it also allows for greater flexibility of the molecular chain and also in some cases better alignment of the molecules when the molecules contains surfactant-like structures of hydrophobic and hydrophilic segments. Considering the size of the IL molecule, a pancake like conformation would result in approximately 1.2 molecules/nm^2, whereas the obtained values were 1, 1.9, and 3 for IL1, IL2, and IL3, respectively. Thus, it is likely that IL3 assembles in a predominantly mushroom conformation rather than as a pancake-like conformation based on the dimension of the molecules, whereas IL1 may be less ordered and does not form a regular, ordered layer compared to IL3. This indicates that the conformation is likely driven by chain entanglement and steric hindrance, which resulted in increased distinction between the heterocyclic imidazolium component and the alkyl spacer.

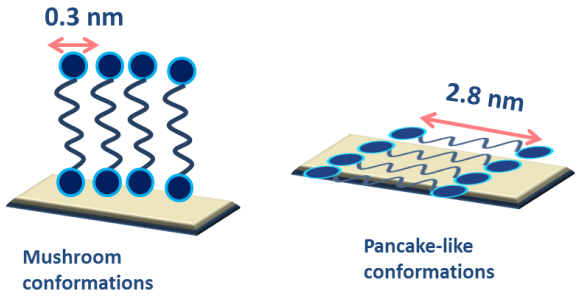


Figure 6.5 Schematic diagrams of possible ILs chain conformations on steel surface

6.5.3 Adsorption mechanism and rate of the adsorption

All of the ILs in this study consist of an anionic (Br^-) part and a cationic part, which contains an imidazolium ring with vinyl and alkyl groups. As the anion is a simple salt, the mechanism of adsorption onto the steel surface (and thus the corrosion inhibition mechanism) of these ILs will be affected mainly by the electron densities around the adsorption centres in the inhibitors (Figure 6.6). In fact, in general the polar group of the IL molecules can be expected to be directly attached to the metal surface and the

nonpolar end oriented in a vertical direction to the metal surface. In order to obtain a better understanding of the inhibition mechanism, a corrosion mechanism similar to that of iron in salt solution was proposed. The anodic dissolution of iron follows the steps:[18]

$$Fe + Cl^{-} \rightleftharpoons (FeCl^{-})_{ads} \quad (a)$$

$$(FeCl^{-})_{ads} \rightleftharpoons (FeCl)_{ads} + e^{-} \quad (b)$$

$$(FeCl)_{ads} \rightarrow (FeCl^{+}) + e^{-} \quad (c)$$

$$(FeCl^{+}) \rightleftharpoons Fe^{2+} + Cl^{-} \quad (d)$$

On the anodic sites, it is assumed that firstly Cl^{-} anion is adsorbed onto the positively charged metal surface by coulombic attraction. However, in the presence of inhibitors, electrostatic interaction between the positively charged inhibitor and the negatively charged metal surface leads to the adsorption of the inhibitor molecules (Figure 6.6 (b)), forming a barrier to the adsorption of Cl^{-} ions. Furthermore, these adsorbed molecules interact with $(FeCl^{-})_{ads}$ species to form monolayers (by forming a complex) on the steel surface. These layers protect the steel surface from attack by chloride ions.[18-19] Thus, step (b→d) in the above equations, which is the oxidation reaction of $(FeCl^{-})_{ads}$ can be prevented.

This adsorption of the IL also affects the cathodic sites, where the N atoms of the imidazolium ring and the –C=N– group will form π bond with entering unoccupied orbitals of iron through Van der Waals forces, which is known as chemisorption (Figure 6.6(a)). This way the cationic part is adsorbed on the metallic surface and a physical barrier is formed to prevent the adsorption of hydronium ions (H_3O^{+}). Then, the nonpolar carbon chain will cover the surface and form a hydrophobic barrier layer to repel corrosive ion attacks. As the long carbon chain is non-polar and water is polar molecular, when the carbon chain is sufficiently long, it will be able to prevent or reduce the diffusion of water molecules.[20] The long hydrophobic chain also increases the electron density of N atom and adds a steric effect to increase adsorption ability. Thus, higher corrosion inhibition of IL3 is ascribed to higher adsorption ability and steric effect of the hydrophobic side chains. Whereas IL1 with short carbon chain length cannot completely retard water molecules, so it shows weaker corrosion inhibition behaviour. In addition, the vinyl group of ILs participated may also scavenge acidic

protons through the hydrogenation reaction by taking the hydrogen atoms to form an ethylic group, and changing from an unsaturated to a saturated group (Figure 6.6 (c)).[21]

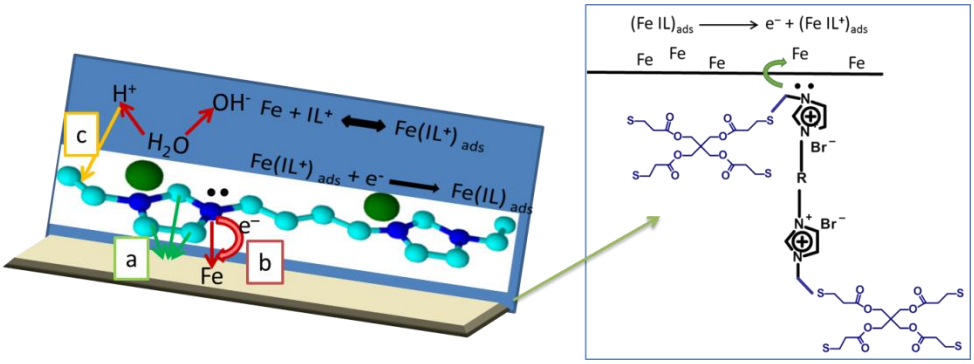


Figure 6.6 Proposed corrosion inhibition mechanism of IL on steel surface in aqueous media: (a) chemisorptions, (b) electrostatic interaction, and (c) hydrogenation reaction of vinyl group

To compare the adsorption behaviour of the three ILs at various concentrations, cumulative mass uptake was plotted against concentration and shown in Figure 6.4. As evident from the steepness of the curve in Figure 6.4, IL3 exhibit faster adsorption compared with other ILs. Furthermore, the cumulative mass adsorption results of QCM plots demonstrate a linear relation with concentration for all three ILs, where the slope of the straight line indicates the rate of mass adsorption (Figure 6.7). The adsorption rate is very similar to that seen from steepness of the curve in Figure 6.4, and is decreasing in the order of IL3>IL2>IL1. This is consistent with our previous observation where IL3 shows the highest packing density and ordering amongst the three ILs, and thus it also shows the highest rate of adsorption.

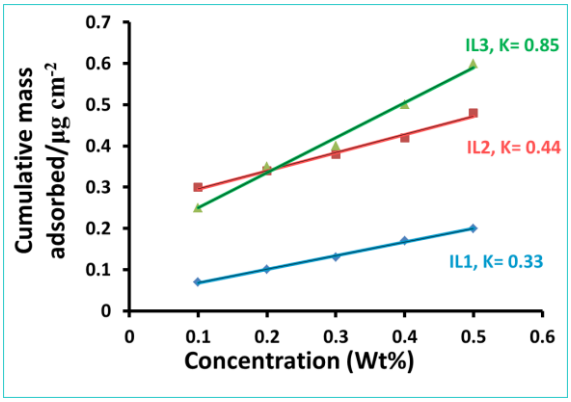


Figure 6.7 Rate of mass adsorption vs concentration for three different ILs

Moreover, to investigate the stability of the adsorbed inhibitor layer on the steel surface, at the conclusion of QCM experiment, water was flowed for a prolonged period of time. As shown with the red arrow in Figure 6.4b, the inhibitor layer was very stable and only a small desorption occurred during the washing stage and after that the mass remained constant without further changes. The mass loss is likely attributed to secondary or tertiary adsorbed species that are above the first layer directly adsorbed on the steel surface. These results show that the ILs can form a stable inhibitor layer on the steel surface. Table 6.2 shows the summary of results obtained from the QCM-D study of ILs with different spacers.

Table 6.2 Summary of QCM-D study on adsorption behaviour of ILs on steel surface

ILs	Δm (μg)	Rate of adsorption (μg/cm^2)	Packing density (molecules /nm^2)
IL1	0.03	0.33	1
IL2	0.04	0.44	1.9
IL3	0.1	0.85	3

From the above results, it can be concluded that the IL inhibitors prevent active dissolution of the metal due to their ability to form an adsorbed layer on the metal surface, which is due to a coordinate bond between the inhibitor ILs' electron donor and the vacant d orbital of the metal or metal ions. It can also be seen that in this study the octyl spacer shows the best performance, with the highest and fastest mass adsorption on steel surfaces observed for IL3, followed by IL2 and then IL1.

6.5.4 Inhibition effect and adsorption study using PIL gel

Since imidazolium based ionic liquids (ILs) have been shown to have anticorrosion properties,[1, 22] an investigation with immersion test and an adsorption study was carried out in order to understand their behaviour as corrosion inhibitors. A representative system of IL1-PETKMP gel (referred as PIL1 gel) was chosen for this purpose. In this experiment, blank metal was immersed in water and salt solution with and without the PIL1 gel in bulk form. The samples were monitored over a period of 1 month. Figure 6.8 shows the inhibition study with water and salt solution of blank metal in presence and absence of PIL1 gels after 4 weeks. The solution containing PIL1 did not show any

significant changes during this time, whereas the blank sample started corrosion after only one hour of immersion and corrosion continued vigorously during the one month period. This clearly shows that the presence of the PIL1 gel in the solution leads to a strong corrosion inhibition effect, which requires a further in-depth investigation of this behaviour.

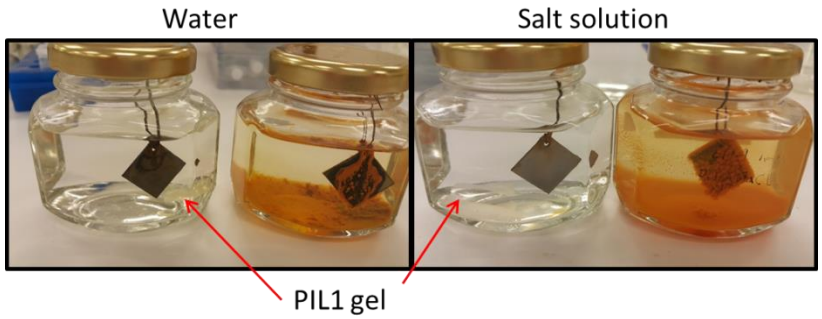


Figure 6.8 Corrosion inhibition performance of blank metal in water and 3.5 wt% salt solutions in presence and absence of PIL1 gel

In order to examine the observed inhibition characteristics of the PIL1 gel, different techniques were used. Conductivity of the aqueous solution in which the PIL1 gel was immersed was measured after 4 weeks and shows a value of around 400 µs (microsiemens), whereas deionised water used for this study shows a value of 0.4 µs. This reveals that there are ionic species present in the solution of the PIL1 gel; however, there is no sign of corrosion. To understand such strong inhibition behaviour of the ionic gel further, the aqueous solution from immersion of the PIL gel in deuterated water (D_2O) was analysed with the ^1H NMR spectrum to investigate the ionic species present. Figure 6.9 depicts ^1H-NMR of the gel soaked solution (in D_2O) after two weeks. The NMR spectrum indicates that there are no unreacted divinyl or thiol groups from the monomer; however, it shows peaks that can be attributed to the alkyl groups present in both PETKMP (the thiol crosslinker) and DVIMBr (the imidazolium-containing IL), which are indicated in the spectrum as thiol protons and IL. As these peaks are due to water-soluble species that are present in the solution, it is most likely due to the presence of low molecular weight oligomers that are not fully crosslinked within the thiol-ene gel network. These oligomers behave as corrosion inhibitors in the solution and lead to corrosion prevention of the metal surface. As discussed earlier in this chapter, the inhibition mechanism of ILs is due to the electrostatic interactions

between the positively charged species in the solution and the negatively charged metal surface.[23] Indeed, as the conductivity measurements showed there are ionic species in the solution that can form a complex with the iron of the metal surface and the solution acts as a redox inhibitor to protect the metal from corrosive species and mitigates the corrosion process significantly.

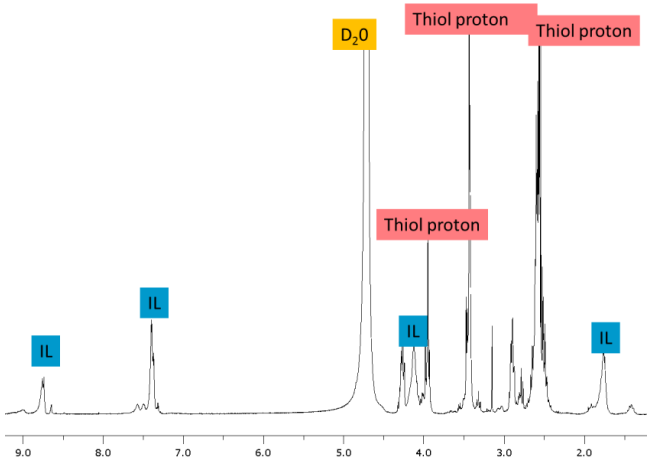


Figure 6.9 ^{1}H-NMR spectrum of PIL1 gel soaked in D_2O after two weeks

Furthermore, after the immersion test the remaining solution was dried and the extracted part and remaining PIL1 gel in the solution were investigated using elemental analysis to obtain a better understanding of the chemical structure of the leached out components. The mass of the PIL1 gel before and after the corrosion study was calculated to determine the mass of the leached fraction that was present in the solution. Results show that 37% of the mass of the PIL1 gel was leached out during the corrosion experiment. Elemental analyses of this leached fraction and remaining PIL1 gel (Table 6.3) show a very similar elemental composition, with no significant difference in the sulphur to nitrogen molar ratio between the PIL1 gel and the extracted, water soluble liquid fraction (1.64 to 1.71 respectively). This supports our hypothesis that the leached species are oligomers or low molecular weight branched polymer species, as the similar S/N ratio indicates that the ratio between the PETKMP and IL1 are similar for both the PIL1 gel and extracted fractions. The slightly higher S/N ratio also indicates that the leached species may be thiol-terminated, and the presence of these oligomers results from hydrolytic attack on PIL1 releasing oligomers, which can act as controlled delivery corrosion inhibitors through redox action.[24]

Table 6.3 Elemental analysis of the PIL1 gel after leaching in water for 7 days. All values are in % mass.

Sample fraction	**Carbon**	**Nitrogen**	**Sulphur**	**Hydrogen**
Extracted dry PIL1 gel	9.23	1.62	6.08	40.84
Water soluble fraction from extraction	5.01	1.38	5.38	33.49

To evaluate the corrosion protection mechanism of the PIL1 gel, potentiodynamic polarization measurements were also carried out. The potentiodynamic polarization study of metal in a salt solution (3.5 wt% NaCl) containing the PIL1 gel and also blank metal in salt solution without any inhibitor was carried out. The results are shown in Figure 6.10 for both the initial and 24 hour measurements. The corrosion current density (I_{corr}) and corrosion potential (E_{corr}) values were then estimated by fitting the anodic and cathodic polarization curves (Tafel plot) using CORRVIEW software and the values are presented in Table 6.4.

Table 6.4 Corrosion potential and current determined from potentiodynamic polarisation the blank metal with and without PIL1 gel before and after immersing in 3.5 % wt/v NaCl solution for 24 hours.

Sample	Condition	I_{corr} ($A.cm^{-2}$)	E_{corr} (V)
Blank metal	Initial	1.33×10^{-5}	-0.815
	After 24h	2.22×10^{-5}	-0.832
Blank metal with PIL1 gel	Initial	6.75×10^{-6}	-0.542
	After 24h	8.44×10^{-6}	-0.516

The results of this study indicate that the presence of the PIL1 gel was able to significantly arrest the corrosion of steel in a salt solution, with the E_{corr} values shifting to more noble potential from -0.542 V to -0.516 V vs SCE after 24 hours. This is significantly improved compared with that of blank metal, which shows an E_{corr} of around -0.815 V (which remained similar after 24 hours). These results show that the controlled leaching of ionic species from the PIL1 gel has a tendency to react with metal surface and form a protective film, which leads to corrosion inhibition of the steel surface.

The I_{corr} values also show significant improvement for the samples with the PIL1 gel, with a corrosion current that is lower by an order of magnitude compared to the blank samples with an I_{corr} of 6.75 x 10^{-6} A.cm^{-2} for the sample with the PIL1 gel compared to 1.33 x 10^{-5} A.cm^{-2} for the blank metal. The values also remained relatively unchanged after 24 hours, indicating that the corrosion current is quite stable. The more noble potential and the lower corrosion current in the presence of the PIL1 gel indicates that the leached species is also capable of adsorbing onto the metal with strong adhesion and forming chelate between iron and the ligand imidazole inhibitor, as proposed in Figure 6.6, resulting in a significant inhibition effect on the steel substrate. The decrease in dissolution of metal and hence corrosion is due to adsorption of the IL1 oligomers through the slow release of ionic species from PIL1.

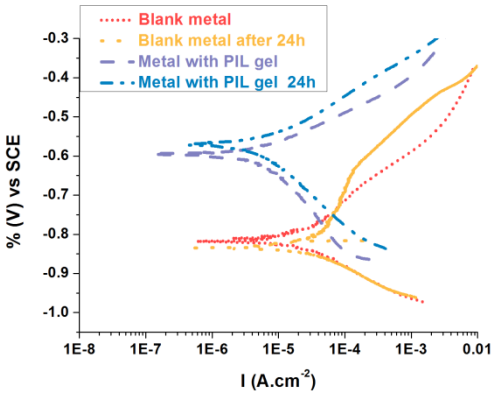


Figure 6.10 Potentiodynamic analysis of a metal in 3.5% NaCl solution with and without the PIL1 gel

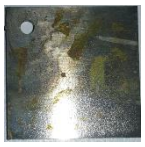
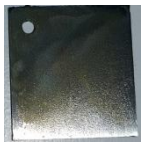
To compare the inhibition efficiency of IL1 with PIL1, a weight loss experiment was conducted following a simple method. Cleaned steel metals were placed in salt solution with and without inhibitors, IL1 and PIL1. The weight loss measurement was used in the following equation to calculate the inhibition efficiency (η_w %):[25]

$$\eta_W\,(\%) = \frac{W_{corr} - W'_{corr}}{W_{corr}} \times 100 \qquad \text{Eq.3}$$

where W_{corr} and W'_{corr} are the average weight loss of duplicate samples in salt solution without and with inhibitors, respectively. The weight loss experiment is summarized in Table 6.5. The obtained data showed 73.5 % inhibition efficiency for IL1 and 88.4 % efficiency for PIL1. Samples that were immersed in salt solution with the PIL1 inhibitor shows a mostly glossy surface after 24 hours compared to quite glossy and partially

corroded surface with the IL inhibitor and fully corroded surface without an inhibitor. (Table 6.5)

Table 6.5 Summary of weight loss experiment for IL1 in salt solution

	Salt solution without inhibitor	Salt solution with 0.5wt% IL1	Salt solution with PIL1(0.5 g PIL gel)
0 h			
24 h			
Average weight loss at 24h	30.2 mg	14.8 mg	5.2 mg

The results show that PIL1 gel has higher inhibition efficiency (88.4 %) compared with IL1 monomer (73.5%) (Table 6.5). The difference in inhibitor efficiency between IL1 and PIL1 is due to the presence of two different heteroatoms in two cases with PIL1 containing additional S containing groups. These are sites for the adsorption progress. The strength of the adsorption depends on the electron donating ability of the donor atom, which follows the order of S >N> O. Thus, sulphur containing PILs are more effective as they are excellent electron donor.

The same method was also used to study the inhibition effect of IL1-MPTS. However, this gel did not show similar behaviour as a corrosion inhibitor in the bulk form as the IL1-PETKMP gel. Therefore, in the next chapter another approach for the application of IL1-MPTS gel as a corrosion inhibitor will be studied.

6.6 Conclusion

The corrosion inhibition effects of divinyl imidazolium based ILs and PIL gels were studied in situ and in real time adsorption using the quartz crystal microbalance with dissipation (QCM-D) and electrochemical polarization measurements. The results show that both ILs and PILs show excellent inhibition properties against mild steel corrosion. The inhibition efficiency of the ILs increased with concentration and was dependent on the spacer alkyl chain size following the order IL3 > IL21 > IL1. The inhibition mechanism of ILs was attributed to the presence of heteroatoms and heterocyclic groups, which increased the adsorption ability of these molecules to form a protective layer that isolates the mild steel surface from an aggressive environment. However, PIL1 gel showed higher inhibition efficiency (88.4 %) compared with the monomer IL1 (73.5 %). This is due to the fact that extra heteroatoms in the PIL gel (S) enhanced the interaction between heteroatoms and the iron of metal surface and resulted in higher inhibition efficiency. Also, it has been shown that spacer chain lengths of the PIL gel do not play a significant role in their thermal stability, which was more dependent more on the type of crosslinker used. Finally, the results from the immersion test and electrochemistry confirm that the PIL gels can act as controlled delivery type corrosion inhibitors through the release of oligomeric IL species over a prolonged period of time.

6.7 Reference

1. Ashassi-Sorkhabi, H.; Es'haghi, M. *Mater. Chem. Phys.* **2009,** *114* (1), 267-271.
2. Obot, I. B.; Obi-Egbedi, N. O. *Corros. Sci.* **2010,** *52* (1), 198-204.
3. Guzmán-Lucero, D.; Olivares-Xometl, O.; Martínez-Palou, R.; Likhanova, N. V.; Domínguez-Aguilar, M. A.; Garibay-Febles, V. *Ind. Eng. Chem. Res.* **2011,** *50* (12), 7129-7140.
4. Gašparac, R.; Martin, C. R.; Stupnišek-Lisac, E.; Mandic, Z. *J. Electrochem. Soc.* **2000,** *147* (3), 991-998.
5. Otmačić, H.; Stupnišek-Lisac, E. *Electrochimica Acta* **2003,** *48* (8), 985-991.
6. Tan, Y. S.; Srinivasan, M. P.; Pehkonen, S. O.; Chooi, S. Y. M. *Corros. Sci.* **2006,** *48* (4), 840-862.
7. Scendo, M. *Corros. Sci.* **2007,** *49* (7), 2985-3000.
8. Taghavikish, M.; Subianto, S.; Dutta, N. K.; de Campo, L.; Mata, J. P.; Rehm, C.; Choudhury, N. R. *ACS Omega* **2016,** *1* (1), 29-40.
9. Yuan, J.; Antonietti, M. *Macromolecules* **2011,** *44* (4), 744-750.
10. Muldoon, M. J.; Gordon, C. M. *J. Polym. Sci., Part A: Polym. Chem.* **2004,** *42* (15), 3865-3869.
11. Boyere, C.; Favrelle, A.; Leonard, A. F.; Boury, F.; Jerome, C.; Debuigne, A. *J. Mater. Chem. A* **2013,** *1* (29), 8479-8487.
12. Taghavikish, M.; Subianto, S.; Dutta, N. K.; Choudhury, N. R. *ACS Appl. Mater. Interfaces* **2015,** *7* (31), 17298-17306.
13. Sauerbrey, G. *Zeitschrift für physik* **1959,** *155* (2), 206-222.
14. Ho, T. T.; Bremmell, K. E.; Krasowska, M.; Stringer, D. N.; Thierry, B.; Beattie, D. A. *Soft matter* **2015,** *11* (11), 2110-2124.
15. Reviakine, I.; Johannsmann, D.; Richter, R. P. *Anal. Chem.* **2011,** *83* (23), 8838-8848.
16. Ngadi, N.; Abrahamson, J.; Fee, C.; Morison, K. *Int J Chem Biol Eng* **2008,** *1*, 125-129.
17. Mivehi, L.; Bordes, R.; Holmberg, K. *Langmuir* **2011,** *27* (12), 7549-7557.
18. Quraishi, M. A.; Rafiquee, M. Z. A.; Khan, S.; Saxena, N. *J. Appl. Electrochem.* **2007,** *37* (10), 1153-1162.
19. Li, W.; He, Q.; Pei, C.; Hou, B. *Electrochimica Acta* **2007,** *52* (22), 6386-6394.
20. Scendo, M.; Trela, J. *Int. J. Electrochem. Sci.* **2013,** *8*, 8329-8347.

21. Likhanova, N. V.; Olivares-Xometl, O.; Guzmán-Lucero, D.; Domínguez-Aguilar, M. A.; Nava, N.; Corrales-Luna, M.; Mendoza, M. C. *Int. J. Electrochem. Sci* **2011,** *6* (10), 4514-4536.
22. Ashassi-Sorkhabi, H.; Shaabani, B.; Seifzadeh, D. *Electrochimica Acta* **2005,** *50* (16), 3446-3452.
23. Quraishi, M.; Rafiquee, M.; Khan, S.; Saxena, N. *J. Appl. Electrochem.* **2007,** *37* (10), 1153-1162.
24. Kharkar, P. M.; Rehmann, M. S.; Skeens, K. M.; Maverakis, E.; Kloxin, A. M. *ACS Biomater. Sci. Eng.* **2016,** *2* (2), 165-179.
25. Bentiss, F.; Lagrenee, M.; Traisnel, M.; Hornez, J. *Corros. Sci.* **1999,** *41* (4), 789-803.

Chapter 7: Novel Thiol-Ene Hybrid Coating for Metal Protection

This chapter of the thesis is presented as a research article “Taghavikish, M.; Subianto, S.; Dutta, N. K.; Choudhury, N. R. Novel thiol-ene hybrid coating for metal protection. Coatings 2016, 6, 17”, published and reproduced by permission of the Coatings, Copyright 2016.

7.1 Research article

coatings

MDPI

Article

Novel Thiol-Ene Hybrid Coating for Metal Protection

Mona Taghaviksih [1], Surya Subianto [1], Naba Kumar Dutta [1,2,*] and Namita Roy Choudhury [1,2,*]

[1] Future Industries Institute, University of South Australia, Mawson Lakes Campus, Mawson Lakes, Adelaide, SA 5095, Australia; mona.taghavikish@mymail.unisa.edu.au (M.T.); surya.subianto@unisa.edu.au (S.S.)

[2] School of Chemical Engineering, The University of Adelaide, Adelaide, SA 5005, Australia

* Correspondence: namita.choudhury@unisa.edu.au (N.K.D.); naba.dutta@unisa.edu.au (N.R.C.); Tel.: +61-883-023-719 (N.K.D.); +61-883-023-546 (N.R.C.)

Academic Editor: Alessandro Lavacchi

Received: 13 January 2016; Accepted: 25 March 2016; Published: 7 April 2016

Abstract: A novel hybrid anticorrosion coating with dual network of inorganic (Si–O–Si) and organic bonds (C–S–C) was prepared on metal through an *in situ* sol-gel and thiol-ene click reaction. This novel interfacial thin film coating incorporates (3-mercaptopropyl) trimethoxysilane (MPTS) and 1,4-di(vinylimidazolium) butane bisbromide based polymerizable ionic liquid (PIL) to form a thiol-ene based photo-polymerized film, which on subsequent sol-gel reaction forms a thin hybrid interfacial layer on metal surface. On top of this PIL hybrid film, a self-assembled nanophase particle (SNAP) coating was employed to prepare a multilayer thin film coating for better corrosion protection and barrier performance. The novel PIL hybrid film was characterised for structure and properties using Fourier transform infrared spectroscopy (FTIR), differential scanning calorimetry (DSC), and thermogravimetric analysis (TGA). The corrosion protection performance of the multilayer coating was examined using potentiodynamic polarization and electrochemical impedance spectroscopy (EIS). The results reveal that this novel double layer coating on metal offers excellent protection against corrosion and has remarkably improved the barrier effect of the coating.

Keywords: hybrid film; (3-mercaptopropyl)trimethoxysilane (MPTS); polymerizable ionic liquid (PIL); thiol-ene reaction

1. Introduction

Surface polymerisation offers great potential for surface functionalization of various substrates for biomedical, barrier, and anticorrosion applications. Amongst various polymerisation routes, thiol-ene click chemistry offers a facile route to cross-linked polymer network prepared via thiol-ene reaction and is very popular for developing thin films and coatings in biomedical application. On the other hand, sol-gel derived thin film coatings are an excellent candidate for environmentally compliant alternatives for conventional toxic chromate coatings [1–3]. Over the past 30 years, sol-gel chemistry has emerged as a promising approach for a wide range of thin film applications due to its advantages including chemical inertness, room temperature synthesis, commercially demonstrated scale-up potential and good adhesion to both metallic substrates and organic top coats [4,5]. An excellent adhesion of sol-gel films to metals derives from the formation of strong covalent Si–O–M bonds [6]. However, inorganic sol-gel derived films cannot provide adequate barrier properties to prevent the aggressive environmental species to interact with the surface due to their brittle nature and the pores and cracks resulting during the drying process. Incorporation of an organic component to the sol-gel systems leads to the formation of more flexible and functionalized films with improved protective ability [7]. Therefore, the synergistic combination of inorganic and organic materials is ideal for the development of hybrid materials; where two different phases with complementary physical and chemical properties can be combined [8]. However, the resultant properties of such hybrid materials

depend not only on the properties of the individual components, but also on the synergy between these components. Thus, control of the structures of the organic and inorganic components and their degrees of organization and interactions are crucial parameters for tailored properties.

In principle, the hybrid inorganic-organic sol-gel coating [9] can be prepared by two ways: (i) the organic and inorganic components are linked through strong chemical bonds or (ii) the organic and inorganic component can be merely embedded into each other without any strong interaction [5]. One facile method for the fabrication of these sol-gel coatings is the Self-assembled Nanoparticle Phase (SNAP) method developed by Donley *et al.* [10]. The SNAP coating process involves selection of precursor compounds based on the desired functionality, formation of "particle-like" nano-sized functionalized siloxane oligomers *in situ* in an aqueous-based high water content solution; and subsequently crosslinking the siloxane oligomers upon application to form a thin, dense film [11]. While SNAP coatings have certain inherent advantages, however, often their usages are limited by their brittleness and the presence of micro-cracks and defects. On the other hand, organic coatings can be easily formulated, containing chemical substances such as binders or additives with highly cross-linkable molecules. They can form a dense coating with better toughness and elastic properties. But these coatings are often mechanically weak, display poor wetting and adhesion properties to the polar substrate and poor thermal resistance. To overcome the limitations, a new class of hybrid coating is proposed using a molecular level combination of organic and inorganic components. A new approach in the design of such hybrid material of superior characteristics is to use ionic liquids (ILs). The ILs are liquid-phase organic salts (*i.e.*, ionic compounds) with negligible vapor pressure, high thermal stability, and intrinsic solubility for certain gases. Also room temperature IL (RTIL) derivatives can be made with polymerizable moiety (PIL) that can be processed to films or for making polymer-based capsules as an active ingredient for self-healing coating. Poly(ionic liquid)s (PILs) stand for a subclass of polyelectrolytes, the repeating unit of which has ionic liquid (IL) character. Recently, PILs have attracted significant attention due to their unique characteristics, and the research scope in PILs has significantly expanded. It is generally accepted that the incorporation of IL moieties into the polymer chain combines some of the unique characters of ILs along with the common features of polymers. The synergistic effect immediately produces a variety of new (multi)functional materials. Recently, cross-linked polymer networks prepared via photo-initiated thiol-ene reaction have gained significant interest for developing flexible films and coatings using such facile protocol. Thiol-ene films are attractive for use in coating science due to their adhesive properties; partially because thio-ether linkages have high affinity for adhesion to a range of substrates, including metals. The high strength of adhesion for a thiol-ene film to a substrate also stems from the minimized build-up of stress in the film network. This lower network stress is a result of both the step-growth polymerization mechanism and the delayed onset of gel formation, which are characteristic of crosslinked thiol-ene networks. The choice of (3-mercaptopropyl) trimethoxysilane (MPTS) for click chemistry and as organo-alkoxysilane as precursor to sol-gel coating to improve the protection of metal surface against corrosion is unique. Its particular structure contains both a silane terminal function ($-SiO(Me)_3$), known for its grafting abilities on oxidised substrates; and a thiol group ($-SH$), which usually reacts with metals in their metallic states [12]. The anti-corrosion effect of MPTS on Cu and Al has been reported [12,13]; however, there is no investigation to employ MPTS based thiol-ene hybrid coating for the preparation of sol-gel coating on steel.

Earlier work shows that under certain conditions the mercapto group can be prone to oxidation [14], which may cause coating degradation. To arrest such degradation and any corrosion, it is necessary to either arrest the cathodic/anodic reaction or insert in the circuit a large resistance, which can impede the movement of ions. Therefore, a multilayer protective coating between the metal and the surrounding is an effective way to arrest these reactions and improve barrier and corrosion performance. Thus, through combining the functionalities of sol-gel, thiol-ene, and PIL chemistry, the aim of our investigation is to create a unique hybrid interfacial network, which would exhibit significant anti-corrosive and barrier performance. The introduction of organo-silane and

subsequent thiol-ene reaction in the grafted layers was investigated in detail using surface, thermal, and microscopic analysis. On top of this PIL hybrid film, a self-assembled nanophase particle (SNAP) coating was employed to prepare multilayer thin film coatings for better corrosion protection and barrier performance. The novel PIL hybrid film was characterized for chemical structure and properties employing thermogravimetric analysis (TGA), differential scanning calorimetry (DSC), photo-acoustic Fourier-transform infra-red (PA FTIR) study, ^{1}H-nuclear magnetic resonance (NMR) and solid state NMR. The corrosion protection performance of the multilayer coating was examined using potentiodynamic polarization and electrochemical impedance spectroscopy (EIS).

2. Experimental Section

2.1. Materials

1-Vinylimidazole, 3-glycidoxypropyltrimethoxysilane(GPTMS), 1,4-dibromobutane, benzophenone (BP), 3-aminopropyltriethoxysilane, (3-mercaptopropyl) trimethoxysilane (MPTS), tetraethylorthosilicate (TEOS), diethyl ether, acetic acid, and methanol were all obtained from Sigma-Aldrich (Sydney, Australia) and used without further purification Fluorosurfactant FC-4432 was obtained from 3M (Sydney, Australia). Double distilled water (DDW) was used for all experiments.

2.2. Synthesis of 1,4-di (vinylimidazolium) Butane Bisbromide

1,4-di (vinylimidazolium) butane bisbromide (DVIMBr) was synthesized by stirring a mixture containing 2:1 molar ratio of 1-vinylimidazole to 1,4-dibromobutane in methanol at 60 °C for 15 h. After cooling down, the reaction mixture was added drop-wise into 1 L of diethyl ether. The white precipitate was filtered off, washed, and dried at room temperature until constant weight with a yield of 68% [15]. ^{1}H-NMR (300 MHz, D_2O, δ, ppm): 8.98 (2H), 7.69 (2H), 7.49 (2H), 7.04 (2H), 5.75 (2H), 5.33 (2H), 4.21 (4H), 1.87 (4H).

2.3. Fabrication of Hybrid Material by Thiol-Ene Reaction

Organic-inorganic PIL hybrid film was prepared using thiol-ene photo polymerization method with stoichiometric ratio of precursors. In a typical synthesis method, a 2:1 mole ratio of (3-mercaptopropyl) trimethoxysilane (MPTS) (1 mmol, 0.2 g) and DVIMBr (0.5 mmol, 0.2 g) was dissolved in the minimum volume of methanol (0.2 mL) and small amount of BP (1 mol % of the thiol group). The reaction mixture was stirred for approximately 30 min in 4 mL vial while protecting from light and oxygen. The thiol-ene mixture was poured and cast onto a glass slide, and the cast samples were irradiated with a 365 nm UV lamp (light intensity = 85 mW/cm^2) in air for 5 min. This PIL hybrid film has been used for further structural investigation.

2.4. Preparation of Hybrid Coating on Metal

The mild steel (Mild Steel CA3SN-G, 0.08% carbon contents, thickness 0.6 mm of 1.7 cm × 1.7 cm) substrates were sequentially polished using abrasive papers with grit numbers 800, 1000, and 1200 prior to cleaning by sequential immersion for 10 min each in acetone, hexane, and ethanol solutions to remove surface oils. The substrates were rinsed with distilled water and dried between each solvent wash and after the final solvent wash. Finally, the dried substrate was treated with a 0.4 wt % solution of NaOH for 30 min and rinsed with distilled water, acetone, and dried with nitrogen purge.

The coating solutions with total volume of 20 mL were prepared by diluting (with methanol) the thiol-ene mixture, which was prepared as discussed above to reach a required volume for dip coating. The final mixtures were vigorously stirred and applied to cleaned metal substrates by dip coating at a withdrawal speed of 10 cm/min in a dip coater. The sample was then exposed for 5 min with a UV lamp. After UV irradiation, the solvent evaporated and the organic-inorganic PIL hybrid film formed on the metal surface. At the same time due to the exposure of the solution to methanol, hydrolysis occurred; where O–CH_3 groups were converted to OH groups. The hydrolyzed silicon alkoxides were

condensed to form inorganic Si–O–Si networks and simultaneous thiol-ene photo-polymerization of the thiol groups at the other end leading to the formation of highly cross-linked dense networked structure (Figure 1).

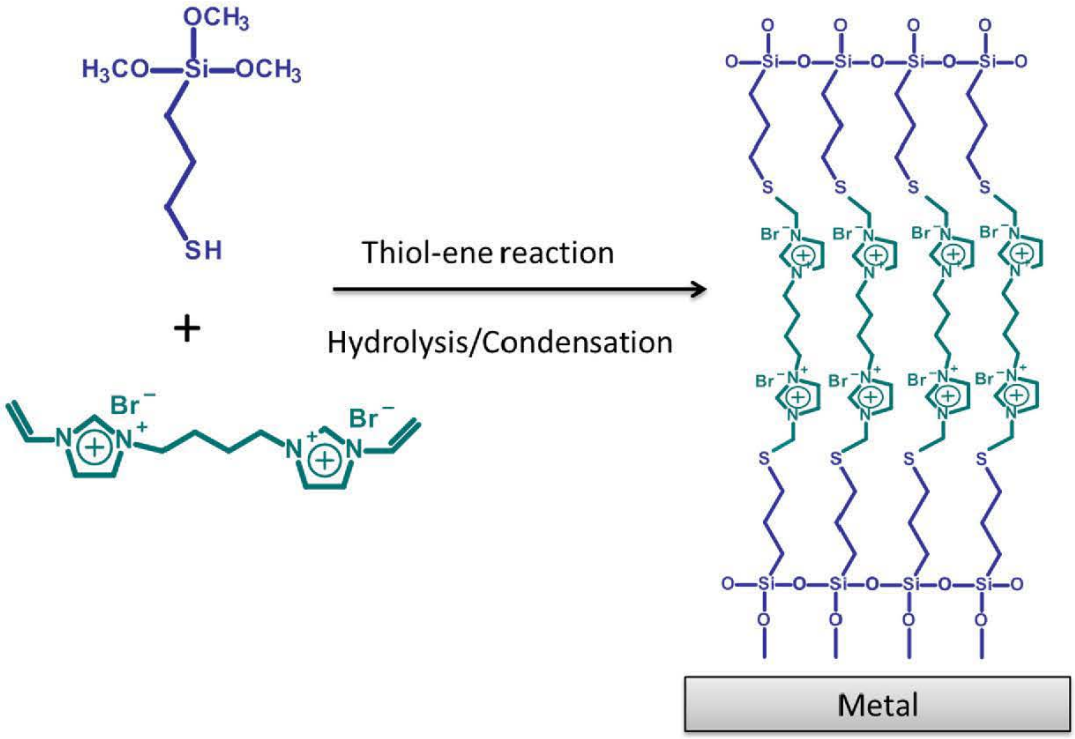


Figure 1. Proposed structure of the MPTS-DVIMBr hybrid film coated on metallic substrate.

2.5. Preparation of Sol-Gel Coating

The top layer of the multilayer coating has been produced using the self-assembled nanophase particle (SNAP) as a matrix for coating. In a typical procedure, the SNAP solution was prepared with drop-wise addition of 42 mL (0.19 mol) 3-glycidoxypropyltrimethoxysilane (GPTMS) and 13.4 mL (0.06 mol) tetraethylorthosilicate (TEOS) to 64.8 mL solution of acetic acid in doubly distilled water (DDW) under N_2. The solution was continuously stirred for 1 h during addition. The TEOS:GPTMS molar ratio used was (1:3 mol ratio), respectively. Hydrolysis and condensation of silanes were conducted at high water/silane ratio of 15. After all of the silanes had been added and hydrolyzed, the solution was aged in a closed container for three days under continued stirring at ambient temperature.

The coating solution was prepared by diluting the aged SNAP solution with DDW by a factor of 1.75 and subsequent addition of crosslinking agent (aminosilane) and surfactant (3M FC-4432, 0.04 wt/v %). The final mixture was vigorously stirred and applied to PIL hybrid coated substrates by dip coating at a withdrawal speed of 10 cm/min. The coating was made within a time frame of 10–30 min, from the point of addition of the crosslinking agent. The coated sample was dried at room temperature for 24 h to allow solvent evaporation. The coating was thermally cured at 80 °C, 60% humidity overnight in a humidity oven (ESPEC-model SH-241).

2.6. Characterization

^{1}H-NMR analysis was performed on a 300 MHz Bruker Avance spectrometer at room temperature using D_2O as the solvent. Solid state ^{29}Si CP-MAS NMR measurements were carried out using a Bruker Avance III 400 MHz spectrometer operating at 79 MHz equipped with a 7 mm probe. Sample was

spun at 2.5 kHz. The spectral width used was 201 ppm, the acquisition time employed was 15 ms, and the recycle delay applied was 5 s.

Infrared spectra of the PIL hybrid film were acquired using Nicolet Magna-IR Spectrometer 750 in photo-acoustic mode, 256 numbers of scans, using carbon black as reference.

Differential scanning calorimetry (DSC) measurement was conducted using TA Instruments Discovery DSC. The instrument was calibrated for baseline and cell constant prior to running the experiments. The samples were sealed in hermetic aluminum pans for use in the DSC experiment, and an empty pan was used as the reference. The temperature range for the experiment was −70 °C to 200 °C with a heating rate of 10 °C/min under controlled nitrogen gas flow rate of 50 mL/min. Thermogravimetric analysis (TGA) was performed using a TA Instruments Discovery TGA with an aluminum pan. The experimental samples were subjected to a 10 °C/min heating rate from 100 °C to 700 °C under a nitrogen atmosphere. The morphology of the coated metal's surface was observed using a scanning electron microscope (SEM, ZEISS Gemini SEM. The samples were placed and images were taken without any further coating at an accelerating voltage of 10 kV.

The electrochemical characterization of the uncoated and the coated samples was carried out using a standard corrosion cell (1 L, Pine Research Instrumentation, Durham, NC, USA) with conventional three electrode set-up in non-deaerated 3.5 wt % NaCl solution prepared from analytical grade chemicals (ChemSupply, Gillman, Australia) and distilled water (Milli Q). A saturated calomel electrode (SCE, Pine Research Instrumentation, +0.24 V *vs.* Normal Hydrogen Electrode, NHE) was employed as the reference electrode. A graphite rod of 2 mm diameter was used as the counter electrode and the sample under test was the working electrode. All the reported potentials in this paper (determined using electrochemical techniques) are with reference to SCE. Initially, the open circuit potential (OCP) of the specimens was monitored as a function of time and samples were allowed to stabilize at their OCP for 1 h before measurements. Low carbon steel coupons (thickness 0.6 mm) of 1.7 cm × 1.7 cm (both coated and uncoated) were used as the samples for electrochemical testing. The sample holder is made of Teflon and a platinum sheet and a platinum wire was used for electrical connection. The area exposed to the electrolyte solution was controlled using inner and outer "O" rings for an electrode area of 0.785 cm^2. All the measurements were carried out at least in duplicates. Potentiodynamic polarization study was conducted at a scan rate of 1 $mV{\cdot}s^{-1}$ in the potential range of ±300 mV relative to OCP. The Electrochemical Impedance Spectroscopy (EIS) measurements were performed using a Solartron 1260 impedance/gain-phase analyzer in combination with a Solartron 1280 B electrochemical interface. The impedance measurements were carried out in a 1 MHz to 10 kHz frequency range with 40 steps per decade. All the spectra were recorded at open circuit potential with applied 10 mV sinusoidal perturbation.

3. Results and Discussion

3.1. Structural Evolution of the PIL Hybrid Film

FTIR was used to evaluate the final chemical structure of the double network PIL hybrids. The FTIR spectra of MPTS, DVIMBr, and the PIL hybrid film (2:1 ratio) are shown in Figure 2. The bands at 2570 cm^{-1}, 1644 cm^{-1}, and 2928–3080 cm^{-1} that are present in the unreacted MPTS and DVIMBr monomers correspond to the thiol groups, C=C stretching of the vinyl group, stretching of −CH groups of the imidazole ring of the PIL, and vinylic proton =C–H stretching, respectively [16]. These bands disappeared in the cured PIL hybrid film indicating the reaction between double bond of vinyl group in PIL, and subsequent network formation through the thiol-ene photo-polymerization.

The FTIR spectrum of MPTS shows a characteristic absorption band at 2850 cm^{-1} corresponding to Si–OCH_3 group [17]. This characteristic absorption band due to Si–OCH_3 disappeared after PIL hybrid film formation due to hydrolysis of MPTS [18]. During hydrolysis, methoxy groups are converted to Si–OH groups and broad peaks at ~910 cm^{-1} and ~3500 cm^{-1} appear indicating the presence of Si–OH groups in PIL hybrid film [19]. Moreover, the condensation reactions led to the formation of

O–Si network in the PIL hybrid film. This is evident from the absorption band at 1030 cm^{-1} [9]. is from the FTIR studies, the formation of MPTS-DVIMBr hybrid film through thiol-ene reaction ld be inferred.

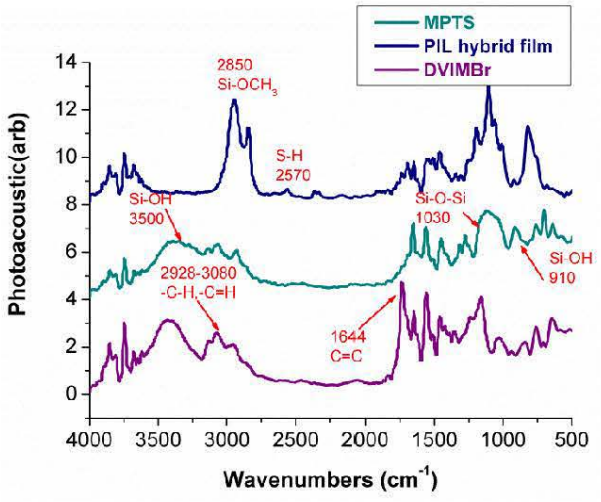


Figure 2. FTIR spectra of MPTS, DVIMBr, and PIL hybrid film.

Scanning electron microscopy (SEM) was employed to investigate film surface morphology. ure 3 shows the SEM images of the polished steel surface compared to samples coated with SNAP . SNAP/PIL hybrid films. The SEM images show that both the coatings on the metal surface uniform, defect-free and well adhered to the substrate surface. The comparison of SEM images bare (Figure 3a) and coated metals (Figure 3b,c) shows that the coatings have fully covered the al surfaces in homogeneous manner. Although, the addition of the PIL interfacial layer appears narginally increase the surface roughness; the SNAP/PIL hybrid film still shows a very smooth, form surface without cracks or other defects. This observation indicates a uniform distribution of SNAP particles over the metallic substrate, which would result in a dense, uniform coating.

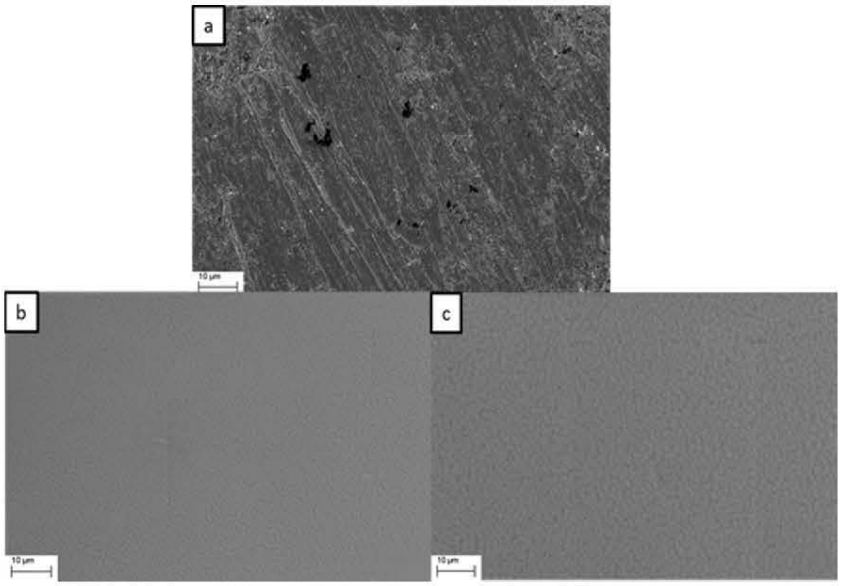


Figure 3. SEM image of (**a**) polished metal; (**b**) SNAP coated metal; and (**c**) SNAP/PIL hybrid film coated metal.

The solid state CP MAS ^{29}Si NMR of the SNAP/PIL hybrid material also shows that the condensation of the silanes has occurred. The NMR spectrum in Figure 4 shows peaks that can be predominantly attributed to T3 species at −61 and −69 ppm, with smaller peaks at −37 ppm due to T2 species, −101 ppm due to Q3 and at −111 ppm due to the presence of Q4 species [20].

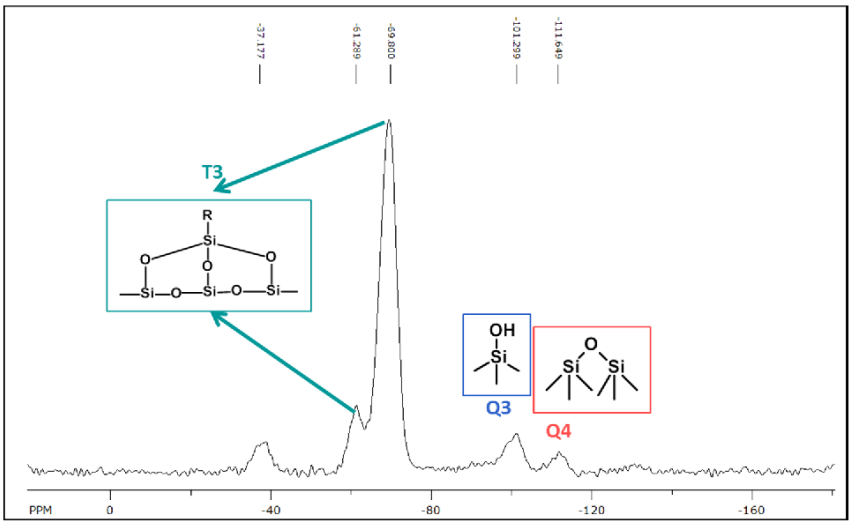


Figure 4. Solid state CP MAS ^{29}Si NMR of the SNAP/PIL hybrid material.

The predominance of the T3 peak is due to the nature of the SNAP nanoparticle, where the main component is GPTMS, where the silica is connected to the glycidol functionality, and thus after condensation the formed SNAP nanoparticles would consist predominantly of silica with T3 structure. In the PIL species the silane used was also mercaptosilane, which can also give rise to a T3 peak when cured and may be the source of the smaller T3 peak at −61 ppm. The presence of the peak at −37 ppm is likely due to the presence of some incomplete crosslinking and maybe a mixture of T2 and T1 species, however based on their respective peak area this is only a small fraction of the material (1:30 ratio of the T2/T1 to T3 peak area). The Q3 species likely arises from the TEOS in the SNAP nanoparticles; which, being only 3 nm in diameter have a large surface area and thus the Si species would be a mixed of R–Si(O)$_3$ and HO–Si(O–Si)$_3$ as can be expected based on the chemical structure of the SNAP nanoparticle. There is also a small peak due to Q4 species (Si(OSi)$_4$), which is likely due to further condensation of the silanes; however this peak represents only a small portion of the bulk material due to the low temperature used in curing these SNAP/PIL hybrid film (80 °C). Q4 species are generally the result of higher temperature thermal treatment.

3.2. *Thermal Stability of the PIL Hybrid Film*

The thermal degradation behavior of the prepared PIL hybrid materials and the monomers were examined using TGA. The TGA curve of MPTS-DVIMBr hybrid film shows one main degradation peak at around 60 wt. % weight loss at onset temperature of 250 °C and peak degradation temperature of 340 °C (Figure 5). The TGA also indicates an initial weight loss at 100–250 °C for PIL hybrid film, which could be attributed to the presence of a trace amount of solvent and unreacted precursor trapped in the PIL hybrid film. The degradation process at high temperature involves the cleavage of C–Si, Si–O–Si and Si–OH bonds in the PIL hybrid film, which is almost 10 °C higher than that of the PIL, and more than 200 °C higher than MPTS. Thus the results of TGA confirm the thermal stability of the PIL hybrid film, which is attributed to the highly cross-linked network of the hybrid through the formation of Si–O–Si, Si–OH networks and an organic network through the thiol-ene photo-polymerization. In order to obtain an estimation of the inorganic content of both the PIL hybrid film and the SNAP/PIL

hybrid film; TGA was carried out under oxygen up to 900 °C. As it has been illustrated in Figure 5c PIL film without SNAP contains 22% residue compared with 43% for PIL/SNAP hybrid film. This is due to the fact that PIL/SNAP hybrid film contains two major inorganic components plus S, N, and Si elements; and thus can be expected to have more residue compared to PIL film alone. The PIL film alone is more organic in nature as the bulk of the material is the organic PIL, with the residue expected to come from the mercaptosilane end-caps and nitrogen from PIL, whereas in SNAP/PIL hybrid film the SNAP itself is silica-based. Also PIL/SNAP hybrid film shows two degradation temperatures. The second degradation around 600 °C could be related to the degradation of nonsilica and other oraganic components of SNAP/PIL hybrid film.

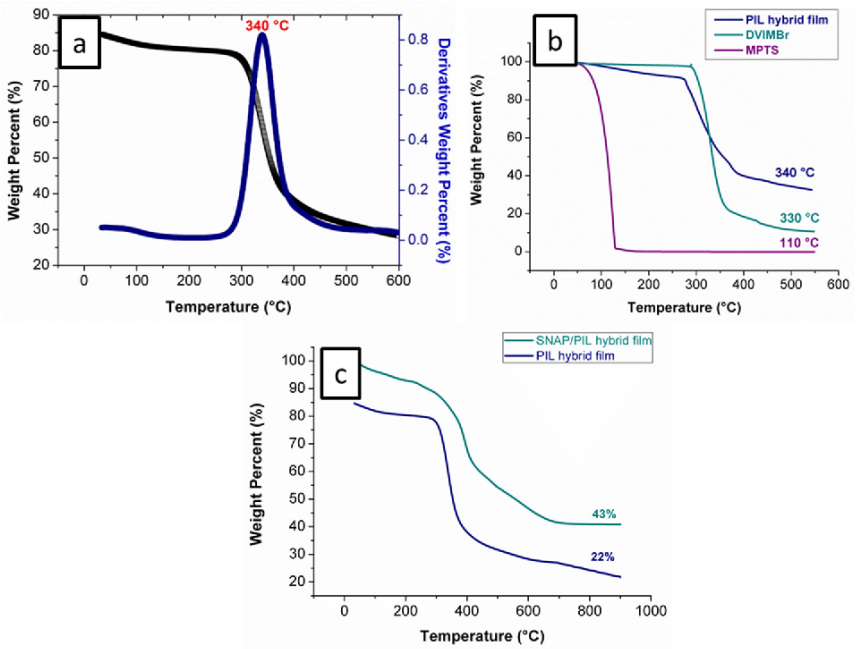


Figure 5. TGA curves of (**a**) PIL hybrid film with first derivative *vs.* temperature; (**b**) degradation behavior of the PIL hybrid film and the precursors; and (**c**) TGA under oxygen.

The glass transition (T_g) temperature of the PIL hybrid film is a critical parameter, which correlates to the barrier properties and establishes maximum service temperature of the film, and has been determined from differential scanning calorimetry (DSC). The T_g of the PIL hybrid material is found to be 21 °C, whereas T_g of crosslinked DVIMBr have been observed around −40 °C (Figure 6).

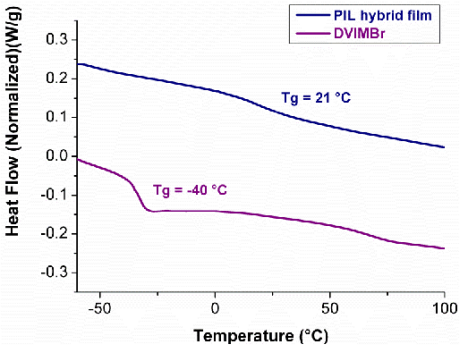


Figure 6. DSC thermogram showing the glass transition temperature, T_g of PIL hybrid film and DVIMBr.

This positive shift in T_g could be explained by the presence of extensive crosslinking, which limits segmental mobility of the chains and makes a more rigid structure at room temperature. No melting or crystallization peak is observed in DSC curve. The increase in T_g in the PIL hybrid material compared to DVIMBr can be attributed to the presence of extensive network formation as observed from FTIR.

3.3. Electrochemical Analysis

Potentiodynamic polarization investigation of the metal coupons coated with SNAP and the PIL/SNAP hybrid film was carried out to determine the electrochemical performance of the PIL hybrid film interfacial layer. Initially, the corrosion potential (E_{corr}) and corrosion current (I_{corr}) obtained from the Tafel plot is quite similar between the samples with and without the PIL hybrid interfacial layer; with the SNAP showing a slightly more noble E_{corr} but with similar I_{corr} to the PIL hybrid containing sample (Figure 7). However, after 24 h immersion in 3.5% salt solution, there was a significant difference between the two, in both E_{corr} and I_{corr}. The values for the PIL/SNAP hybrid film coated samples only changed marginally, especially for I_{corr}, indicating that the coatings have resisted corrosion quite well (Table 1). In contrast, SNAP-only coated samples show a significant increase in I_{corr} of two orders of magnitude; which indicates a significant increase in the corrosion rate after 24 h immersion. This observation reveals that, despite the good adhesion between the metal and SNAP, the coating may still allow diffusion of electrolyte thus over time corrosion occurs on the metal surface. The presence of the PIL hybrid film interfacial layer forms a barrier on the metal surface, thus preventing corrosion. The reason can be attributed to several factors; firstly, due to the thiol-ene click reaction, which can improve PIL hybrid film/SNAP coating's interfacial adhesion and crosslinking density. Secondly, the PIL hybrid film interfacial layer may also act as anticorrosion layer as PIL will act as radical scavengers [21]. Thirdly, MPTS improves coating's barrier effect through forming a well-organized organic crosslinking structure (C–S–C) and enables the decrease in corrosion of the underlying metal substrate.

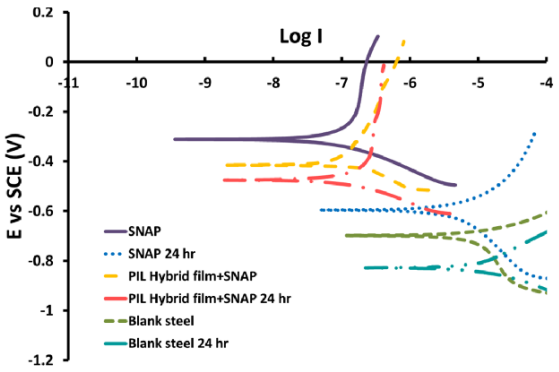


Figure 7. Tafel plot of the SNAP-coated samples with and without the PIL interfacial layer.

Table 1. Corrosion potential (E_{corr}) and current (I_{corr}) of the SNAP-coated samples with and without the PIL hybrid film interfacial layer.

Metal Sample	E_{corr} (V)	I_{corr} (A)	E_I (%)
Blank metal	−0.674	7.9×10^{-6}	–
SNAP coated	−0.312	7.4×10^{-8}	–
PIL/SNAP Hybrid film coated	−0.395	1.3×10^{-7}	–
Blank metal 24 h	−0.937	4.9×10^{-6}	–
SNAP coated 24 h	−0.613	4.1×10^{-6}	16.3
PIL/SNAP Hybrid film coated 24 h	−0.479	1.5×10^{-7}	96.9

Moreover, inhibition efficiency E_I (%) is calculated from the values of I_{corr} using the following equation [22]:

$$E_I\,(\%) = \frac{I_{corr} - I'_{corr}}{I_{corr}} \times 100 \quad (1)$$

where I_{corr} and I'_{corr} are uninhibited and inhibited corrosion current densities, respectively. The results revealed that the addition of PIL into the SNAP coating increase the *EI* (%) from 16.3% to 96.9% after 24 h immersion (Table 1).

This observation was also confirmed with the electrochemical impedance analysis, which shows a significant shift in the phase angle for samples with the PIL/SNAP-coated samples. As shown in Figure 8b, the impedance modulus is greater for samples coated with PIL/SNAP hybrid film interfacial layer compared to those coated with SNAP alone. The impedance modulus in the bode plot also remained almost unchanged after 24 h immersion in salt solution, compared to samples coated with only SNAP, where there is an order of magnitude drop in impedance modulus after 24 h. The phase angle shown in Figure 8a also shows significant differences in the samples coated with PIL/SNAP hybrid film, which appears as an additional time-constant at middle frequencies.

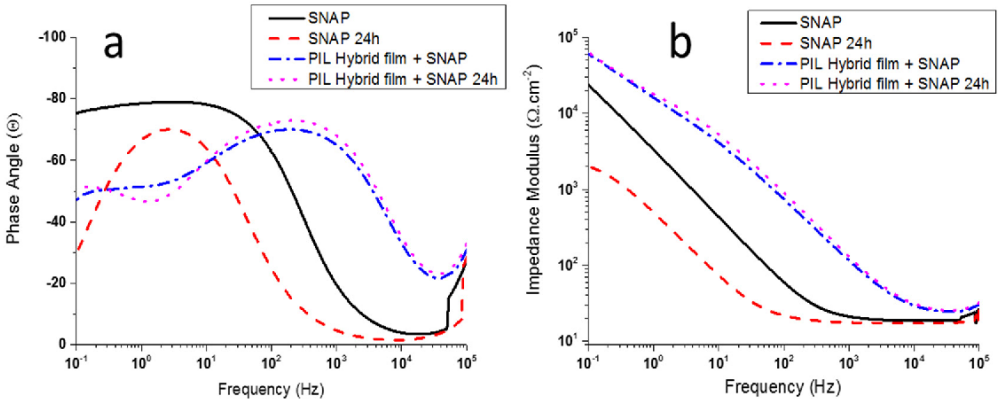


Figure 8. (**a**) Phase angle; (**b**) Impedance modulus of the SNAP-coated samples with and without the PIL interfacial layer.

These observations confirm the presence of the interfacial layer (which manifests as an additional capacitance) which changes the coating behavior from resistive to capacitive at these frequencies as it acts as a barrier to charge transfer. Similarly to the impedance modulus, the sample coated with the PIL/SNAP hybrid film also shows very little change after 24 h immersion in salt solution, indicating that it is structurally unchanged. In contrast, the phase angle of the sample coated only with SNAP coating shows a transition from a capacitor-like behavior to a resistor-like behaviors after 24 h, indicating that it may allow increased charge transport and diffusion.

This observation indicates a greater resistance of the coating, of which the resistance due to interfacial charge transfer and diffusion through the bulk coating can be modelled using an appropriate equivalent circuit (Figure 9). The analyses and fitting of the impedance curves of these samples (Table 2 and Figure 10) show that the presence of the PIL interfacial layer initially reduces the interfacial resistance by an order of magnitude, possibly due to the SNAP only coating forming a denser coating on the interface without the interfacial layer. However, it also significantly increased the coating resistance by several orders of magnitude, indicating that the coating itself becomes less permeable and more resistive compared to the SNAP-only coating as were seen from the bode plots and phase angle diagram. The capacitance values obtained are also initially similar, and was within the expected range for sol-gel coated samples [23]. However, after 24 h immersion in salt solution there was a significant drop in the interfacial and coating resistance of the SNAP only sample, with a decrease from 1.7 MΩ to 2.6 kΩ in interfacial resistance for the SNAP sample while the interfacial resistance of the PIL/SNAP

Moreover, inhibition efficiency E_I (%) is calculated from the values of I_{corr} using the following equation [22]:

$$E_I\,(\%) = \frac{I_{corr} - I'_{corr}}{I_{corr}} \times 100 \quad (1)$$

where I_{corr} and I'_{corr} are uninhibited and inhibited corrosion current densities, respectively. The results revealed that the addition of PIL into the SNAP coating increase the *EI* (%) from 16.3% to 96.9% after 24 h immersion (Table 1).

This observation was also confirmed with the electrochemical impedance analysis, which shows a significant shift in the phase angle for samples with the PIL/SNAP-coated samples. As shown in Figure 8b, the impedance modulus is greater for samples coated with PIL/SNAP hybrid film interfacial layer compared to those coated with SNAP alone. The impedance modulus in the bode plot also remained almost unchanged after 24 h immersion in salt solution, compared to samples coated with only SNAP, where there is an order of magnitude drop in impedance modulus after 24 h. The phase angle shown in Figure 8a also shows significant differences in the samples coated with PIL/SNAP hybrid film, which appears as an additional time-constant at middle frequencies.

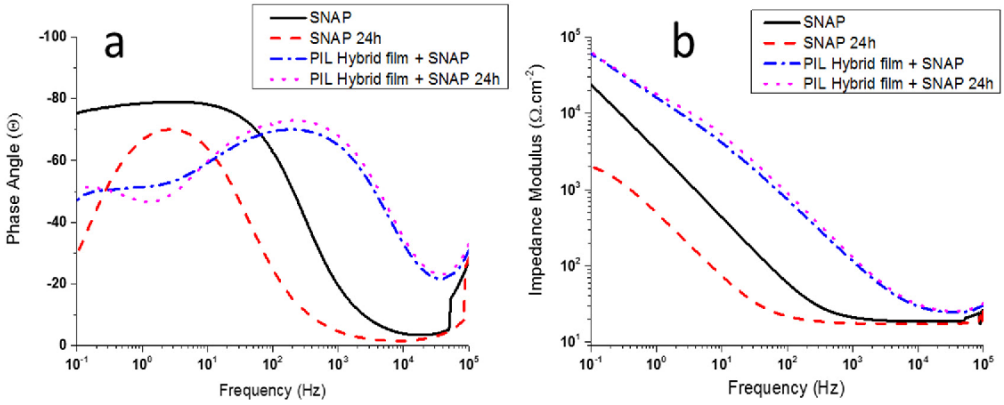


Figure 8. (**a**) Phase angle; (**b**) Impedance modulus of the SNAP-coated samples with and without the PIL interfacial layer.

These observations confirm the presence of the interfacial layer (which manifests as an additional capacitance) which changes the coating behavior from resistive to capacitive at these frequencies as it acts as a barrier to charge transfer. Similarly to the impedance modulus, the sample coated with the PIL/SNAP hybrid film also shows very little change after 24 h immersion in salt solution, indicating that it is structurally unchanged. In contrast, the phase angle of the sample coated only with SNAP coating shows a transition from a capacitor-like behavior to a resistor-like behaviors after 24 h, indicating that it may allow increased charge transport and diffusion.

This observation indicates a greater resistance of the coating, of which the resistance due to interfacial charge transfer and diffusion through the bulk coating can be modelled using an appropriate equivalent circuit (Figure 9). The analyses and fitting of the impedance curves of these samples (Table 2 and Figure 10) show that the presence of the PIL interfacial layer initially reduces the interfacial resistance by an order of magnitude, possibly due to the SNAP only coating forming a denser coating on the interface without the interfacial layer. However, it also significantly increased the coating resistance by several orders of magnitude, indicating that the coating itself becomes less permeable and more resistive compared to the SNAP-only coating as were seen from the bode plots and phase angle diagram. The capacitance values obtained are also initially similar, and was within the expected range for sol-gel coated samples [23]. However, after 24 h immersion in salt solution there was a significant drop in the interfacial and coating resistance of the SNAP only sample, with a decrease from 1.7 MΩ to 2.6 kΩ in interfacial resistance for the SNAP sample while the interfacial resistance of the PIL/SNAP

hybrid film remains similar to before. This trend indicates that the interface between the metal and SNAP coating has corroded, as the SNAP coating is still permeable to electrolyte. When the PIL hybrid film interfacial layer is present, the interfacial resistance remained high and actually increased to 300 kΩ after 24 h immersion, which indicates that the PIL hybrid layer provides a significant barrier protection and passivation of the metal surface. The more stable capacitance values of the PIL/SNAP hybrid film coated samples also indicate that they are more stable and maintained the integrity of the interfacial layer after 24 h immersion.

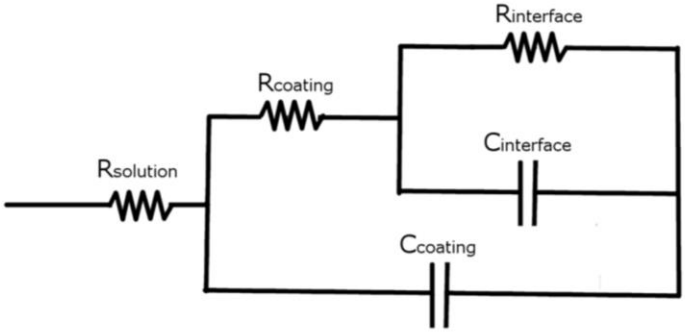


Figure 9. The equivalent circuit used to model the impedance data of a permeable coating.

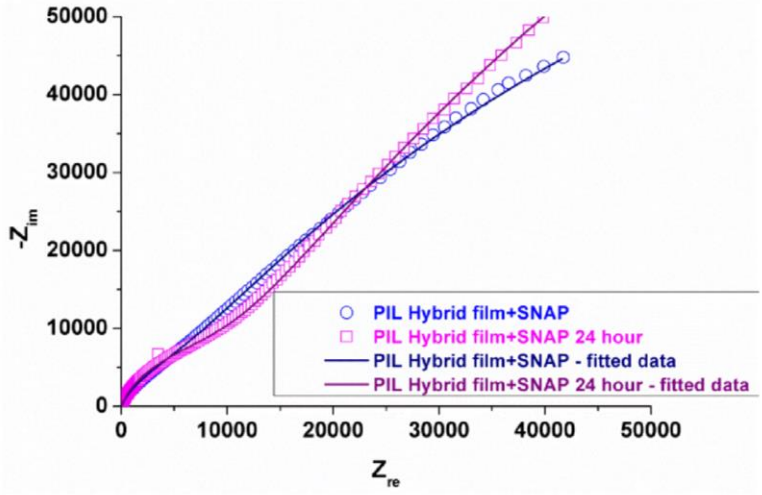


Figure 10. Nyquist plot and modelling result of the impedance data for PIL hybrid film/SNAP coated samples.

Table 2. Resistance and capacitance values obtained from EIS modelling (using the model in Figure 9).

SAMPLE	$R_{solution}$ (Ω)	$R_{coating}$ (Ω)	$C_{coating}$ (F)	$R_{interface}$ (Ω)	$C_{interface}$ (F)
SNAP only	21	158	4.16×10^{-5}	1.17×10^{6}	2.08×10^{-5}
SNAP only 24 h	12	18	8.44×10^{-6}	2613	4.08×10^{-4}
PIL/SNAP hybrid film	23	15,257	7.04×10^{-6}	1.54×10^{5}	1.44×10^{-5}
PIL/SNAP hybrid film 24 h	21	15,009	4.45×10^{-6}	3.19×10^{5}	1.84×10^{-5}

Interestingly, the presence of the PIL hybrid layer also seems to impart anti-corrosion properties even in the presence of deliberately-induced defects. When the surface of the sample coated with PIL/SNAP hybrid film was scratched, the impedance spectra (Figure 11a) show a decrease in

impedance modulus to values similar to that of uncoated metal, which is expected due to the fact that the electrochemical response of the scratched samples would be largely due to the exposed metal surface. However, upon 72 h immersion in salt solution the impedance spectra of the scratched PIL/SNAP hybrid film coated samples show less change compared to an uncoated metal samples over 3 h. Although the impedance of the sample did not return to values of a fully intact coating, there was a marginal increase in impedance modulus after 12 h; and over the 72 h duration there was a slow shift in the phase angle towards middle frequencies as was observed with uncoated metal samples, although after 72 h the shift was less than the uncoated metal after 3 h (Figure 11b). This observation indicates that the PIL hybrid film acts as an active, anti-corrosion layer, and has the potential to impede corrosion in the defect area.

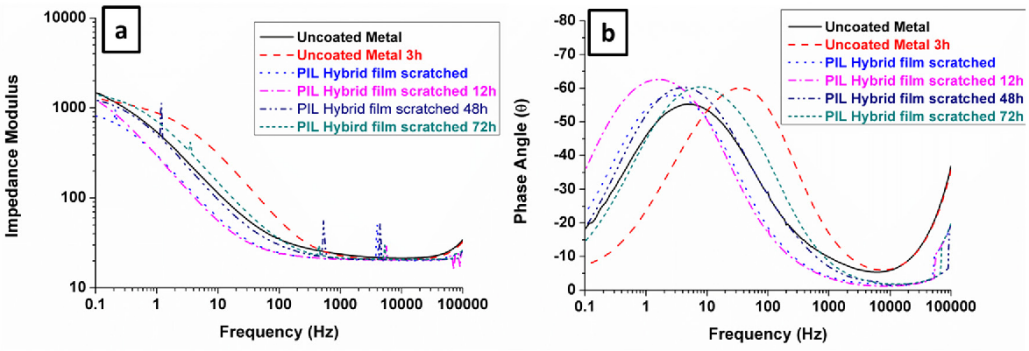


Figure 11. (**a**) Bode plot; (**b**) phase angle of the impedance of a scratched PIL hybrid film/SNAP coated sample over 72 h compared with uncoated metal samples.

4. Conclusions

We have successfully prepared the novel MPTS/PIL hybrid anticorrosive film for multilayer coating and investigated the chemical structure and thermal properties of the PIL hybrid film. Thermal analysis of MPTS/PIL hybrid film showed the high thermal stability of the PIL hybrid film with higher T_g due to the strong dual network formation of thiol-ene and sol-gel reaction. Further study using electrochemical investigation shows that PIL hybrid film offers significant protection and passivation of the metal surface in addition to imparting anti-corrosion properties under damaged condition. These results show that these MPTS/PIL hybrid films are promising interfacial layer in anti-corrosion applications.

Acknowledgments: The authors gratefully acknowledge the financial support of the Australian Research Council's Linkage grant for carrying out this work and also the industry partner Wave rider Energy for financial support of this work. The authors would like to thank Martin Johnston of Flinders University for assistance with the solid state NMR.

Author Contributions: N.K.D and N.R.C contributed to develop the concept and designed the experiments along with M.T. M.T. synthesized the materials and performed the experiments. S.S. supported M.M. to perform the electrochemical characterization. M.T. analyzed the data in collaboration with N.R.C, N.K.D. and S.S.M.T. wrote the draft with support from N.K.D., N.R.C.; and the manuscript was finalized through contributions of all the authors. All authors have given approval to the final version of the manuscript.

Conflicts of Interest: The authors declare no conflict of interest.

References

1. Khramov, A.N.; Balbyshev, V.N.; Voevodin, N.N.; Donley, M.S. Nanostructured sol-gel derived conversion coatings based on epoxy- and amino-silanes. *Prog. Org. Coat.* **2003**, *47*, 207–213. [CrossRef]
2. Rahimi, H.; Mozaffarinia, R.; Hojjati Najafabadi, A. Corrosion and wear resistance characterization of environmentally friendly sol-gel hybrid nanocomposite coating on AA5083. *J. Mater. Sci. Technol.* **2013**, *29*, 603–608. [CrossRef]

3. Rahimi, S.K.; Potrekar, R.; Dutta, N.K.; Choudhury, N.R. Anticorrosive interfacial coatings for metallic substrates. *Surf. Innov.* **2013**, *1*, 112–137. [CrossRef]
4. Vijayalakshmi, U.; Rajeswari, S. Synthesis and characterization of sol-gel derived glass-ceramic and its corrosion protection on 316L SS. *J. Sol-Gel Sci. Technol.* **2007**, *43*, 251–258. [CrossRef]
5. Zheludkevich, M.L.; Salvado, I.M.; Ferreira, M.G.S. Sol-gel coatings for corrosion protection of metals. *J. Mater. Chem.* **2005**, *15*, 5099–5111. [CrossRef]
6. He, X.; Shi, X. Self-repairing coating for corrosion protection of aluminum alloys. *Prog. Org. Coat.* **2009**, *65*, 37–43. [CrossRef]
7. Metroke, T.L.; Parkhill, R.L.; Knobbe, E.T. Passivation of metal alloys using sol-gel-derived materials—A review. *Prog. Org. Coat.* **2001**, *41*, 233–238. [CrossRef]
8. Sanchez, C.; de A. A. Soler-Illia, G.J.; Ribot, F.; Lalot, T.; Mayer, C.R.; Cabuil, V. Designed hybrid organic-inorganic nanocomposites from functional nanobuilding blocks. *Chem. Mater.* **2001**, *13*, 3061–3083. [CrossRef]
9. Kannan, A.G.; Choudhury, N.R.; Dutta, N.K. Synthesis and characterization of methacrylate phospho-silicate hybrid for thin film applications. *Polymer* **2007**, *48*, 7078–7086. [CrossRef]
10. Vreugdenhil, A.J.; Balbyshev, V.N.; Donley, M.S. Nanostructured silicon sol-gel surface treatments for Al 2024-T3 protection. *J. Coat. Technol.* **2001**, *73*, 35–43. [CrossRef]
11. Donley, M.S.; Mantz, R.A.; Khramov, A.N.; Balbyshev, V.N.; Kasten, L.S.; Gaspar, D.J. The self-assembled nanophase particle (SNAP) process: A nanoscience approach to coatings. *Prog. Org. Coat.* **2003**, *47*, 401–415. [CrossRef]
12. Sinapi, F.; Forget, L.; Delhalle, J.; Mekhalif, Z. Self-assembly of (3-mercaptopropyl)trimethoxysilane on polycrystalline zinc substrates towards corrosion protection. *Appl. Surf. Sci.* **2003**, 464–471. [CrossRef]
13. Sinapi, F.; Delhalle, J.; Mekhalif, Z. XPS and electrochemical evaluation of two-dimensional organic films obtained by chemical modification of self-assembled monolayers of (3-mercaptopropyl)trimethoxysilane on copper surfaces. *Mater. Sci. Eng.* **2002**, *22*, 345–353. [CrossRef]
14. Bagiyan, G.A.; Koroleva, I.K.; Soroka, N.V.; Ufimtsev, A.V. Oxidation of thiol compounds by molecular oxygen in aqueous solutions. *Russ. Chem. Bull.* **2003**, *52*, 1135–1141. [CrossRef]
15. Yuan, J.; Antonietti, M. Poly(ionic liquid) latexes prepared by dispersion polymerization of ionic liquid monomers. *Macromolecules* **2011**, *44*, 744–750. [CrossRef]
16. Taghavikish, M.; Subianto, S.; Dutta, N.K.; Choudhury, N.R. Facile fabrication of polymerizable ionic liquid based-gel beads via thiol-ene chemistry. *ACS Appl. Mater. Interfaces* **2015**, *7*, 17298–17306. [CrossRef] [PubMed]
17. Tremont, R.; de Jesús-Cardona, H.; García-Orozco, J.; Castro, R.J.; Cabrera, C.R. 3-mercaptopropyltrimethoxysilane as a Cu corrosion inhibitor in KCL solution. *J. Appl. Electrochem.* **2000**, *30*, 737–743. [CrossRef]
18. Damia, C.; Sarda, S.; Deydier, E.; Sharrock, P. Study of two hydroxyapatite/poly(alkoxysilane) implant coatings. *Surf. Coat. Technol.* **2006**, *201*, 3008–3015. [CrossRef]
19. Piwoński, I.; Grobelny, J.; Cichomski, M.; Celichowski, G.; Rogowski, J. Investigation of 3-mercaptopropyltrimethoxysilane self-assembled monolayers on Au(111) surface. *Appl. Surf. Sci.* **2005**, *242*, 147–153. [CrossRef]
20. Bauer, F.; Ernst, H.; Decker, U.; Findeisen, M.; Gläsel, H.-J.; Langguth, H.; Hartmann, E.; Mehnert, R.; Peuker, C. Preparation of scratch and abrasion resistant polymeric nanocomposites by monomer grafting onto nanoparticles, 1 FTIR and multi-nuclear NMR spectroscopy to the characterization of methacryl grafting. *Macromol. Chem. Phys.* **2000**, *201*, 2654–2659. [CrossRef]
21. Xu, A.; Zhang, F.Z.; Jin, F.; Zhang, R.; Luo, B.; Zhang, T. The evaluation of coating performance by analyzing the intersection of bode plots. *Int. J. Electrochem. Sci.* **2014**, *9*, 5116–5125.

22. Messaadia, L.; ID El mouden, O.; Anejjar, A.; Messali, M.; Salghi, R.; Benali, O.; Cherkaoui, O.; Lallam, A. Adsorption and corrosion inhibition of new synthesized pyridazinium-based ionic liquid on carbon steel in 0.5 M·H_2SO_4. *J. Mater. Environ. Sci.* **2015**, *6*, 598–606.
23. Galio, A.F.; Lamaka, S.V.; Zheludkevich, M.L.; Dick, L.F.P.; Müller, I.L.; Ferreira, M.G.S. Inhibitor-doped sol-gel coatings for corrosion protection of magnesium alloy AZ31. *Surf. Coat. Technol.* **2010**, *204*, 1479–1486. [CrossRef]



© 2016 by the authors; licensee MDPI, Basel, Switzerland. This article is an open access article distributed under the terms and conditions of the Creative Commons by Attribution (CC-BY) license (http://creativecommons.org/licenses/by/4.0/).

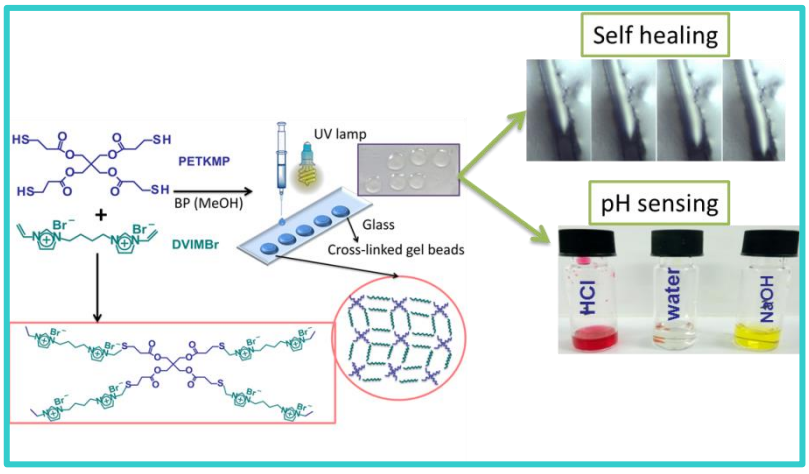
Chapter 8: Summary and Recommendations

8.1 Summary

This chapter summarises the outcomes of the research investigations carried out in this thesis. In this work, polymerized ionic liquid (PIL) corrosion inhibitors in three different forms; gels, nanoparticles, and films have been synthesised using thiol-ene based click chemistry. A fundamental understanding of the structure-property relationship of these PILs has been developed using a range of advanced techniques, and their application as corrosion inhibitors within a sol-gel coating has been evaluated.

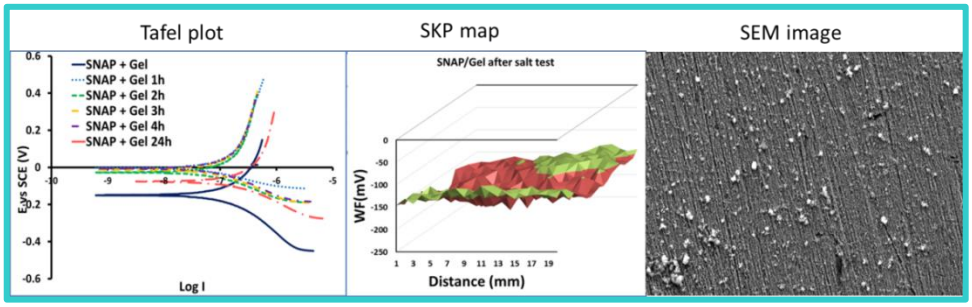
The key research outcomes and highlights of the present investigation are as follows:

1) In chapter 3, the fabrication of multifunctional PIL gel beads using vinyl imidazolium based ionic liquid through click-type reactions was investigated. These PIL gels exhibited multiple characteristics including 1) self-healing characteristics due to their rubbery nature, 2) the ability to uptake active molecules which acts as corrosion inhibitors, and 3) pH sensing through the incorporation of indicator molecules. These functionalities demonstrate the potential of PIL gels as a multifunctional material for the control, detection and inhibition of corrosion.

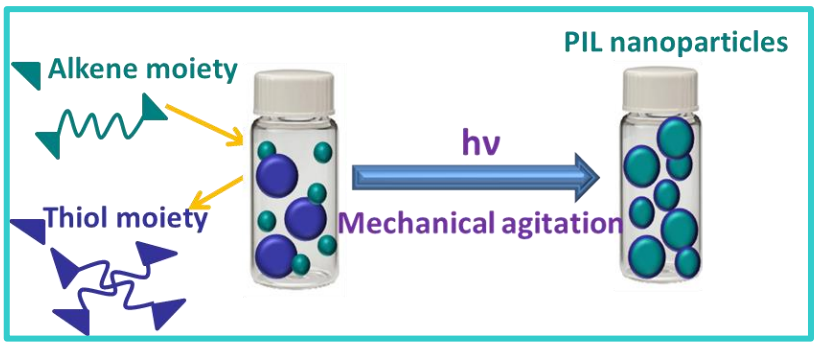


2) The unique characteristics of the PIL gel synthesized in chapter 3 show their potential use in anticorrosion applications. Thus, in chapter 4 the inhibition performance of PIL gel microparticles in a sol-gel, self-assembled nanophase particles (SNAP) coatings on carbon steel was investigated using

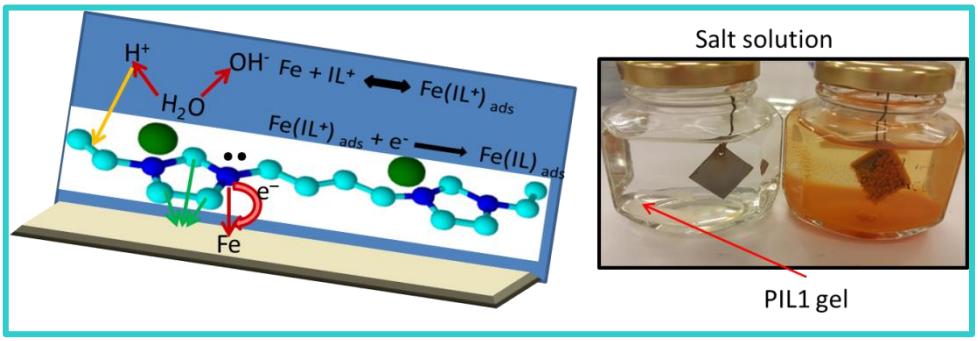
electrochemical techniques. The PIL gel exhibited strong interaction and adsorption into the mild steel surface, which formed a protective layer that protects the steel surface from an aggressive environment (which simulates marine environments). Based on the obtained results, it was concluded that the presence of S and N in the structure of PIL provides free electron pairs that promoted chemical adsorption on the metallic surface. Also, the surface work function distributions on the sample surface were measured using scanning kelvin probe (SKP) demonstrated the strong surface interaction of SNAP loaded with PIL gel particle compared to SNAP alone. This chapter demonstrates a unique and simple way of applying the PIL corrosion inhibitors in a coating, which has not been previously investigated.



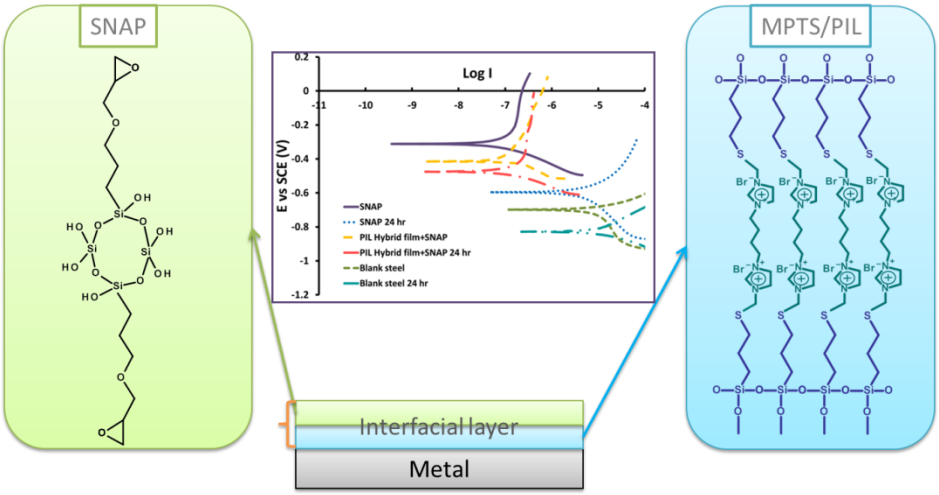
3) In chapter 5, the synthesis and application of another form of imidazolium based PIL corrosion inhibitor in a SNAP coating was investigated. Thiol-ene photo-polymerization in a mini-emulsion system was used to fabricate crosslinked PIL nanoparticle dispersions in an aqueous medium. The optimum concentration of PIL nanoparticle for achieving greater efficiency on a SNAP coating interfacial layer was examined. The PIL nanoparticles exhibited improved inhibitor properties to the coating due to the interaction between the –C=N– group and electronegative nitrogen in the PIL with the metal surface. This work provides another new and rapid way for the synthesis of PIL based corrosion inhibitors in an environmentally friendly medium, which enhances the corrosion protection ability of SNAP-based coatings.



4) The corrosion inhibition properties of imidazolium based PIL gel and nanoparticles were evaluated in Chapters 3 and 5. However, further study into the mechanism of inhibition was required in order to obtain valuable information about the adsorption behaviour of these corrosion inhibitors. Thus, a fundamental study into the mechanism and differences in inhibition effect of ionic liquids (ILs) and PIL based on three different imidazolium ILs with different spacer chain lengths are presented in chapter 6, which covers adsorption behaviour of ILs as corrosion inhibitors onto steel surface. It was observed that the adsorption, and thus inhibition efficiency, of ILs increased with concentration and was dependent on the alkyl chain spacer length. Based on the obtained results, it was also concluded that extra heteroatoms in PIL gel crosslinked by thiol-ene chemistry further improved the interaction between heteroatoms and iron of metal surface and resulted in higher inhibition efficiency compared to the base IL. These PIL gel were also shown to act as a controlled delivery type corrosion inhibitor over a prolonged period of time through the release of oligomeric species.



5) The formation of a unique PIL hybrid interfacial layer in the form of a thin film combining the functionalities of sol-gel and thiol-ene chemistry as well as the PIL was studied for the first time in chapter 7. In addition, SNAP coating was employed on top of this PIL hybrid film to prepare a multilayer thin film coating for enhanced corrosion protection. The excellent protection of metal surfaces against corrosion with the application of the PIL hybrid film was studied by electrochemical analysis. This work demonstrates the potential of the combined approach using (3-mercaptopropyl) trimethoxysilane (MPTS) for anchoring the hybrid film onto the metal surface through click chemistry as precursor to sol-gel coating to improve the protection of metal surface against corrosion. Based on the obtained results, it was concluded that this PIL hybrid film shows great potential for a targeted approach in its use as an interfacial layer in anti-corrosion applications.



8.2 Recommendations

This research demonstrates the fabrication of PIL based corrosion inhibitors in three different forms of varying size scales. It also shows the potential of these three forms of PIL as corrosion inhibitors in SNAP coatings. The PIL gel beads were fabricated using thiol-ene chemistry and the optimal stoichiometric ratio was established. The PIL gel beads corrosion inhibitor demonstrate the ability to uptake active molecules such as corrosion inhibitors and the ability for pH sensing or controlled release of active anticorrosion agents. Due to time constraints, the study into the properties of these PIL

gel beads was only undertaken in relation to their bulk form and significant scope remains for future work to study the application of such properties on the coating in the future. Furthermore, the potential of the PIL gel beads as self-healing material has been demonstrated, but this was studied only in the bulk form of the gel; further investigation on the application of the self-healing aspect of PIL gel beads in a coating would greatly enhance its multifunctional dimension in anticorrosion applications, but was not possible within the timeframe of this thesis. In the future, it would be useful and informative to further develop the fabrication and study of PIL gel bead and nanoparticles with regards to molecular design features such as different spacer length of the imidazolium based PIL, with the corresponding study into their application as corrosion inhibitor to compare their anticorrosion properties and inhibition efficiency in a coating. Although the PIL gels and nanoparticles have been fully characterised using a range of techniques, further analysis to support the characterization using other techniques including solid state NMR, matrix-assisted laser desorption/ionization (MALDI), and gel permeation chromatography (GPC) would provide further valuable and complimentary information on the physicochemical properties of this material; however these were not possible within the time constraints of this research project.

In this study, we have also reported our preliminary investigation into the mechanism and fundamentals of the corrosion protection of the IL and PIL on steel surfaces. However, due to time constraints the current study on the inhibition effect of IL and PIL gel has been limited predominantly to those containing a butyl spacer. It is recommended to carry out further investigation on inhibition mechanism of IL and PIL gel with other spacer length (hexyl and octyl), which showed better potential for corrosion inhibition application. The quartz crystal microbalance with dissipation (QCM-D) and polarization study provided an insight into the mechanism and adsorption behaviour of IL and PIL gel corrosion inhibitors. Since our initial results on the effect of alkyl spacer lengths (hexyl and octyl) show that the length of the alkyl group have a significant effect on the properties of these PIL, it can be expected to lead to further enhancement or variety in their applications in the field of anticorrosion coating. Regardless, further study into the chemical structure and mechanism of adsorbed layer on the steel surface with X-ray photoelectron spectroscopy (XPS) and SEM/EDS experiments as well as complementary techniques such as MALDI and NMR are required in order to fully characterize this adsorbed layer.

In conclusion, this research contributes to the overall goal of developing a new class of PIL based corrosion inhibitors using click-chemistry with fundamental understanding of structure-property relationship and evaluating their performances as corrosion inhibitors. Although further work is needed in order to fully understand the structure-property relationship of these PILs and their anticorrosion properties, the work presented in this thesis have shown that these PILs present a class of multifunctional material combining unique properties, versatility, and facile fabrication with strong potential in anticorrosion applications.